NOTCH-ROOT ELASTIC-PLASTIC STRAIN-STRESS ESTIMATIONS IN PARTICULATE METAL MATRIX COMPOSITES (PMMCS) UNDER GENERAL LOADING CONDITIONS

BY

GBADEBO MOSES OWOLABI

A Thesis submitted to

the Faculty of Graduate Studies

In Partial Fulfillment of the Requirements for the Degree of

DOCTOR OF PHILOSOPHY

Department of Mechanical and Industrial Engineering

University of Manitoba

Winnipeg, Manitoba

© Gbadebo Moses Owolabi, December 2004

THE UNIVERSITY OF MANITOBA

FACULTY OF GRADUATE STUDIES

*****

COPYRIGHT PERMISSION

"Notch-Root Elastic-Plastic Strain-Stress Estimations in Particulate Metal Matrix Composites (PMMCS) Under General Loading Conditions"

BY

Gbadebo Moses Owolabi

A Thesis/Practicum submitted to the Faculty of Graduate Studies of The University of Manitoba in partial fulfillment of the requirement of the degree

Of

DOCTOR OF PHILOSOPHY

Gbadebo Moses Owolabi © 2004

Permission has been granted to the Library of the University of Manitoba to lend or sell copies of this thesis/practicum, to the National Library of Canada to microfilm this thesis and to lend or sell copies of the film, and to University Microfilms Inc. to publish an abstract of this thesis/practicum.

This reproduction or copy of this thesis has been made available by authority of the copyright owner solely for the purpose of private study and research, and may only be reproduced and copied as permitted by copyright laws or with express written authorization from the copyright owner.

ABSTRACT

Determining the stress and strain histories at the point of highest stress concentration in particulate metal matrix composites (PMMCs) is complicated particularly when they have a finite concentration of particles, the matrix material in the vicinity of the notch is elastic-plastic, and when multiaxial cyclic loads are applied to the component. In this research, two alternative analytical models are developed and implemented to estimate the composite elastic-plastic strain and stress histories in PMMC components subjected to multiaxial cyclic loads. The models are formulated using proposed energy-based approximate relations and the developed PMMCs elastic-plastic constitutive model. Each model consists of a set of nonlinear relations that can be solved to estimate the notch root parameters, from an elastic analysis. The models presented thus provide an easy to implement approximation to the otherwise rather complex non-linear problem.

The analytical results are compared to the local strains, obtained using 3D image correlation technology, at the depth of circumferential notched PMMC specimens subjected to multiaxial cyclic non-proportional loading. The results of the comparison show that the proposed models work well for the geometries and load paths considered. Both models are in good agreement with the experimental results in terms of the trends of the local shear and axial strains, and also agree quantitatively well with the experimental results.

As stated, the formulated notch root approximate relations require the development or adoption of a suitable elastic-plastic constitutive model. In this thesis,

two cyclic plasticity models developed originally for homogeneous materials, the Mróz multi-surface model and the endochronic theory of plasticity, were incorporated into two constitutive models that were developed to respect the heterogeneous nature of PMMCs. The models results were compared to experimental results obtained on tubular PMMCs specimens made of 6061 aluminum alloy reinforced with 10 and 20% by volume of alumina (Al_2O_3) subjected to multiaxial cyclic loads. It was observed that the developed models correlate well with the trends observed in the experimental results. However, for the load paths investigated, the endochronic theory-based PMMCs constitutive model gave better qualitative predictions of the experimental results than did the Mróz-based PMMCs constitutive model predictions, and was used in the notch root elastic-plastic strain-stress formulations.

ACKNOWLEDGEMENTS

I would like to express my deep sense of gratitude to my thesis advisor, Dr. M.N.K. Singh for her guidance and suggestions throughout the course of this research, and also for her careful reading and invaluable suggestions during the paper publications and thesis write ups. I would also like to thank every member of my doctoral advisory committee: Dr M.N. Bassim, Dr. C. Wu, and Dr. D. Polyzois for all their contributions and also for making themselves available to be part of this committee. Special thanks also go to Robert Thom (Zeus Engineering Ltd., Calgary, Alberta) and Tim Schmidt (Trilion Quality System, PA, USA) for their priceless technical contributions, instructions and guidance during the experimentations. Also, special thanks go to Paul Krueger (Mechanical Engineering Technologist) and Irwin Penner (Mechanical Engineering Machinist) for the assistance during the machining of the specimens used. I would like to thank Kim Majury (System Analyst) for assisting in repairing the PC when the need arose. The suggestions and guidance given by Dr. Abba Gumel (Department of Mathematics) during the implementation of the non-linear sets of equations and the brotherly pieces of advice, friendship, and encouragements given by Dr. M. Tachie are also highly appreciated.

I am especially grateful to my wife, Adenike Owolabi, for her constant support, love and prayers and for the encouragements given to me as the needs arise. Special thanks also go to every member of our families (the Owolabis and the Bamgbades) for their thoughtfulness and prayers. There are numerous friends that I might not be able to mention by names, who have supported me throughout the duration of this program. I

really thank you all for your friendships and encouragements. Special thanks go to my good friend, Ogunlola Raimi, for being such a wonderful friend and a friend at all times.

The financial supports provided by the University of Manitoba in form of Graduate Fellowship, the graduate awards provided by the Faculty of Engineering in form of Edward R. Toporeck Fellowship and Trans-Canada Pipeline Fellowships, and also the research grants provided by National Science and Engineering Research Council of Canada (NSERC), and the Canadian Foundation for Innovation (CFI) are highly appreciated.

Finally, unto that King Eternal, the Only Wise God be all the glory forever and ever. Thy kingdom come, O Lord, and thy will be done.

DEDICATION

This Doctoral Thesis is Dedicated to:

My Wife,

Adenike Owolabi;

My Parents,

Pa J.A Owolabi and Mrs. Ester Owolabi;

and above all

The Lord Jesus,

The King Eternal, the Only Wise God, who was, is, and forever will be, my ALL IN ALL. In Him, I live, move and have my being.

TABLE OF CONTENTS

ABSTRACT ii

ACKNOWLEDGEMENTS iv

DEDICATION vi

TABLE OF CONTENTS vii

LIST OF TABLES xi

LIST OF FIGURES xii

NOMENCLATURE xviii

CHAPTER ONE: INTRODUCTION 1

1.1 Particulate Metal Matrix Composites (PMMCs) 1

1.2 Research Motivation and Objectives 6

1.3 Components of Research and Summary of Thesis 10

CHAPTER TWO: BACKGROUND AND LITERATURE REVIEW 14

2.1 Constitutive Models for PMMCs 16

2.1.1. Elastic Constitutive Models 16

2.1.2 Elastic-Plastic Constitutive Models 23

2.2 Notch-Root Stress-Strain Estimation Methods 28

2.2.1 Neuber's Rule and Equivalent Strain Energy Density (ESED) Method 28

2.2.2 Multiaxial Notch Root Approximation Relations 31

2.3 Experimental Measurements of Notch Root Strains 33

2.4 Summary of Literature Review 38

CHAPTER THREE: ELASTIC-PLASTIC CONSTITUTIVE RELATIONS FOR PMMCS 43

3.1 Elastic Stress-Strain Components 45

3.2 Cyclic Plasticity Models 49

3.2.1 Mróz Model 50

3.2.2 Endochronic Theory of Plasticity 64

3.3 PMMCs Elastic-Plastic Constitutive Models 73

3.3.1 Constitutive Relations Based on Mróz Model 74

3.3.2 Constitutive Relations Based on Endochronic Theory 75

3.4 Implementation Procedure 77

3.4.1 Mróz-Based PMMCs constitutive Model Implementation 78

3.4.2 Endochronic Theory-Based PMMCs Constitutive Model Implementation 81

3.5 Summary of Chapter Three 82

CHAPTER FOUR: MULTIAXIAL APPROXIMATE RELATIONS FOR PMMCS 92

4.1 Proposed Incremental Strain Equivalent Strain Energy Density for PMMCs 93

4.2 Proposed Incremental Neuber's Rule for PMMCs 97

4.3 Notch Root Parameters Estimation Relations 99

4.4 Solution Methodology 103

4.5 Implementation Procedure for the Simplified Methods 115

4.6 Summary of Chapter Four 118

CHAPTER FIVE: MATERIAL DESCRIPTIONS AND EXPERIMENTAL TECHNIQUES 123

5.1 Testing Equipment Descriptions 124

5.1.1 Load Frame 124

5.1.2 Optical Strain Measurement 126

5.1.3 Point Strain Measurement 129

5.1.4 Data Acquisition System 132

5.2 Test Specimens 134

5.3 Experimental Tests 135

5.3.1 Set-Up Verification Tests 136

5.3.2 Constitutive Models Validation Tests 137

5.3.3 Elastic Stress Concentration factors Determination Tests 139

5.3.4 Notch-Root Parameters Validation Tests 141

5.3.4.1 Non-Proportional Monotonic Loading 141

5.3.4.2 Proportional Cyclic Loading 142

5.3.4.3 Non-Proportional Cyclic Loading 142

5.4 Summary of Chapter Five 144

CHAPTER SIX: COMPARISONS OF ANALYTICAL AND EXPERIMENTAL RESULTS 160

6.1 Results of Experimental Set-Up Verification Tests 160

6.2 Constitutive Model Results and Discussions 161

6.3 Results of Elastic Stress concentration Factors Tests 167

6.4 Comparisons of Proposed Models and Experimental Results 168

6.4.1 Monotonic Non-Proportional Loading 168

6.4.2 Cyclic Proportional Loading 170

6.4.3 Constant Amplitude Non-Proportional Loading 171

6.4.4 Unbalanced Loading 173

6.4.5 Variable Amplitude Non-Proportional Loading 174

CHAPTER SEVEN: CONCLUSIONS AND RECOMMENDATIONS 202

7.1 Conclusions 202

7.2 Recommendations 206

REFERENCES 208

LIST OF TABLES

Table 5.1: Chemical Compositions of 6061 alloy 145

Table 5.2: Tensile Properties (Typical and Minimum Values) 145

Table 5.3: Summary of Notched Specimens Load Paths 146

Table 6.1: Dirichlet Constants 175

Table 6.2 Stress Concentration Factors for the Mild Notched Specimens 175

Table 6.3 Stress Concentration Factors for the Relatively Sharp Notched Specimens 175

LIST OF FIGURES

Fig. 2.1: Stress Components of a Notched PMMC Representative Element under Multiaxial Loads 40

Fig. 2.2: Eshelby's Model: (a); Homogeneous Inclusion Composite (b) Inhomogeneous Composite 41

Fig. 2.3: Graphical Representation (a) Incremental ESED Method, (b) Incremental Neuber's Rule 42

Fig. 3.1: Kinematic Hardening 84

Fig. 3.2: Descritization of the Material Stress-Strain Curve and the Corresponding Hardening Surfaces 84

Fig. 3.3: Loading/Unloading Criterion for Classical Theory of Plasticity 85

Fig. 3.4: Matrix Elastic-Plastic Loading during Elastic Unloading Increment 85

Fig. 3.5: Descritizaton of the Material Stress-Plastic Strain Curve into Segments to Estimate the Material Constants for Endochronic theory 86

Fig. 3.6a: Flow Chart for Mróz-based PMMCs Constitutive Model 87

Fig. 3.6b: Continuation of Fig. 3.6a (Flow Chart for Mróz-Based PMMCs Constitutive Model) 88

Fig. 3.7: Computer Flow Chart for Matrix Plastic Straining Using Mróz-Based PMMCs Plasticity Model 89

Fig. 3.8a: Flow Chart for Stress-Controlled Endochronic Theory-Based PMMCs Constitutive Model 90

Fig. 3.8b: Continuation of Fig. 3.8a (Flow Chart for Stress-Controlled Endochronic Theory-Based PMMCs Constitutive Model) 91

Fig. 4.1: Illustration of Simplified Method 120

Fig. 4.2a: Flow Chart for Notch Root Elastic-Plastic Strain-Stress Analysis for PMMCs 121

Fig. 4.2b: Continuation of Fig. 4.2a: (Flow Chart for Notch Root Elastic-Plastic Strain-Stress Analysis for PMMCs) 122

Fig. 5.1 Experimental Set Up 147

Fig. 5.2: Servohydraulic System (a) Load Frame and Controller (b) Hardware and Software Interfaces 148

Fig. 5.3: Optical Measuring System 148

Fig. 5.4: A Three-Element Rosettes Strain Gage 149

Fig. 5.5: Signal Conditioners and Circuit (a) 2100 System Signal Conditioner/Amplifier (b)Wheatstone Bridge Circuit 149

Fig. 5.6: 2620 Series Instron Dynamic Extensometer 150

Fig.5.7: 6061/Al_2O_3/xx-T6 PMMCs Monographs 150

Fig. 5.8: Geometry of the Smooth Solid Specimen 151

Fig. 5.9: Geometry of the Smooth Tubular Specimen 151

Fig. 5.10: Geometry of the Mild Notched Specimen 152

Fig. 5.11: Geometry of the Relatively Sharp Notched Specimen 152

Fig. 5.12: A Schematic Representation for Strain Measurements with Three Independent Measuring Devices 152

Fig. 5.13: Data Acquisition Graphical Programming Flow Chart 153

Fig. 5.14: Box-Shaped Cyclic Non-Proportional Load Path 154

Fig.5.15: Cyclic Proportional Tension-Torsion Load Path 154

Fig. 5.16: Variable Amplitude Non-Proportional Load Paths 155

Fig. 5.17: Non-Zero Mean stress Load Path 155

Fig. 5.18: Notched Specimens with Random Pattern 156

Fig. 5.19: Monotonic Torsion-Combined Tension-Torsion Load path 156

Fig.5.20: Balanced Load with Equal Frequencies in Torsion and Tension 157

Fig. 5.21 Balanced Load Paths with Unequal Frequencies 158

Fig. 5.22: Load paths for Non-Zero Mean stress 158

Fig. 5.23: Variable Amplitudes Non-Proportional Load Paths 159

Fig. 6.1: Strain-Stress Curve for 10% Volume Fractions of Composite Using Various Measuring Devices 176

Fig. 6.2: Strain-Stress Curve for 20% Volume Fractions of Composite Using Various Measuring Devices 176

Fig. 6.3: Experimental and Ideal Load Paths 177

Fig. 6.4: Axial Vs. Shear Strains for Three Box-Paths Shown in Figures 5.12 117

Fig. 6.5: Typical Axial Strain Results in the Notch Root Area. (a) Section-Line Across the Notch Area (b) Axial Strain Distribution along the Section Line for Increasing Load 178

Fig. 6. 6: Descretization of 6061-Alloy Uniaxial Stress-Plastic Strain Curve 178

Fig. 6.7: Uniaxial Stress Strain Curves Produced by Combining Terms of the Dirichlet Series 179

Fig. 6.8: Variation of the Kernel Function with Intrinsic Time 179

Fig. 6.9: Axial Stress-Strain Curves for Various Volume Fractions of Reinforcement (Mróz-Based PMMCs Constitutive Model) 180

Fig. 6.10: Axial Stress-Strain Curves for Various Volume Fractions of Reinforcement (Endochronic Theory-Based Constitutive Model) 180

Fig. 6.11: Shear Stress-Strain Curves for Various Volume Fractions of Reinforcement (Mróz-Based PMMCs Constitutive Model) 181

Fig. 6.12: Shear Stress-Strain Curves for Various Volume Fractions of Reinforcement (Endochronic Theory-Based PMMCs Constitutive Model) 181

Fig. 6.13: Experimental and Simulated Axial Stress Vs. Axial Strain 182

Fig. 6.14: Experimental and Simulated Shear Stress Vs. Shear Strain 182

Fig. 6.15: Experimental and Simulated Shear Strains Vs. Axial Strains for Hollow Tube Specimen under Proportional Cyclic Load 183

Fig. 6.16: Experimental and Simulated Shear Strains Vs. Axial Strains for Hollow Tube Specimen under a variable Amplitude Load Path (Fig. 5.16 a) 183

Fig. 6.17: Experimental and Simulated Shear Strains Vs. Axial Strains for Hollow Tube Specimen under a variable Amplitude Load Path (Fig. 5.16 b) 184

Fig. 6.18: Experimental and Simulated Shear Strains Vs. Axial Strains for Hollow Tube Specimen under a Mean Stress Triangular Load Path 185

Fig. 6.19: Notch Root Shear Strains Vs. Axial Strains for Torsion, Combined Tension-Torsion Load Path 185

Fig. 6.20: Notch Root Shear Strains Vs. Axial Strains for Proportional Cyclic Load Path, Mild Notch 186

Fig. 6.21: Notch Root Shear Strains Vs. Axial Strains for Proportional Cyclic Load Path,

Relatively Sharp Notch 186

Fig. 6.22: Notch Root Shear Strains Vs. Axial Strains for Box-Shape Load Path, Mild Notch 187

Fig. 6.23: Notch Root Shear Strains Vs. Axial Strains for Box-Shape Load Path, Relatively Sharp Notch 187

Fig. 6.24: Notch Root Shear Strains Vs. Axial Strains for Rhombic-Shape Load Path 188

Fig 6.25: Notch Root Shear Strains Vs. Axial Strains for X-Shape Load Path, 10 % Volume Fraction 189

Fig. 6.26: Notch Root Shear Strains Vs. Axial Strains for X-Shape Load Path, 20 % Volume Fraction 190

Fig. 6.27: Notch Root Shear Strains Vs. Axial Strains for Tension-Torsion Frequency Ratio 1:3 Loading Path, 10% Volume Fraction 191

Fig. 6.28: Notch Root Shear Strains Vs. Axial Strains for Tension-Torsion Frequency Ratio 1:3 Load Path, 20% Volume Fraction 192

Fig 6.29: Notch Root Shear Strains Vs. Axial Strains for Tension-Torsion Frequency Ratio 1:3 Load Path (Sine Wave), 10% Volume Fraction 193

Fig. 6.30: Notch Root Shear Strains Vs. Axial Strains for Tension-Torsion Frequency Ratio 1:3 Load Path (Sine Wave), 20% Volume Fraction 194

Fig. 6.31: Notch Root Shear Strains Vs. Axial Strains for Tension-Torsion Frequency Ratio 1:5 Load Path (Sine Wave), 10% Volume Fraction 195

Fig. 6.32: Notch Root Shear Strains Vs. Axial Strains for Tension-Torsion Frequency Ratio 1:5 Load Path (Sine Wave), 20% Volume Fraction 196

Fig. 6.33: Notch Root Shear Strains Vs. Axial Strains for Elliptical-Shape Tension-Torsion Load Path with Non-Zero Mean Stress, 10% Volume Fraction 197

Fig. 6.34: Notch Root Shear Strains Vs. Axial Strains for Tension-Torsion Load Path with Non-Zero Mean Stress (Sine Wave), 20% Volume Fraction 198

Fig. 6.35: Notch Root Shear Strains Vs. Axial Strains for Linear-Shape Tension-Torsion Load Path with Non-Zero Mean Stress, 10% Volume Fraction 199

Fig. 6.36: Notch Root Shear Strains Vs. Axial Strains for Linear-Shape Tension-Torsion Load Path with Non-Zero Mean Stress, 20% Volume Fraction 200

Fig. 6.37: Notch Root Shear Strains Vs. Axial Strains for Variable Amplitude Load Path (Fig. 5.23 a) 201

Fig. 6.38: Notch Root Shear Strains Vs. Axial Strains for Variable Amplitude Load Path (Fig. 5.23 b) 201

NOMENCLATURE

C_f reinforcement stiffness tensor

C_m matrix stiffness tensor

C_r material constants

F yield function

$\mathbf{I}$ identity matrix

i,j,k,l,m,n indices, i,j,k,l,m,n = 1,2,3 (summation convention)

$\hat{n}$ unit outward normal

K_p hardening modulus

r r-th component

S_{ij} components of deviatoric stress tensor

S_{ijkl} components of Eshelby's tensor

$\mathbf{S}$ Eshelby's tensor

V_f reinforcement volume fraction

V_m matrix volume fraction

z, z' intrinsic time scale

C_r material constants

α_{ij}^{l} components of back stress tensor of surface l

δ Kronecker delta

Δ finite difference

ε_{ij} components of strain tensor

$\tilde{\varepsilon}_{ij}$ components of strain disturbance tensor

ε_{ij}^{c} components of constraint strain tensor

ε_{ij}^{t} components of transformation strain tensor

$d\mu$ magnitude of translation

$\rho(\,)$ memory function

σ_{ij} components of stress tensor

$\tilde{\sigma}_{ij}$ components of stress disturbance tensor

σ_{ij}^{c} components of constraint stress tensor

σ_{ij}^{t} components of transformation stress tensor

σ_{o}^{l} yield stress of surface l

$d\mu$ magnitude of translation

ζ intrinsic time measure

ξ_{ij} deviatoric components of α_{ij}

$d(.)$ differential form of variable or constant

$(.)^{e}$ elastic components of a variable

$(.)_{(f)}$ reinforcement component of a variable or constant

$(.)l$ component with reference to surface l

$(.)_{(m)}$ matrix components of a variable or constant

$(.)^{p}$ plastic components of a variable

$(.)_{q}$ q-th step component of a variable

$(.)^{T}$ total components of a variable

P axial Load

T	torque
V	composite volume
W	strain energy density
W_c	complementary strain energy density
α,β	Indices, $\alpha,\beta = 1,2,3$, no summation is implied.
$\rho( )$	memory function
ρ	Notch root radius
Ω	total strain energy density

CHAPTER ONE: INTRODUCTION

This chapter gives a general overview of the research carried out in this thesis. An introduction to particulate metal matrix composites (PMMCs) is given in Section 1.1. In Section 1.2, the research motivation and objectives are stated. Finally, in Section 1.3, the components of the research are stated along with the summary of the thesis.

1.1 Introduction to Particulate Metal Matrix Composites

Advancements in modern technology have resulted in an increasing demand for engineering materials. Significant progress has been made over the past few decades in the development of high performance composite materials. Accordingly, they are replacing conventional materials in large sectors such as in the aircraft, infrastructural, and automobile industries.

The broad definition of a composite as a compound made of various parts or elements, tends to be misleading. That is, the definition is too broad and can be interpreted to include virtually any material used today since it is almost impossible to produce a pure form of any substance. Consequently, a more restrictive definition is necessary. A composite has been defined [1] as a material consisting of two or more distinct parts, constituents or phases. It is only when the constituent phases have significantly different physical properties and thus the composite properties are noticeably different from the constituents properties that we have to come to recognize

these materials as composites. To establish reasonable and practical restrictions, and for the purpose of this research, the following criteria have been presented [2] and completely define a composite material:

a) A composite material must be a combination of at least two chemically distinct constituent materials, one of which can be regarded as the matrix phase, and the other represents the reinforcement phase(s). The matrix is the body constituent, it encloses the composite. The reinforcements are generally the additive phase. The reinforcements improve the strength and stiffness of the matrix material.

b) The size of each constituent must be such that it can be discernible and distinguishable.

c) The composite material should be created so that the new material has useful properties not possessed by the individual components.

d) The reinforcement phase(s) must not be by-products of a phase transformation occurring upon cooling after thermal treatment.

Based on the matrix material, composites can be grouped into three main categories: metal matrix composites (MMCs), ceramic matrix composites (CMCs), and polymer matrix composites (PMCs). Metal matrix composites have been the focus of substantial attention due to their potential to provide a significant increase in the stiffness and high-temperature strength of lightweight matrix alloys such as aluminum and titanium [3]. Initially, only continuously reinforced MMCs were developed. Of all the MMCs used in the aerospace industry, continuously reinforced MMCs provide the largest increase in strength and stiffness available. However continuously reinforced metal matrix composites are anisotropic materials and are quite expensive to manufacture. In

the 1970s and 1980s, emphasis shifted from a performance-alone to a cost motivation particularly in the applications of MMCs in aerospace and defense. Consequently, while continuously reinforced MMCs have a proven technical feasibility, they are not cost effective, and their applications are currently limited to military and highly specialized applications.

There has been a remarkable interest in the production of discontinuously reinforced MMCs, a family of MMCs that includes both whiskers (short fibres) and particulates. Whiskers are believed to have a better combination of strength and thermal stability than particulates. However, they have not been used to their full potential because of their high associated costs.

Particulate metal matrix composites (PMMCs) consist of a metallic matrix reinforced with relatively stiff ceramic particles. The selection of the matrix used is essential in producing metal matrix composites since the composite mechanical behavior is dependent on the matrix properties. Aluminum and magnesium alloys appear to be the most widely used matrix materials due to their low density and high thermal conductivity. Aluminum alloys are the most attractive due to their low density, good corrosion resistance, and their high thermal and electrical conductivity. Silicon carbide (SiC) and alumina (Al_2O_3) have been found to be the most widely used reinforcement materials due to their high strength and stiffness at room and elevated temperatures. They are furthermore compatible with the above common matrix materials and provide a good bond strength. The wear resistance of the PMMCs is also improved by the hard ceramic particles. Alumina is generally preferred over SiC, particularly in reinforcing wrought

aluminum based composites because SiC can be thermodynamically unstable in some aluminum alloys.

Particulate metal matrix composites have been produced by predominantly two methods. The first method is through powder metallurgy. Producing PMMCs through powder metallurgy does not allow significant chemical reaction or reinforcement fracture. The resulting composites are amenable to subsequent deformation processing through extrusion, forging and rolling [3]. The second method of PMMC production is the infiltration of particles or whiskers into liquid metals. Using this approach, excellent reinforcement properties can be taken advantage of.

In the past three decades, there has been considerable interest in the development of PMMCs. Some of the reasons attributed to the increasing interest include the fact that the composite properties are nearly isotropic, as such standard or near standard metal working methods can be used to form these materials. Furthermore, PMMCs are producing remarkable benefits in terms of energy savings, weight reduction and fatigue performance. PMMCs have been used in some industrial applications. The industrial applications of PMMCs are often related to niche applications where attainable property combinations such as high stiffness and modulus, high thermal conductivity and low coefficient of thermal expansion, or high wear resistance and low weight are essential for the proper functioning of components [4]. Some of these specialized applications range from aerospace access panel/doors and electronic packaging, automobile brake components and drive shafts, diesel engine pistons to automotive engine cylinder liners, and computer disc drives.

Although, remarkable progress has been made in the development of PMMCs and several attractive features have been stated that make them potential lightweight replacements to conventional materials in several applications, yet, they are not a choice material in many engineering (structural and non-structural) applications that the composite industry desires. In [5], Mortenson states that the question is not whether PMMCs are relevant engineering materials with an industrial potential, but rather if these high-tech, and often tailor-made materials will become large-scale bulk materials such as aluminum. Mortenson concludes that the materials will remain "high-tech" niche materials, designed and produced for specific classes of applications. Mortenson's comments are in response to the barriers that must be overcome in order to enhance the engineering applications of PMMCs.

One of the challenges facing the use of PMMCs is their relatively higher cost as compared to more conventional homogeneous engineering materials. To lower the cost of producing PMMCs, the composite industry should address the raw material, the design, and the product manufacturing costs. The high cost of raw materials is a major financial constraint contributing to the limited widespread applications of the materials. As noted in [3], the secondary processing method for wrought products is relatively underdeveloped, resulting in high costs for semi-finished product fabrication. Further developments in their manufacturing and improved machining and forging techniques will aid in lowering the cost of these materials [2]. In addition, research investigations into the economical production of high strength reinforcement particles will likely reduce the cost of production of the composites.

The largest barrier to the widespread application of PMMCs in component design is the lack of experimentally validated engineering tools available to predict their mechanical behavior under service loading conditions. This statement has been attributed [2]-[3], [6]-[7] to the lack of related experimental and theoretical systematic investigations. In [3], for example; it is stated that there is a need for a systematic database that relates parameters (i.e. stresses, strains, energy, etc) to PMMC materials properties, reliable correlations between test data and actual performance, and validated property data for use in finite element analysis. Also, Lease et. al. [6] state that one of the remaining obstacles that must be overcome to make PMMCs a more viable material in the engineering community involves the lack of experimental data concerning their behavior under fatigue type loading and suitable validated fatigue life design tools.

1.2 Research Motivation and Objectives

Although the previous section summarized the beneficial attributes of PMMCs, it also highlighted the need for fundamental analytical and experimental research aimed at defining the mechanical behavior of the material under service loading conditions. To maintain generality, service loads may consist of a random or regular system of loads applied in such a manner as to induce a multiaxial cyclic stress and strain state within the component. Although, multiaxial stress states can occur at some locations within a component that is subjected to loading in one direction (uniaxial loading), they certainly occur when a component is subjected to external loading that is applied along more than one axis (multiaxial loading). Such cyclic loading conditions often lead to premature

component failure due to fatigue. Fatigue failures often constitute a serious compromise to human safety and are associated with substantial economic losses; at least half of all mechanical failures are due to fatigue [8].

The fatigue behavior of PMMCs can be defined by a model that respects such associated complexities as external (geometric) and internal (heterogeneity, matrix plasticity) non-linearities. Engineering components generally contain geometric discontinuities (notches) such as bolt holes, keyways, fillet, etc. These discontinuities result in the intensification of the stress field when the components are subjected to external loads. Complex stress and strain histories in which the directions of the principals change during the loading cycle frequently occur at such critical locations. In components made of PMMCs, the stress field in the vicinity of these discontinuities may additionally be raised due to the material discontinuity at the particle-matrix interface. Although the bulk of the composite and all ceramic reinforcements may undergo elastic deformation, the highly stressed metal matrix material in the vicinity of notches may undergo significant plastic deformation during the loading cycles. If the plastic deformation is not properly accounted for, or the effect of the stress raisers is not reduced during the design stage, cracks may initiate at a notch root. That is, premature component fatigue failure in engineering materials is generally due to the initiation of a crack at critical locations. To predict the fatigue life of PMMC components, researchers and designers need a more comprehensive knowledge of the mechanical behavior of the components at critical locations. This is essential to insure their reliable operation and to provide tools for design and optimization.

Fatigue life prediction tools that account for the plastic deformation inherent at notch roots have recently been evaluated for PMMCs. Specifically, critical plane based [6] and the energy based [9] methods of fatigue life prediction originally developed for homogeneous materials, have shown good agreement with experimental results for PMMC components under multiaxial cyclic loading. These models provide as output the number of cycles a component can withstand before a crack will initiate at a notch root. However, in order to predict the fatigue life of components using these methods, both the elastic-plastic strain and stress histories at a components critical location must be known.

Estimating the notch root elastic-plastic stress and strain histories is the most difficult step in fatigue life prediction. Generally, three methods have been used to determine the notch-root stress-strain histories for homogeneous materials. These include experimental methods, finite element analysis (FEA), and simplified analytical methods. Experimental methods involve a variety of experimental techniques that are used to evaluate and/or correct analytical and/or FEA results. However, experimental investigations are time consuming and prohibitively costly in standard design environments. Detailed FEA are frequently employed to obtain elaborate information about complex stress-strain fields at notch roots. This attribute has been used extensively to determine the components that experience the greatest normal and shear stresses during the stress-strain history. Finite element analysis also provides a method of developing unique insight into the plastic deformation process in components. Finite element analysis is a very powerful analytical tool, and is enabled by rapidly growing computational technology. However, non-linear FEA is often a difficult and time

consuming process particularly when the components being modeled are subjected to lengthy histories of multiaxial loads.

To make fatigue life prediction methods more conducive to average design environments and to shorten design lead times, there has been a great effort employed to develop simplified analytical techniques that approximate the actual elastic-plastic notch root material behavior. Several simplified models, discussed in the subsequent chapter, have been developed and experimentally validated for homogeneous materials under a variety of loading conditions. Most of the simplified models developed are based on assumptions necessary to simplify the complex nature of the problem and have been applied to various general loading conditions. These methods therefore enable relatively simple calculations of elastic-plastic notch-root strain and stress histories for homogeneous materials. However, little research has been conducted in the development of simplified analytical tools for determining the notch root elastic-plastic strain-stress history in PMMC components subjected to multiaxial loading, perhaps due to the inherent difficulties in modeling a finite concentration of inclusions, the matrix material elastic-plastic behavior in the vicinity of the discontinuity, and multiaxial external loading. Without these tools, fatigue life predictions, using crack initiation models mentioned above, cannot easily be obtained.

It should be mentioned that a complete notch root elastic-plastic strain and stress histories definition, whether found from experimental, FEA, or approximate methods, requires the adoption of a cyclic constitutive model. Inelastic constitutive models for homogeneous materials that address multiaxial cyclic loading are numerous and still evolving. Only a few cyclic plasticity models applicable to PMMC components under

multiaxial non-proportional loading have recently appeared in the literature [10]. As a result, advances in fatigue design tools depend directly on advances in constitutive models capable of modeling PMMC elastic-plastic behavior.

The main objectives of this research are to develop, implement, and verify simplified and sufficiently accurate analytical tools that will provide acceptable results for modeling notch root elastic-plastic strain-stress histories in components made of PMMCs that are subjected to multiaxial external loading conditions. In addition, since one of the key challenges limiting the widespread application of PMMCs is a lack of experimental data to validate existing and any proposed analytical tools, the research is also aimed at providing experimental results for PMMC specimens subjected to a variety of multiaxial cyclic loading conditions.

1.3 Components of Research and Summary of Thesis

To meet the aforementioned objectives, the following tasks were carried out and were presented in this thesis.

a) A Literature review of previous studies conducted on the elastic-plastic constitutive behavior of PMMCs, notch root elastic-plastic strain-stress approximation methods, and experimental methods used to validate existing models was first conducted.

b) Two constitutive models capable of predicting the elastic-plastic strain-stress response of the matrix, reinforcement, and the PMMC under multiaxial cyclic loading conditions were first developed. Specifically, the elastic components of

the matrix and reinforcement strains and stresses were obtained from the applied incremental stresses or strains by implementing known relations specific to composites. The matrix plastic strain components were obtained using two alternative cyclic plasticity routines originally developed for homogeneous materials. The elastic and plastic (matrix only) strains were superimposed to obtain the constituents constitutive relations. The composite constitutive relation was finally obtained by applying the known work principal. These models are capable of predicting the constitutive behavior of PMMCs under a variety of loading conditions and are dependent on the properties of the matrix and the properties, volume fraction and geometry of the reinforcing particles.

c) Two simplified analytical tools for predicting the notch root elastic-plastic behavior in PMMCs under multiaxial cyclic loading conditions were developed. They are defined by two independent nonlinear energy-based relations that assume that the plasticity is local to the notch root. The models developed require the results of an elastic notch root analysis and predict the actual elastic-plastic behavior. All relations were developed to respect the heterogeneous nature of PMMCs.

d) One of the developed constitutive models in (b) was coupled with the developed simplified relations in (c) to define two alternative solutions that independently estimate notch root elastic-plastic strain and stress histories under multiaxial cyclic loading conditions. Two computer programs were developed to solve the two sets of nonlinear equations. Each program calculates the composite elastic-plastic strain and stress histories at a geometric discontinuity given the composites

material properties and notch root strain-stress histories obtained from an elastic solution.

e) To assess the capability of the two constitutive models in (b) to predict the elastic-plastic constitutive behavior of PMMCs, several experimental tests were conducted. Specifically, biaxial cyclic loads were applied to tubular PMMC specimens made of 6061 aluminum alloy reinforced with 10 and 20% by volume alumina (Al_2O_3). The surface strains measured were compared with those obtained using the developed models.

f) Experimental tests were carried out to assess the capability of the two analytical tools in (d) to predict the elastic-plastic notch root strains and stresses. The tests consisted of conducting biaxial cyclic load-controlled tests on a series of two different notched specimens made of 6061 aluminum alloy reinforced with 10 and 20% by volume alumina (Al_2O_3). The notch root strains measured were compared to those obtained by implementing the models developed in (d).

A literature review of the previous research work on elastic-plastic constitutive behavior of PMMCs, notch root approximation models, and strain measurement techniques relevant to this research is presented in Chapter Two. Chapter Three describes the elastic-plastic constitutive models developed as part of the analysis along with their implementation procedure. The developed simplified models and their implementation procedure are presented in Chapter Four. The facilities used, materials, specimen geometries, experimental set-up, load paths, and experimental procedure are subsequently presented in Chapter Five. Comparisons of the analytical and experimental results

obtained are presented in Chapter Six. Finally, conclusions of the thesis and recommendations for future research are presented in Chapter Seven.

CHAPTER TWO: BACKGROUND AND LITERATURE REVIEW

Figure 2.1 shows a circumferentially notched bar made of a PMMC along with a representative infinitesimal element taken at the notch root. The bar is subjected to an axial force P, and a torsional load T applied at its boundary. This gives rise to a non-linear triaxial stress field in the plane of the notch, with the highest stress concentration being located near the discontinuity. The notch imposes constraints on its local deformation due to the lower stress bulk material away from the higher stressed material at the notch root. For this, and any other external notch geometry or, with few exceptions system of applied mechanical loads, the state of stress at the notch root is biaxial due to the traction free surface. The states of stress and strain at the notch root with reference to the coordinate system given in Fig. 2.1 are respectively:

$$\sigma_{ij} = \begin{bmatrix} 0 & 0 & 0 \\ 0 & \sigma_{22} & \sigma_{23} \\ 0 & \sigma_{32} & \sigma_{33} \end{bmatrix}, \tag{2.1}$$

and

$$\varepsilon_{ij} = \begin{bmatrix} \varepsilon_{11} & 0 & 0 \\ 0 & \varepsilon_{22} & \varepsilon_{23} \\ 0 & \varepsilon_{32} & \varepsilon_{33} \end{bmatrix}. \tag{2.2}$$

Based on the assumption of equilibrium at the notch root, $\sigma_{23} = \sigma_{32}$, and $\varepsilon_{23} = \varepsilon_{32}$, there are seven unknown notch root parameters: three stresses and four strains. Consequently, seven independent equations are required to completely define the components of the notch root stress and strain tensors.

The approximate analytical method defined in this research to estimate the local elastic-plastic strain and stress histories at the notch root in a PMMC component is comprised of two sets of relations. The first are the constitutive relations and the second are the approximate relations. Together, these equation sets form the relations necessary to estimate the seven unknown components of the composite stress and strain tensors defined in Eqs. (2.1) and (2.2). In this chapter, previous research pertaining to the development of constitutive models and mean field theory are first presented (Section 2.1). A review of the approximate relations developed for metals and PMMCs is subsequently given in Section 2.2. Finally, the background on the experimental strain measurement system used in this research is detailed in Section 2.3.

For the purpose of the review, it is appropriate to differentiate here between proportional and non-proportional external loading, and monotonic and cyclic loading. In proportional loading, (P/T = constant in Fig. 2.1), it is generally assumed that the deviatoric stresses at the notch root remain in fixed proportion throughout the loading history. For this type of loading, the relatively simpler deformation theory of plasticity can be used in the formulation. However, if the loads are not applied in proportion, the deviatoric stresses increase in a non-proportional manner, and the notch root stress-strain histories are dependent on the loading path. As such, all relations that incorporate non-proportionality in the loading path must be developed in incremental form. Non-

proportional loading is thus the more general loading type. Monotonic loading denotes a non-reversed increasing load applied to a component, while cyclic loading involves a repeated loading sequence.

2. 1 Constitutive Models for PMMCs

Constitutive models describe the relationship between stress and strain when a component is loaded. In this section, constitutive models that have been developed to address PMMCs are presented by first assuming elastic composite behavior (Section 2.1.1) and subsequently assuming that the metallic matrix undergoes elastic-plastic deformation (Section 2.1.2).

2.1.1 Elastic Constitutive Models

Most research studies that described the constitutive behavior of PMMCs assume that the composites remain elastic as the loads are applied [11]-[13]. Goodier's work [14] on modeling a spherical and a cylindrical inclusion in a matrix provided the first detailed analysis of the elastic stress-strain response of composite materials. Subsequently, Sadowisky and Sterberg [15] derived relations defining the elastic stress-field around an ellipsoidal cavity under plane stress conditions.

The general problem of elastic field inside, and at the interface of an ellipsoidal inclusion was solved by Eshelby [16]. By a series of cutting, straining, and welding, Eshelby [16] first considered the elastic field about a misfitting inclusion embedded

within an infinite isotropic matrix of the same elastic constants as the inclusions (elastic homogeneous problem) as illustrated in Fig. 2.2a. The first step in Eshelby's model (see diagram A in Fig. 2.2a) is to perform an imaginary cutting procedure to remove the inclusion from the body before it undergoes a transformation. Once the inclusion is free from the body, it is allowed to undergo the transformation free from the constraint. This unconstrained transformation will take the inclusion from one stress free state to another stress free state, producing a transformation strain, ε^t. The transformation strain has a finite value in the inclusions and zero outside the inclusion. On removing the inclusion, the matrix at this stage contains a hole left by the inclusion and the matrix is free from any internal or external stresses. The second step in the Eshelby's model (diagram D in Fig. 2.2a) is to put the inclusion back into its original position in the matrix. As illustrated in Fig. 2.2a, a surface traction must first be applied to the transformed inclusion to restore it to the previous size and shape before it can be put back into its original position. The final step in the Eshelby's model procedure (diagram E in Fig. 2.2a) is to allow the inclusion to undergo its constrained transformation inside the matrix. Eventually, the matrix and the inclusion will set up a constrained strain, ε^c, at all points in the matrix and in the inclusion. Although the solution for the constrained strain field in the matrix is quite complex, for an ellipsoidal-shaped inclusion with a uniform prescribed transformation strain, Eshelby [16] presented a relation between the constrained strain, the stress free transformation strain, and the 6x6 Eshelby tensor [**S**]. Eshelby's tensor depends mainly on the aspect ratio of the inclusions and the matrix Poisson's ratio. The relation is given by:

$$\varepsilon_{ij}^c = S_{ijkl}\varepsilon_{kl}^t. \tag{2.3}$$

The components of stress in the inclusion, $\sigma_{ij(f)}$, can be obtained using the Hooke's law as:

$$\sigma_{ij(f)} = C_{ijkl(m)}(\varepsilon^{c}_{kl} - \varepsilon^{t}_{kl}), \tag{2.4}$$

where the subscripts "m" and "f" denote matrix and reinforcement parameters respectively, and $C_{ijkl(m)}$ are components of the matrix stiffness tensor. Substituting Eq. (2.3) into Eq. (2.4) yields:

$$\sigma_{ij(f)} = C_{ijst(m)}(S_{stkl} - I)\varepsilon^{t}_{kl}, \tag{2.5}$$

where "I" is the identity matrix. Using Eqs. (2.3) and (2.5), the stress and strain components in the inclusion can be estimated. It should be noted that these equations are only applicable if the elastic properties of the matrix and the inclusion are similar. In [16], it is assumed that the stress field inside the inclusion is uniform, and that, by an equivalent principle, the interfacial stress in the matrix may be readily evaluated in terms of equivalent transformation strain.

Eshelby's inclusion principle can be applied to an inhomogeneous problem in which the ellipsoidal region is an inhomogeneity (i.e. the ellipsoidal region is made of a material different from that of the matrix) rather than an inclusion. In this problem, both the matrix and the inhomogeneity are assumed to behave elastically, with the elastic constant of the inhomogeneity, $C_{(f)}$, being different from that of the matrix, $C_{(m)}$. Unlike the inclusion problem, the ellipsoidal inhomogeneity does not have a known transformation strain. If it is assumed that an external traction, σ_{ij}, is applied to the body,

the total stress within the composite will be the addition of the stress previously calculated in the homogeneous inclusion problem and the applied stress. For points far away from the inhomogeneity, the stress in the matrix will be equal to the applied stress. For such points, the strain components in the matrix, ε_{ij}, are related to the stress through the generalized Hooke's law as:

$$\varepsilon_{ij} = \left(C_{ijkl(m)}\right)^{-1} \sigma_{kl}. \tag{2.6}$$

However, in the portion of the matrix close to the inhomogeneity, and also within the inhomogeneity, both the matrix and the inclusion undergo the additional stress and strain. The stress field within the inhomogeneity can be expressed as:

$$\sigma_{ij(f)} + \sigma_{ij} = C_{ijkl(m)}\left(\varepsilon^{c}_{kl} - \varepsilon^{t}_{kl}\right) + C_{ijkl(m)}\varepsilon_{kl}. \tag{2.7}$$

Equations (2.3) and (2.7) can then be used to find the strain and the stress in the inhomogeneity as a function of the transformation strain. It should be noted that in contrast to the inclusion problem, the transformation strain in this case is unknown, and must be calculated.

For an externally stressed elastically inhomogeneous system, both the inhomogeneous and the equivalent homogeneous system undergo different deformations. Eshelby's inclusion principle [16] results in,

$$\sigma_{ij(f)} + \sigma_{ij} = C_{ijkl(f)}(\varepsilon^c_{kl} + \varepsilon_{kl}) = C_{ijkl(m)}(\varepsilon^c_{kl} + \varepsilon_{kl} - \varepsilon^t_{kl}). \tag{2.8}$$

The transformation strain can be determined in terms of the strain associated with the known external traction by substituting Eq. (2.3) into Eq. (2.8). The stress in the inhomogeneity can then be found using Eq. (2.8). The inhomogeneity strain components are obtained from the stress components using the generalized Hooke's law. The local stress and strain in the immediate vicinity of the inhomogeneity are not calculated in the above Eshelby's analysis.

Eshelby's theory of equivalent inclusions is perhaps the most accepted elastic constitutive model applicable to PMMCs. However, Eshelby's method is only applicable to composites with very small volume fraction of the reinforcement ($V_f \leq 5\%$). For higher values of V_f, Eshelby's method has to be modified to account for the interaction in the stress field between the reinforcements. The concept of average stress and strain in the composite and its constituents has been used extensively in the past to account for the interactions in the stress field between the particles. The self-consistent theory [17]-[18], and the Mori-Tanaka mean-field theory [19], both based on the concept of average stress and strain, are the commonly used models. The self-consistent theory was originally developed to model the average constitutive behavior of polycrystals. The self-consistent theory has been used to estimate the macroscopic elastic moduli of two-phase composites and also the average internal non-uniformity of strain and stresses in the matrix and particles of a composite system. Hutchinson [20] has used this theory to estimate the elastic-plastic incremental relations of polycrystals and composites. Although straightforward, the method does not provide acceptable results when the matrix contains

either voids or perfectly rigid inclusions [21]. Consequently, Mori-Tanaka's mean field theory has been more widely used, and due to its use in this research, it is detailed below.

The Mori-Tanaka mean field theory [19] assumes that for a composite system with a finite volume fraction of particles, the average stress in the matrix differs from the remotely applied stress by an unknown amount referred to as the average perturbed stress, $\tilde{\sigma}$. The corresponding average strain in the matrix also differs from the strain associated with the remotely applied stress by an unknown perturbed strain, $\tilde{\varepsilon}$. This perturbed strain takes into account the interactions in the stress fields of adjacent particles. This method is referred to as mean field theory, since Mori-Tanaka's modifications involves replacing the complex position dependent states of stress and strain in the matrix with an average stress and strain. Due to these modifications, the Eshelby's equivalent principle given in Eq. (2.8) becomes:

$$\sigma_{ij(f)} = C_{ijkl(f)}(\varepsilon_{kl} + \tilde{\varepsilon}_{kl} + \varepsilon^c_{kl}) = C_{ijkl(m)}(\varepsilon^c_{kl} + \tilde{\varepsilon}_{kl} + \varepsilon_{kl} - \varepsilon^t_{kl}). \tag{2.9}$$

Substituting Eq. (2.3) into Eq. (2.9) yields:

$$C_{ijkl(f)}(\varepsilon_{kl} + \tilde{\varepsilon}_{kl} + S_{ijkl}\varepsilon^t_{kl}) = C_{ijkl(m)}\varepsilon_{kl} + C_{ijkl(m)}(\tilde{\varepsilon}_{kl} + S_{ijkl}\varepsilon^t_{kl} - \varepsilon^t_{kl}). \tag{2.10}$$

Equation (2.10) contains two unknowns, $\tilde{\varepsilon}_{kl}$ and ε^t_{kl}. Consequently, one additional relation is necessary to obtain a complete solution. In Eq. (2.10), the second term of the

right hand side of the equation is referred to as the constrained stress, σ_{ij}^{c}, and is expressed mathematically as:

$$\sigma_{ij}^{c} = C_{ijkl(m)}(\tilde{\varepsilon}_{kl} + S_{ijkl}\varepsilon_{kl}^{t} - \varepsilon_{kl}^{t}). \tag{2.11}$$

In [19], Mori and Tanaka have shown that for a macroscopically homogeneous body in static equilibrium, the volume integral over the entire composite domain of the stress disturbance given in Eq. (2.11) vanishes. From this, Mori and Tanaka obtained an expression relating the constrained, the perturbed, and the transformation strains as:

$$\tilde{\varepsilon}_{kl} = -V_f\left(\varepsilon_{kl}^{c} - \varepsilon_{kl}^{t}\right). \tag{2.12}$$

The perturbed strain, $\tilde{\varepsilon}_{kl}$ and the transformation strain, ε_{kl}^{t}, can be obtained by simultaneously solving Eqs. (2.10) and (2.12). The constrained strain, and the reinforcement stress are then obtained using Eqs. (2.3) and (2.9) respectively. The reinforcement strain is obtained from the calculated stress using the Hooke's law. The perturbed stress is found from Eq. (2.11). The matrix stress can be obtained by adding the calculated perturbed stress to the remotely applied stress, while the matrix strain is then obtained from the calculated matrix stress using Hooke's law.

2.1.2 Elastic-Plastic Constitutive Models

The original Mori-Tanaka approach [19] has been used mainly to evaluate the elastic behavior of composite materials. The emphasis on elasticity shows its importance in applications, and gives the means for developing practical design methods. It is, however, unrealistic to assume that all components being modeled behave in a linear manner. That is, although the ceramic particles are generally relatively stiff, and thus, elastic material behavior can be assumed, the metallic matrix can behave in an elastic-plastic manner. It is apparent [3], [6], [22]-[23] that limited work has been done with regard to the plastic behavior of PMMCs due to the complexity of the associated analysis.

In [23], Tandon and Weng considered the elastic-plastic stress-strain behavior of spherical particle reinforced composites under multiaxial loading using the secant moduli of the ductile, work hardening matrix. Specifically, in [23], the elastic-plastic behavior of the composites was analyzed by applying the concept of secant properties to the elastic Mori-Tanaka mean field theory [19]. In the Tandon-Weng model, the secant modulus of the matrix in the plastic range changes with an increase in plastic deformation. Since the change is not known beforehand, at each state of stress or strain, an initial value has to be assumed for the matrix effective plastic strain. Although the model received attention from the research community, it can only be applied if the loads are applied in a proportional manner and cannot be applied if there is a load reversal.

In an attempt to study the elastic-plastic deformation of multiphase composites materials under non-proportional loading, Li and Chen [24] reformulated the mean field theory in an incremental form. The method is aimed at application to multiphase

materials in which the components exhibit different elastic-plastic material behavior under non-proportional or reverse loading. The application of the Li and Chen's model [24] to two-phase composites, is an integral part of this research and will be detailed in Chapter Three. Since the Li and Chen's model [24] is essentially a reformulation of the mean field theory in an incremental form, theoretically, it could be used to study the elastic-plastic deformation of composite materials under non-proportional monotonic and cyclic loadings. However Li and Chen only implemented and validated their model for uniaxial monotonic loading. That is, in [24], the model was not validated for the case of multiaxial cyclic loading. Generally, the Li and Chen's model [24] can be used in conjunction with any cyclic plasticity model developed for homogeneous materials to predict the constituents plastic strain components.

Inelastic constitutive models for homogeneous metals subjected to cyclic loads (cyclic plasticity models) are still evolving. Two classes of such cyclic plasticity models are described in [25]. The models in the first classification are based on thermodynamic concepts in which it is assumed that the present state of the material depends on the present values of observable variables and a set of internal variables. Included in this category are the Prager model [26], Ziegler model [27], Mróz model [28], and the Armstrong and Frederick model [29], modified by Chaboche et. al. [30]. In this class, to explain the plastic behavior of materials upon loading beyond the yield point and upon reloading, the concept of yield stress and loading/unloading conditions are used. One of the major drawbacks of the classical plasticity model involves the difficulty of defining the point at which yielding has occurred, since the phenomenon of yield itself is a gradual transition from a linear to a non-linear stress-strain response. For some materials, it is

often difficult to know the configuration of the subsequent yield surface, and also difficult to find it experimentally in the fully three dimensional case. The second class of plasticity models is based on the thermodynamic concept that the present state of material depends on the present values and the past history of observable variables only (total strains, temperature etc), giving rise to hereditary theories. The endochronic theory of plasticity [31]-[34] is based on this concept. It was developed to circumvent some of the problems associated with the first class of plasticity theory.

For homogeneous materials, in [35]-[38], research investigations were carried out to compare the effectiveness of different classical cyclic plasticity models in modeling the experimentally observed material responses. Prager model [26] and Ziegler model [27] have been found to poorly predict the hardening behavior of homogeneous materials subjected to non-proportional loading [37]. The Mróz model [28] was subsequently observed to better model the constitutive response of components subjected to non-proportional loading. However, the Mróz model [28] requires a large number of surfaces, and a large amount of computer storage. To address these problems, several modifications of the Mróz model have been proposed. Some of the modifications include the two-surface plasticity model [39]-[40], the Garud model [41], and the Chu model [42]. It is important to state that the advancements in computer technology have also alleviated the non-availability of computer storage space. However, the Mróz model and its various modifications still require a clearly defined yield point to give good results, thus implying a finite elastic region. Theoretically, a finite region is essential because of the requirement that the increment in plastic strain must be normal to the yield surface. Consequently, the direction of the plastic strain depends on the configuration of the yield

surface. In some materials, plastic effects appear immediately upon loading, thus the onset of yielding is difficult to define. That is, if plastic effects were to begin immediately upon loading, the region of the yield surface will collapse to a point. Since all directions are normal to a point, the direction of the plastic strain increment may be impossible to determine. It may even be inappropriate to define a concept of yielding for such materials except possibly as an approximation. The endochronic theory, where the definition of a yield point is not essential, provides an alternative approach to modeling the constitutive behavior of materials. The theory has the capability to model plastic strains at the onset of loading, and subsequent unloading. The endochronic theory is a relatively new plasticity model. It provides a unified point of view to describe the elastic-plastic behavior of materials since it does not require a yield surface and loading/unloading conditions. It has also been shown in [32] that for homogeneous materials, the endochronic theory of plasticity can better predict some of the transient effects associated with non-proportional variable amplitude cyclic loading. In [43]-[45], it has been shown that the endochronic theory would apply precisely to situations involving loading and cyclic behavior of metals, as well as wave propagation in the plastic region.

Very few of the aforementioned cyclic plasticity models have been developed to study the plastic behavior of PMMCs under multiaxial loading conditions [2], [10], [46]. In [46], Ogarevic formulated a composite constitutive model based on the Li and Chen's model [24], the incremental theory of plasticity, and the Prager linear kinematic hardening rule [26] to study the uniaxial cyclic deformation of discontinuously reinforced metal matrix composites (MMCs) both at room and elevated temperatures. The model was demonstrated only analytically for externally applied uniaxial cyclic loading. A

major relevant model that deals with the biaxial proportional case was developed by Lease [2], and Lease et. al. [10]. In [2] and [10], the Li and Chen model [24] was used with Chaboche et. al.'s [30] incremental plasticity theory to simulate the constitutive behavior of the composite system. The model was demonstrated both analytically and experimentally for cyclic axial and biaxial proportional loading. Although the axial and torsional elastic-plastic strain and stress seemed to accurately simulate the monotonic tests, the elastic loading/unloading portions of the cyclic uniaxial and biaxial tests show some obvious differences that increase with increasing strain range [2].

Other relevant research investigations on the elastic-plastic constitutive behavior of PMMCs include the work of Koh et. al. [9], Ellyin and Xia [47], Zihui et. al. [48], and Ellyin et. al. [49]. The research investigations presented in these papers are mainly experimental and computational (FEA). The plastic constitutive model used in the FEA is a rate independent two surface constitutive model formulated by Ellyin and Xia [47]. In [48] some experimental results were presented for both uniaxial and biaxial tension-compression cyclic tests on tubular specimens made of PMMCs.

To date, there has been no research investigation conducted for the case of non-proportional variable amplitude loading of PMMCs. In addition, there has been virtually no attempt yet to determine the suitability of the aforementioned generally accepted cyclic plasticity models developed for homogeneous materials in predicting the plastic behavior of PMMCs.

2.2 Notch-Root Stress-Strain Estimation Methods

It can be shown that the material constitutive models provide four of the seven relations require to completely define the matrix notch root stress-strain histories (Eqs. 2.1 and 2.2). The additional three equations can be obtained using approximate relations. For homogeneous materials, several simplified methods have been proposed to estimate the notch root elastic-plastic strain and stress. These methods are based on the assumption that the plastic deformation localized in the notch root area, is controlled by a relatively large surrounding elastic field. In making this assumption, the local elastic-plastic strain and stress histories can be obtained using the results of a relatively easier elastic analysis From several of the previously developed analytical models, two methods, the Neuber's method [50] and the equivalent strain energy method (ESED) proposed by Moski and Glinka [51], have been the most frequently used by various researchers. These methods were originally developed for the case of uniaxial loading and then generalized to address multiaxial external loading and are categorized as such in the following sections.

2.2.1 Uniaxial Notch Root Approximate Relations

The original Neuber's method [50] was proposed for a notched body under pure shear stress, but it is often used for notches under tension and bending. Neuber's rule states that the elastic stress concentration (K_t) is equal to the geometric mean of the actual stress and strain concentration factors. This can be mathematically represented as:

$$K_t^2 = K_\sigma K_\varepsilon = \frac{\sigma\varepsilon}{\sigma_{n.s}\varepsilon_{n.s}}, \tag{2.13}$$

where K_σ and K_ε are the stress and strain concentration factors respectively, $\sigma_{n.s}$ and $\varepsilon_{n.s}$ are the nominal stress and strain in the net section respectively, and σ and ε are the local stress and strain respectively. Neuber's rule can be used with the material uniaxial stress-strain curve to predict the local elastic-plastic strain and stress. That is, in substituting the material curve into Eq. (2.13), the local stress and strain can be found knowing the component geometry and the elastic nominal stress and strain associated with the applied loads.

The equivalent energy density method (ESED) [51] was originally developed for a body in plane stress, where there is a uniaxial stress condition at the notch root. The ESED method assumes that the strain energy density at the notch root in the elastic-plastic body can be estimated assuming material was to hypothetically remain elastic. Based on this assumption, the ESED has been mathematically represented as:

$$K_t^2 = \frac{W_\sigma}{W_s} = \frac{\int \sigma d\varepsilon}{\int \sigma_{n.s} d\varepsilon_{n.s}}. \tag{2.14}$$

In Eq. (2.14), W_σ and W_s are the strain energy densities at the notch root and in the net section respectively. In [51], the true stress-strain curve (e.g. the Ramberg-Osgood equation) was substituted into Eq. (2.14) for the case of local yielding to obtain the local

parameters. To account for large plastic yielding at the notch root, Glinka [52] introduced a plastic zone correction factor.

It has been shown for uniaxial loading in [53] that the Neuber's rule overestimates, while the ESED method underestimates the experimentally measured notch root strains. Specifically, Neuber's rule predicts an upper bound, and the ESED method predicts a lower bound approximation to the notch root strains obtained from experiments.

As mentioned, the Neuber's and ESED models were originally developed for the case of plane stress, where a uniaxial stress state prevails at the notch root. For situations where the plane stress condition is no longer valid (e.g. plane strain, with biaxial state of stress, transverse constraint), the models or the constitutive relations have to be modified. Several researchers have attempted this in the past. Walker [54] used the original Neuber's rule but modified the material constitutive relation. Walker obtained a new stress-strain curve in the maximum principal direction through the modification of the uniaxial stress-strain curve to reflect the effect of the minor principal stresses. By assuming a state of plane strain, Dowling et. al. [55] also modified the uniaxial stress curve to generate the vanishing transverse strain at the surface of a constraint notch root. Glinka et. al. [53] used a similar approach and modified the plane stress ESED method to address the plane strain condition. Topper et. al. [56] also modified the Neuber's rule to make it applicable to cyclic loading.

2.2.2 Multiaxial Notch Root Approximate Relations

For multiaxial elastic-plastic strain-stress analysis, most of the existing models are extensions of the Neuber and the ESED uniaxial approximation methods. For the case of proportional loading, Hoffman and Seeger [57] developed a generalization of Neuber's rule, and Moftakhar et. al. [58] developed an alternative generalization of Neuber's rule and of the ESED method.

For non-proportional loading, simplified methods are still evolving. Some of the existing models attempt to either incorporate the effect of the notch into the constitutive relations or develop the Neuber's rule and ESED method in incremental form. Some of the models that have incorporated the effect of the notch into the constitutive models include those presented in [59]-[62]. In [63], Singh attempted the reformulation of Neuber's and ESED methods in incremental forms to account for the path dependent nature of non-proportional loading. This approach is the most relevant to this research and would be discussed briefly in this section.

For the incremental Neuber's rule, in [63], it was proposed that for a given increment in the external load, the corresponding increase in the total strain energy density (i.e. sum of the increment in strain energy density and complementary strain energy density) at the notch root in an elastic-plastic homogeneous body can approximated by that obtained if the body was to hypothetically remain elastic through out the loading history. Mathematically, this can be represented as:

$$\sigma_{ij}^{e}\Delta\varepsilon_{ij}^{e}+\varepsilon_{ij}^{e}\Delta\sigma_{ij}^{e}=\sigma_{ij}^{N}\Delta\varepsilon_{ij}^{N}+\varepsilon_{ij}^{N}\Delta\sigma_{ij}^{N}, \tag{2.15}$$

where "e" represents notch root components that can be found from an elastic analysis, "N" represents elastic-plastic notch root components as estimated by the incremental Neuber's rule, and Δ stands for an increment in the variable (in this case, stress or strain). Equating elastic and elastic-plastic energies at only the point of highest stress concentration is justified in [63] based on the assumption of localized plasticity. That is, the plastic zone around the notch root is small, and thus its behavior is largely controlled by that of the surrounding elastic field. Equation (2.15) reduces to the original form of Neuber's rule given in [50] for a body in plane stress.

For the incremental ESED method, in [63], the method states that for a given increment in the applied load, the increment in the strain energy density at the notch root in an elastic-plastic homogeneous body is the same as that which would be obtained at the notch root if the body were to hypothetically remain elastic as the loads were applied. The hypothesis can be represented mathematically as:

$$\sigma_{ij}^{e}\Delta\varepsilon_{ij}^{e} = \sigma_{ij}^{E}\Delta\varepsilon_{ij}^{E}, \tag{2.16}$$

where "E" represents elastic-plastic notch root components as estimated by the incremental ESED method. A graphical representation of ESED method and Neuber's rule are shown in Figs. 2.3 (a-b). In [63], these methods were used in conjunction with the Mróz [28] plasticity model to determine the notch root stress-strain history in a homogeneous component subjected to non-proportional loading. Favorable results were obtained when compared to experimental results presented in [59].

All the approximate relations aforementioned were developed originally for homogeneous materials such as metals. For PMMCs under uniaxial cyclic loading, in [46], it has been indicated that the uniaxial simplified methods for notch root elastic-plastic strain-stress prediction, and the stabilized hysteresis loop could theoretically be used to predict the fatigue life of a composite system. However, the development or applications were not given. To date, research has not been conducted on developing such simplified models for determining the elastic-plastic strain and stress histories at notch root in PMMC components subjected to multiaxial cyclic loads. As noted in Chapter One, in order to properly provide such models, complexities in modeling the mechanical behavior of PMMCs in the presence of external (geometric and loading) and internal (heterogeneous, matrix elastic-plastic behavior) non-linearities must first be overcome from a theoretical viewpoint. If accomplished, the developed models must be experimentally validated for reliability and thus acceptance. For experimental validation, several strain measuring devices have been used in the past to measure strains in specimens with notches. In the next section, the background of the strain measurement system used in this research is detailed.

2.3 Experimental Measurement of Notch-Root Strains

A conventional technique for measuring notch root strain is the application of strain gages. Measurement of elastic-plastic strains of notched specimen started with Griffith work [64] in 1948. Griffith investigated the effect of plastic flow in a tension panel with a circular hole. electromagnetic strain gage was used to measure the strains at

the specimens inner edge. Although capacitance and inductance-based strain gages have been constructed, their sensitivity to vibration, mounting requirements, and circuit complexity have limited their applications. The electrical resistance strain gages are the most popular point strain measuring device. Electrical resistance strain gages are capable of monitoring strains over a wide range of values, from 1 micro-strain to well over 10,000 micro-strains in either tension or compression. Electrical resistance strain gages are available in a wide variety of gage lengths and configurations, and operate over a wide range of temperatures. In addition, they are relatively inexpensive and have been used in a variety of applications. Papirno [65] used resistance strain gage, about 0.04 inch long, to measure the monotonic notch root strains for a notched specimens with a notch root radius of about 0.159 inch. Barkey [59] and Barkey et. al. [60] used the strain gage rosette to measure the notch root strains of circumferentially notched solid shaft specimens made of 2070 steel subjected to a variety of proportional and non-proportional stress-controlled loading paths. Although relatively inexpensive, and effective for some applications, the validity of strain gage in measuring strains is not without suspect due to the possibility of adhesive debonding, and grid breakage particularly during cyclic loading. The use of strain gages for design optimization in an intensive, time-critical development effort is limited because strain gages require time-consuming and careful applications [66]. In addition, strain gages only measure strain at a point where they are attached. Consequently, they cannot capture true peak strain or high resolution information when applied in regions having large strain gradients [66]. That is, measuring strains at the notch roots is almost impossible using the conventional strain gages, and particularly so for notches with very small root radii.

For measuring strain in region with large strain gradients, optical strain measuring techniques such as laser-based interferometric strain/displacement gage and holography interferometries have been used. Optical measuring technique is becoming popular due to readily available light sources, detectors, and optical components. Measurement of elastic-plastic strains using optical techniques dates back to the 1960s. A suitable optical instrument for measuring strains is a laser-based interferometric strain/displacement gage (ISDG) developed by Guillot and Sharpe [67] in 1983. It has a gage length that is as short as 25 micrometer, but is usually 150 or 200 micrometer. A latter version of the equipment permits the biaxial strain measurement at the notch roots [68]. To use this equipment for strain measurement in a specimen, two tiny indentations are made in the notch root area of the specimen. These indentations serve as the gage length. When the indentations are illuminated with a laser, interference fringe patterns are formed in space. As the material is deformed, the gage length changes, these changes are indicated by the displacement of the fringes. This displacement is then translated into strain using a computer-controlled program. However, the effect of the indentations on the local field, especially in the plastic region is a matter of concern. In addition, the diffraction phenomena, which are related to the characteristics of the fringe patterns, depend also on the size of the indents. The larger the size of the indents, the more the intensity in the fringe patterns. This effect, though favorable to IDSG optical system, however, reduces the spread of the fringe pattern. There is a tendency that the whole fringe pattern may move out of the photosensor due to the fact that the positions of the photosensors are fixed in ISDG system and fringe patterns are swept across the slits through servomirrors. This effect is a

critical disadvantage. The equipment is also vulnerable to ambient vibration since vibration can cause the shifting of the fringe patterns.

Holography interferometry is a well-established method for measuring small displacements and strains. Electronic speckle pattern interferometry (ESPI) [66] is considered an electronic version of holographic interferometry. When compared to ISDG, ESPI is relatively new strain measuring equipment, and it does not require any indentation to measure strain in a specimen. It is a full-field non-contact experimental measuring technique that allows rapid and highly accurate measurement of the three dimensional (3D) deformation and surface strains with high resolution [66]. Electronic speckle pattern interferometry uses a CCD camera to acquire and store fringe images. The 3D deformation and surface strains are obtained using a computer that processes the images. The system gathers data like conventional strain gages, but the video detector provides the equivalent data of approximately 5000 strain gages. It has several advantages over the conventional strain gage measuring technique. Electronic speckle pattern interferometry measuring technique provides full-field strain distribution with a non-contact method, and it has a high spartial resolution, and it is well suited to capture true peak strain in high-strain gradient regions. It also has high measuring sensitivities. Electronic speckle pattern interferometry gives accurate strain data, and it can be applied to any object with simple or complex geometry, as long as the test region is optically accessible. However, one of the major disadvantages of ESPI is its high cost. In addition, although, ESPI is sensitive to small displacement, unfortunately, the ESPI is also susceptible to equally small ambient vibrations, and any other disturbances within the measuring environment [66]. It should also be noted that ESPI system measures, and

displays each direction of displacement sequentially, and not simultaneously. Consequently, it takes more than a second to take a complete 3D measurement. In addition, the load level and ambient conditions must be held constant when taking the measurement. Some of the problems associated with ESPI, such as sensitivity issues, can be overcome by using pulsed 3D ESPI. However, pulsed 3D ESPI is very large, and extremely expensive. In addition, measurement of in-plane deformations in pulsed 3D ESPI is based on comparison of images from three sensors. Consequently, any imperfections in one of the sensors can result in a large error in the measured in-plane deformation.

In this research, a novel optical measuring device known as 3D image correlation system [69] is used. As in ESPI, 3D image correlation provides full 3D measurements, which are critical for accurately measuring the strains in highly 3D material subjected to complex loading conditions. 3D image correlation system is based on photogrammetric principles, and uses ordinary light rather than coherent laser light. The equipment is substantially robust and has a greater dynamic range than other full-field imaging technologies. The robustness of 3D image correlation becomes clearest when measuring dynamic deformations. Unlike ESPI, which is not dynamic, 3D image correlation system is a dynamic system. Consequently, for fatigue measurement using 3D image correlation, the experimentation will not have to be halted every time a strain measurement is taken. Halting of a fatigue test, as it is usually done when using ESPI, is time consuming, and may introduce a large amount of experimental error. 3D image correlation system is simpler to use and less expensive than ESPI. It is well suited for measuring strain in cylindrical specimens, while the ESPI is ideal for flat specimens. Specifically, for

measuring strains in circular specimen using ESPI, in addition to the two additional illumination angles needed for the system, the system must be affixed to the specimen, which is more difficult for curved surfaces. Furthermore, 3D image correlation system is less sensitive to environmental noise and vibration than ESPI, hence, it is very adequate for use with servohydraulic load frames, which often introduce a small amount of vibration into the specimen. Some specific areas in which 3D image correlation have been successfully applied include, measurement of a crack tip with three point bending, high speed fracture of a rubber sample, road wheel tire dynamometer testing, spin pin testing, etc [70]. Details of the principle of operation of the 3D image correlation system will be discussed in Chapter Five.

2.4 Summary of Literature Review

This chapter presented a literature review of elastic-plastic constitutive models for PMMCs, and the approximate relations necessary for obtaining the local stress-strain histories in engineering components. It also presented the background on the experimental strain measurement system used in this research. Although various related research work for PMMCs has been discussed, the chapter also highlighted the need for more fundamental analytical and experimental research aimed at defining the mechanical behavior of the PMMC components under service loading conditions. It is apparent that to date, the following research investigations have not been carried out for PMMCs:

a) There has been no cyclic plasticity model applicable to PMMCs that has been validated experimentally for cyclic non-proportional loading, and particularly so for variable amplitude loading type.

b) There has been no simplified method developed for PMMCs under cyclic non-proportional loading.

c) There has been no experimental work conducted to evaluate constitutive models for PMMCs for cyclic non-proportional loading.

d) There has been no experimental work conducted to evaluate stress-strain estimation methods for notched PMMCs under non-proportional loading.

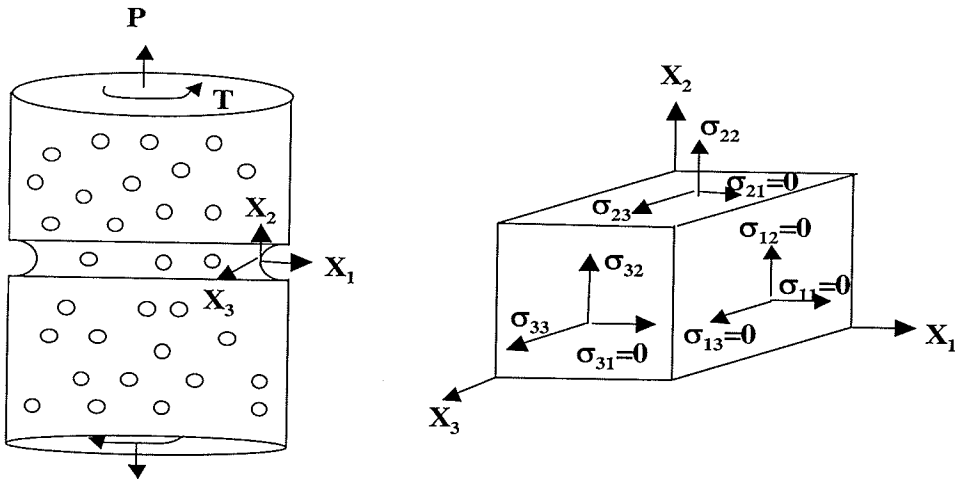

Figure 2.1: Stress Components at the Notch Root of a Representative PMMC Bar

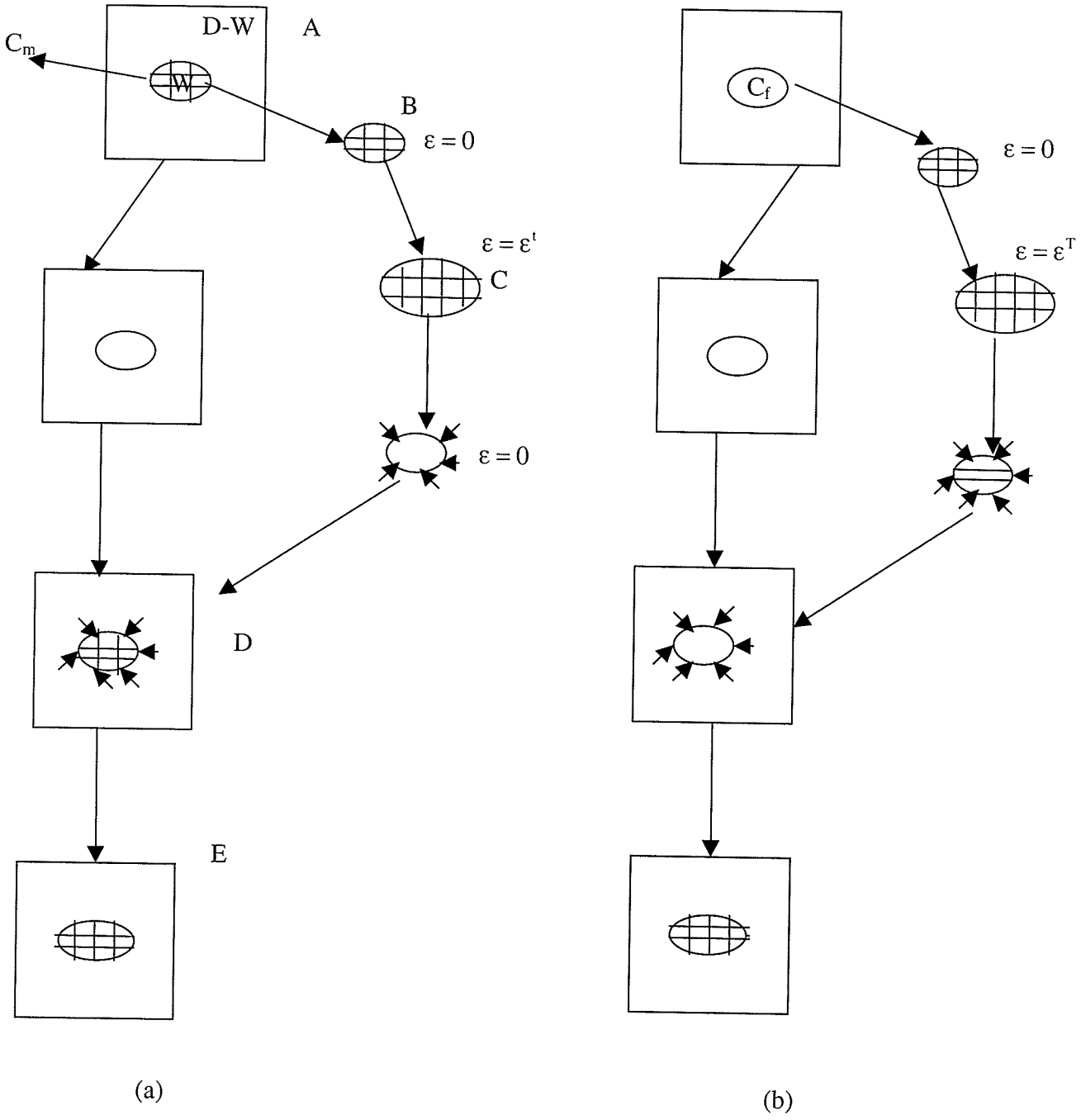

Figure 2.2: Eshelby's Model: (a) Homogeneous Inclusion Composite (b) Inhomogeneous Composite

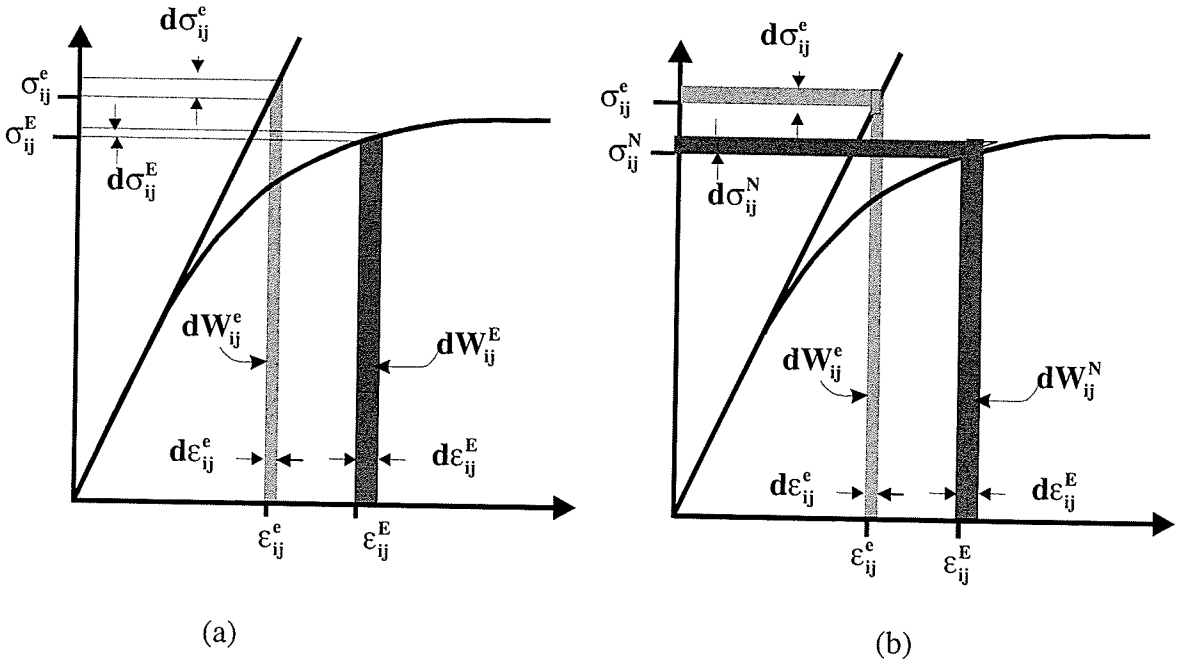

Figure 2.3: Graphical Representation (a) Incremental ESED Method, (b) Incremental Neuber's Rule

CHAPTER THREE: ELASTIC-PLASTIC CONSTITUTIVE RELATIONS FOR PMMCS

As stated in Chapter One, there are barriers limiting the widespread applications of PMMCs. One of the barriers is the lack of analytical tools that can be used to predict their mechanical behavior under service loading conditions. With increasing interest in the application of these materials in both structural and non-structural applications, the need to understand, model, and predict the mechanical response and fatigue life of the materials to applied multiaxial cyclic loads also increases. Fundamental continuum mechanics suggests that this response is found by solving the set of governing field relations. One of these relations is defined by the material stress-strain relation referred to as the constitutive relation. In Chapter Two, relevant research investigations into the constitutive behavior of PMMCs have been presented. However, the chapter highlighted the need for more fundamental analytical and experimental research aimed at defining the constitutive behavior of PMMCs under cyclic non-proportional loading. Furthermore, as noted in Chapters One and Two, a constitutive relation capable of modeling the stress-strain response of a PMMC component under cyclic external loads must also be known before a complete notch root strain-stress analysis can be conducted. Consequently, the development of a suitable cyclic constitutive relation capable of modeling the inelastic stress-strain behavior of PMMCs under cyclic non-proportional loading conditions is critical in engineering design. This chapter gives the details of two constitutive models developed and implemented for PMMCs in this research.

Both of the developed models are based on the decomposition of the total matrix and reinforcement strain tensors into their elastic and plastic parts. That is, in a composite system, the matrix follows the elastic-stress strain relation with zero plastic strains until the state of stress in the matrix satisfies the yield conditions. For small deformations, the increments in the components of the total matrix strain tensor, $d\varepsilon^{T}_{ij(m)}$, can be decomposed into the elastic, $d\varepsilon^{e}_{ij(m)}$, and plastic, $d\varepsilon^{p}_{ij(m)}$, components given as:

$$d\varepsilon^{T}_{ij(m)} = d\varepsilon^{e}_{ij(m)} + d\varepsilon^{p}_{ij(m)}. \tag{3.1}$$

Since the reinforcement remains relatively stiff, the increment in the reinforcement strain, $d\varepsilon^{T}_{ij(f)}$, is composed of only the elastic component, $d\varepsilon^{e}_{ij(f)}$, or,

$$d\varepsilon^{T}_{ij(f)} = d\varepsilon^{e}_{ij(f)}. \tag{3.2}$$

Following the approach used for PMMCs in [2] and [10], in this research, the elastic components of the matrix and reinforcement strains and stresses are obtained from the applied incremental stresses or strains using the incremental form of the mean field theory developed by Li and Chen [24], detailed in Section 3.1. The differences between [2] and the two models developed here lie in the plastic components of the matrix strain. These plastic components are obtained using two alternative cyclic plasticity models, described in Section 3.2. The developed constitutive relations for PMMCs are presented

in Section 3.3 and the method of implementing these models is given in Section 3.4. Finally, Section 3.5 summarises the chapter.

3.1 Elastic Stress-Strain Components

As stated in Chapter Two, Li and Chen [24] reformulated the Mori-Tanaka mean field theory [19] in an incremental form to make it applicable to elastic-plastic non-proportional analysis. On the basis of Li and Chen model [24], the approach used to determine the incremental elastic stress and strain components in the matrix, reinforcement, and composite is presented in this section. This approach is suitable for PMMCs with high volume fractions of reinforcement, since it accounts for the interactions in the stress fields between the reinforcing particles.

Consider an elastic component that is subjected to an increment in external load or displacement tensor. In the absence of reinforcement, the external load would give rise to an increase in the uniform stress field, $d\sigma_{ij}$, which can be related to the increment in the strain field, $d\varepsilon_{ij}$, by writing Hooke's law (Eq. 2.6) in an incremental form as:

$$d\varepsilon_{ij} = \left(C_{ijkl(m)}\right)^{-1} d\sigma_{kl}. \tag{3.3}$$

Following the approach introduced by Mori and Tanaka mean field theory [19], the average incremental stress in the matrix, $d\sigma_{ij(m)}$, differs from the applied incremental stress by a perturbed incremental stress, $d\tilde{\sigma}_{ij(m)}$, or,

$$d\sigma_{ij(m)} = d\sigma_{ij} + d\tilde{\sigma}_{ij(m)}. \tag{3.4}$$

Although the presence of reinforcement would give rise to local non-linear stress gradients, in [19], Mori and Tanaka find it acceptable to define the average stress and strain between particles because relating the actual state of stress to strain at a point in a composite system is a complex non-linear problem. As noted in Chapter Two, the mean field theory provides a simplification to the rather complex non-linear problem.

The incremental perturbed stress is related to the corresponding incremental perturbed strain, $d\tilde{\varepsilon}_{ij(m)}$, by the Hooke's law as:

$$d\tilde{\sigma}_{ij(m)} = C_{ijkl(m)} d\tilde{\varepsilon}_{ij(m)}, \tag{3.5}$$

where $d\tilde{\varepsilon}_{ij(m)}$ is the matrix incremental strain disturbance that results from the presence of the particles. The average incremental stress in the matrix is given by:

$$d\sigma_{ij(m)} = d\sigma_{ij} + d\tilde{\sigma}_{ij(m)} = C_{ijkl(m)}(d\varepsilon_{kl} + d\tilde{\varepsilon}_{kl(m)}) = C_{ijkl(m)} d\varepsilon_{kl(m)}. \tag{3.6}$$

The particles average incremental stress and strain are also different from that of the matrix. Applying Eshelby's equivalent inclusions principle, as stated in Eq. (2.8), yields:

$$d\sigma_{ij(f)} = C_{ijkl(f)}(d\varepsilon_{kl} + d\tilde{\varepsilon}_{kl(m)} + d\varepsilon^{c}_{kl}) = C_{ijkl(m)}(d\varepsilon_{kl} + d\tilde{\varepsilon}_{kl(m)} + d\varepsilon^{c}_{kl} - d\varepsilon^{t}_{kl}). \tag{3.7}$$

Using the rule of mixtures, the composite stress is obtained as the weighted sum of the constituents stresses, or,

$$d\sigma_{ij} = V_f d\sigma_{ij(f)} + V_m d\sigma_{ij(m)}, \tag{3.8}$$

where V_m is matrix volume fractions. Equations (3.6)-(3.8) can be combined to give:

$$d\tilde{\sigma}_{ij(m)} V_m = V_f d\sigma_{ij(f)}. \tag{3.9}$$

The incremental strain disturbance in the matrix can be found using Eqs. (3.6)-(3.7), and (3.9) as:

$$d\tilde{\varepsilon}_{ij(m)} = (1 - V_m)(I - S_{ijkl})(d\varepsilon^t_{kl}). \tag{3.10}$$

Equations (3.6), (3.9), and (3.10), and the incremental form of Eq. (2.3) can be manipulated to obtain the incremental transformation strain, $d\varepsilon^t_{ij}$. The resulting incremental transformation strain is given as:

$$d\varepsilon^t_{ij} = L^{-1}(C_{klst(f)} - C_{klst(m)})\left(C^{-1}_{klst(m)} d\sigma_{ij}\right), \tag{3.11}$$

where,

$$L = [(V_f - 1)C_{ijkl(m)}(I - S_{ijkl}) + C_{ijkl(f)}[V_f(S_{ijkl} - I) - S_{ijkl}]. \tag{3.12}$$

Substituting Eq. (3.11) into Eq. (3.10), and the resulting equation into Eq. (3.6), yields the average incremental stress in the matrix, or,

$$d\sigma_{ij(m)} = d\sigma_{ij} - V_f C_{klst(m)} \left(S_{klst} - I\right) L^{-1} (C_{klst(f)} - C_{klst(m)}) C^{-1}_{klst(m)} d\sigma_{ij}. \tag{3.13}$$

The incremental matrix elastic strain can be calculated using the Hooke's law as:

$$d\varepsilon^{e}_{ij(m)} = C^{-1}_{ijkl(m)} d\sigma_{kl(m)}. \tag{3.14}$$

The average incremental stress in the reinforcement is obtained from Eqs. (3.7) and (3.11) as:

$$d\sigma_{ij(f)} = d\sigma_{ij} + V_m C_{klst(m)} \left(S_{klst} - I\right) L^{-1} (C_{klst(f)} - C_{klst(m)}) C^{-1}_{klst(m)} d\sigma_{ij}. \tag{3.15}$$

The incremental elastic strain in the reinforcement can then be calculated using the Hooke's law as:

$$d\varepsilon^{e}_{ij(f)} = C^{-1}_{ijkl(f)} d\sigma_{kl(f)}. \tag{3.16}$$

The increments in the average strains or stresses in the composite can be estimated using an approximate technique proposed by Li and Chen in [24]. For a multi-phase composite system, the technique assumes that the work done by an average stress or strain increment in the composite is equal to the weighted sum of the work done by the

stress or strain increment of each particle and the matrix. Applying this technique to a two-phase composite system yields:

$$d\sigma_{ik}d\varepsilon_{kj} = V_m d\sigma_{ik(m)}d\varepsilon_{kj(m)} + V_f d\sigma_{ik(f)}d\varepsilon_{kj(f)}. \tag{3.17}$$

This relation has been used in [2], [10], [24] to calculate the stress or strain increments in the composite from the constituents stress or strain increments. Using the relations presented above, i.e. Eqs. (3.3)-(3.17), that outlined the incremental mean field theory, the average increments in stress and strain in an elastic PMMC and its constituents can be determined knowing the strain and stress field that would arise in the component if it was hypothetically made of the homogeneous matrix material, and the composite material properties.

3.2 Cyclic Plasticity Models

Once the matrix has exceeded its initial yield limit, the increment in the total matrix strain can be found using Eqs. (3.1), (3.13), (3.14), and a suitable plastic constitutive model. To obtain the increment in the matrix plastic strain tensor in Eq. (3.1) it is essential to implement an incremental plasticity model within the framework of the Li and Chen [24] incremental mean field theory.

As emphasized in Chapter Two, several cyclic plasticity models are currently being used to describe the stress-strain relationship in homogeneous materials. Of these, only few have been incorporated into formulation targeted at describing the constitutive

behavior of PMMCs. As also noted in Chapter Two, the incremental plasticity model based on the Mróz model [28] was observed to accurately model the constitutive response of homogeneous components subjected to cyclic non-proportional loading. Although the Mróz type model is more widely known, the endochronic theory, emanating from thermodynamic principles, has a benefit of not requiring the knowledge of the yield surface and thus has been gaining wide interest. Furthermore, it has also been shown in [32] that for homogeneous materials, the endochronic theory of plasticity can better predict some of the transient effects associated with cyclic non-proportional loading.

In this research, two sets of elastic-plastic constitutive relations are identified as applicable to PMMCs. Specifically, using the Mróz model (Section 3.2.1) and the endochronic theory of plasticity (Section 3.2.2) as their bases, two constitutive models are developed that describe the increments in the matrix plastic strain given in Eq. (3.1). These sets of relations account for the interaction in stress fields between adjacent particles in PMMCs.

3.2.1 Mróz Model

The formulation of the matrix incremental classical plasticity theory using the Mróz model [28] is based on three major components: a yield surface, a flow rule and a hardening rule.

The yield surface is used to define the onset of plastic deformation for a material subjected to multiaxial loading. The yield function is generally formulated by postulating a yield criterion. Several yield criteria have been proposed for homogeneous materials

among which the von-Mises criterion, which uses the distortional energy to predict the onset of plastic yielding, is the most widely used. For the matrix material, the von-Mises yield criterion can be mathematically represented as:

$$F\left(S_{ij(m)}\right)=\frac{3}{2}\left(S_{ij_{(m)}}\right)\left(S_{ij_{(m)}}\right)-\sigma_{o(m)}^{2}=0, \tag{3.18}$$

where $S_{ij,\text{ and }}\ \sigma_{o(m)}$ represent the deviatoric components of the matrix stress, $\sigma_{ij(m)}$, and material yield stress respectively. The matrix deviatoric stress tensor can be obtained from:

$$S_{ij(m)}=\sigma_{ij(m)}-\left(\frac{1}{3}\right)\sigma_{kk(m)}\delta_{ij}, \tag{3.19}$$

where δ_{ij} is the Kronecker delta.

The flow rule relates the strain and stress increments. It assumes that the increments in plastic strains are usually proportional to the partial derivatives of a stress potential function. When the potential function is the same as the yield function, the resulting flow rule is termed the associated flow rule; the direction of plastic strain being associated with the yield function.

The associated flow rule is given by:

$$d\varepsilon_{ij(m)}^{p}=\lambda\frac{dF\left(\sigma_{ij(m)}\right)}{d\sigma_{ij(m)}}. \tag{3.20}$$

The flow rule can be re-written in the general form as:

$$d\varepsilon^{p}_{ij(m)} = \frac{1}{K_{p(m)}} \hat{n}_{ij} (\hat{n}_{kl} d\sigma_{kl(m)}), \tag{3.21}$$

where $K_{p(m)}$ and $\hat{n}_{ij}$ represent the matrix hardening modulus and the unit outward normal associated with the yield surface respectively. The outward normal to the yield surface is given by,

$$\hat{n}_{ij} = \frac{\dfrac{\partial F}{\partial S_{ij(m)}}}{\left(\dfrac{\partial F}{\partial S_{kl(m)}} \dfrac{\partial F}{\partial S_{kl(m)}} \right)^{\frac{1}{2}}}. \tag{3.22}$$

The hardening rule indicates how the yield function changes during the plastic deformation of the material. There are two major classifications of hardening rules developed for homogeneous materials that include the isotropic and the kinematic hardening rules. The isotropic hardening model assumes that the center of the yield surface remains fixed but the size of the yield surface increases during plastic deformation. However, the isotropic hardening rule is not suitable for modeling cyclic deformation of materials since it does not account for the anisotropy associated with plastic deformation (the Bauschinger effect). To account for this effect, the kinematic hardening model, which assumes that the size and the shape of the yield surface remains unchanged while the center of the surface translates by an amount $d\xi_{ij}$ in the stress space (shown in Fig. 3.1), is used. In the kinematic hardening model, $\xi_{ij(m)}$ represent the deviatoric components of the backstress tensor, α_{ij}. To date, most of the existing

classical cyclic plasticity models are formulated based on the idea of a translating yield surface. However, their difference lies in the rule governing the translation.

In [28], Mróz modeled the nonlinear response of a material by introducing a field of "l " initially concentric work hardening surfaces and prescribing a translation rule for the surfaces moving with respect to one another. A given surface, $n(1 \le n \le l)$, is defined by its center coordinates, α_{ij}^{n}, a yield stress, σ_{o}^{n}, and a plastic tangent, $E_{p(m)}^{t(n)}$, as illustrated in Fig. 3.2. The model assumes that each surface can be described by the same relationship as the yield criterion. If the von-Mises yield criterion is used, a given surface can be represented by,

$$F^{n}\left(S_{ij(m)}, \xi_{ij(m)}\right) = \frac{3}{2}\left(S_{ij_{(m)}} - \xi_{ij(m)}^{n}\right)\left(S_{ij_{(m)}} - \xi_{ij(m)}^{n}\right) - \sigma_{o(m)}^{n\ 2} = 0. \qquad (3.23)$$

If the state of stress lies on a given surface, it is referred to as the active surface, and the subsequent increment in the plastic strain can be found by combining Eqs. (3.21), (3.22) and (3.23) giving:

$$d\varepsilon_{ij(m)}^{p} = \frac{3}{2}\frac{\left(S_{ij_{(m)}} - \xi_{ij(m)}^{n}\right)\left(S_{kl(m)} - \xi_{kl(m)}^{n}\right)d\sigma_{kl(m)}}{K_{p(m)}^{n}\sigma_{o(m)}^{(n)2}}. \qquad (3.24)$$

To obtain the yield stresses, $\sigma_{o(m)}^{(n)}$, and hardening moduli, $K_{p(m)}^{n}$, of each of the surfaces, the matrix material uniaxial stress-strain curve is divided into segments. Each segment can be described by its tangent modulus, $E_{p(m)}^{t(n)}$, and an equivalent stress, as shown in Fig. 3.2. The yield stress associated with a particular surface (n), is obtained

from the equivalent stress of surface (n). If the matrix material stress-strain curve is known, the hardening modulus associated with a particular surface (n) can be obtained as follows. For uniaxial loading, using the notation in Fig. 2.1, Eq. (3.24) reduces to,

$$d\varepsilon^{p}_{22(m)} = \frac{3}{2}\frac{\left(S_{22(m)} - \xi^{n}_{22(m)}\right)^{2} d\sigma_{(m)}}{K^{n}_{p(m)}\sigma^{(n)2}_{o(m)}}. \tag{3.25}$$

In Eq. (3.25), $\sigma^{(n)2}_{o(m)}$ can be obtained from Eq. (3.23) as:

$$\sigma^{n\ 2}_{o(m)} = \frac{3}{2}\left[\left(S_{11(m)} - \xi^{n}_{11(m)}\right)^{2} + \left(S_{22(m)} - \xi^{n}_{22(m)}\right)^{2} + \left(S_{33(m)} - \xi^{n}_{33(m)}\right)^{2}\right]. \tag{3.26}$$

The deviatoric stress and backstress tensors for uniaxial loading are expressed respectively as:

$$S_{ij(m)} = \begin{bmatrix} \frac{-1}{3}\sigma_{22(m)} & 0 & 0 \\ 0 & \frac{2}{3}\sigma_{22(m)} & 0 \\ 0 & 0 & \frac{-1}{3}\sigma_{22(m)} \end{bmatrix}, \tag{3.27}$$

and,

$$\xi_{ij(m)} = \begin{bmatrix} \frac{-1}{3}\alpha_{22(m)} & 0 & 0 \\ 0 & \frac{2}{3}\alpha_{22(m)} & 0 \\ 0 & 0 & \frac{-1}{3}\alpha_{22(m)} \end{bmatrix}. \tag{3.28}$$

Substituting Eqs. (3.27) and (3.28) into Eq. (3.26) and rearranging gives:

$$\sigma_{o(m)}^{(n)2} = \frac{9}{4}\left(S_{22(m)} - \xi_{22(m)}^{n}\right)^2. \tag{3.29}$$

Substituting Eq. (3.29) into Eq. (3.25) gives:

$$K_{p(m)}^{n} = \frac{2}{3}\frac{d\sigma_{22(m)}}{d\varepsilon_{22(m)}^{p}}. \tag{3.30}$$

The matrix uniaxial stress-strain curve, illustrated in Fig. 3.2, can be divided into segments in such a way that the resulting strain at any point R can be related to the stress by the expression:

$$\varepsilon(R) = \frac{\sigma_o^{(1)}}{E} + \sum_{i=1}^{n-1}\frac{\sigma_o^{(i+1)}}{E_p^{t(i)}} + \frac{\sigma(R) - \sigma_o^{(n)}}{E_p^{t(n)}}. \tag{3.31}$$

Differentiating Eq. (3.31) with respect to the matrix plastic strain component, and substituting the resulting relation into Eq. (3.30) yield the hardening modulus of the active matrix surface as:

$$K_{p(m)}^{n} = \frac{2}{3}\frac{d\sigma_{(m)}}{d\varepsilon_{(m)}^{p}} = \frac{2}{3}\left[\frac{1}{\frac{1}{E_{p(m)}^{t}} - \frac{1}{E_m}}\right]. \tag{3.32}$$

At the beginning of an initial load increment, it is assumed that the matrix strains are elastic, and can be obtained using Eqs. (3.13) and (3.14). This initial elastic region continues until the innermost matrix yield surface (i.e. F^1) is reached. This is achieved when the equation,

$$F^1\left(S_{ij(m)}\right)=\frac{3}{2}\left(S_{ij(m)}\right)\left(S_{ij(m)}\right)-\sigma^{1\ 2}_{o(m)}=0, \tag{3.33}$$

is satisfied.

During plastic straining, it is required that the plastic deformation must be consistent with the changes in the yield surface. That is, the stress state must always lie on a yield surface. When the stress lies on the yield surface, the subsequent straining may be due to elastic-plastic loading or elastic unloading with the possibility of elastic-plastic loading. The actual occurrence is determined by the loading/unloading criterion. Consider the yield stress function (illustrated in Fig. 3.3). If the current matrix stress lies on the active yield surface, and further increment in this stress results in a new state of stress that lies within the yield surface, then the subsequent loading clearly yields elastic unloading. In other words, if the angle, θ, between the directions of the outward normal to the current yield surface and the current stress increment is obtuse, then this stress increment moves inward from the yield surface. This condition for elastic unloading can be mathematically represented as:

$$\frac{\partial F}{\partial S_{ij}}dS_{ij}\leq 0. \tag{3.34}$$

On the other hand, if the angle θ, is acute, then the stress increment is directed toward the exterior of the yield surface, thus, leading to elastic-plastic loading. This elastic-plastic loading criterion can be expressed mathematically as:

$$\frac{\partial F}{\partial S_{ij}} dS_{ij} > 0. \tag{3.35}$$

It should be noted that if the angle θ, is 90°, the inequality in Eq. (3.34) is equal, then the stress increment will be tangential to the yield surface. This is referred to as a neutral loading. For computer implementation, an algorithm is needed to ensure that the matrix stresses for neutral loading remain on the yield surface. However, since the implementation of this unloading criterion makes it almost impossible to locate neutral loading, it is generally presented as an unloading condition. Consequently, an elastic stress increment is added to the current stress while no movement in the yield surface occurs. Equations (3.34)-(3.35) can be combined into a single equation as:

$$LP \begin{cases} > 0 & \text{Elastic} - \text{plastic Loading} \\ \leq 0 & \text{Elastic Unloading} \end{cases}, \tag{3.36}$$

where LP is found by substituting Eq. (3.23) into Eq. (3.34) to obtain,

$$LP = \left(S_{ij} - \xi_{ij}\right) \Delta\sigma_{ij}. \tag{3.37}$$

Mróz Model: Elastic Unloading

If the external load results in elastic unloading, as dictated by Eq. (3.36), the stress point moves within the innermost material yield surface. The unloading constitutive response of the matrix is then represented by the incremental mean field theory (Eqs. (3.13)-(3.14)). Additionally if the elastic unloading criterion is satisfied in Eq. (3.36), it is important to find out whether or not the matrix will further experience an elastic-plastic deformation during this load increment. A procedure for determining this is illustrated in Fig. 3.4. In Fig. 3.4, the initially calculated matrix stress state lies on the inner yield surface, if the unloading occurs during this increment, the stress path has to follow the elastic analysis. Hence, during the elastic unloading, the matrix stress and deviatoric stress increment could be obtained using Eq. (3.13) and Eq. (3.19). If the matrix stress increment $\left(\Delta S_{ij(m)}\right)$ intersects the yield surface at $S'_{ij(m)}$, then this new stress could be found by using the equation:

$$S'_{ij(m)} = S_{ij} + k\Delta S_{ij(m)}, \tag{3.38}$$

where k is the parameter (greater than zero) that represents where and if the loading path intersects the yield surface. To determine parameter k, it is required that the new matrix stress state, $S'_{ij(m)}$, must lie on the innermost yield surface (i.e. F^1). Substituting Eq. (3.38) into Eq. (3.23), and simplifying the resulting equation yield:

$$\left[\Delta S_{ij(m)}.\Delta S_{ij(m)}\right]k^2+\left[2\Delta S_{ij(m)}.\left(S_{ij_{(m)}}-\xi^1_{ij(m)}\right)\right]k+ \left[\left(S_{ij_{(m)}}-\xi^1_{ij(m)}\right).\left(S_{ij_{(m)}}-\xi^1_{ij(m)}\right)\right]-\frac{2}{3}\sigma_o^{(1)2}=0. \tag{3.39}$$

Equation (3.39), when solved, yields two values of k. The correct root is the larger value that is greater than zero. The correct root dictates whether or not elastic-plastic loading will occur following an elastic unloading event, or,

$$k\begin{cases}<1 & \text{elastic}-\text{plastic loading will occur}\\ =1 & \text{new matrix stress state lies on the yield surface .}\\ >1 & \text{new matrix stress state is elastic}\end{cases} \tag{3.40}$$

If a fraction of the stress increment is found to result in elastic-plastic loading, then the corresponding strain increment must be found using the procedure below for elastic-plastic loading.

Mróz Model: Elastic-Plastic Loading

If in accordance with Eq. (3.36) or (3.40) elastic-plastic unloading has occurred, the matrix plastic strain increment can be found using Eq. (3.24). However, in doing so, the active surface and the location of each surface in stress space must be determined. Again, the active surface is the surface on which the stress state is located. The initial surface in stress space is the surface associated with material yielding in tension, and the outer surfaces become active at higher stress levels. Accordingly, initially the center coordinate of each yield surface is zero. For matrix plastic straining, after obtaining the

increment in the matrix stress tensor, it is essential to update the yield surface configuration using the Mróz translation rule. In [28], Mróz prescribes a translation rule for surfaces moving with respect to each other over distances given by the stress increments. Mróz based the translation of the surface on the concept of mutual tangency. That is, Mróz assumed that upon elastic-plastic loading, the surfaces move within each other and they do not intersect. If, however, they come in contact or become mutually tangent, they move together as a rigid body. The active surface is then determined by the largest surface tangent to the active yield surface. The translation rule for the active surface (n) is given in [28] as:

$$d\xi^{n}_{ij(m)} = d\mu\left(S^{n+1}_{ij(m)} - S^{n}_{ij(m)}\right), \tag{3.41}$$

where $d\mu$ is the magnitude of the active surface translation, and the term $\left(S^{n+1}_{ij(m)} - S^{n}_{ij(m)}\right)$ governs the direction of its translation. The quantity $S^{n+1}_{ij(m)}$ is the point on a surface F^{n+1}, immediately outer to the active surface F^{n}, having the same unit normal as the active surface at the actual current stress state, $S^{n}_{ij(m)}$. It is obtained from Mróz translation rule as:

$$S^{n+1}_{ij(m)} = \xi^{n+1}_{ij(m)} + \frac{\sigma^{n+1}_{o(m)}}{\sigma^{n}_{o(m)}}\left(S_{ij(m)} - \xi^{n}_{ij(m)}\right), \tag{3.42}$$

where $\sigma^{n+1}_{o(m)}$ and $\sigma^{n}_{o(m)}$ are the yield stresses of surfaces (n+1) and (n) respectively.

The magnitude of translation is given by the consistency condition that assures that the stress point lies on the yield surface during plastic deformation, or,

$$d\mu = \frac{\left(S_{ij(m)} - \xi^{n}_{ij(m)}\right) dS_{ij(m)}}{\left(S_{kl(m)} - \xi^{n}_{kl(m)}\right)\left(S^{n+1}_{kl(m)} - S_{kl(m)}\right)}. \tag{3.43}$$

All inner surfaces remain tangent at the loading point during the elastic-plastic loading and thus the center of the inner surfaces can be obtained from:

$$\xi^{n-1}_{ij(m)} = S_{ij(m)} - \frac{\sigma^{n-1}_{(m)}}{\sigma^{n}_{(m)}}\left(S_{ij(m)} - \xi^{n}_{ij(m)}\right) \quad . \tag{3.44}$$

Before applying the translation rule, it is essential to determine the surface that is active after the increment in the matrix stress tensor has been applied. In other words, if surface F^n is the active surface before the matrix stress increment, it is essential to determine whether the new matrix stress state remains on surface F^n or if it lies on the outer surface, F^{n+1}. This can be achieved by finding the fraction, κ, of the matrix stress increment that results in a stress state that lies on the outer surface F^{n+1}. This fraction of the matrix stress, $\Delta\sigma_{ij(m)}$, is determined such that the new matrix stress, $\sigma_{ij(m)} + \kappa\Delta\sigma_{ij(m)}$, lies on the outer yield surface. This is obtained by substituting the matrix deviatoric stress tensor, $S_{ij(m)} + \kappa\Delta S_{ij(m)}$, into Eq. (3.23), using the outer surface yield stress, giving:

$$\left[\left(\Delta S_{ij(m)} + \kappa \Delta S_{ij(m)}\right) + \xi_{ij(m)}^{(n+1)}\right] \cdot \left[\left(\Delta S_{ij(m)} + \kappa \Delta S_{ij(m)}\right) + \xi_{ij(m)}^{(n+1)}\right] - \frac{2}{3}\sigma_o^{(n+1)2} = 0. \quad (3.45)$$

The value of κ can be found by simplifying Eq. (3.45) yielding:

$$\left[\Delta S_{ij(m)} \cdot \Delta S_{ij(m)}\right]\kappa^2 + \left[2\Delta S_{ij(m)} \cdot \left(S_{ij_{(m)}} - \xi_{ij(m)}^{n+1}\right)\right]\kappa + \left[\left(S_{ij_{(m)}} - \xi_{ij(m)}^{n+1}\right)\left(S_{ij_{(m)}} - \xi_{ij(m)}^{n+1}\right)\right] - \frac{2}{3}\sigma_o^{(n+1)2} = 0. \quad (3.46)$$

The correct value of κ is the positive root of Eq. (3.46), greater than zero, and it determines the active matrix yield surface as:

$$\kappa \begin{cases} \leq 1 & \text{the new active surface is } F^{n+1} \\ > 1 & F^n \text{ remains the active surface} \end{cases}. \quad (3.47)$$

The matrix plastic strain tensor can be obtained from the given incremental composite stress tensor using the properties associated with the active surface in the normality flow rule (Eq. 3.24). The total matrix strain tensor can then be found by substituting Eqs. (3.13)-(3.14) and (3.24) into Eq. (3.1). If the value of κ is less than unity, then the matrix updated stress state, $\sigma_{ij(m)} + \kappa \Delta \sigma_{ij(m)}$, lies on the surface F^{n+1}. The increment in the composite stress tensor that brought the matrix stress state to this new yield surface has to be divided into two increments. Specifically, the first increment is required to bring the new matrix elastic-plastic strain and stress state to the new yield surface, and the second is required for subsequent straining of the new surface.

To obtain the fraction of the increment in the composite stress tensor that brought the elastic-plastic strain and stress increment of the matrix to the new surface, the work relation in Eq. (3.17) is used without the superscripts to indicate a single equation rather than individual components of the equations. In this equation, the increment in the matrix stress tensor is known. It is the matrix stress increment tensor given by, $\kappa\Delta\sigma_{ij(m)}$, and the matrix strain increment tensor can be obtained from the stress tensor using Eq. (3.14) on the active surface F^n. The corresponding increment in composite and reinforcement stress tensors can be obtained by finding the fraction, κ^a, of the increment in composite tensor, $\Delta\sigma_{ij}$, (i.e. $\kappa^a\Delta\sigma_{ij}$) that satisfies Eq. (3.17). The composite strain increment can be obtained from this portion of the composite stress increment using the relation:

$$\Delta\varepsilon_{ij} = C_m\left[I + V_f\left(V_m\left(C_f - C_m\right)S + C_m\right)^{-1}\left(C_f - C_m\right)\right]\Delta\sigma_{ij}. \tag{3.48}$$

For the portion of the composite increment stress tensor, i.e. $\kappa^a\Delta\sigma_{ij}$, the increment in the reinforcement stress tensor is obtained from Eq. (3.15), and the increment in the reinforcement strain tensor is subsequently obtained using Eq. (3.16). Substituting these increments in the reinforcement and matrix stress and strain tensors into Eq. (3.17), and combining the resulting equation with Eq. (3.48) yields:

$$\begin{aligned}&\left[\begin{aligned}&C_m\left(\Delta\sigma_{ij}\Delta\sigma_{ij}\right)\left[I + V_f\left(V_m\left(C_f - C_m\right)S + C_m\right)^{-1}\left(C_f - C_m\right)\right] - \\ &\left[V_f\left(\Delta\sigma_{ij} + V_m C_{klst(m)}\left(S_{klst} - I\right)L^{-1}\left(C_{klst(f)} - C_{klst(m)}\right)C^{-1}_{klst(m)}d\sigma_{ij}\right)C^{-1}_{ijkl(f)}\sigma_{ij}\right]\end{aligned}\right]\left(\kappa^a\right)^2 \\ &= V_m\left[\begin{aligned}&\kappa^2 C^{-1}_{ijkl(m)}C^{-1}_{ijkl(m)} \\ &\left(\Delta\sigma_{ij(m)}d\sigma_{ij(m)}\right)\end{aligned}\right].\end{aligned} \tag{3.49}$$

Equation (3.49) yields two values of, κ^a, the correct value is the one between zero and unity. Consequently, $\kappa^a \Delta\sigma_{ij}$, produces the matrix elastic-plastic strain-stress state that lies on the active surface F^{n+1}. The remaining portion, i.e. $\left(1-\kappa^a \Delta\sigma_{ij}\right)$ produces the elastic-plastic strain-stress state that moves with the surface F^{n+1}. Note that the value of κ in Eq. (3.49) is obtained in Eq. (3.46).

3.2.2 Endochronic Theory of Plasticity

The endochronic theory of plasticity was developed based on the observation that the state of stress in the neighborhood of a point in an elastic-plastic material depends on the set of all previous states of deformation in that neighborhood, but it does not depend on the rapidity at which such deformation states have succeeded one another [31]. The endochronic theory encompasses all cyclic plasticity theories in which the state of stress at a particular load increment is a function of the history of strain with respect to a time scale (referred to as intrinsic time scale), which is not the absolute time scale measured by a clock. Different material behavior/responses are obtained simply by changing the form of the intrinsic time scale [34]. For the non-proportional loading case, where the states of stress and strain depend on the loading path, the definition of an appropriate strain path is a fundamental task that must be carried out before the strain increments can be obtained.

Originally in [31], Valanis defined the intrinsic time scale in terms of the length of the path in total strain space. However in [71], Sandler indicated that the original theory does not produce a correct reloading response and that it violates the Drucker's

postulate of stability. As a result, in [33], Valanis reformulated the intrinsic time scale in terms of the length of the path in plastic strain space as opposed to the length of the strain path in total strain space as in [31]. This has led to the revised endochronic theory of plasticity, used in this research to predict the increment in the matrix plastic strain from a given increment in stress. Here, all relations are developed to respect the heterogeneous nature of PMMCs.

Since the endochronic theory implemented here deals with the plastic behavior of the matrix, all of the material constants and equation sets are for the matrix material. The endochronic constitutive equation for plastically incompressible, rate-independent, initially isotropic materials is given by:

$$S_{ij(m)} = 2\int_0^z \rho\left(z - z'\right)\frac{d\varepsilon^p_{ij(m)}\left(z'\right)}{dz'}dz', \tag{3.50}$$

where,

$$dz = \frac{d\zeta}{f\left(\zeta\right)} \tag{3.51}$$

and,

$$d\zeta = \left(d\varepsilon^p_{ij(m)}d\varepsilon^p_{ij(m)}\right)^{1/2}. \tag{3.52}$$

In Eqs. (3.50)-(3.52), $f(\zeta)$ and $\rho(z)$ are material functions referred to as the hardening and hereditary functions respectively, z is the intrinsic time scale, and ζ is the intrinsic time measure that defines the memory path in the plastic strain space. $d\zeta$ is the distance between two neighboring points in plastic strain space. Deformation history effects of the material are introduced into the constitutive equations through these parameters. The

intrinsic time scale keeps a record of the changes in internal structure that occur as the material deforms. Since elastic straining does not induce any changes in the internal structure of the material, the value of the intrinsic time scale must not be affected by the elastic component of the strain tensor. The definition of the intrinsic time in terms of the plastic strain components ensures that the intrinsic time scale increment, dz, is zero whenever plastic deformations do not take place. Equation (3.50) expresses the fact that stress is a linear hereditary function of the history of plastic strain expressed in terms of the intrinsic time scale.

It is important to note that the endochronic theory characterizes the phenomenon of hardening and softening (i.e. transient effects) by stretching the memory path by the hardening function $f(\zeta)$. The hardening function can be determined from a set of transient uniaxial cyclic stress-strain data. However, in this research investigation, as in [72], transient effects were not considered. That is, a stabilized cyclic response is assumed and therefore the hardening function is equal to one (i.e. $f(\zeta) = 1$). Assuming a stabilized response has been justified in [2] where it was reported that aluminum alloy (6061-T6) based PMMCs, used also for the experimental tests conducted in this research, appear to exhibit little, if any, cyclic transient hardening or softening at low load levels. However, at higher load levels, it was reported in [2] that the material slightly cyclically hardens during the first ten applied cycles before exhibiting stabilized behavior. Thus, at higher load levels, $f(\zeta)$ can be assumed to be equal to one.

In Eq. (3.50), the hereditary function (otherwise known as kernel function), $\rho(z)$, has a weak singularity at the origin but can be integrated in the domain $0 \leq z' \leq \infty$. The

singularity generates initially elastic unloading, and thus implies a very small elastic domain. The hereditary function is represented by an n-order Dirichlet series given as:

$$\rho(z) = \sum_{r=1}^{n} C_r e^{-\alpha_r z}, \tag{3.53}$$

where C_r and α_r are material constants determined from the uniaxial cyclic stress-strain curve of the material. Equation (3.53) is used with the requirements that C_r and α_r must be positive, and satisfy the following conditions:

$$\sum_{r=1}^{\infty} C_r = \infty, \tag{3.54}$$

and,

$$\sum_{r=1}^{\infty} \frac{C_r}{\alpha_r} \leq \infty. \tag{3.55}$$

Equation (3.54) ensures that $\rho(0)$ (i.e. the hereditary function when the intrinsic time scale $z = 0$) is sufficiently large in order to give an instantaneous elastic response at the onset of loading, or subsequent unloading, while Eq. (3.55) enables the integrability of the hereditary function over a finite domain of the intrinsic time scale. The form of $\rho(z)$ given in Eq. (3.53) is suitable for computer implementation since only the information of the previous loading step is needed to find the present response of the material. This leads to the simplification of the path dependent constitutive equations and also saves time and storage space.

The determination of suitable values of the material constants in Eq. (3.53) is a vital step in the implementation of the endochronic theory of plasticity. However, one of the major problems associated with the use of the endochronic theory of plasticity is the fact that although there has been ground breaking work in establishing procedures for determining endochronic material constants in Eq. (3.53), the existing procedures appear too complex, and it is unlikely that the procedure will become a part of engineering practice without further simplification [32]. Researchers have primarily used trial and error methods to extract the material functions. In this research, the material constants are obtained by descritizing the cyclically stable uniaxial stress-strain curve into a suitable number of segments, as illustrated in Fig. 3.5. Each segment is described by an approximate equation relating the variation of the material stress with the plastic strain. The procedure is described below.

For uniaxial loading of the material, using the notation in Fig. 2.1, Eq. (3.52) can be expressed as:

$$d\zeta = \sqrt{\frac{3}{2}} d\varepsilon^{p}_{22(m)}. \tag{3.56}$$

Since the material is assumed to be cyclically stable, then $f(\zeta) = 1$. Substituting $f(\zeta) = 1$ into Eq. (3.51) yields:

$$dz = d\zeta. \tag{3.57}$$

Substituting Eq. (3.57) into Eq. (3.56) and rearranging the resulting equation yield:

$$\frac{d\varepsilon^{p}_{22(m)}}{dz} = \sqrt{\frac{2}{3}}. \tag{3.58}$$

The uniaxial form of Eq. (3.50) is given as:

$$S_{22(m)} = 2\int_0^z \rho\left(z - z'\right)\frac{d\varepsilon^{p}_{22(m)}\left(z'\right)}{dz'}dz'. \tag{3.59}$$

Substituting Eqs. (3.27), (3.53) and (3.58) into (3.59) yields:

$$\sigma_{22} = \sqrt{6}\int_0^z C_r e^{-\alpha_r\left(z-z'\right)}dz' \quad . \tag{3.60}$$

Substituting Eq. (3.58) into the results obtained by integrating Eq. (3.60) yields:

$$\sigma_{22} = \sum_{r=1}^{n}\sigma_r, \tag{3.61}$$

where,

$$\sigma_r = D_r\left(1 - e^{-\alpha_r\sqrt{\frac{3}{2}}\varepsilon^{p}_{22}}\right). \tag{3.62}$$

In Eq. (3.62),

$$D_r = \sqrt{6}\frac{C_r}{\alpha_r}. \tag{3.63}$$

Equations (3.61) and (3.62) relate the uniaxial stress to the plastic strain. Thus, theoretically, this equation can be curve-fitted into the experimentally obtained uniaxial tension or cyclic stress-plastic strain curve to obtain the materials constants. Achieving this may be a difficult task in a case where the number of terms necessary to define the material stress-plastic strain curve is high. As stated earlier, in this research, the experimental matrix material stress-plastic strain curve is descritized into a number of segments. Using the notation shown in Fig. 3.5, the stresses and plastic strains at different points on each segment can be substituted into Eqs. (3.62) and (3.63) in order to obtain possible values of the material constants. An averaging scheme can then be used to obtain the approximate values of the constants for the segments. The results obtained for different segments are combined using Eq. (3.61) to obtain the material stress-plastic strain curve. This procedure is repeated until the stress-plastic strain curve obtained is very close to the experimental stress-plastic strain curve. In [73], Fan developed an alternative approach by formulating a set of equations that relate the material constants, the stresses, and plastic strains at various points on the material uniaxial stress-strain curve.

After numerically obtaining the material constants, the matrix plastic strain components can be obtained by integrating Eq. (3.50) with respect to the intrinsic time scale. To do so, the deviatoric stress in the matrix is first obtained by substituting Eq. (3.53) into Eq. (3.50) yielding:

$$S_{ij(m)} = \sum_{r=1}^{n} 2 \int_0^z C_r e^{-\alpha_r (z-z')} \frac{d\varepsilon^p_{ij(m)}}{dz'} dz. \qquad (3.64)$$

For stress-controlled simulations, the load path is divided into q-steps. Assuming small increments, Eq. (3.64) can be written as:

$$\left(S_{ij(m)}\right)_q = \sum_{r=1}^{n}\left(S^r_{ij(m)}\right)_q, \tag{3.65}$$

where,

$$\left(S^r_{ij(m)}\right)_q = \left(S^r_{ij(m)}\right)_{q-1} e^{-\alpha_r \Delta z} + 2\frac{C_r}{\alpha_r}\frac{\Delta\varepsilon^p_{ij(m)}}{\Delta z_q}\left(1-e^{-\alpha_r \Delta z}\right). \tag{3.66}$$

In Eqs. (3.65) and (3.66), q is the current loading step, q-1 is the previous loading step, and Δ is a finite difference between the current and previous loading steps. If $(\Delta\varepsilon^p_{ij})_q$ and Δz are known, Eq. (3.66) implies that $(S^r_{ij(m)})_q$ can be found by knowing the previous value $(S^r_{ij(m)})_{q-1}$. Consequently, only the values of $(S^r_{ij(m)})$ at the previous loading condition need to be stored, a vital point from numerical application viewpoint.

The incremental stress deviator can be calculated using Eqs. (3.65) and (3.66) yielding the incremental value $(\Delta S^r_{(m)})_q$ given by:

$$\left(\Delta S_{ij}\right)_{q(m)} = 2\left[\frac{1}{\Delta z}\sum_{r=1}^{n}\frac{C_r}{\alpha_r}\left(1-e^{-\alpha_r \Delta z}\right)\right]\left(\Delta\varepsilon^p_{ij(m)}\right)_q + \sum_{r=1}^{n}\left(S^r_{ij(m)}\right)_{q-1}\left(e^{-\alpha_r \Delta z}-1\right). \tag{3.67}$$

The increment in the matrix plastic strain tensor can be obtained from Eq. (3.67) after rearrangement as:

$$\Delta\varepsilon^p_{ij(m)} = \frac{a_{ij}\Delta z}{b}, \tag{3.68}$$

where

$$a_{ij} = \frac{1}{2}\left[\left(\Delta S_{ij(m)}\right)_q + \sum_{r=1}^{n}\left(S^r_{ij(m)}\right)_{q-1}\left(1-e^{-\alpha_r \Delta z}\right)\right], \tag{3.69}$$

and,

$$b = \left[\sum_{r=1}^{n} C_r \frac{\left(1-e^{-\alpha_r \Delta z}\right)}{\alpha_r}\right]. \tag{3.70}$$

Equations (3.68), (3.69), and (3.70) imply that the increment in the matrix strain can be found if Δz is known.

The increment in the intrinsic time scale, Δz, can be found by first substituting Eq. (3.57) into Eq. (3.52), and changing the resulting equation to incremental form giving:

$$(\Delta z)^2 = (\Delta \zeta)^2 = \Delta \varepsilon^p_{ij} \Delta \varepsilon^p_{ij}. \tag{3.71}$$

Taking the inner product of Eq. (3.67) and using Eq. (3.71) in the resulting equation yield:

$$b^2 - a_{ij}a_{ij} = f(\Delta z). \tag{3.72}$$

Equation (3.72) is a function of Δz. Consequently, for a given increment of composite stress tensor, Eq. (3.72) can be used to solve for Δz using the Secant method to find the roots of the equation. For the composite system, Eqs. (3.1), (3.13), (3.14), (3.68)-(3.72) are used to calculate the increments in the matrix incremental elastic, plastic and total strain components from the given composite stress components.

It is important to note that in [33], Valanis has shown that by introducing the hereditary function of the form,

$$\rho(z) = \rho_1(z) + \tau_y^0 \delta(z), \tag{3.73}$$

where $\rho_1(z)$ is a singular function, $\delta(z)$ is Dirac-delta function, and τ_y^0 is a positive material constant, into Eq. (3.50) leads to the existence of a yield surface. Consequently, the classical theories of plasticity have been regarded as special cases of the endochronic theory. This work has divided research in the endochronic theory into two schools: one utilizing the Dirac delta function and the resulting concept of yield surface and the other school sticks to the original theory without a yield surface, though with a modified form of intrinsic time scale function to correct the objections raised in [71]. The second approach, given in Eq. (3.50), is used in this research for PMMCs.

3.3 PMMCs Elastic-Plastic Constitutive Relations

Two models that completely define the constitutive response of the matrix, reinforcement, and PMMCs are presented in this section. The first model (Section 3.3.1) couples the elastic constitutive response defined by the incremental mean field theory (Section 3.1) with the Mróz model (Section 3.2.1). The second model (Section 3.3.2) differs from the first in that in the second, the endochronic theory of plasticity (Section 3.2.2) is used to define the increments in the matrix plastic strain components.

3.3.1 Constitutive Relations Based on Mróz Model

For multiaxial cyclic loading, using the Mróz-based model, the incremental mean field theory, and the work relation, the following constitutive relations can be developed to predict the constituents and the composite elastic-plastic strain and stress increments.

Matrix Constitutive Model

The matrix constitutive relation can be finalized by substituting Eqs. (3.13), (3.14) , (3.24) into Eq. (3.1), while changing the differential to small increments for numerical implementation, yielding:

$$\Delta\varepsilon_{ij(m)} = \frac{1+\upsilon}{E_m}\left[\Delta\sigma_{ij} - V_f C_{klst(m)}\left(S_{klst} - I\right)L^{-1}(C_{klst(f)} - C_{klst(m)})C^{-1}_{klst(m)}\Delta\sigma_{ij}\right]$$
$$\frac{\upsilon}{E_{(m)}}\left[\Delta\sigma_{kk} - V_f C_{ilst(m)}\left(S_{ilst} - I\right)L^{-1}(C_{ilst(f)} - C_{ilst(m)})C^{-1}_{ilst(m)}\Delta\sigma_{kk}\right]\delta_{ij}$$
$$+\frac{1}{K^1_{p(m)}}\hat{n}^1_{ij}\left[\hat{n}^1_{kl}\left(\Delta\sigma_{kl} - V_f C_{klst(m)}\left(S_{klst} - I\right)L^{-1}(C_{klst(f)} - C_{klst(m)})C^{-1}_{klst(m)}\Delta\sigma_{kl}\right)\right]. \tag{3.74}$$

Reinforcement Constitutive Model

The reinforcement, being relatively stiff, has only the elastic strain components. The reinforcement constitutive relation can be finalized by substituting Eqs. (3.15), (3.16) , into Eq. (3.2), while changing the differential to small increments for numerical implementation, yielding:

$$\Delta\varepsilon_{ij(f)} = \frac{1+\upsilon}{E_m}\left[\Delta\sigma_{ij} + V_m C_{klst(m)}\left(S_{klst} - I\right)L^{-1}(C_{klst(f)} - C_{klst(m)})C^{-1}_{klst(m)}\Delta\sigma_{ij}\right]$$
$$-\frac{\upsilon}{E_{(m)}}\left[\Delta\sigma_{kk} + V_m C_{ilst(m)}\left(S_{ilst} - I\right)L^{-1}(C_{ilst(f)} - C_{ilst(m)})C^{-1}_{ilst(m)}\Delta\sigma_{kk}\right]\delta_{ij}.$$

(3.75)

Composite Constitutive Model

The composite constitutive relation can be finalized by substituting Eqs. (3.13), (3.15), (3.74), and (3.75) , into Eq. (3.17), changing the differential to small increments for numerical implementation, yielding:

$$\Delta\varepsilon_{ij} = V_m\left[\Delta\sigma_{kl}\right]^{-1}\left[\Delta\sigma_{kl} - V_f C_{klst(m)}\left(S_{klst} - I\right)L^{-1}(C_{klst(f)} - C_{klst(m)})C^{-1}_{klst(m)}\Delta\sigma_{kl}\right]$$
$$\left[\begin{array}{l}\frac{1+\upsilon}{E_m}\left[\Delta\sigma_{ij} - V_f C_{klst(m)}\left(S_{klst} - I\right)L^{-1}(C_{klst(f)} - C_{klst(m)})C^{-1}_{klst(m)}\Delta\sigma_{ij}\right] - \\ \frac{\upsilon}{E_{(m)}}\left[\Delta\sigma_{kk} - V_f C_{ilst(m)}\left(S_{ilst} - I\right)L^{-1}(C_{ilst(f)} - C_{ilst(m)})C^{-1}_{ilst(m)}\Delta\sigma_{kk}\right]\delta_{ij} + \\ \frac{1}{K^1_{p(m)}}\hat{n}^1_{ij}\left[\hat{n}^1_{kl}\left(\Delta\sigma_{kl} - V_f C_{klst(m)}\left(S_{klst} - I\right)L^{-1}(C_{klst(f)} - C_{klst(m)})C^{-1}_{klst(m)}\Delta\sigma_{kl}\right)\right]\end{array}\right].$$
$$+V_f\left[\Delta\sigma_{kl}\right]^{-1}\left[\Delta\sigma_{kl} + V_m C_{klst(m)}\left(S_{klst} - I\right)L^{-1}(C_{klst(f)} - C_{klst(m)})C^{-1}_{klst(m)}\Delta\sigma_{kl}\right]$$
$$\left[\begin{array}{l}\frac{1+\upsilon}{E_m}\left[\Delta\sigma_{ij} + V_m C_{klst(m)}\left(S_{klst} - I\right)L^{-1}(C_{klst(f)} - C_{klst(m)})C^{-1}_{klst(m)}\Delta\sigma_{ij}\right] - \\ \frac{\upsilon}{E_{(m)}}\left[\Delta\sigma_{kk} + V_m C_{ilst(m)}\left(S_{ilst} - I\right)L^{-1}(C_{ilst(f)} - C_{ilst(m)})C^{-1}_{ilst(m)}\Delta\sigma_{kk}\right]\delta_{ij}\end{array}\right]$$

(3.76)

3.3.2 Constitutive Relations Based on Endochronic Theory

For multiaxial cyclic loading, using the endochronic theory-based model, the

incremental mean field theory, and the work relation, the following constitutive relations are developed to predict the constituents and the composite elastic-plastic strain and stress increments.

Matrix Constitutive Model

The matrix constitutive relation can be finalized by substituting Eqs. (3.13), (3.14) , (3.68)-(3.70) into Eq. (3.1), while changing the differential to small increments for numerical implementation, yielding:

$$\Delta\varepsilon_{ij(m)} = \frac{1+\upsilon}{E_m}\left[\Delta\sigma_{ij} - V_f C_{klst(m)}\left(S_{klst} - I\right)L^{-1}(C_{klst(f)} - C_{klst(m)})C^{-1}_{klst(m)}\Delta\sigma_{ij}\right]$$
$$-\frac{\upsilon}{E_{(m)}}\left[\Delta\sigma_{kk} - V_f C_{ilst(m)}\left(S_{ilst} - I\right)L^{-1}(C_{ilst(f)} - C_{ilst(m)})C^{-1}_{ilst(m)}\Delta\sigma_{kk}\right]\delta_{ij} \,. \qquad (3.77)$$
$$+\frac{\frac{1}{2}\left[\left(\Delta S_{ij(m)}\right)_q + \sum_{r=1}^{n}\left(S^r_{ij(m)}\right)_{q-1}\left(1-e^{-\alpha_r\Delta z}\right)\right]\Delta z}{\left[\sum_{r=1}^{n} C_r \frac{\left(1-e^{-\alpha_r\Delta z}\right)}{\alpha_r}\right]}$$

Reinforcement Constitutive Model

The reinforcement, being relatively stiff, has only the elastic strain components. Consequently, the reinforcement constitutive relation is the same as in the Mróz-based PMMCs constitutive model given by Eq. (3.75).

Composite Constitutive Model

The composite constitutive relation can be finalized by substituting Eqs. (3.13),

(3.15), (3.75) and (3.77) into Eq. (3.17), changing the differential to small increments for numerical implementation, yielding:

$$\begin{aligned}\Delta\varepsilon_{ij} = {} & V_m\left[\Delta\sigma_{kl}\right]^{-1}\left[\Delta\sigma_{kl} - V_f C_{klst(m)}\left(S_{klst} - I\right)L^{-1}(C_{klst(f)} - C_{klst(m)})C^{-1}_{klst(m)}\Delta\sigma_{kl}\right] \\ & \left[\begin{array}{l}\dfrac{1+\upsilon}{E_m}\left[\Delta\sigma_{ij} - V_f C_{klst(m)}\left(S_{klst} - I\right)L^{-1}(C_{klst(f)} - C_{klst(m)})C^{-1}_{klst(m)}\Delta\sigma_{ij}\right] - \\ \dfrac{\upsilon}{E_{(m)}}\left[\Delta\sigma_{kk} - V_f C_{ilst(m)}\left(S_{ilst} - I\right)L^{-1}(C_{ilst(f)} - C_{ilst(m)})C^{-1}_{ilst(m)}\Delta\sigma_{kk}\right]\delta_{ij} + \dfrac{a_{ij}\Delta z}{b}\end{array}\right] \\ & + V_f\left[\Delta\sigma_{kl}\right]^{-1}\left[\Delta\sigma_{kl} + V_m C_{klst(m)}\left(S_{klst} - I\right)L^{-1}(C_{klst(f)} - C_{klst(m)})C^{-1}_{klst(m)}\Delta\sigma_{kl}\right] \\ & \left[\begin{array}{l}\dfrac{1+\upsilon}{E_m}\left[\Delta\sigma_{ij} + V_m C_{klst(m)}\left(S_{klst} - I\right)L^{-1}(C_{klst(f)} - C_{klst(m)})C^{-1}_{klst(m)}\Delta\sigma_{ij}\right] - \\ \dfrac{\upsilon}{E_{(m)}}\left[\Delta\sigma_{kk} + V_m C_{ilst(m)}\left(S_{ilst} - I\right)L^{-1}(C_{ilst(f)} - C_{ilst(m)})C^{-1}_{ilst(m)}\Delta\sigma_{kk}\right]\delta_{ij}\end{array}\right]\end{aligned}. \quad (3.78)$$

In Eq. (3.78), a_{ij} and b are as given in Eqs. (3.69) and (3.70) respectively.

3.4 Implementation Procedure

In this section, the numerical procedure for evaluating the constitutive models presented in this chapter is given. Specifically, two MATLAB [74] programs developed, one for each of the Mróz-based PMMCs constitutive model and the endochronic theory-based PMMCs constitutive model are given. Each program calculates either the elastic-plastic composite strain or stress history from a known stress or strain history.

3.4.1 Mróz-Based PMMCs Constitutive Model Implementation

The global computer flow chart for the program is shown in Figs. 3.6 (a-b). The inputs to the program are the matrix and reinforcement volume fractions and material properties, the hardening moduli and yield stresses of the matrix yield surfaces, and the known stress or strain history. The tangent moduli and yield stresses (corresponding to the equivalent stresses) of the Mróz model surfaces, illustrated in Fig. 3.1, are obtained by descretizing the homogenous matrix uniaxial stress-strain curve. The hardening moduli of the surfaces are obtained from the tangent moduli using Eq. (3.32). It is important to state that the number of surfaces and load increments used in the developed Mróz-based PMMCs constitutive model may influence the predicted results. However, a quantitative relation between the number of surfaces, load increments, and the predicted results is difficult to formulate.

Some of the steps taken to implement the developed Mróz-based PMMCs constitutive model, assuming a stress-based formulation (i.e. for calculating strains from a given stress history), are stated below. Note that any given composite stress/load path has one or more load steps, and each load step is divided to a certain number of load increments.

a) Initialize the composite, reinforcement and matrix stress and strain tensors to zero.

b) Input the matrix and reinforcement volume fractions and material properties, and the hardening moduli and yield stresses of the matrix yield surfaces.

c) Input the number of load steps in the given stress/load path (assume it to be L).

d) Input the given composite stress tensor for the current load step.

e) Input the number of increments to which the current load step is divided (assume it to be N)

f) Calculate the increment of the composite stress tensor of the current load step (i.e. step (d) divided by step (e) above).

g) For each increment in the composite stress tensor obtained in step (f), calculate the increments in the reinforcement stress and strain tensors using Eqs. (3.15) and (3.16) respectively. Since it is assumed that the reinforcement deforms only elastically, the total increment in reinforcement strain is the same as its elastic increments.

h) For each increment in the composite stress tensor, obtained in step (f), the elastic, plastic, and total increments of the matrix strains are calculated using the models described in Eqs. (3.13)-(3.14), Eqs. (3.18)-(3.49), and (3.1) respectively as follows:

   i) All matrix strains are initially assumed to be elastic and consequently, the centers of the hardening surfaces are concentric and centered at the origin. In this region, Eqs (3.13)-(3.14), and (3.33) apply.

   ii) Immediately after the matrix yields, it is essential in subsequent load increments to determine whether or not the matrix stresses lie on the active surface. If they do, the unloading criterion, Eq. (3.36), is used to determine whether the matrix is undergoing elastic-plastic loading or elastic unloading with the possibility of elastic-plastic loading (determined by Eq. (3.40)) during the current composite stress increment. If the matrix

stresses do not lie on the active surface, then they are elastic. In this case the entire increment may be associated with elastic unloading or with elastic unloading followed by elastic-plastic loading.

A vital part of the program is the developed Mróz-based PMMCs constitutive model plasticity routine for the matrix elastic-plastic loading. The computer flow chart for the plasticity process is illustrated in Fig. 3.7. For each increment in composite stress step that results in matrix plastic deformation, the matrix stress and strain tensors are updated. Equations (3.45)-(3.47) are used to determine whether or not the updated matrix stresses exceed the surface outer (n+1) to the current active surface (n). Based on the outcome, the following steps are taken:

iii) If the matrix stresses are found to exceed the outer surface, then the matrix stress tensor is updated only to the point on the active surface where the updated stresses lie. The active surface is subsequently translated using the Mróz translation rule, Eqs. (3.41)-(3.43), and the inner surfaces to the current active surface, if any, are translated using Eq. (3.44). The outer surface then becomes the new active surface. The remaining portion of the composite stress tensor is used to calculate the new increment in the matrix stress and strain tensors.

iv) If the matrix stresses remain on the current active matrix yield surface, then the surface is translated using Eqs. (3.41)-(3.43) and the inner surfaces to the current active surface, if any, are translated using the Eq. (3.44).

i) For each increment in composite stress, determine the increments in the composite strain tensor from the calculated increments in the stress and strain tensors (whether elastic or elastic-plastic) of the constituents, and Eq. (3.17).

j) Add the composite stress and strain increment tensors to the composite previous stress and strain tensors to obtain the composite updated stress and strain tensors.

k) Repeat steps (g) to (j) until the current load step has been completed.

l) Repeat steps (d) to (k) until the entire load steps in the given load path have been completed.

3.4.2 Endochronic Theory-Based PMMCs Constitutive Model Implementation

In the implementation of the endochronic theory-based PMMCs constitutive model, the inputs to the program are the matrix and reinforcement volume fractions and material properties, the matrix Dirichlet constant in Eq. (3.53), and the known stress or strain history. The computer flow chart used for the implementation of the developed endochronic theory-based PMMCs constitutive relations program is shown in Figs. 3.8 (a-b). As stated earlier, one of the major problems associated with the use of the endochronic theory of plasticity is the difficulty of obtaining the material constants in Eq. (3.53). In this research, Eqs. (3.61)-(3.63) were used to extract the material constants.

After determining the material constants, the steps taken in applying the endochronic theory-based PMMCs constitutive model in a stress-based formulation are:

a) Follow steps (a) to (c) detailed above for the Mróz-based PMMCs constitutive model.

b) Follow steps (d) detailed above for the Mróz-based PMMCs constitutive model.

c) Follow steps (e) to (f) detailed above for the Mróz-based PMMCs constitutive model.

d) Follow steps (g) detailed above for the Mróz-based PMMCs constitutive model.

e) Calculate the increment in matrix stress tensor using Eqs. (3.13) and (3.14). Use the Secant method to numerically solve Eq. (3.72) to obtain the unknown intrinsic time (Δz) from the calculated matrix stress. The elastic, plastic and total strains of the matrix are calculated using Eqs. (3.14), (3.68)-(3.70) and (3.1) respectively. The matrix variables are then updated using Eq. (3.66).

f) Follow steps (i) to (j) detailed above for the Mróz-based PMMCs constitutive model.

g) Repeat steps (c) to (f) until the current load step has been completed.

h) Repeat steps (b) to (g) until the entire load steps in the given load path have been completed.

3.5 Summary of Chapter Three

As noted earlier, the development of a suitable cyclic constitutive relation capable of modeling the inelastic constitutive behavior of PMMCs under cyclic non-proportional loading conditions is critical in engineering design. This chapter gives the details of the two elastic-plastic constitutive models developed and implemented for PMMCs in this research. It is important to note that all of the relations presented in this chapter are valid for any given cyclic non-proportional (constant or variable amplitude) loading. Either

model can be employed knowing the material properties, and either the stress or strain history, although presented specifically for a stress-controlled simulation. In Chapter Six, the results obtained using the models are presented and compared to experimental results.

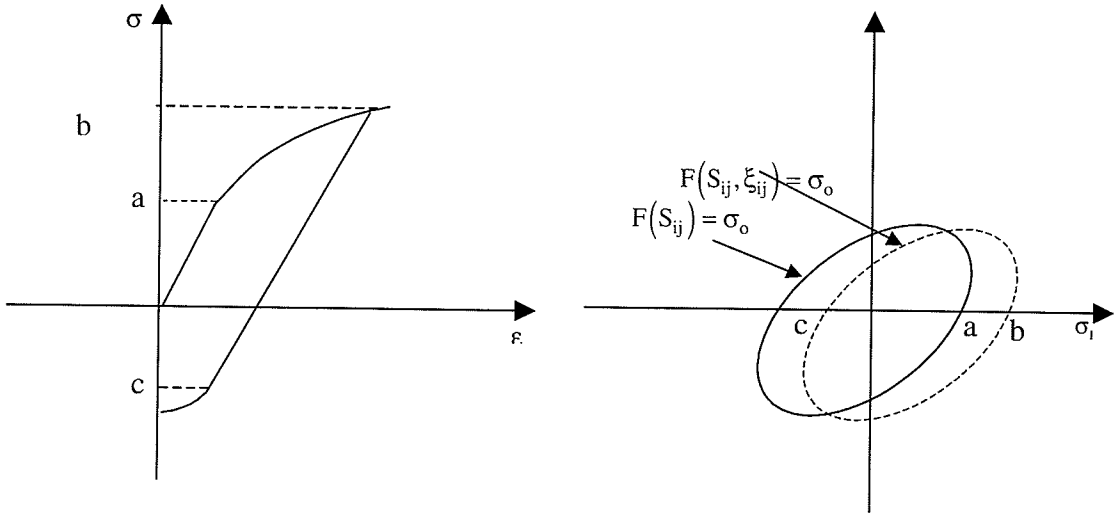

Figure 3.1: Kinematic Hardening

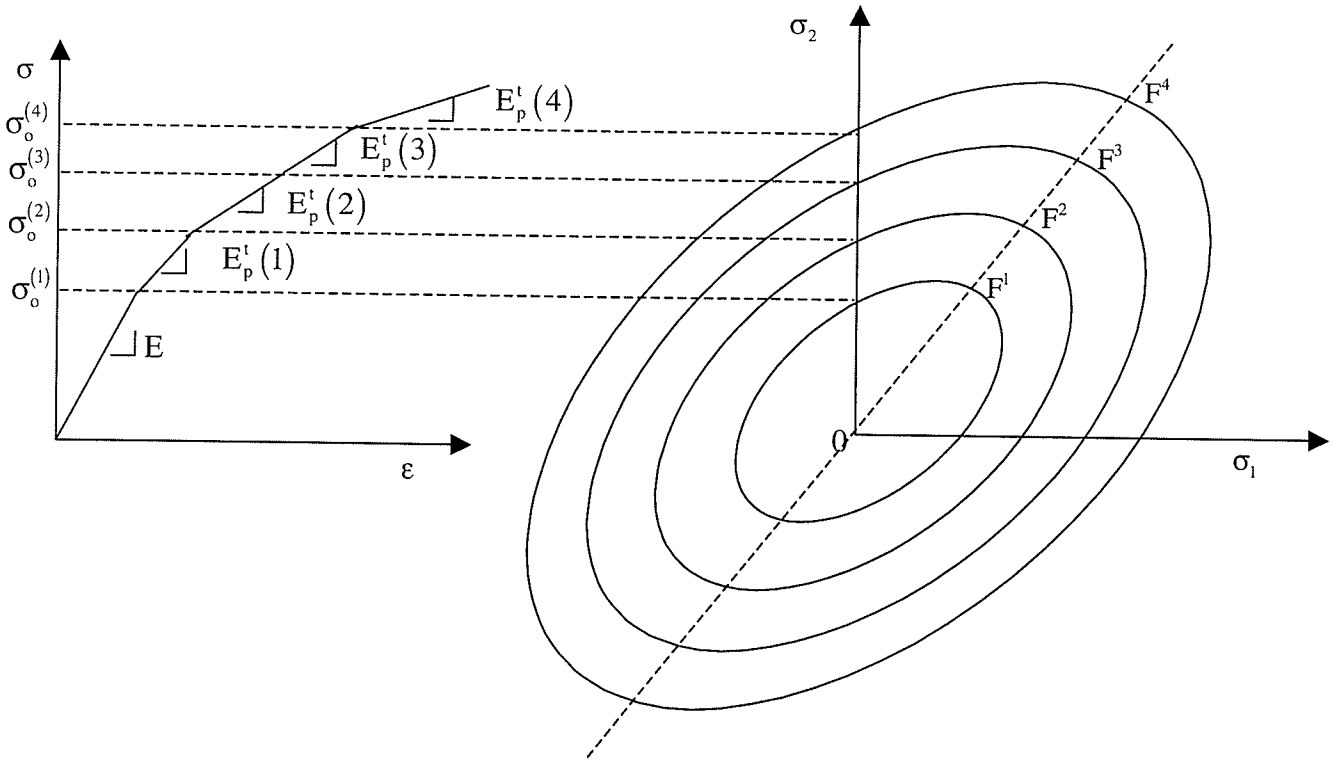

Figure 3.2: Descritizaton of the Material Stress-Strain Curve and the Corresponding Hardening Surfaces

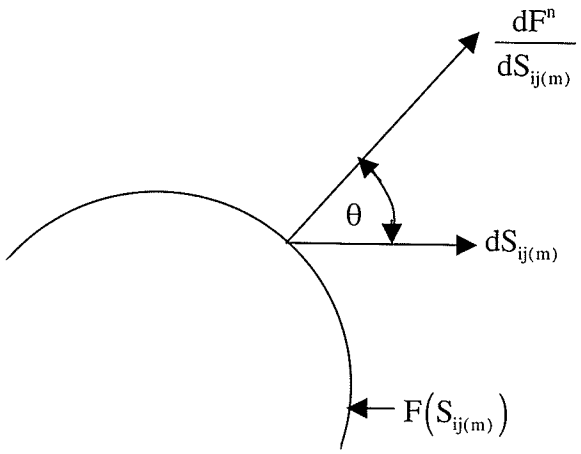

Figure 3.3: Loading/Unloading Criterion for Classical Theory of Plasticity

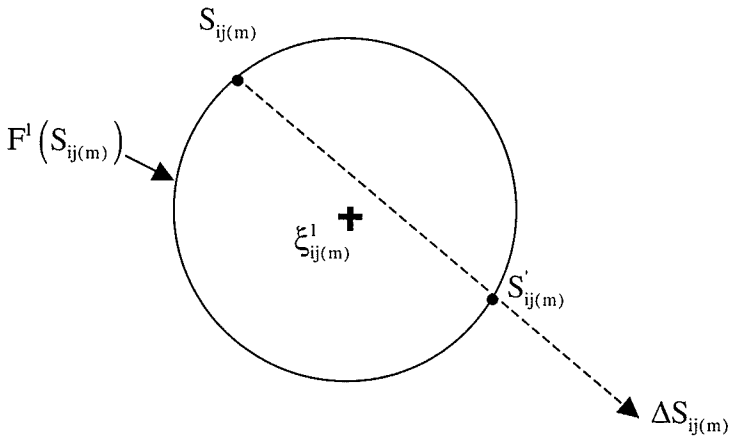

Figure 3.4: Matrix Elastic-Plastic Loading during Elastic Unloading Increment

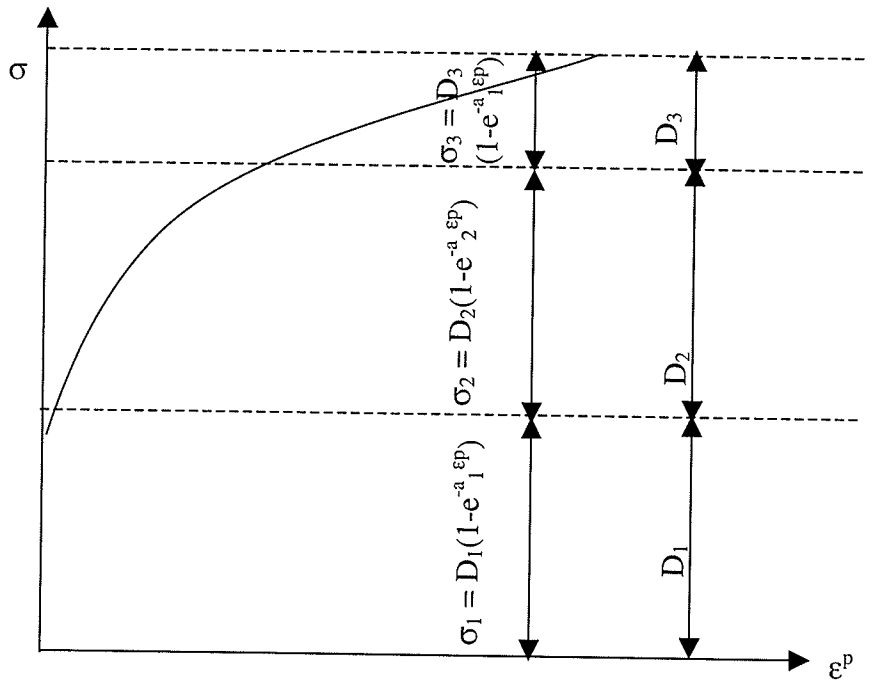

Figure 3.5: Descritizaton of the Material Stress-Plastic Strain Curve into Segments to Estimate the Material Constants for Endochronic theory

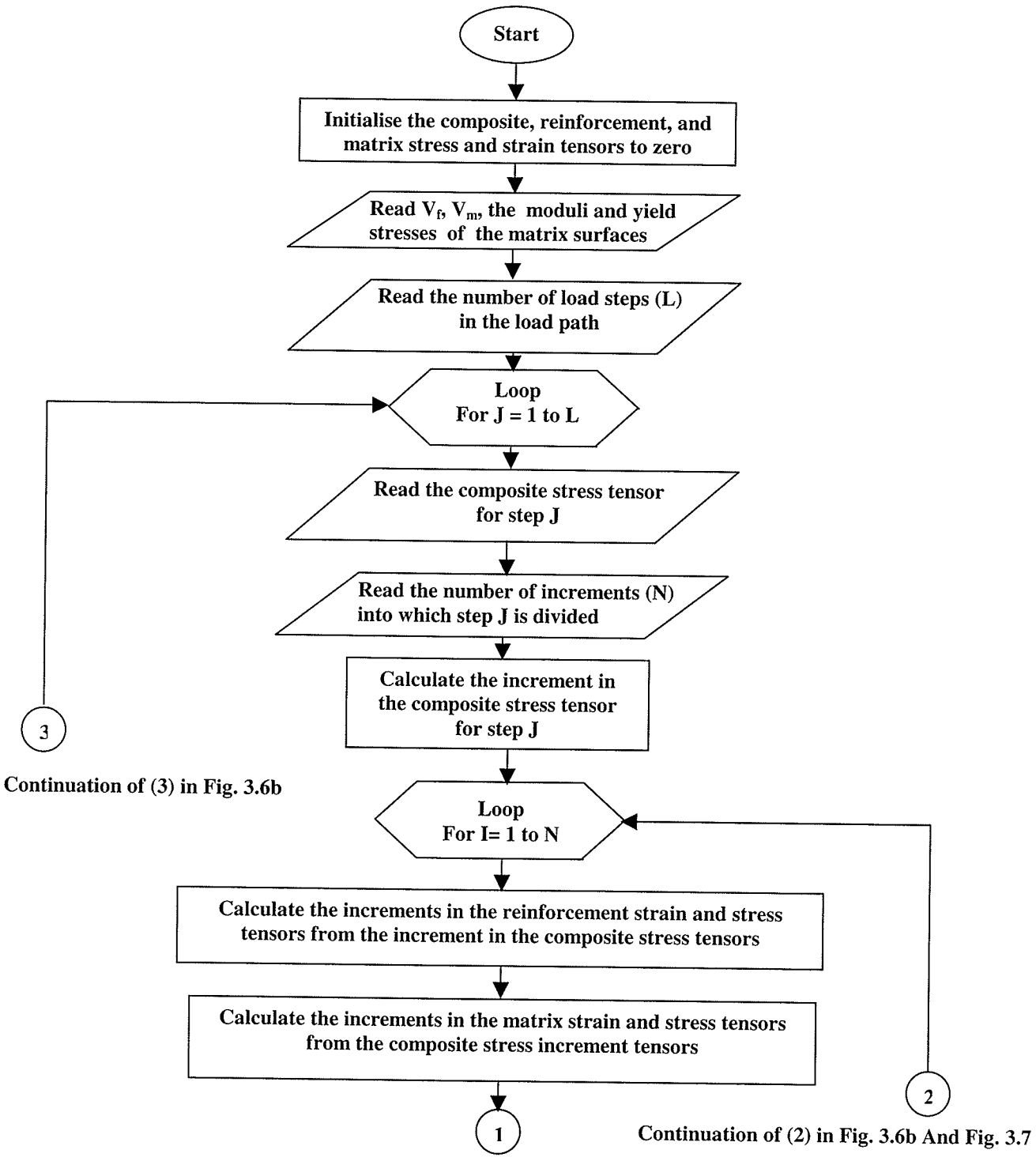

Figure 3.6a: Flow Chart for Mróz-Based PMMCs Constitutive Model

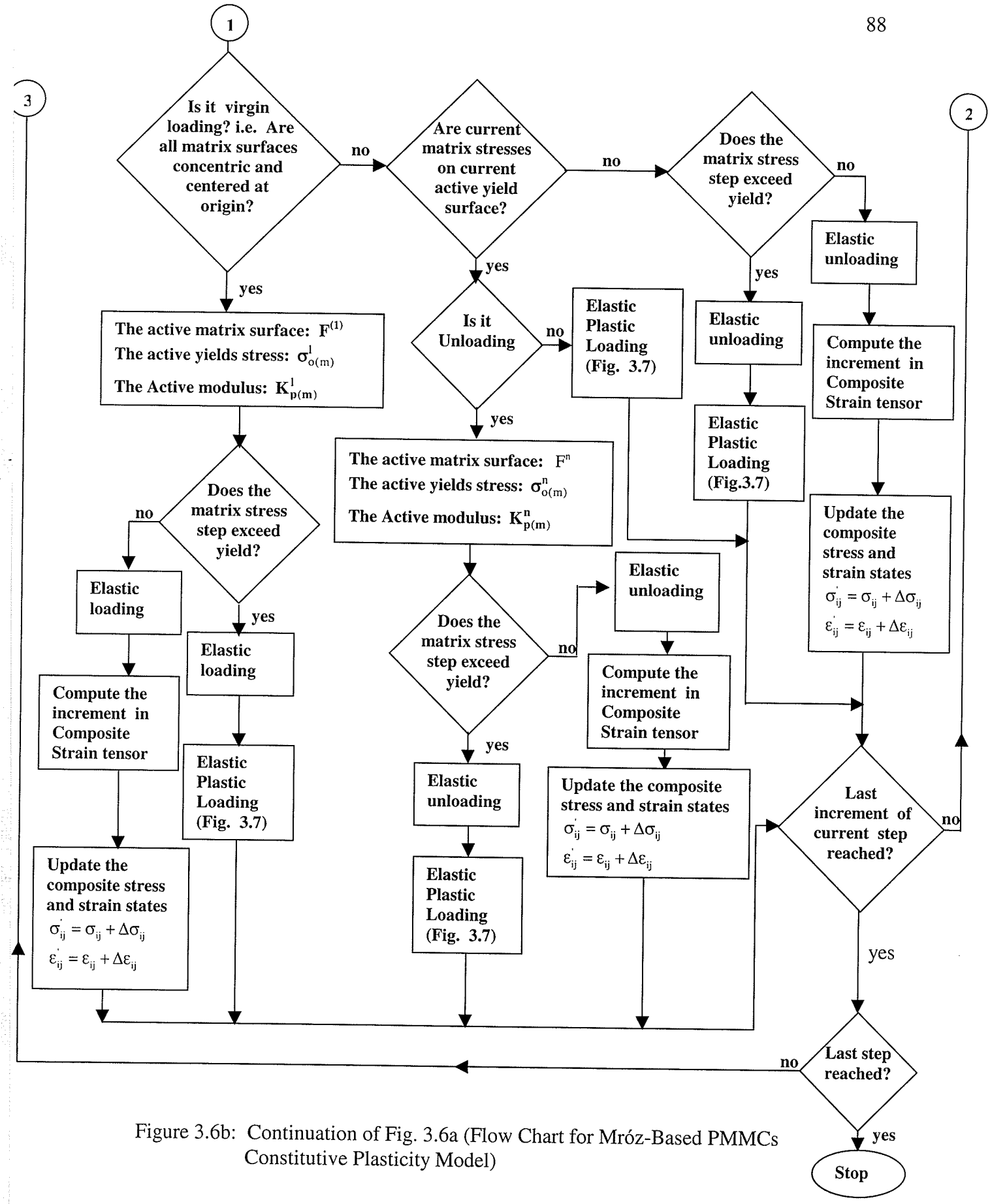

Figure 3.6b: Continuation of Fig. 3.6a (Flow Chart for Mróz-Based PMMCs Constitutive Plasticity Model)

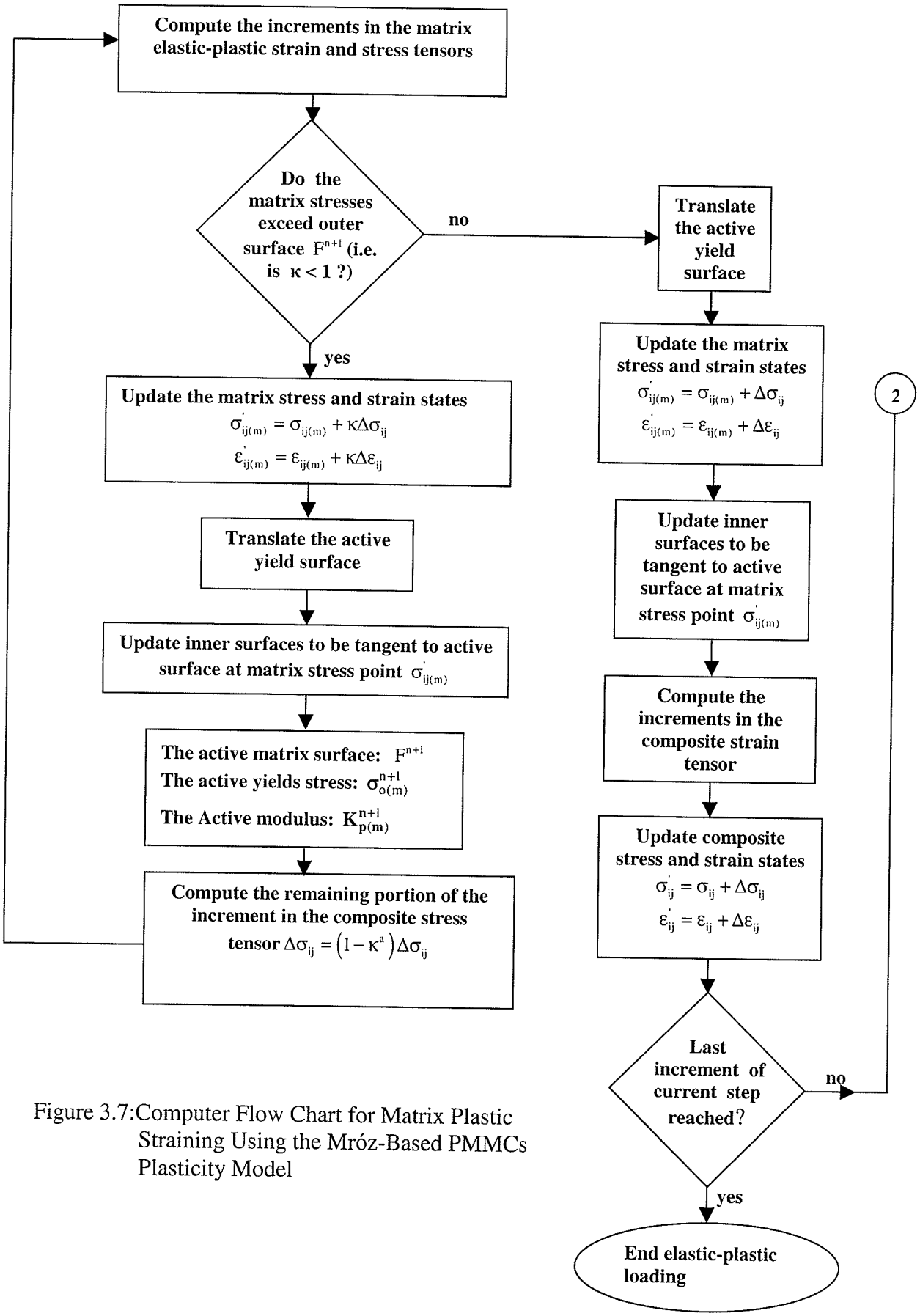

Figure 3.7:Computer Flow Chart for Matrix Plastic Straining Using the Mróz-Based PMMCs Plasticity Model

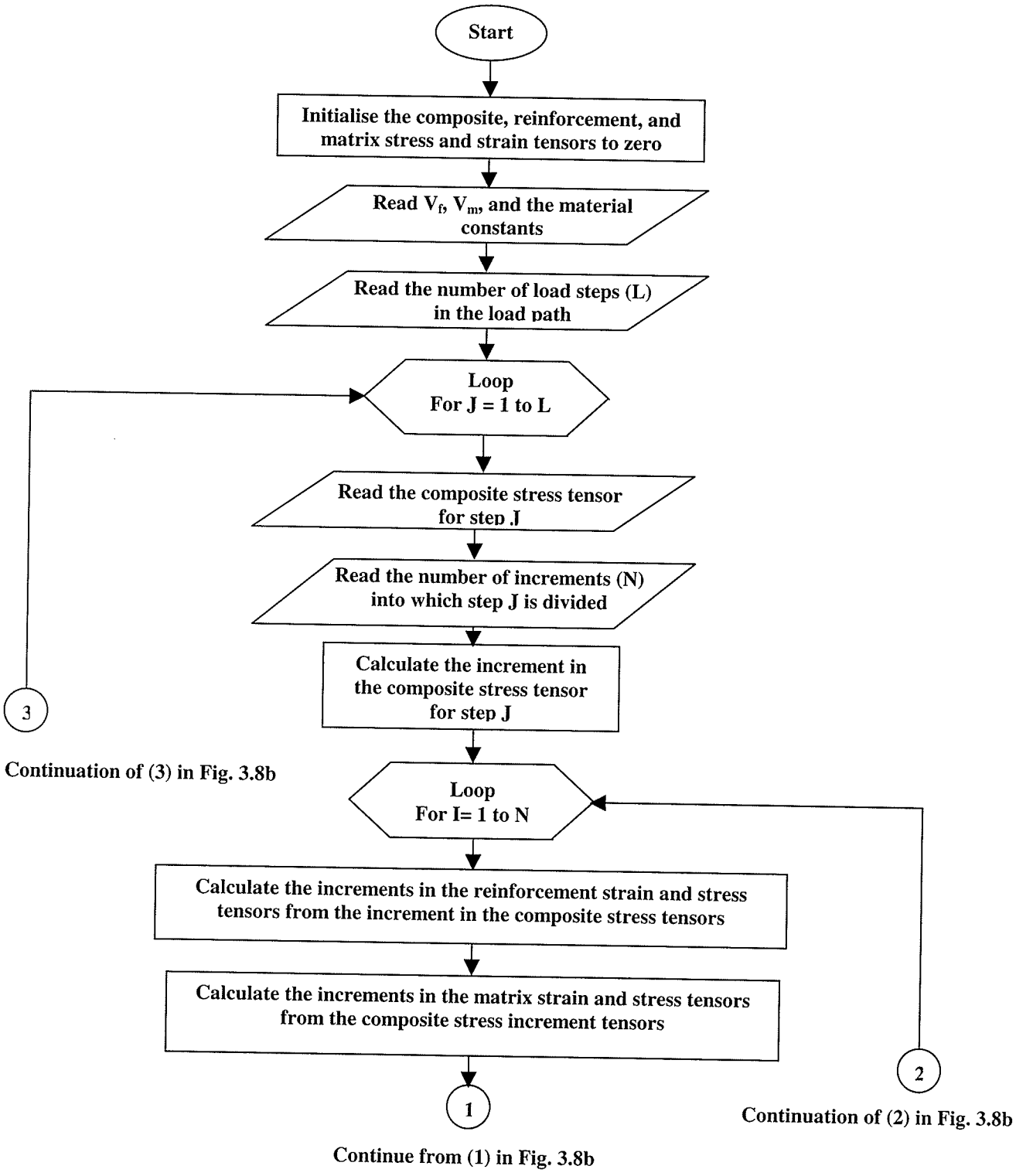

Figure 3.8a: Flow Chart for Stress-Controlled Endochronic Theory-Based PMMCs Constitutive Model

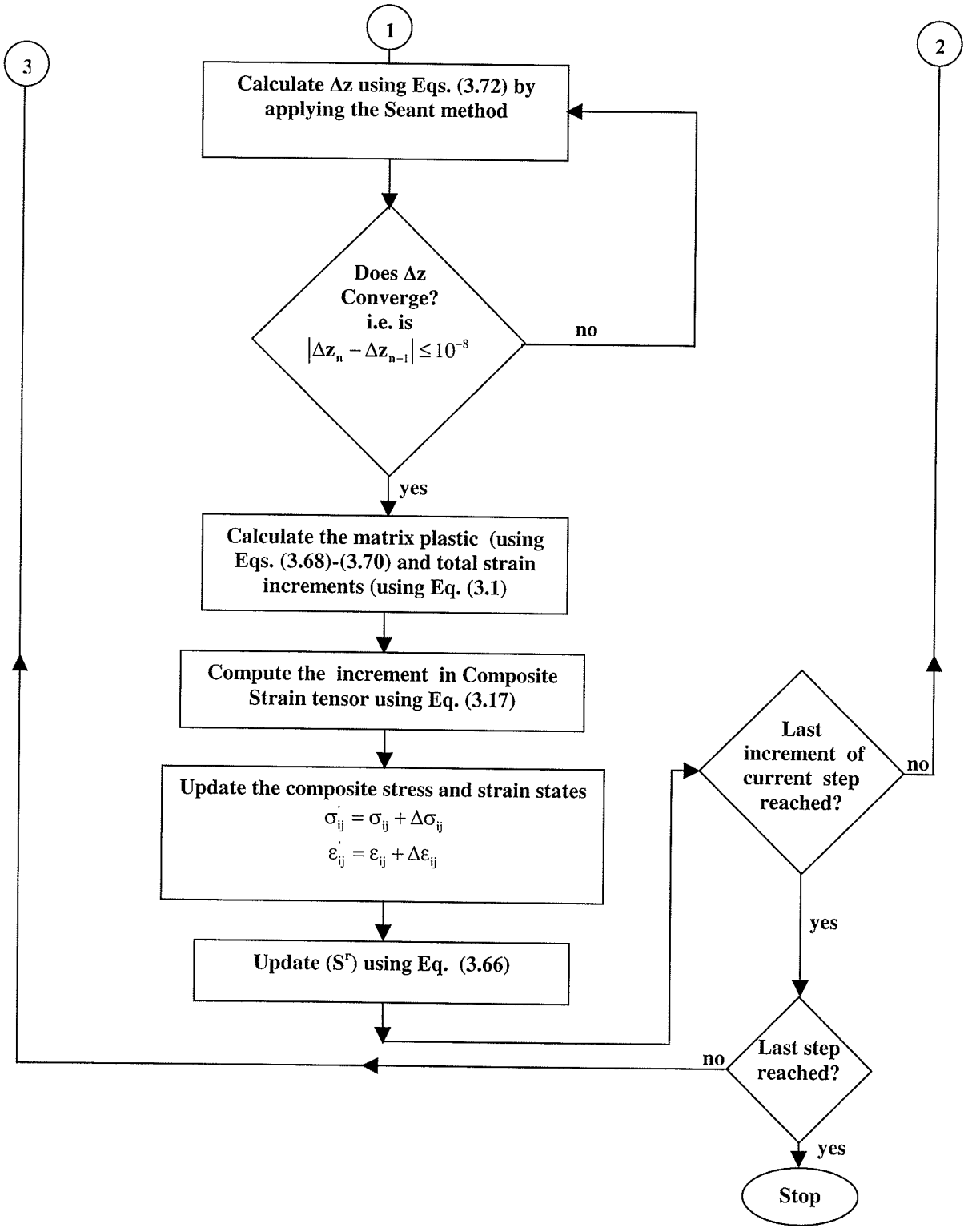

Figure 3.8b: Continuation of Fig. 3.8a (Flow Chart for Stress-Controlled Endochronic Theory-Based PMMC Model)

CHAPTER FOUR: MULTIAXIAL APPROXIMATE RELATIONS FOR PMMCS

The previously stated objective of this research is to develop and implement sufficiently accurate analytical methods for estimating the notch root elastic-plastic strain and stress histories in PMMC components subjected to general loading conditions. In Chapter Two, it was illustrated that in order to completely define the notch root stresses and strains, a set of relations must be established. Some of the relations can be obtained using the material constitutive relations developed in Chapter Three. This Chapter presents two proposed alternative sets of the additional approximate relations that can independently be used to completely define the notch root parameters. Specifically, they are defined by two independent nonlinear energy-based principles referred to here as the incremental strain energy density method (ESED) for PMMCs (Section 4.1), and the incremental Neuber's rule for PMMCs (Section 4.2). Section 4.3 presents the two sets of nonlinear equations developed when expressed fully on the notch root element. In Section 4.4, the complete relations developed for estimating the notch root parameters are presented and Section 4.5 presents the method of numerically solving the developed models. It is important to state that all relations are developed to respect the heterogeneous nature of PMMCs.

In the formulation of the approximate relations, it is assumed that the reinforcement behaves elastically throughout the loading history, due to their high stiffness. Thus, the local stress in the reinforcement can be estimated from a linear elastic

analysis using Eqs. (3.15)-(3.16), and the elastic stress concentration factors of the notched geometry modeled. However, the matrix is assumed to behave elastic-plastically. Since general or non-proportional multiaxial loading is assumed, all pertinent relations must be developed in incremental forms. The matrix stress and strain components at the notch root are thus written in incremental forms and are given as:

$$\Delta\sigma_{ij(m)} = \begin{bmatrix} 0 & 0 & 0 \\ 0 & \Delta\sigma_{22(m)} & \Delta\sigma_{23(m)} \\ 0 & \Delta\sigma_{32(m)} & \Delta\sigma_{33(m)} \end{bmatrix} \tag{4.1}$$

and,

$$\Delta\varepsilon_{ij(m)} = \begin{bmatrix} \Delta\varepsilon_{22(m)} & 0 & 0 \\ 0 & \Delta\varepsilon_{22(m)} & \Delta\varepsilon_{22(m)} \\ 0 & \Delta\varepsilon_{32(m)} & \Delta\varepsilon_{33(m)} \end{bmatrix}. \tag{4.2}$$

The final state of stress and strain at a load increment (q) can then be obtained by adding the increments to the previous stress-strain history at load increment (q-1) given by:

$$\sigma_{ij(m)q} = \sigma_{ij(m)q-1} + \Delta\sigma_{ij(m)q}, \tag{4.3}$$

$$\varepsilon_{ij(m)q} = \varepsilon_{ij(m)q-1} + \Delta\varepsilon_{ij(m)q}. \tag{4.4}$$

4.1 Proposed Incremental Equivalent Strain Energy Density for PMMCs

As stated in Chapter Two, the generalized incremental strain energy density method (ESED) [63] was developed to address the path dependent nature of the elastic-

plastic strain-stress at the notch root in a homogenous body subjected to non-proportional multiaxial loading. In this research, a new form of incremental strain energy density method is proposed for PMMCs.

Duva and Hutchinson [75] have shown that the constitutive relation of composite could be expressed with the macro strain energy density. The macro strain energy density of multiphase composites is given as:

$$W = \frac{1}{V} \sum_{k=0,1}^{n} \int_{V_k} W_k dV, \tag{4.5}$$

where V is the composite material volume. V_k, W_k ($k > 0$) are the volume fraction and strain energy density of kth reinforcement component respectively, while V_k, W_k ($k = 0$) are the volume fraction and strain energy density of matrix respectively. For a two-phase composite system, the above equation reduces to:

$$W = \frac{1}{V} \int_{V_m} W_m dV + \frac{1}{V} \int_{V_f} W_f dV, \tag{4.6}$$

where W_f and W_m are the reinforcement and matrix strain energy densities respectively.

Following a similar approach as given in [63] for homogeneous materials, for PMMCs, it is proposed that as long as the notch root plasticity is localized, parameters that define the actual notch root behavior can be found by comparing them to the notch root behavior obtained in a geometrically identical elastic body subjected to the same external tractions (see Fig. 4.1). Specifically, it is proposed here that for a given increment in composite external load, the corresponding increment in the composites

weighted strain energy density at the notch root in an elastic-plastic body can be approximated by that which would have been obtained if the composite system were to remain elastic through out the loading history. This proposed hypothesis can be expressed as,

$$dW^{e} = (1-V_f)dW^{E}_{(m)} + V_f dW^{e}_{(f)}. \tag{4.7}$$

Equation (4.7) can be rewritten by adopting the definition of strain energy density, or,

$$dW = \sigma_{ij} d\varepsilon_{ij} \tag{4.8}$$

as,

$$\sigma^{e}_{ij} d\varepsilon^{e}_{ij} = (1-V_f)\sigma^{E}_{ij(m)} d\varepsilon^{E}_{ij(m)} + V_f \sigma^{e}_{ij(f)} d\varepsilon^{e}_{ij(f)}. \tag{4.9}$$

In Eq. (4.9), "e" represents notch root components that can be found from an elastic analysis, and "E" represents matrix elastic-plastic notch root components as estimated by the PMMCs incremental ESED method. It should be emphasized here that the elastic components "e" in Eq. (4.9) are not nominal values, but values obtained at the notch root. These values can be found using Eqs. (3.3)-(3.17), and the stress concentration factors of the notched geometry modeled. If $V_f = 0$, thus indicating a homogeneous material, Eq.(4.9), reduces to Eq. (2.16), and for plane stress, the original form of ESED rule given in [51]. It should be again emphasized that being based on Eq. (2.15), Eq. (4.9) is valid under the assumption of localized notch root plasticity.

Two additional equations are required to completely define the matrix notch-root elastic-plastic strain and stress. In this research, it is proposed that for the composite system, the weighted contribution of each of the elastic-plastic strain-stress components of the composite to the increment in strain energy density at the notch root is the same as the contribution of each stress-strain component to the increment in composite strain energy density at the notch root when obtained from elastic analysis. This proposal can be mathematically expressed as,

$$\frac{\sigma^{e}_{\alpha\beta}d\varepsilon^{e}_{\alpha\beta}}{\sigma^{e}_{ij}d\varepsilon^{e}_{ij}}=\frac{(1-V_f)\sigma^{E}_{\alpha\beta(m)}d\varepsilon^{E}_{\alpha\beta(m)}+V_f\sigma^{E}_{\alpha\beta(f)}d\varepsilon^{E}_{\alpha\beta(f)}}{(1-V_f)\sigma^{E}_{ij(m)}d\varepsilon^{E}_{ij(m)}+V_f\sigma^{e}_{ij(f)}d\varepsilon^{e}_{ij(f)}}. \tag{4.10}$$

In Eq. (4.10), the indices, i, j, α, β = 1, 2, 3 and summation is assumed over i, j, while for α, β, summation is not implied. Using Eq. (4.9) in Eq. (4.10) and rearranging the resulting relation yields:

$$\sigma^{e}_{\alpha\beta}d\varepsilon^{e}_{\alpha\beta}-V_f\sigma^{e}_{\alpha\beta(f)}d\varepsilon^{e}_{\alpha\beta(f)}=(1-V_f)\sigma^{E}_{\alpha\beta(m)}d\varepsilon^{E}_{\alpha\beta(m)}. \tag{4.11}$$

It should be noted that Eq. (4.11) yields three relations, and when used in conjunction with the four relations defined by a suitable cyclic plasticity model, they are sufficient to solve for the seven unknown matrix notch root elastic-plastic strain and stress components. The set of equations requires as input the results of a relatively simpler elastic analysis, reinforcement and matrix material properties.

4.2 Proposed Incremental Neuber's Rule for PMMCs

The weighted total strain energy density, Ω, of a composite with two phases is expressed in this research as:

$$\Omega = \frac{1}{V}\int_{V_f} W_f dV + \frac{1}{V}\int_{Vf} W_{c(f)} dV + \frac{1}{V}\int_{Vm} W_m dV + \frac{1}{V}\int_{Vm} W_{c(m)} dV . \qquad (4.12)$$

In Eq. (4.12), $W_{c(f)}$ and $W_{c(m)}$ are the reinforcement and matrix complementary strain energy densities respectively. In this research, it is proposed that for an increment in load in the composite system, the corresponding increment in the composite weighted total strain energy density at the notch root in an elastic-plastic body ($\Omega^e_{(f)}$ $\Omega^N_{(m)}$) can be approximated by that which would have been obtained if the composite system were to remain elastic through out the loading history, Ω^e (Fig. 4.1). Using Eq. (4.12) this proposed hypothesis can be expressed as:

$$d\Omega^e = (1 - V_f) d\Omega^N_{(m)} + V_f d\Omega^e_{(f)}. \qquad (4.13)$$

The formulation can be re-written, using the definition of an incremental total strain energy density, or,

$$d\Omega = \sigma d\varepsilon + \varepsilon d\sigma, \qquad (4.14)$$

as,

$$\sigma^e_{ij} d\varepsilon^e_{ij} + \varepsilon^e_{ij} d\sigma^e_{ij} = (1 - V_f)\left(\sigma^N_{ij(m)} d\varepsilon^N_{ij(m)} + \varepsilon^N_{ij(m)} d\sigma^N_{ij(m)}\right) + V_f\left(\sigma^e_{ij(f)} d\varepsilon^e_{ij(f)} + \varepsilon^e_{ij(f)} d\sigma^e_{ij(f)}\right). \qquad (4.15)$$

In Eq. (4.15), if $V_f = 0$, thus indicating a homogeneous material, the equation reduces to Eq. (2.15), and for plane stress, the original form of Neuber's rule given in [50]. Also as in the PMMCs ESED model, it should be pointed out that being based on Eq. (2.15), Eq. (4.15) is valid under the assumption of localized notch root plasticity.

Two additional equations are required to completely define the matrix notch-root elastic-plastic strain and stress. Here, it is proposed that for the composite system, the weighted contribution of each of the elastic-plastic strain-stress component of the constituents to the increment in total energy density at the notch root is the same as the contribution of each stress-strain component to the increment in composite total strain energy density at the notch root when obtained from elastic analysis. The proposal can be expressed as:

$$\frac{\sigma^e_{\alpha\beta}\Delta\varepsilon^e_{\alpha\beta}+\varepsilon^e_{\varepsilon\beta}\Delta\sigma^e_{\alpha\beta}}{\sigma^e_{ij}\Delta\varepsilon^e_{ij}+\varepsilon^e_{ij}\Delta\sigma^e_{ij}}=\frac{(1-V_f)\left(\sigma^N_{\alpha\beta(m)}\Delta\varepsilon^N_{\alpha\beta(m)}+\varepsilon^N_{\alpha\beta(m)}\Delta\sigma^N_{\alpha\beta(m)}\right)+V_f\left(\sigma^e_{\alpha\beta(f)}\Delta\varepsilon^e_{\alpha\beta(f)}+\varepsilon^e_{\alpha\beta(f)}\Delta\sigma^e_{\alpha\beta(f)}\right)}{(1-V_f)\left(\sigma^N_{ij(m)}\Delta\varepsilon^N_{ij(m)}+\varepsilon^N_{ij(m)}\Delta\sigma^N_{ij(m)}\right)+V_f\left(\sigma^e_{ij(f)}\Delta\varepsilon^e_{ij(f)}+\varepsilon^e_{ij(f)}\Delta\sigma^e_{ij(f)}\right)}. \tag{4.16}$$

Using Eq. (4.15) in Eq. (4.16) and rearranging the resulting relation yields:

$$\sigma^e_{\alpha\beta}\Delta\varepsilon^e_{\alpha\beta}+\varepsilon^e_{\alpha\beta}\Delta\sigma^e_{\alpha\beta}-V_f\left(\sigma^e_{\alpha\beta(f)}\Delta\varepsilon^e_{\alpha\beta(f)}+\varepsilon^e_{\alpha\beta(f)}\Delta\sigma^e_{\alpha\beta(f)}\right)=(1-V_f)\left(\sigma^N_{ij(m)}\Delta\varepsilon^N_{\alpha\beta(m)}+\varepsilon^N_{\alpha\beta(m)}\Delta\sigma^N_{\alpha\beta(m)}\right). \tag{4.17}$$

It should be noted that Eq. (4.17) yields three relations of the seven equations that are necessary to obtain the seven unknown matrix notch root elastic-plastic strain and stress components. The remaining four equations can be found from the material constitutive

model. As in the PMMCs ESED model, the PMMCs Neuber model requires as input the results of a simple elastic analysis, and the reinforcement and matrix properties.

4.3 Notch-Root Parameters Estimation Relations

As noted in this chapter, seven equations are necessary to completely define the matrix notch root elastic-plastic stress-strain history. Four of the equations can be obtained using either of the material constitutive relations presented in Chapter Three, and the remaining three can be obtained using the approximate relations developed in this chapter. The results obtained in this research (shown in Chapter Six) indicate that the endochronic theory-based PMMCs constitutive model should be used since its predictions are closer to the experimental results than the Mróz model-based PMMCs constitutive model predictions, particularly so for the measured and predicted strain amplitudes that are essential for fatigue life predictions. Furthermore, as noted in Chapters Two and Three, it has also been shown in [32] that for homogeneous materials, the endochronic theory of plasticity can better predict some of the transient effects associated with cyclic non-proportional loading. Thus, in this research the endochronic theory-based PMMCs constitutive model developed in Chapter Three is used in conjunction with the simplified models presented in this chapter to completely define the set of equations necessary to obtain the notch root parameters.

In this section, the two sets of relations are written fully on the notch root element of a circumferentially notched bar shown in Fig. 2.1. Although highlighted for this case, these relations should apply for any notch root that has a traction free surface. Since the

constitutive relations and the intrinsic time scale relations (presented in Chapter Three) are common to both methods, they will first be presented (See Eq. (4.18) to Eq. (4.22)). Relations specific to the PMMCs incremental ESED method (See Eq. (4.23) to Eq. (4.25) and PMMCs Neuber's rule (See Eq. (4.26) to Eq. (4.28)) are subsequently presented.

Elastic-Plastic Constitutive Relations (E/N indicate that either PMMCs ESED or Neuber's elastic-plastic values can be substituted).

Writing Eq. (3.77) fully on the notch root elements gives:

$$\Delta\varepsilon_{11(m)}^{E/N}=\left[\frac{-\upsilon_m}{E_m}-\frac{1}{6}\left(\sum_{r=1}^{3}C_r\left(\frac{1-e^{-\alpha_r\Delta z}}{\alpha_r}\right)\right)^{-1}\Delta z\right]\left(\Delta\sigma_{22(m)}^{E/N}+\Delta\sigma_{33(m)}^{E/N}\right)+$$
$$\frac{1}{2}\sum_{r=1}^{3}\left[\left(C_r\frac{1-e^{-\alpha_r\Delta z}}{\alpha_r\Delta z}\right)^{-1}S_{11}^{E/N(r)}\left(1-e^{-\alpha_r\Delta z}\right)\Delta z\right], \tag{4.18}$$

$$\Delta\varepsilon_{22(m)}^{E/N}=\left[\frac{1}{E_m}+\frac{1}{3}\left(\sum_{r=1}^{3}C_r\left(\frac{1-e^{-\alpha_r\Delta z}}{\alpha_r}\right)\right)^{-1}\Delta z\right]\Delta\sigma_{22(m)}^{E/N}-\left[\frac{-\upsilon_m}{E_m}-\frac{1}{6}\left(\sum_{r=1}^{3}C_r\left(\frac{1-e^{\alpha_r\Delta z}}{\alpha_r}\right)\right)^{-1}\Delta z\right]\Delta\sigma_{33(m)}^{E/N}$$
$$+\frac{1}{2}\sum_{1}^{3}\left[\left(C_r\frac{1-e^{\alpha_r\Delta z}}{\alpha_r}\right)^{-1}S_{22}^{E/N(r)}\left(1-e^{-\alpha_r\Delta z}\right)\Delta z\right], \tag{4.19}$$

$$\Delta\varepsilon_{33(m)}^{E/N}=\left[\frac{1}{E_m}+\frac{1}{3}\left(\sum_{r=1}^{3}C_r\left(\frac{1-e^{\alpha_r\Delta z}}{\alpha_r}\right)\right)^{-1}\Delta z\right]\Delta\sigma_{33(m)}^{E/N}-\left[\frac{-\upsilon_m}{E_m}-\frac{1}{6}\left(\sum_{r=1}^{3}C_r\left(\frac{1-e^{\alpha_r\Delta z}}{\alpha_r}\right)\right)^{-1}\Delta z\right]\Delta\sigma_{22(m)}^{E/N}$$
$$+\frac{1}{2}\sum_{1}^{3}\left[\left(C_r\frac{1-e^{\alpha_r\Delta z}}{\alpha_r}\right)^{-1}S_{33}^{E/N(r)}\left(1-e^{-\alpha_r\Delta z}\right)\Delta z\right], \tag{4.20}$$

and,

$$\Delta\varepsilon_{23(m)}^{E/N}=\left[\frac{1+\upsilon_m}{E_m}+\frac{1}{2}\left(\sum_{r=1}^{3}C_r\left(\frac{1-e^{\alpha_r\Delta z}}{\alpha_r}\right)\right)^{-1}\Delta z\right]\Delta\sigma_{23(m)}^{E/N}+\frac{1}{2}\sum_{1}^{3}\left[\left(C_r\frac{1-e^{\alpha_r\Delta z}}{\alpha_r}\right)^{-1}S_{23}^{E/N(r)}\left(1-e^{-\alpha_r\Delta z}\right)\Delta z\right]. \tag{4.21}$$

Intrinsic Time Scale-Stress Equation

Writing Eq. (3.72) fully on the notch root elements gives:

$$\begin{aligned}&\left[\sum_{r=1}^{n}C_r\frac{\left(1-e^{-\alpha_r\Delta z}\right)}{\alpha_r}\right]^2-\frac{1}{4}\left[\left(\Delta S_{11(m)}^{E/N(r)}\right)^2+\left(\Delta S_{22(m)}^{E/N(r)}\right)^2\left(\Delta S_{33(m)}^{E/N(r)}\right)^2+2\left(\Delta S_{23(m)}^{E/N(r)}\right)^2\right]+\\&-\frac{1}{4}\left[\begin{array}{l}\left(2\left(\Delta S_{11(m)}^{E/N(r)}\right)\left(S_{11(m)}^{E/N(r)}\left(1-e^{-\alpha_r\Delta z}\right)\right)\right)+\left(2\left(\Delta S_{22(m)}^{E/N(r)}\right)\left(S_{22(m)}^{E/N(r)}\left(1-e^{-\alpha_r\Delta z}\right)\right)\right)+\\\left(2\left(\Delta S_{33(m)}^{E/N(r)}\right)\left(S_{33(m)}^{E/N(r)}\left(1-e^{-\alpha_r\Delta z}\right)\right)\right)+\left(4\left(\Delta S_{23(m)}^{E/N(r)}\right)\left(S_{23(m)}^{E/N(r)}\left(1-e^{-\alpha_r\Delta z}\right)\right)\right)\end{array}\right]\\&-\frac{1}{4}\left[\begin{array}{l}\left(\sum_{r=1}^{3}S_{11(m)}^{E/N(r)}\left(1-e^{-\alpha_r\Delta z}\right)\right)^2+\left(\sum_{r=1}^{3}S_{22(m)}^{E/N(r)}\left(1-e^{-\alpha_r\Delta z}\right)\right)^2+\\\left(\sum_{r=1}^{3}S_{33(m)}^{E/N(r)}\left(1-e^{-\alpha_r\Delta z}\right)\right)^2+2\left(\sum_{r=1}^{3}S_{23(m)}^{E/N(r)}\left(1-e^{-\alpha_r\Delta z}\right)\right)^2\end{array}\right]=0\end{aligned} \tag{4.22}$$

Proposed Incremental PMMCs ESED Method:

It should be noted that Eq. (4.11) yields three relations. When expanded at the notch root and changing differentials to small increments give:

$$\begin{aligned}&\left(\sigma_{22}^{e}\Delta\varepsilon_{22}^{e}+\frac{1}{2}\Delta\sigma_{22}^{e}\Delta\varepsilon_{22}^{e}\right)-V_f\left(\sigma_{22(f)}^{e}\Delta\varepsilon_{22(f)}^{e}+\frac{1}{2}\Delta\sigma_{22(f)}^{e}\Delta\varepsilon_{22(f)}^{e}\right)\\&-V_m\left(\sigma_{22(m)}^{E}\Delta\varepsilon_{22(m)}^{E}+\frac{1}{2}\Delta\sigma_{22(m)}^{E}\Delta\varepsilon_{22(m)}^{E}\right)=0,\end{aligned} \tag{4.23}$$

$$\left(\sigma_{33}^{e}\Delta\varepsilon_{33}^{e}+\frac{1}{2}\Delta\sigma_{33}^{e}\Delta\varepsilon_{33}^{e}\right)-V_{f}\left(\sigma_{33(f)}^{e}\Delta\varepsilon_{33(f)}^{e}+\frac{1}{2}\Delta\sigma_{33(f)}^{e}\Delta\varepsilon_{33(f)}^{e}\right)$$
$$-V_{m}\left(\sigma_{33(m)}^{E}\Delta\varepsilon_{33(m)}^{E}+\frac{1}{2}\Delta\sigma_{33(m)}^{E}\Delta\varepsilon_{33(m)}^{E}\right)=0, \tag{4.24}$$

and,

$$\left(\sigma_{23}^{e}\Delta\varepsilon_{23}^{e}+\frac{1}{2}\Delta\sigma_{23}^{e}\Delta\varepsilon_{23}^{e}\right)-V_{f}\left(\sigma_{23(f)}^{e}\Delta\varepsilon_{23(f)}^{e}+\frac{1}{2}\Delta\sigma_{23(f)}^{e}\Delta\varepsilon_{23(f)}^{e}\right)$$
$$-V_{m}\left(\sigma_{23(m)}^{E}\Delta\varepsilon_{23(m)}^{E}+\frac{1}{2}\Delta\sigma_{23(m)}^{E}\Delta\varepsilon_{23(m)}^{E}\right)=0. \tag{4.25}$$

Note that the higher order terms render the set of equations nonlinear. The nonlinear terms are introduced to increase the accuracy of the model.

Proposed Incremental PMMCs Neuber's Rule:

It should be noted that Eq. (4.17) yields three relations. When expanded at the notch root and changing differentials to small increments, they give:

$$\left(\sigma_{22}^{e}\Delta\varepsilon_{22}^{e}+\varepsilon_{22}^{e}\Delta\sigma_{22}^{e}+\Delta\sigma_{22}^{e}\Delta\varepsilon_{22}^{e}\right)-V_{f}\left(\sigma_{22(f)}^{e}\Delta\varepsilon_{22(f)}^{e}+\varepsilon_{22(f)}^{e}\Delta\sigma_{22(f)}^{e}+\Delta\sigma_{22(f)}^{e}\Delta\varepsilon_{22(f)}^{e}\right)-$$
$$V_{m}\left(\sigma_{22(m)}^{N}\Delta\varepsilon_{22(m)}^{N}+\varepsilon_{22(m)}^{N}\Delta\sigma_{22(m)}^{N}+\Delta\sigma_{22(m)}^{N}\Delta\varepsilon_{22(m)}^{N}\right)=0, \tag{4.26}$$

$$\left(\sigma_{33}^{e}\Delta\varepsilon_{33}^{e}+\varepsilon_{33}^{e}\Delta\sigma_{33}^{e}+\Delta\sigma_{33}^{e}\Delta\varepsilon_{33}^{e}\right)-V_{f}\left(\sigma_{33(f)}^{e}\Delta\varepsilon_{33(f)}^{e}+\varepsilon_{33(f)}^{e}\Delta\sigma_{33(f)}^{e}+\Delta\sigma_{33(f)}^{e}\Delta\varepsilon_{33(f)}^{e}\right)-$$
$$V_{m}\left(\sigma_{33(m)}^{N}\Delta\varepsilon_{33(m)}^{N}+\varepsilon_{33(m)}^{N}\Delta\sigma_{33(m)}^{N}+\Delta\sigma_{33(m)}^{N}\Delta\varepsilon_{33(m)}^{N}\right)=0, \tag{4.27}$$

and,

$$\left(\sigma_{23}^{e}\Delta\varepsilon_{23}^{e}+\varepsilon_{23}^{e}\Delta\sigma_{23}^{e}+\Delta\sigma_{23}^{e}\Delta\varepsilon_{23}^{e}\right)-V_{f}\left(\sigma_{23(f)}^{e}\Delta\varepsilon_{23(f)}^{e}+\varepsilon_{23(f)}^{e}\Delta\sigma_{23(f)}^{e}+\Delta\sigma_{23(f)}^{e}\Delta\varepsilon_{23(f)}^{e}\right)-$$
$$V_{m}\left(\sigma_{23(m)}^{N}\Delta\varepsilon_{23(m)}^{N}+\varepsilon_{23(m)}^{N}\Delta\sigma_{23(m)}^{N}+\Delta\sigma_{23(m)}^{N}\Delta\varepsilon_{23(m)}^{N}\right)=0. \tag{4.28}$$

4.4 Solution Methodology

Either the PMMCs incremental ESED relations (Eqs. (4.23)-(4.25)) or the PMMCs incremental Neuber's relations (Eqs. (4.26)-(4.28)) can be used in conjunction with the matrix elastic-plastic constitutive relations (Eqs. (4.18)-(4.21) and the intrinsic time-stress relation (Eq. (4.22)) to define the relationships needed to solve for the increments in the matrix elastic-plastic notch root strain and stress tensors and the increment in the intrinsic time scale. Each set consists of eight relations with eight unknowns (i.e. four increments in matrix strain and three increments matrix stress components, and the intrinsic time scale). Newton-Raphson's numerical method for solving systems of non-linear equations can be employed to solve for the eight unknowns for the each increment in applied loads. However, using the eight equations may be CPU time consuming, especially under complex cyclic loading. Consequently, each set of equations was reduced to four non-linear equations with four unknowns as follows.

Simplified PMMCs ESED Energy Ratio Equations

Substituting Eqs. (4.19)-(4.21) into Eqs. (4.23)-(4.25) and re-arranging the resulting set of equations yield the following three relations:

$$V_m\left[\sigma_{22}^E\left(\frac{1}{E_m}+\frac{1}{3}\left(\sum_{r=1}^{3}C_r\left(\frac{1-e^{\alpha_r\Delta z}}{\alpha_r}\right)\right)^{-1}\Delta z\right)+\frac{1}{4}\sum_{1}^{3}\left(\left(C_r\frac{1-e^{\alpha_r\Delta z}}{\alpha_r}\right)^{-1}S_{22}^{E(r)}\left(1-e^{-\alpha_r\Delta z}\right)\Delta z\right)\right]\Delta\sigma_{22(m)}^E$$

$$+V_m\sigma_{22}^E\left[\frac{-\upsilon_m}{E_m}-\frac{1}{6}\left(\sum_{r=1}^{3}C_r\left(\frac{1-e^{\alpha_r\Delta z}}{\alpha_r}\right)\right)^{-1}\Delta z\right]\Delta\sigma_{33(m)}^E$$

$$+\frac{1}{2}V_m\left[\frac{-\upsilon_m}{E_m}-\frac{1}{6}\left(\sum_{r=1}^{3}C_r\left(\frac{1-e^{\alpha_r\Delta z}}{\alpha_r}\right)\right)^{-1}\Delta z\right]\Delta\sigma_{22(m)}^E\Delta\sigma_{33(m)}^E$$

$$+\frac{1}{2}V_m\left[\frac{1}{E_m}+\frac{1}{3}\left(\sum_{r=1}^{3}C_r\left(\frac{1-e^{\alpha_r\Delta z}}{\alpha_r}\right)\right)^{-1}\Delta z\right]\left(\Delta\sigma_{22(m)}^E\right)^2$$

$$+\frac{1}{2}V_m\sigma_{22}^E\left[\left(\sum_{r=1}^{3}C_r\left(\frac{1-e^{\alpha_r\Delta z}}{\alpha_r}\right)\right)^{-1}S_{22}^{E(r)}\left(1-e^{-\alpha_r\Delta z}\right)\right]\Delta z$$

$$-\left[\left(\sigma_{22}^e\Delta\varepsilon_{22}^e+\frac{1}{2}\Delta\sigma_{22}^e\Delta\varepsilon_{22}^e\right)-V_f\left(\sigma_{22(f)}^e\Delta\varepsilon_{22(f)}^e+\frac{1}{2}\Delta\sigma_{22(f)}^e\Delta\varepsilon_{22(f)}^e\right)\right]=0, \tag{4.29}$$

$$V_m\left[\sigma_{23}^E\left(\frac{1+\upsilon_m}{E_m}+\frac{1}{2}\left(\sum_{r=1}^{3}C_r\left(\frac{1-e^{\alpha_r\Delta z}}{\alpha_r}\right)\right)^{-1}\Delta z\right)+\frac{1}{4}\sum_{r=1}^{3}\left(\left(C_r\frac{1-e^{\alpha_r\Delta z}}{\alpha_r}\right)^{-1}S_{23}^{E(r)}\left(1-e^{-\alpha_r\Delta z}\right)\Delta z\right)\right]\Delta\sigma_{23(m)}^E$$

$$+\frac{1}{2}V_m\left[\frac{1+\upsilon_m}{E_m}+\frac{1}{2}\left(\sum_{r=1}^{3}C_r\left(\frac{1-e^{\alpha_r\Delta z}}{\alpha_r}\right)\right)^{-1}\Delta z\right]\left(\Delta\sigma_{23(m)}^E\right)^2$$

$$+\frac{1}{2}V_m\sigma_{23}^E\left[\sum_{r=1}^{3}\left(\left(C_r\frac{1-e^{\alpha_r\Delta z}}{\alpha_r}\right)^{-1}S_{23}^{E(r)}\left(1-e^{-\alpha_r\Delta z}\right)\Delta z\right)\right]$$

$$-\left[\left(\sigma_{23}^e\Delta\varepsilon_{23}^e+\frac{1}{2}\Delta\sigma_{23}^e\Delta\varepsilon_{23}^e\right)-V_f\left(\sigma_{23(f)}^e\Delta\varepsilon_{23(f)}^e+\frac{1}{2}\Delta\sigma_{23(f)}^e\Delta\varepsilon_{23(f)}^e\right)\right]=0, \tag{4.30}$$

and,

$$V_m\sigma_{33}^E\left[\frac{-\upsilon_m}{E_m}-\frac{1}{6}\left(\sum_{r=1}^{3}C_r\left(\frac{1-e^{\alpha_r\Delta z}}{\alpha_r}\right)\right)^{-1}\Delta z\right]\Delta\sigma_{22(m)}^E$$
$$+V_m\left[\sigma_{33}^E\left(\frac{1}{E_m}+\frac{1}{3}\left(\sum_{r=1}^{3}C_r\left(\frac{1-e^{\alpha_r\Delta z}}{\alpha_r}\right)\right)^{-1}\Delta z\right)+\frac{1}{4}\sum_{1}^{3}\left(\left(C_r\frac{1-e^{\alpha_r\Delta z}}{\alpha_r}\right)^{-1}S_{33}^{E(r)}\left(1-e^{-\alpha_r\Delta z}\right)\Delta z\right)\right]\Delta\sigma_{33(m)}^E$$
$$+\frac{1}{2}V_m\left[\frac{-\upsilon_m}{E_m}-\frac{1}{6}\left(\sum_{r=1}^{3}C_r\left(\frac{1-e^{\alpha_r\Delta z}}{\alpha_r}\right)\right)^{-1}\Delta z\right]\Delta\sigma_{22(m)}^E\Delta\sigma_{33(m)}^E$$
$$+\frac{1}{2}V_m\left[\frac{1}{E_m}+\frac{1}{3}\left(\sum_{r=1}^{3}C_r\left(\frac{1-e^{\alpha_r\Delta z}}{\alpha_r}\right)\right)^{-1}\Delta z\right]\left(\Delta\sigma_{33(m)}^E\right)^2$$
$$+\frac{1}{2}V_m\sigma_{33}^E\left[\left(\sum_{r=1}^{3}C_r\left(\frac{1-e^{\alpha_r\Delta z}}{\alpha_r}\right)\right)^{-1}S_{33}^{E(r)}\left(1-e^{-\alpha_r\Delta z}\right)\right]\Delta z$$
$$-\left[\left(\sigma_{33}^e\Delta\varepsilon_{33}^e+\frac{1}{2}\Delta\sigma_{33}^e\Delta\varepsilon_{33}^e\right)-V_f\left(\sigma_{33(f)}^e\Delta\varepsilon_{33(f)}^e+\frac{1}{2}\Delta\sigma_{33(f)}^e\Delta\varepsilon_{33(f)}^e\right)\right]=0. \tag{4.31}$$

Equations (4.29)-(4.31) when used in conjunction with Eq. (4.22) provide the four equations that are sufficient to solve for the three unknown matrix notch root stresses and the intrinsic time scale. The increments in the matrix strain components are then obtained separately using Eqs. (4.18)-(4.21).

Simplified PMMCs Neuber Energy Ratio Equations

Substituting Eqs. (4.19)-(4.21) into Eqs. (4.26)-(4.28) and re-arranging the resulting set of equations yield the following three relations:

$$V_m\left[\sigma_{22}^N\left(\frac{1}{E_m}+\frac{1}{3}\left(\sum_{r=1}^{3}C_r\left(\frac{1-e^{\alpha_r\Delta z}}{\alpha_r}\right)\right)^{-1}\Delta z\right)+\varepsilon_{22}^N+\frac{1}{2}\sum_{1}^{3}\left(\left(C_r\frac{1-e^{\alpha_r\Delta z}}{\alpha_r}\right)^{-1}S_{22}^{N(r)}\left(1-e^{-\alpha_r\Delta z}\right)\Delta z\right)\right]\Delta\sigma_{22(m)}^N$$
$$+V_m\sigma_{22}^N\left[\frac{-\upsilon_m}{E_m}-\frac{1}{6}\left(\sum_{r=1}^{3}C_r\left(\frac{1-e^{\alpha_r\Delta z}}{\alpha_r}\right)\right)^{-1}\Delta z\right]\Delta\sigma_{33(m)}^N$$
$$+V_m\left[\frac{-\upsilon_m}{E_m}-\frac{1}{6}\left(\sum_{r=1}^{3}C_r\left(\frac{1-e^{\alpha_r\Delta z}}{\alpha_r}\right)\right)^{-1}\Delta z\right]\Delta\sigma_{22(m)}^N\Delta\sigma_{33(m)}^N$$
$$+V_m\left[\frac{1}{E_m}+\frac{1}{3}\left(\sum_{r=1}^{3}C_r\left(\frac{1-e^{\alpha_r\Delta z}}{\alpha_r}\right)\right)^{-1}\Delta z\right]\left(\Delta\sigma_{22(m)}^N\right)^2$$
$$+\frac{1}{2}V_m\sigma_{22}^N\left[\left(\sum_{r=1}^{3}C_r\left(\frac{1-e^{\alpha_r\Delta z}}{\alpha_r}\right)\right)^{-1}S_{22}^{N(r)}\left(1-e^{-\alpha_r\Delta z}\right)\right]\Delta z$$
$$-\left[\left(\sigma_{22}^e\Delta\varepsilon_{22}^e+\varepsilon_{22}^e\Delta\sigma_{22}^e+\Delta\sigma_{22}^e\Delta\varepsilon_{22}^e\right)-V_f\left(\sigma_{22(f)}^e\Delta\varepsilon_{22(f)}^e+\varepsilon_{22(f)}^e\Delta\sigma_{22(f)}^e+\Delta\sigma_{22(f)}^e\Delta\varepsilon_{22(f)}^e\right)\right]=0, \tag{4.32}$$

$$V_m\sigma_{33}^N\left[\frac{-\upsilon_m}{E_m}-\frac{1}{6}\left(\sum_{r=1}^{3}C_r\left(\frac{1-e^{\alpha_r\Delta z}}{\alpha_r}\right)\right)^{-1}\Delta z\right]\Delta\sigma_{22(m)}^N$$
$$+V_m\left[\sigma_{33}^N\left(\frac{1}{E_m}+\frac{1}{3}\left(\sum_{r=1}^{3}C_r\left(\frac{1-e^{\alpha_r\Delta z}}{\alpha_r}\right)\right)^{-1}\Delta z\right)+\varepsilon_{33}^N+\frac{1}{2}\sum_{1}^{3}\left(\left(C_r\frac{1-e^{\alpha_r\Delta z}}{\alpha_r}\right)^{-1}S_{33}^{N(r)}\left(1-e^{-\alpha_r\Delta z}\right)\Delta z\right)\right]\Delta\sigma_{33(m)}^N$$
$$+V_m\left[\frac{-\upsilon_m}{E_m}-\frac{1}{6}\left(\sum_{r=1}^{3}C_r\left(\frac{1-e^{\alpha_r\Delta z}}{\alpha_r}\right)\right)^{-1}\Delta z\right]\Delta\sigma_{22(m)}^N\Delta\sigma_{33(m)}^N$$
$$+V_m\left[\frac{1}{E_m}+\frac{1}{3}\left(\sum_{r=1}^{3}C_r\left(\frac{1-e^{\alpha_r\Delta z}}{\alpha_r}\right)\right)^{-1}\Delta z\right]\left(\Delta\sigma_{33(m)}^N\right)^2$$
$$+\frac{1}{2}V_m\sigma_{33}^N\left[\left(\sum_{r=1}^{3}C_r\left(\frac{1-e^{\alpha_r\Delta z}}{\alpha_r}\right)\right)^{-1}S_{33}^{N(r)}\left(1-e^{-\alpha_r\Delta z}\right)\right]\Delta z$$
$$-\left[\left(\sigma_{33}^e\Delta\varepsilon_{33}^e+\varepsilon_{33}^e\Delta\sigma_{33}^e+\Delta\sigma_{33}^e\Delta\varepsilon_{33}^e\right)-V_f\left(\sigma_{33(f)}^e\Delta\varepsilon_{33(f)}^e+\varepsilon_{33(f)}^e\Delta\sigma_{33(f)}^e+\Delta\sigma_{33(f)}^e\Delta\varepsilon_{33(f)}^e\right)\right]=0, \tag{4.33}$$

and,

$$V_m\left[\begin{array}{l}\sigma_{23}^N\left(\dfrac{1+\upsilon_m}{E_m}+\dfrac{1}{2}\left(\sum_{r=1}^{3}C_r\left(\dfrac{1-e^{\alpha_r\Delta z}}{\alpha_r}\right)\right)^{-1}\Delta z\right)+\varepsilon_{23}^N\\ +\dfrac{1}{2}\sum_{r=1}^{3}\left(\left(C_r\dfrac{1-e^{\alpha_r\Delta z}}{\alpha_r}\right)^{-1}S_{23}^{N(r)}\left(1-e^{-\alpha_r\Delta z}\right)\Delta z\right)\end{array}\right]\Delta\sigma_{23(m)}^N$$
$$+V_m\left[\frac{1+\upsilon_m}{E_m}+\frac{1}{2}\left(\sum_{r=1}^{3}C_r\left(\frac{1-e^{\alpha_r\Delta z}}{\alpha_r}\right)\right)^{-1}\Delta z\right]\left(\Delta\sigma_{23(m)}^N\right)^2$$
$$+\frac{1}{2}V_m\sigma_{23}^N\left[\sum_{r=1}^{3}\left(\left(C_r\frac{1-e^{\alpha_r\Delta z}}{\alpha_r}\right)^{-1}S_{23}^{N(r)}\left(1-e^{-\alpha_r\Delta z}\right)\Delta z\right)\right]$$
$$-\left[\left(\sigma_{23}^e\Delta\varepsilon_{23}^e+\varepsilon_{23}^e\Delta\sigma_{23}^e+\Delta\sigma_{23}^e\Delta\varepsilon_{23}^e\right)-V_f\left(\sigma_{23(f)}^e\Delta\varepsilon_{23(f)}^e+\varepsilon_{23(f)}^e\Delta\sigma_{23(f)}^e+\Delta\sigma_{23(f)}^e\Delta\varepsilon_{23(f)}^e\right)\right]=0. \tag{4.34}$$

Equations (4.32)-(4.34), when used in conjunction with Eq. (4.22), provide the four equations that are sufficient to solve for the three unknown matrix notch root stresses and the intrinsic time scale. The increments in the matrix strain components are then obtained separately using Eqs. (4.18)-(4.21).

The resulting two sets of non-linear equations are given by Eqs. (4.22) , (4.29)-(4.31) and Eqs (4.22), (4.32)-(4.34) for the PMMCs ESED and the PMMCs Neuber methods respectively. Each set can be solved using the Newton-Raphson's numerical method for solving systems of nonlinear relations. The Newton-Ralphson's solution to system of non-linear equations is written as:

$$X_{n+1}=X_n+J^{-1}f_n, \tag{4.35}$$

where J is the Jacobian matrix of the set of equations (i.e. 4x4 matrix of the partial derivatives of each equation with respect to the unknowns), X_{n+1} and X_n are 4x1 matrices

of the actual and the initial guess values of the unknowns respectively, and n stands for the number of iterations. f_n is the 4x1 matrix of the four nonlinear equations, each evaluated using the values prior to an iterative step. Equation (4.35) can be expressed as:

$$\begin{bmatrix} \Delta z \\ \Delta\sigma_{22(m)} \\ \Delta\sigma_{33(m)} \\ \Delta\sigma_{23(m)} \end{bmatrix}_{n+1} = \begin{bmatrix} \Delta z \\ \Delta\sigma_{22(m)} \\ \Delta\sigma_{33(m)} \\ \Delta\sigma_{23(m)} \end{bmatrix}_{n} + \begin{bmatrix} \partial f_1/\partial\Delta z & \partial f_1/\partial\Delta\sigma_{22(m)} & \partial f_1/\partial\Delta\sigma_{33(m)} & \partial f_1/\partial\Delta\sigma_{23(m)} \\ \partial f_2/\partial\Delta z & \partial f_2/\partial\Delta\sigma_{22(m)} & \partial f_2/\partial\Delta\sigma_{33(m)} & \partial f_2/\partial\Delta\sigma_{23(m)} \\ \partial f_3/\partial\Delta z & \partial f_3/\partial\Delta\sigma_{22(m)} & \partial f_3/\partial\Delta\sigma_{33(m)} & \partial f_3/\partial\Delta\sigma_{23(m)} \\ \partial f_4/\partial\Delta z & \partial f_4/\partial\Delta\sigma_{22(m)} & \partial f_4/\partial\Delta\sigma_{33(m)} & \partial f_3/\partial\Delta\sigma_{23(m)} \end{bmatrix}_{n} \begin{bmatrix} f_1 \\ f_2 \\ f_3 \\ f_4 \end{bmatrix}_{n}. \tag{4.36}$$

The elements of the Jacobian matrix of the set of four equations given by Eqs. (4.22) , (4.29)-(4.31) and Eqs. (4.22), (4.32)-(4.34) for the ESED and the Neuber methods respectively is obtained as follows:

For PMMCs ESED:

Using Eqs. (4.22) , (4.29)-(4.31), if f_1 = Eq. (4.22), f_2 = Eq. (4.29), f_3 = Eq. (4.30), and f_4 = Eq. (4.31), assume that,

$$h = (1-e^{-\alpha_r \Delta z})^{-1}\Delta z, \quad \text{and} \quad g = (1-e^{-\alpha_r \Delta z})^{2}, \tag{4.37}$$

in Eqs. (4.22), (4.30), (4.29), and (4.34), then,

$$\beta = \partial h/\partial \Delta z = \frac{\left((1-e^{-\alpha_r \Delta z})\right)-\left(\alpha_r \Delta z e^{-\alpha_r \Delta z}\right)}{(1-e^{-\alpha_r \Delta z})^2}, \quad \gamma = \partial g/\partial \Delta z = 2\alpha_r e^{-\alpha_r \Delta z}(1-e^{-\alpha_r \Delta z}). \quad (4.38)$$

Thus, the elements of the Jacobian (J) 4x4 matrix in Eq. (4.36) of the set of non-linear equations (4.22), and (4.29)-(4.31) are as follows:

$$\begin{aligned}
\partial f_1/\partial \Delta z = & \left[\sum_{r=1}^{3}\left(\frac{C_r}{\alpha_r}\right)^2 \gamma\right] + \begin{bmatrix} \frac{1}{6}\left(\sum_{r=1}^{3} S_{11}^{E/N(r)}\left(\alpha_r e^{-\alpha_r \Delta z}\right)\right) - \frac{1}{3}\left(\sum_{r=1}^{3} S_{22}^{r}\left(\alpha_r e^{-\alpha_r \Delta z}\right)\right) + \\ \frac{1}{6}\left(\sum_{r=1}^{3} S_{33}^{E/N(r)}\left(\alpha_r e^{-\alpha_r \Delta z}\right)\right) \end{bmatrix} \Delta\sigma_{22(m)}^{E/N} \\
& + \left[\frac{1}{6}\left(\sum_{r=1}^{3} S_{11}^{E/N(r)}\left(\alpha_r e^{-\alpha_r \Delta z}\right)\right) - \frac{1}{3}\left(\sum_{r=1}^{3} S_{22}^{E/N(r)}\left(\alpha_r e^{-\alpha_r \Delta z}\right)\right) + \frac{1}{6}\left(\sum_{r=1}^{3} S_{33}^{E/N(r)}\left(\alpha_r e^{-\alpha_r \Delta z}\right)\right)\right] \Delta\sigma_{33(m)}^{E/N} \\
& - \left[\frac{1}{2}\left(\sum_{r=1}^{3} S_{23}^{r}\left(\alpha_r e^{-\alpha_r \Delta z}\right)\right)\right] \Delta\sigma_{23(m)}^{E/N} \\
& + \left[\frac{1}{4}\left(\sum_{r=1}^{3}\left(\left(S_{11}^{E/N(r)}\right)^2 + \left(S_{22}^{E/N(r)}\right)^2 \left(S_{33}^{E/N(r)}\right)^2 + \left(S_{23}^{E/N(r)}\right)^2\right)\left(\alpha_r e^{-\alpha_r \Delta z}\right)\right)\right]
\end{aligned} \quad (4.39)$$

$$\begin{aligned}
\partial f_1/\partial \Delta\sigma_{22(m)} = & \left[\frac{1}{6}\left(\sum_{r=1}^{3} S_{11}^{E/N(r)}\left(1-\alpha_r e^{-\alpha_r \Delta z}\right)\right) - \frac{1}{3}\left(\sum_{r=1}^{3} S_{22}^{E/N(r)}\left(1-\alpha_r e^{-\alpha_r \Delta z}\right)\right) + \frac{1}{6}\left(\sum_{r=1}^{3} S_{33}^{E/N(r)}\left(1-\alpha_r e^{-\alpha_r \Delta z}\right)\right)\right] \\
& + \left[\frac{1}{6}\right] \Delta\sigma_{33(m)}^{E/N} - \left[\frac{1}{3}\right] \Delta\sigma_{22(m)}^{E/N}
\end{aligned} \quad (4.40)$$

$$\partial f_1/\partial \Delta\sigma_{33(m)} = \begin{bmatrix} \frac{1}{6}\left(\sum_{r=1}^{3} S_{11}^{E/N(r)}\left(1-\alpha_r e^{-\alpha_r \Delta z}\right)\right) - \frac{1}{3}\left(\sum_{r=1}^{3} S_{22}^{E/N(r)}\left(1-\alpha_r e^{-\alpha_r \Delta z}\right)\right) \\ + \frac{1}{6}\left(\sum_{r=1}^{3} S_{33}^{E/N(r)}\left(1-\alpha_r e^{-\alpha_r \Delta z}\right)\right) \end{bmatrix} + \left[\frac{1}{6}\right] \Delta\sigma_{22(m)}^{E/N} - \left[\frac{1}{3}\right] \Delta\sigma_{33(m)}^{E/N} \quad (4.41)$$

$$\partial f_1 / \partial \Delta\sigma_{23(m)} = -\left[\frac{1}{2}\left(\sum_{r=1}^{3} S_{23}^{E/N(r)}\left(1-\alpha_r e^{-\alpha_r \Delta z}\right)\right)\right] - \left[\frac{1}{2}\right]\Delta\sigma_{23(m)}^{E/N} \tag{4.42}$$

$$\begin{aligned}\partial f_2 / \partial \Delta z = {} & V_m\left[\frac{\sigma_{22(m)}^{E}}{3}\left(\sum_{r=1}^{3}\left(\frac{C_r}{\alpha_r}\right)^{-1}\beta\right)+\frac{1}{4}\left(\sum_{r=1}^{3}\left(\frac{C_r}{\alpha_r}\right)^{-1} S_{22}^{E(r)}\right)\right]\Delta\sigma_{22(m)}^{E} \\ & + V_m\sigma_{22(m)}^{E}\left[-\frac{1}{6}\left(\sum_{r=1}^{3}\left(\frac{C_r}{\alpha_r}\right)^{-1}\beta\right)\right]\Delta\sigma_{33(m)}^{E} + \frac{V_m}{2}\left[-\frac{1}{6}\left(\sum_{r=1}^{3}\left(\frac{C_r}{\alpha_r}\right)^{-1}\beta\right)\right]\Delta\sigma_{22(m)}^{E}\Delta\sigma_{33(m)}^{E} \\ & + \frac{V_m}{2}\left[\frac{1}{3}\left(\sum_{r=1}^{3}\left(\frac{C_r}{\alpha_r}\right)^{-1}\beta\right)\right]\left(\Delta\sigma_{22}^{E}\right)^2 + \frac{V_m\sigma_{22(m)}^{E}}{2}\left[\left(\sum_{r=1}^{3}\left(\frac{C_r}{\alpha_r}\right)^{-1} S_{22}^{E(r)}\right)\right]\end{aligned} \tag{4.43}$$

$$\begin{aligned}\partial f_2 / \partial \Delta\sigma_{22(m)} = {} & V_m\left[\begin{array}{l}\sigma_{22(m)}^{E}\left(\frac{1}{E_m}+\frac{1}{3}\left(\sum_{r=1}^{3} C_r\left(\frac{1-e^{\alpha_r\Delta z}}{\alpha_r}\right)\right)^{-1}\Delta z\right)+ \\ \frac{1}{4}\sum_{1}^{3}\left(\left(C_r\frac{1-e^{\alpha_r\Delta z}}{\alpha_r}\right)^{-1} S_{22}^{E(r)}\left(1-e^{-\alpha_r\Delta z}\right)\Delta z\right)\end{array}\right] \\ & + \frac{1}{2}V_m\left[\frac{-\upsilon_m}{E_m}-\frac{1}{6}\left(\sum_{r=1}^{3} C_r\left(\frac{1-e^{\alpha_r\Delta z}}{\alpha_r}\right)\right)^{-1}\Delta z\right]\Delta\sigma_{33(m)}^{E} \\ & + V_m\left[\frac{1}{E_m}+\frac{1}{3}\left(\sum_{r=1}^{3} C_r\left(\frac{1-e^{\alpha_r\Delta z}}{\alpha_r}\right)\right)^{-1}\Delta z\right]\left(\Delta\sigma_{22(m)}^{E}\right)\end{aligned} \tag{4.44}$$

$$\begin{aligned}\partial f_2 / \partial \Delta\sigma_{33(m)} = {} & V_m\sigma_{22(m)}^{E}\left[\frac{-\upsilon_m}{E_m}-\frac{1}{6}\left(\sum_{r=1}^{3} C_r\left(\frac{1-e^{\alpha_r\Delta z}}{\alpha_r}\right)\right)^{-1}\Delta z\right] \\ & + \frac{1}{2}V_m\left[\frac{-\upsilon_m}{E_m}-\frac{1}{6}\left(\sum_{r=1}^{3} C_r\left(\frac{1-e^{\alpha_r\Delta z}}{\alpha_r}\right)\right)^{-1}\Delta z\right]\Delta\sigma_{22(m)}^{E}\end{aligned} \tag{4.45}$$

$$\partial f_2 / \partial \Delta\sigma_{23(m)} = 0 \tag{4.46}$$

$$\begin{aligned}
\partial f_3 / \partial \Delta z = {} & V_m \sigma^E_{33(m)} \left[-\frac{1}{6} \left(\sum_{r=1}^{3} \left(\frac{C_r}{\alpha_r} \right)^{-1} \beta \right) \right] \Delta\sigma^E_{22} \\
& + V_m \left[\frac{\sigma^E_{33(m)}}{3} \left(\sum_{r=1}^{3} \left(\frac{C_r}{\alpha_r} \right)^{-1} \beta \right) + \frac{1}{4} \left(\sum_{r=1}^{3} \left(\frac{C_r}{\alpha_r} \right)^{-1} S^{E(r)}_{22} \right) \right] \Delta\sigma^E_{33(m)} \\
& + \frac{V_m}{2} \left[-\frac{1}{6} \left(\sum_{r=1}^{3} \left(\frac{C_r}{\alpha_r} \right)^{-1} \beta \right) \right] \Delta\sigma^E_{22(m)} \Delta\sigma^E_{33(m)} \\
& + \frac{V_m}{2} \left[\frac{1}{3} \left(\sum_{r=1}^{3} \left(\frac{C_r}{\alpha_r} \right)^{-1} \beta \right) \right] \left(\Delta\sigma^E_{33(m)} \right)^2 + \frac{V_m \sigma^E_{33(m)}}{2} \left[\left(\sum_{r=1}^{3} \left(\frac{C_r}{\alpha_r} \right)^{-1} S^{E(r)}_{33} \right) \right]
\end{aligned} \tag{4.47}$$

$$\begin{aligned}
\partial f_3 / \partial \Delta\sigma_{22(m)} = {} & V_m \sigma^E_{33(m)} \left[\frac{-\upsilon_m}{E_m} - \frac{1}{6} \left(\sum_{r=1}^{3} C_r \left(\frac{1 - e^{\alpha_r \Delta z}}{\alpha_r} \right) \right)^{-1} \Delta z \right] \\
& + \frac{1}{2} V_m \left[\frac{-\upsilon_m}{E_m} - \frac{1}{6} \left(\sum_{r=1}^{3} C_r \left(\frac{1 - e^{\alpha_r \Delta z}}{\alpha_r} \right) \right)^{-1} \Delta z \right] \Delta\sigma^E_{33(m)}
\end{aligned} \tag{4.48}$$

$$\begin{aligned}
\partial f_3 / \partial \Delta\sigma_{33(m)} = {} & V_m \left[\sigma^E_{33} \left(\frac{1}{E_m} + \frac{1}{3} \left(\sum_{r=1}^{3} C_r \left(\frac{1 - e^{\alpha_r \Delta z}}{\alpha_r} \right) \right)^{-1} \Delta z \right) + \frac{1}{4} \sum_{1}^{3} \left(\left(C_r \frac{1 - e^{\alpha_r \Delta z}}{\alpha_r} \right)^{-1} S^{E(r)}_{22} \left(1 - e^{-\alpha_r \Delta z} \right) \Delta z \right) \right] \\
& + \frac{1}{2} V_m \left[\frac{-\upsilon_m}{E_m} - \frac{1}{6} \left(\sum_{r=1}^{3} C_r \left(\frac{1 - e^{\alpha_r \Delta z}}{\alpha_r} \right) \right)^{-1} \Delta z \right] \Delta\sigma^E_{22(m)} \\
& + V_m \left[\frac{1}{E_m} + \frac{1}{3} \left(\sum_{r=1}^{3} C_r \left(\frac{1 - e^{\alpha_r \Delta z}}{\alpha_r} \right) \right)^{-1} \Delta z \right] \Delta\sigma^E_{33(m)}
\end{aligned} \tag{4.49}$$

$$\partial f_3 / \partial \Delta\sigma_{23(m)} = 0 \tag{4.50}$$

$$\begin{aligned}\partial f_4 / \partial \Delta z = V_m &\left[\sigma^E_{23(m)} \left(\sum_{r=1}^{3} \left(\frac{C_r}{\alpha_r} \right)^{-1} \beta \right) + \frac{1}{4} \left(\sum_{r=1}^{3} \left(\frac{C_r}{\alpha_r} \right)^{-1} S^{E(r)}_{23} \right) \right] \Delta\sigma^E_{23(m)} \\ &+ \frac{V_m}{4} \left[\left(\sum_{r=1}^{3} \left(\frac{C_r}{\alpha_r} \right)^{-1} \beta \right) \right] \left(\Delta\sigma^2_{23(m)} \right)^2 + \frac{V_m \sigma^E_{23(m)}}{2} \left[\left(\sum_{r=1}^{3} \left(\frac{C_r}{\alpha_r} \right)^{-1} S^{E(r)}_{23} \right) \right]\end{aligned} \tag{4.51}$$

$$\partial f_4 / \partial \Delta\sigma_{22(m)} = 0 \tag{4.52}$$

$$\partial f_4 / \partial \Delta\sigma_{33(m)} = 0 \tag{4.53}$$

$$\begin{aligned}\partial f_4 / \partial \Delta\sigma_{23(m)} = V_m &\left[\sigma^E_{23} \left(\frac{1+\upsilon_m}{E_m} + \frac{1}{2} \left(\sum_{r=1}^{3} C_r \left(\frac{1-e^{\alpha_r \Delta z}}{\alpha_r \Delta z} \right) \right)^{-1} \Delta z \right) + \right. \\ &\left. \frac{1}{4} \sum_{r=1}^{3} \left(\left(C_r \frac{1-e^{\alpha_r \Delta z}}{\alpha_r \Delta z} \right)^{-1} S^{E(r)}_{23} \left(1-e^{-\alpha_r \Delta z} \right) \Delta z \right) \right] \\ &+ V_m \left[\frac{1+\upsilon_m}{E_m} + \frac{1}{2} \left(\sum_{r=1}^{3} C_r \left(\frac{1-e^{\alpha_r \Delta z}}{\alpha_r \Delta z} \right) \right)^{-1} \Delta z \right] \Delta\sigma^E_{23(m)}\end{aligned} \tag{4.54}$$

For PMMCs NEUBER:

Using Eqs. (4.22), (4.32)-(4.34), if f_1 = Eq. (4.22), f_2 = Eq. (4.32), f_3 = Eq. (4.33), and f_4 = Eq. (4.34), Eq. (4.36) can also be used to solve for the four unknowns. The elements of the Jacobian are given as:

$\partial f_1/\partial \Delta z$, $\partial f_1/\partial \Delta\sigma_{22(m)}$, $\partial f_1/\partial \Delta\sigma_{33(m)}$, $\partial f_1/\partial \Delta\sigma_{23(m)}$ are as given in Eqs. (4.39)-(4.42).

$$\begin{aligned}\partial f_2/\partial \Delta z = {} & V_m\left[\frac{\sigma^N_{22(m)}}{3}\left(\sum_{r=1}^{3}\left(\frac{C_r}{\alpha_r}\right)^{-1}\beta\right)+\frac{1}{2}\left(\sum_{r=1}^{3}\left(\frac{C_r}{\alpha_r}\right)^{-1}S^{N(r)}_{22}\right)\right]\Delta\sigma^N_{22(m)} \\ & +V_m\sigma^N_{22(m)}\left[-\frac{1}{6}\left(\sum_{r=1}^{3}\left(\frac{C_r}{\alpha_r}\right)^{-1}\beta\right)\right]\Delta\sigma^N_{33}+V_m\left[-\frac{1}{6}\left(\sum_{r=1}^{3}\left(\frac{C_r}{\alpha_r}\right)^{-1}\beta\right)\right]\Delta\sigma^N_{22(m)}\Delta\sigma^N_{33(m)} \\ & +V_m\left[\frac{1}{3}\left(\sum_{r=1}^{3}\left(\frac{C_r}{\alpha_r}\right)^{-1}\beta\right)\right]\left(\Delta\sigma^N_{22(m)}\right)^2+\frac{V_m\sigma^N_{22(m)}}{2}\left[\left(\sum_{r=1}^{3}\left(\frac{C_r}{\alpha_r}\right)^{-1}S^r_{22}\right)\right]\end{aligned} \tag{4.55}$$

$$\begin{aligned}\partial f_2/\partial \Delta\sigma_{22(m)} = {} & V_m\left[\begin{array}{l}\sigma^N_{22(m)}\left(\frac{1}{E_m}+\frac{1}{3}\left(\sum_{r=1}^{3}C_r\left(\frac{1-e^{\alpha_r\Delta z}}{\alpha_r}\right)\right)^{-1}\Delta z\right)+\varepsilon^N_{22(m)}+ \\ \frac{1}{2}\sum_{1}^{3}\left(\left(C_r\frac{1-e^{\alpha_r\Delta z}}{\alpha_r}\right)^{-1}S^{N(r)}_{22}\left(1-e^{-\alpha_r\Delta z}\right)\Delta z\right)\end{array}\right] \\ & +V_m\left[\frac{-\upsilon_m}{E_m}-\frac{1}{6}\left(\sum_{r=1}^{3}C_r\left(\frac{1-e^{\alpha_r\Delta z}}{\alpha_r}\right)\right)^{-1}\Delta z\right]\Delta\sigma^N_{33(m)} \\ & +2V_m\left[\frac{1}{E_m}+\frac{1}{3}\left(\sum_{r=1}^{3}C_r\left(\frac{1-e^{\alpha_r\Delta z}}{\alpha_r}\right)\right)^{-1}\Delta z\right]\Delta\sigma^N_{22(m)}\end{aligned} \tag{4.56}$$

$$\begin{aligned}\partial f_2/\partial \Delta\sigma_{33(m)} = {} & V_m\sigma^N_{22(m)}\left[\frac{-\upsilon_m}{E_m}-\frac{1}{6}\left(\sum_{r=1}^{3}C_r\left(\frac{1-e^{\alpha_r\Delta z}}{\alpha_r}\right)\right)^{-1}\Delta z\right] \\ & +V_m\left[\frac{-\upsilon_m}{E_m}-\frac{1}{6}\left(\sum_{r=1}^{3}C_r\left(\frac{1-e^{\alpha_r\Delta z}}{\alpha_r}\right)\right)^{-1}\Delta z\right]\Delta\sigma^N_{22(m)}\end{aligned} \tag{4.57}$$

$$\partial f_2 / \partial \Delta\sigma_{23(m)} = 0 \tag{4.58}$$

$$\begin{aligned}\partial f_3 / \partial \Delta z = {} & V_m \sigma^N_{33(m)} \left[\frac{-1}{6} \sum_1^3 \left(\frac{C_r}{\alpha_r} \right)^{-1} \beta \right] \Delta\sigma_{22(m)} + V_m \left[\frac{\sigma^N_{33(m)}}{3} \Delta\sigma^N_{22(m)} + \frac{1}{2} \left(\sum_1^3 \left(\frac{C_r}{\alpha_r} \right)^{-1} S^{N(r)}_{22} \right) \right] \Delta\sigma^N_{33(m)} \\ & + \frac{V_m}{2} \left[\frac{-1}{6} \sum_1^3 \left(\frac{C_r}{\alpha_r} \right)^{-1} \beta \right] \Delta\sigma^N_{22(m)} \Delta\sigma^N_{33(m)} + V_m \left[\frac{1}{3} \sum_1^3 \left(\frac{C_r}{\alpha_r} \right)^{-1} \beta \right] \left(\Delta\sigma^N_{33(m)} \right)^2 \\ & + \frac{V_m \Delta\sigma^N_{33(m)}}{2} \left[\sum_1^3 \left(\frac{C_r}{\alpha_r} \right)^{-1} S^{N(r)}_{22} \right]\end{aligned} \tag{4.59}$$

$$\begin{aligned}\partial f_3 / \partial \Delta\sigma_{22(m)} = {} & V_m \sigma^N_{33(m)} \left[\frac{-\upsilon_m}{E_m} - \frac{1}{6} \left(\sum_{r=1}^3 C_r \left(\frac{1 - e^{\alpha_r \Delta z}}{\alpha_r} \right) \right)^{-1} \Delta z \right] \\ & + V_m \left[\frac{-\upsilon_m}{E_m} - \frac{1}{6} \left(\sum_{r=1}^3 C_r \left(\frac{1 - e^{\alpha_r \Delta z}}{\alpha_r} \right) \right)^{-1} \Delta z \right] \Delta\sigma^N_{33(m)}\end{aligned} \tag{4.60}$$

$$\begin{aligned}\partial f_3 / \partial \Delta\sigma_{33(m)} = {} & V_m \left[\begin{array}{l} \sigma^N_{33(m)} \left(\dfrac{1}{E_m} + \dfrac{1}{3} \left(\displaystyle\sum_{r=1}^3 C_r \left(\frac{1 - e^{\alpha_r \Delta z}}{\alpha_r} \right) \right)^{-1} \Delta z \right) + \varepsilon^N_{33} + \\ \dfrac{1}{2} \displaystyle\sum_1^3 \left(\left(C_r \frac{1 - e^{\alpha_r \Delta z}}{\alpha_r} \right)^{-1} S^{N(r)}_{22} \left(1 - e^{-\alpha_r \Delta z} \right) \Delta z \right) \end{array} \right] \\ & + V_m \left[\frac{-\upsilon_m}{E_m} - \frac{1}{6} \left(\sum_{r=1}^3 C_r \left(\frac{1 - e^{\alpha_r \Delta z}}{\alpha_r} \right) \right)^{-1} \Delta z \right] \Delta\sigma^N_{22(m)} \\ & + 2V_m \left[\frac{1}{E_m} + \frac{1}{3} \left(\sum_{r=1}^3 C_r \left(\frac{1 - e^{\alpha_r \Delta z}}{\alpha_r} \right) \right)^{-1} \Delta z \right] \Delta\sigma^N_{33(m)}\end{aligned} \tag{4.61}$$

$$\partial f_3 / \partial \Delta\sigma_{23(m)} = 0 \tag{4.62}$$

$$\begin{aligned} \partial f_4 / \partial \Delta z = {} & V_m \left[\sigma^N_{23(m)} \left(\sum_{r=1}^{3} \left(\frac{C_r}{\alpha_r} \right)^{-1} \beta \right) + \frac{1}{2} \left(\sum_{r=1}^{3} \left(\frac{C_r}{\alpha_r} \right)^{-1} S^{N(r)}_{23} \right) \right] \Delta\sigma^N_{23(m)} \\ & + \frac{V_m}{2} \left[\left(\sum_{r=1}^{3} \left(\frac{C_r}{\alpha_r} \right)^{-1} \beta \right) \right] \Delta\sigma^2_{23} + \frac{V_m \sigma^N_{23(m)}}{2} \left[\left(\sum_{r=1}^{3} \left(\frac{C_r}{\alpha_r} \right)^{-1} S^{N(r)}_{23} \right) \right] \end{aligned} \tag{4.63}$$

$$\partial f_4 / \partial \Delta\sigma_{22(m)} = 0 \tag{4.64}$$

$$\partial f_4 / \partial \Delta\sigma_{33(m)} = 0 \tag{4.65}$$

$$\begin{aligned} \partial f_4 / \partial \Delta\sigma_{23(m)} = {} & V_m \left[\begin{array}{l} \sigma^N_{23} \left(\dfrac{1+\upsilon_m}{E_m} + \dfrac{1}{2} \left(\displaystyle\sum_{r=1}^{3} C_r \left(\frac{1-e^{\alpha_r \Delta z}}{\alpha_r} \right) \right)^{-1} \Delta z \right) + \varepsilon^N_{23} + \\ \dfrac{1}{2} \displaystyle\sum_{r=1}^{3} \left(\left(C_r \frac{1-e^{\alpha_r \Delta z}}{\alpha_r} \right)^{-1} S^{N(r)}_{23} \left(1 - e^{-\alpha_r \Delta z} \right) \Delta z \right) \end{array} \right] \\ & + 2V_m \left[\frac{1+\upsilon_m}{E_m} + \frac{1}{2} \left(\sum_{r=1}^{3} C_r \left(\frac{1-e^{\alpha_r \Delta z}}{\alpha_r} \right) \right)^{-1} \Delta z \right] \Delta\sigma^N_{23(m)} \end{aligned} \tag{4.66}$$

4.5 Implementation Procedure for the Simplified Methods

In this section, the numerical procedure for evaluating the simplified models presented in this chapter is given. Two MATLAB [74] programs, one for each of the

proposed PMMCs Neuber's and PMMCs ESED models were developed. Each program calculates the composite elastic-plastic strain and stress histories at a geometric discontinuity given the composites material properties, the Dirichlet constants from Eq. (3.53) and the elastic notch root strain-stress histories obtained from the elastic solutions. The computer flow charts, shown in Figs. 4.2 (a-b), are the same for both programs.

The composite notch root elastic-plastic strain and stress histories that result in response to a cyclically applied load are evaluated incrementally. That is, they are evaluated for each small increment in the applied load. The elastic-plastic constitutive relations are applicable from the onset of loading. The plastic component of strains tends to zero within the elastic range. In other words, the Dirichlet function $\rho(z)$ is sufficiently large in order to produce an elastic response during initial loading and each subsequent unloading.

For each increment of external load, the increments in the matrix notch root stress and the intrinsic time scale are obtained using the two sets of non-linear equations given by Eqs. (4.22), (4.29)-(4.31) and Eqs (4.22), (4.32)-(4.34) for the PMMCs ESED and the PMMCs Neuber methods respectively. As stated earlier, since the equations are non-linear, a numerical iterative method such as Newton-Raphson method is required to obtain the unknowns. In this research, the linear solutions for the increments in the matrix stress components and the increment in the intrinsic time scale are used as initial guesses for the unknowns in the Newton-Raphson routine. This reduces the computational time required to obtain the unknowns since the linear solutions provide a close approximation to the non-linear solutions. It also ensures that the systems of equations converge. To obtain the linear solutions for the matrix stress-strain increments,

the intrinsic time scale is first obtained from the non-linear equation, Eq. (4.22), using an iterative numerical Secant method. The incremental time scale is then substituted into the linear forms of each set of seven equations (i.e. Eqs. (4.18)-(4.21), (4.23)-(4.25), and Eqs. (4.18)-(4.21), (4.26)-(4.28) for the PMMCs ESED and the PMMCs Neuber's respectively). These linear forms are obtained by ignoring the non-linear terms (i.e. terms with higher orders) in the solution sets. The resulting linear sets of algebraic equations are then solved simultaneously to obtain the linear solutions of the increments in the matrix stress and strain tensors. Using these linear solutions of the matrix stress and the intrinsic time scale obtained as initial guesses, the two set of non-linear equations given by Eqs. (4.22), (4.29)-(4.31) and Eqs (4.22), (4.32)-(4.34) for the PMMCs ESED and the PMMCs Neuber methods respectively are then solved for the unknown increments in the intrinsic time and matrix stress tensor using Eq. (4.36). The increment in the matrix strain tensor is then obtained separately using Eqs. (4.18)-(4.21). The final state of stress and strain at a point can then be obtained by adding the increments to the previous stress-strain history (Eqs. (4.3) and (4.4)). The increments in the reinforcement stress and strain can be obtained from the elastic analysis using Eqs. (3.15)-(3.16), and the elastic stress concentration factors. For each point in the loading history the composite elastic-plastic strain and stress state at the notch root can be obtained using the elastic-plastic matrix strains and stresses, the elastic reinforcement strains and stresses, and Eq. (3.17).

It is important to discuss briefly the convergence criteria used to determine when the Newton-Raphson solution has converged. Since we are determining the solution of a system of nonlinear equations, it is reasonable to assume that the solution converges when the norm of the matrix containing the set of solutions is very small on substituting

the solutions provided at each iteration step (i.e. $\|F(A(q)\|$ is small, where F is the matrix of the function, and A(q) is the matrix of the solution of F at an iteration step q). In this research, the norm was made as small as 10^{-8}. In addition, it is required that the solution at an iteration step is close to the solution as the number of iteration tends to infinity (i.e. $A(q) = A(\infty)$). In other words, it is reasonable to require that ($\|dA(q)\|$ be small, where dA(q) is the difference between successive iterations. Both requirements were used as convergence criteria in this research. This norm was also made to the order of 10^{-8}.

4.6 Summary of Chapter Four

In this chapter, two analytical models have been developed to estimate the composite notch root elastic-plastic strains and stresses in PMMC components subjected to multiaxial cyclic non-proportional loading knowing the constituents material properties, the Dirichlet constants from Eq. (3.53), and the composite stress and strain histories obtained from the elastic solutions. For each increment of external load, the increment in the matrix notch root stress tensor and the incremental time scale can be obtained using either Eqs. (4.22), (4.29)-(4.31) for the PMMCs ESED method or Eqs (4.22), (4.32)-(4.34) for the PMMCs Neuber method. The increments in the reinforcement stress and strain can be obtained from the elastic analysis using Eqs. (3.15)-(3.16), and the elastic stress concentration factors of the notched geometry modeled. The composite elastic-plastic strain and stress states at the notch root are subsequently obtained using the elastic-plastic matrix strains and stresses, the elastic

reinforcement strains and stresses, and Eqs. (3.17). Details of the numerical implementation procedure of the models were outlined in this chapter.

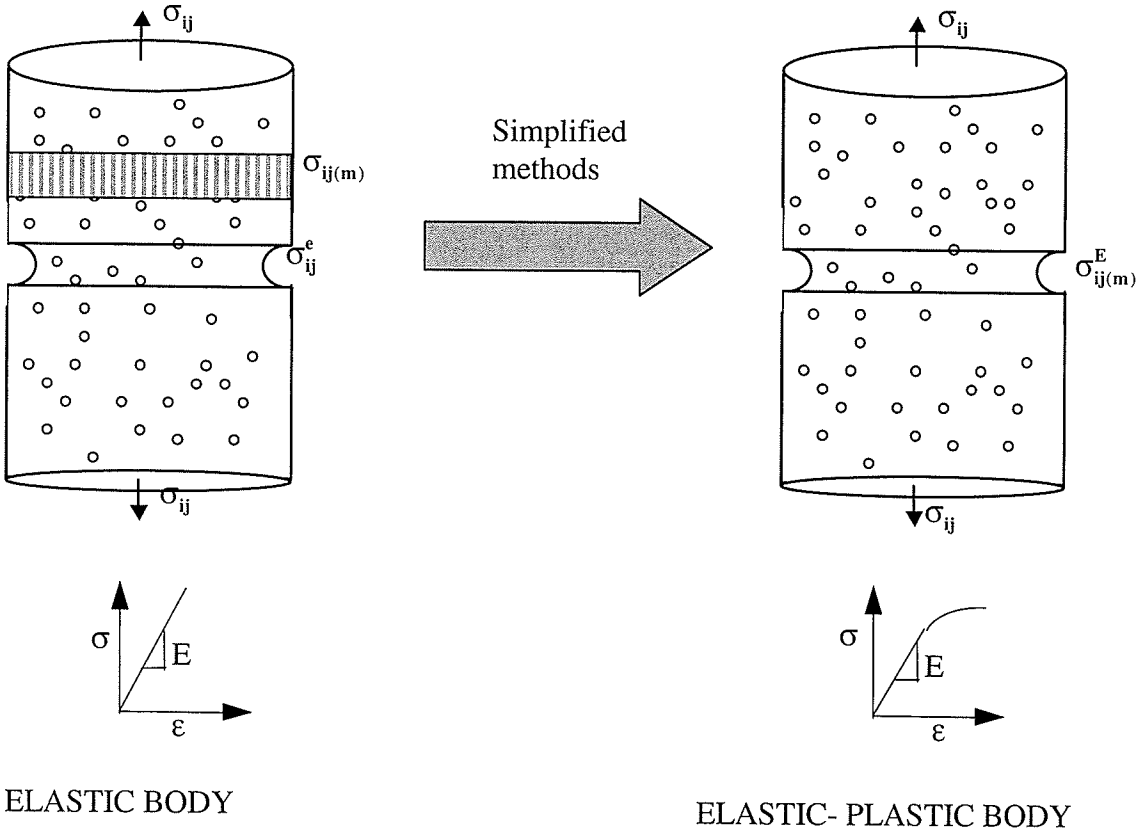

Figure 4.1: Illustration of Simplified Methods

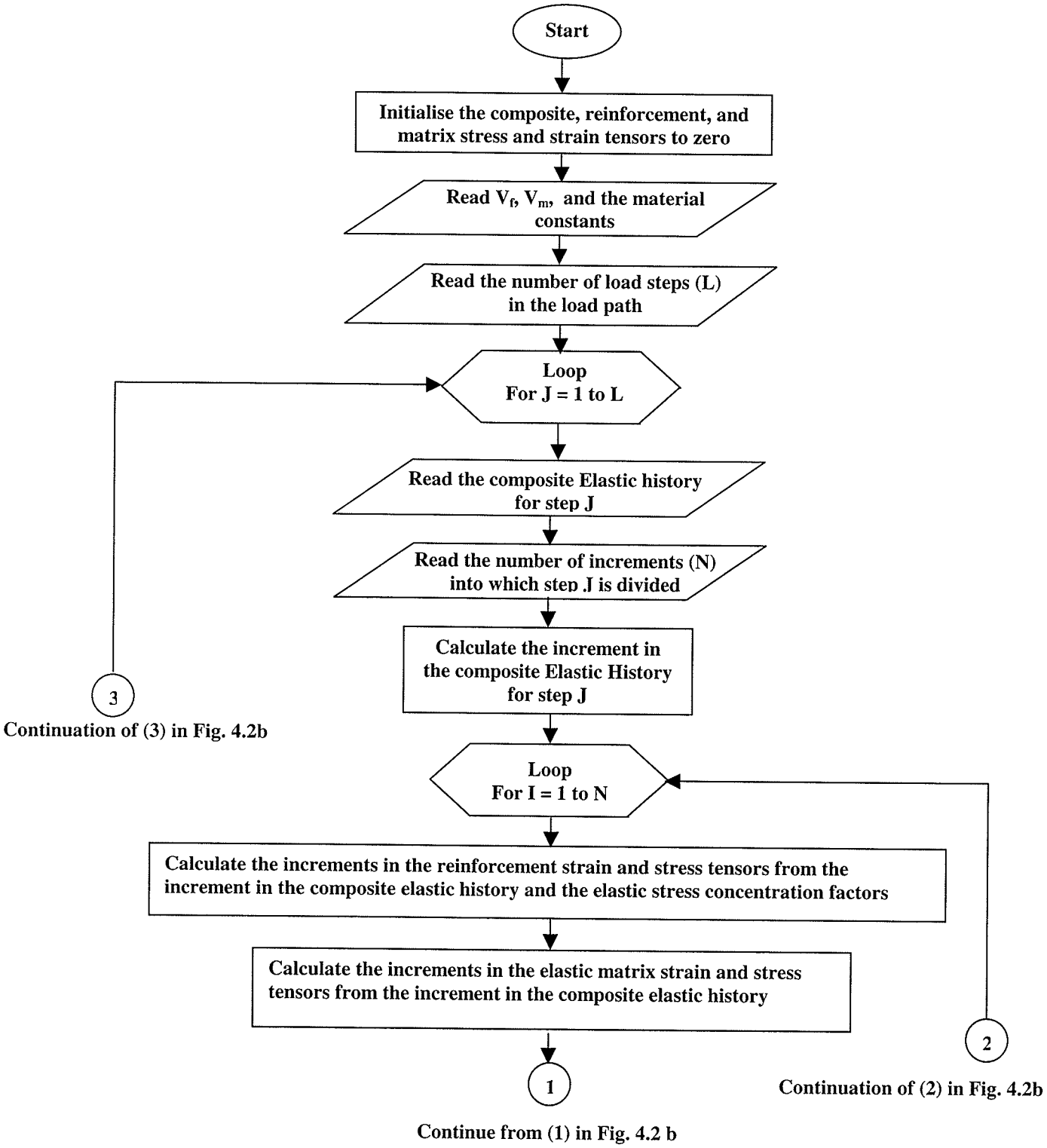

Figure 4.2a: Flow Chart for Notch Root Elastic-Plastic Strain-Stress Analysis for PMMCs

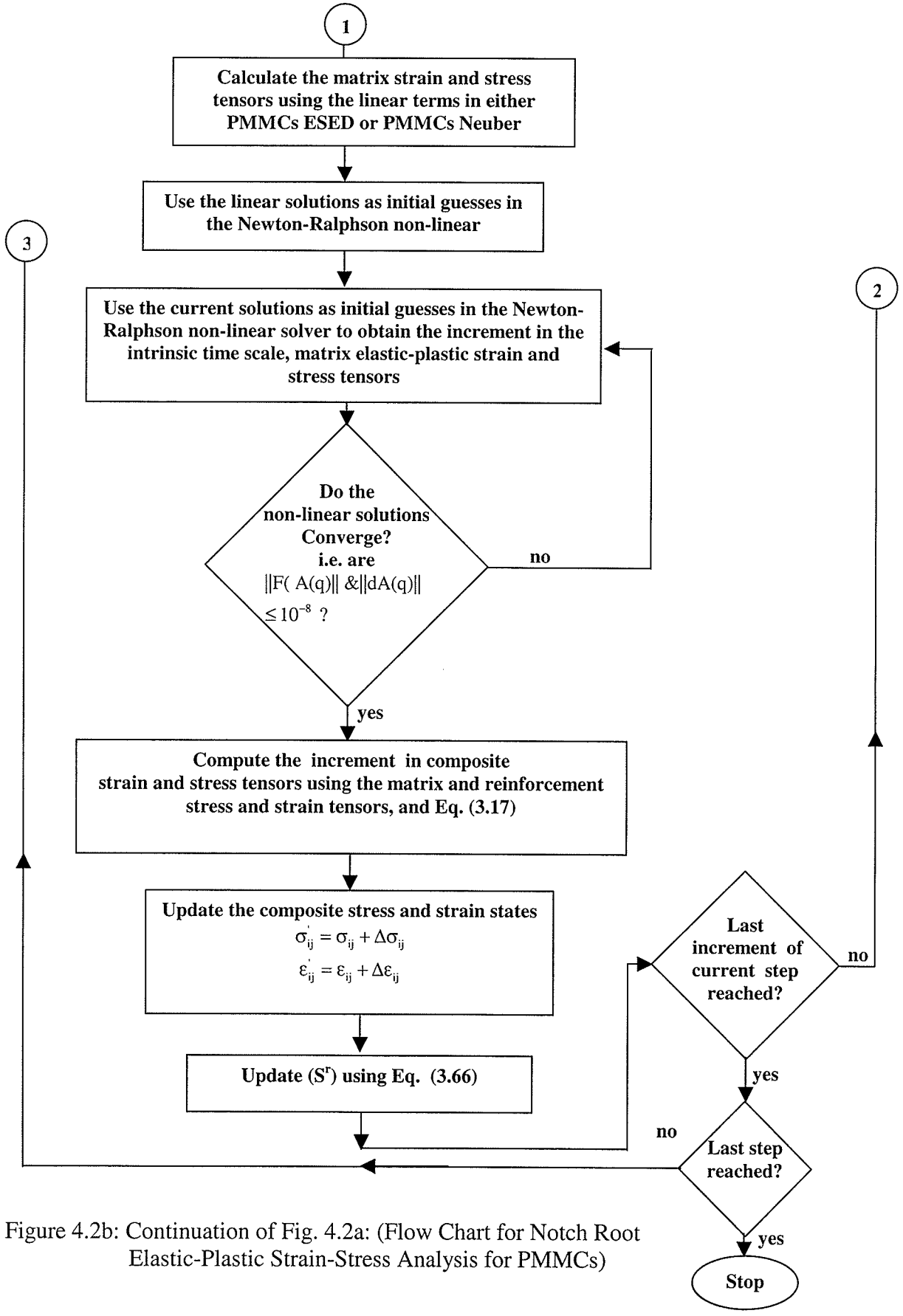

Figure 4.2b: Continuation of Fig. 4.2a: (Flow Chart for Notch Root Elastic-Plastic Strain-Stress Analysis for PMMCs)

CHAPTER FIVE: MATERIAL DESCRIPTIONS AND EXPERIMENTAL TECHNIQUES

As stated in Chapter One, one of the key challenges limiting the widespread application of PMMCs is the lack of experimental data available to validate existing and proposed analytical tools that describe their mechanical behavior. In other words, without an experimental validation of any mechanical behavior prediction model, its proliferation into design environments is difficult. For this purpose, an experimental program aimed at providing support to the constitutive theories, presented in Chapter Three, and the notch root elastic-plastic strain and stress estimation methods, presented in Chapter Four, was developed and implemented. This chapter describes the details of the experimental program. Specifically, the facilities in the Multiaxial Fatigue Research Laboratory in the Department of Mechanical and Manufacturing Engineering at the University of Manitoba, used in the experimental program are first presented in Section 5.1. The material and geometries of the test specimens are presented in Section 5.2. The experimental test program is described in Section 5.3. Finally, Section 5.4 gives the summary of the chapter.

It should be noted that the experimental results obtained in this research investigations can also be used to verify current and future analytical models that describe the constitutive behavior and notch root stress and strain histories of PMMCs.

5.1 Testing Equipment Description

To experimentally assess the developed analytical models, a load frame, an optical strain measuring device, signal conditioners and strain gage consumables, and a data acquisition system, were employed. A schematic of the whole test set up including the data flow is shown in Fig. 5.1.

5.1.1 Load Frame

In order to simulate multiaxial notch root strain and stress states, an Instron [76] servo-hydraulic biaxial load frame, shown in Fig. 5.2a, was used. The system can apply axial and/or torsional loads both monotonically and cyclically. It has an axial and a torsional load capacity of ± 250 KN and ± 2500 Nm respectively. The servohydraulic system essentially consists of two-hardened columns, an adjustable crosshead, a load cell, two actuators (one tensile and one rotary), a one inch collect type grips, a FastTrack 8800© [77] controller (See Fig. 5.2a). For user interface, the system also contains two manual control panels (one for tensile and one for rotary control), and the FastTrack 8800© console computer.

The crosshead is a mounting platform for the load cell. The load cell measures load that is exerted on the test specimen. Resistance strain gages, attached to several points within the load cell, sense the mechanical load and convert the load into an electrical signal. Each load cell has a dedicated cable that contains self-identifying components that allow the test system to recognize the cell type and capacity, and to

perform automatic calibration. The FastTrack 8800© controller has biaxial capacities and it is equipped with advanced features such as adaptive tuning, and automatic transducer recognition. It allows the user to apply loads, through the actuators, to the test specimen. The controller additionally has the capacity to take input from the extensometers or strain gages so that strain-controlled tests can be conducted.

The servohydraulic testing system provides users with a choice between hardware based interface (two control panels) and the software based interface (FastTrack Console), shown in Fig. 5.2b. They are both designed to provide the main interface between the user and the servohydraulic control system. The control panels provide a fast, flexible option for straightforward testing without the need for a computer, and the associated fast track console software. They also provide an immediate feedback on current testing settings. The test conditions such as the real time load, position and strain status, number of cycles, warning and error signals and other information can be seen in a clear form on the control panels. The FastTrack console operates as a stand-alone software based interface to the material test control system. FastTrack console provides real time displays and icons for test system configuration and parameters settings [76] on a personal computer. The FastTrack console screen is always visible, with the area beneath it being occupied by the selected FastTrack application such as LabView™ [76] used for low cycle fatigue tests.

The experimental results can additionally be obtained using a suitable data acquisition system. For data acquisition during the test, one or more high speed data acquisition units (DAU) can be fitted within the tower version of the FastTrack 8800© controller, and each provides up to eight additional channels. The DAU card incorporates

direct current (DC) excitation for sensors, and allows connections of a range of sensor sensitivities from ± 10 mV to ± 10 V [77]. For the software based interface, each axis within the controller has a separate Integrated Axis Controller (IAC) board. The IAC can have up to four Sensor Conditioner Modules (SCMs) mounted on it in order to obtain feedback signals required by the controller, and to obtain data from the tests. The outputs from the SCMs can be read directly on the PC [77].

5.1.2 Optical Strain Measurement

In order to experimentally assess the developed models, the strains at the point of highest stress concentration in the test specimens resulting from the applied loads are required. As noted in Chapter Two, measuring strains at sharp notch roots is almost impossible using the conventional strain gages. Even with relatively large notch root radii, very small size strain gages that can be tedious to install, are required to minimize errors associated with using a finite gage length. In this research, a 3D image correlation device, produced by GOM* in Germany, referred to as Aramis© [69], was used to measure the surface strain fields in the vicinity of notch roots. The Aramis© consists of two CCD cameras (for capturing images), a tripod stand (on which the cameras are mounted), and a personal computer (for data acquisition, image processing, and user interface). Figure 5.3 shows the set up of the Aramis©. All the Aramis© operations (i.e. measurement, evaluation, display, and print functions) are controlled by the software associated with the equipment.

* GOM is the acronym for (Gesellschaft für Optische Messtechnik,), the German name for the company that produces the Aramis.

Specimen preparation is a vital starting point of any test using the Aramis© as a strain measuring device since it directly affects the quality of the measurement. To measure the 3D deformations and surface strains, a random or regular pattern with good contrast is first applied to the area of the specimen under investigation. To insure the adherence of the pattern to the area, before applying the pattern, the area must be polished and washed with solvent, to form a nearly mirror-like surface. In doing so, care must be taken so as to not allow scratches on the surface of the specimen while polishing. A typical pattern consists of a white dye penetrant developer, and black spray paint. The white dye is applied first, allowed to dry, then followed with very black spray paint. The pattern should exhibit a high contrast to the surface otherwise the matching of the captured images, from which the displacements and the surface strains are obtained, cannot be carried out correctly [70]. For good matching, it is essential that the pattern does not exhibit any large areas of constant brightness.

As the loads are applied, the pattern deforms with the test specimen. An image of the deforming pattern is then captured either manually or automatically at desirable load or time intervals by a pair of high resolution digital cameras. The two high resolution CCD cameras enable the 3D image correlation system to register the 3D shape of the object. The initial image processing defines unique correlation areas known as macro-image facets, typically 5-20 pixels square across the entire imaging area. The center of each facet is a measurement point that can be thought of as an extensometer or a strain rosette. The Aramis processes and visualizes the data gathered in order to obtain an impression of the distribution of strains in the object. It recognizes the surface of the specimen in digital images, and attributes coordinates to every pixel in the image. The

system tracks the stochastic pattern applied to the measured surface with sub-pixel accuracy [70]. Hence localized deformation can be tracked as long as the test specimen remains within the cameras field of view. Using photogrametric principles, described in [69], and image processing, the specimens 3D coordinates, the 3D displacements, and surface strains are automatically calculated using the associated software during the post-processing stage.

It is important to state that 3D image correlation does not measure 3D strains. The exact measurement being made is the 3D shape of the object. The out of plane coordinate at each gage point is determined by triangulation using the two calibrated CCD cameras (shown in Fig. 5.3). By subtracting subsequent deformed shapes from a reference shape, 3D displacements are determined. Differentiating these displacements yields the planar strain tensor. GOM also produces a 2D image correlation system that uses only one camera. The 2D image correlation can also be used to measure planar strains. However, there are some critical constraints on the use of 2D image correlation to determine in-plane strains. Imagine a solid circular mark viewed by one camera, if the circle undergoes biaxial tension, it will increase in diameter. The camera will detect this increase, and will report the strain. However, the circle simply moves closer to the camera, hence, it will also appear larger, and therefore a false strain will be reported. In addition, the 2D image correlation is not capable of measuring out-of-plane displacements, and it is also subject to significant strain offset errors in the presence of out-of-plane deformations. Similarly, unless the test object is flat and normal to the camera lens, there will be errors caused by a varying magnification factor across the field of view. Consequently, the purpose of using 3D image correlation is not to measure through-thickness strains, but to ensure that

out-of-plane displacements do not cause errors in the in-plane strain data. There are two methods that can be used to measure through-thickness strains [78]. The first method is to use a second camera set looking at the thickness (edge of the specimen) while simultaneously looking at the front of the specimen using the first camera. The second method is to use the constant volume assumption. In doing so, the quantity thickness reduction, obtained during post-processing represents the out-of-plane strain. The second approach is very suitable for an isotropic material with a uniform cross-section thickness.

5.1.3 Point Strain Measurement

In addition to strain field measurements, point strain measurements were made in verification tests using strain gages. Fundamentally, all strain gages are designed to convert mechanical displacements into an electrical signal. Strain gages provide accurate, repeatable, electrical signals proportional to the surface displacements/strains in the test specimen. Strain gages can be used either singly (uniaxial gage, with a single grid for measuring strain in the grid direction), or in groups (referred to as rosettes). A rosette is a collection of two or more gage elements on a single backing. In this research, Vishay Micro-Measurements[†] strain gages (CEA-06-125UR-120) [79], shown in Fig. 5.4, were affixed to the specimen. These three-element rosettes, with three independent grids oriented at 0, 45, and 90 degrees, are general purpose gages suitable for use in fatigue analysis. They are suitable for determining the principal strains and their directions, and the three independent components of plane strain. Three-element rosettes have a strain

[†] Vishay Micro-Measurements produces an extensive range of devices for precision measurement of mechanical strains, including bondable strain gages, installation accessories and instrumentation.

limit of approximately 3% for gage length that is less than 3.2 mm, and 5% for a gage length that is greater than or equal to 3.2 mm. They have a nominal resistance of 120 Ohms, and can operate at a temperature between -75°C and +175°C.

Proper boding of the strain gage on the test specimen is a very vital step of any test using a strain gage for strain measurement. The test specimen is cleaned and abraded, if necessary, where the strain gage is to be affixed. An adhesive (M-Bond 200) is used to bond the strain gage to the specimen, with the grids in the directions of the strains to be measured. Electrical leads are attached to the solder tabs on the strain gage. It is important to measure the base resistance of the unstrained strain gage after it is mounted. A properly bonded unstrained gage will have an electrical resistance that is equal to the nominal resistance specified by the manufacturer.

During the test, the strain gage deforms with the specimen. This deformation changes the resistance of the strain gage in proportion to the strain sensitivity (also known as the gage factor,) of the grid's resistance. The gage factor, usually provided by the strain gage manufacturer as the nominal value with its tolerance, is the proportionality factor between the relative change of the resistance. For the three-element rosettes used in this research, the gage factor is given as 2.080 ± 0.5%. The grid shape is designed to provide maximum gage resistance while keeping both the length and width of the gage to a minimum.

To measure small changes in resistance of the strain gages, strain gages are almost always connected to an electrical circuit that is capable of amplifying the minute changes. In this research, the gage output signal was amplified using Vishay 2100 signal conditioners [80], shown in Fig. 5.5a. These conditioners are designed to accept low-level

signals from strain gages and amplify them into high-level outputs suitable for display or recording on external equipment (the data acquisition system). For this purpose, the signal conditioners have a Wheatstone bridge with four resistors (R_1, R_2, R_3, and R_4), constant voltage input, V_0, and a voltage output meter, E (usually expressed in millivolts output per volt input), electrically connected as illustrated in Fig. 5.5b. Any of the four resistors can be connected to an active strain gage. Resistors that are not connected to an active strain gage are referred to as completion resistors. The strain gages, however, can occupy one (referred to as quarter-bridge circuit), two (referred to as half-bridge circuit), or four (referred to as full-bridge circuit) arms of the bridge, depending on the application.

Measuring the elongation directly on the gage section of the test specimen with resistance strain gages can be advantageous. However, in some tests, an alternative strain measurement technique may be required for data comparison and verification purposes, and/or for measuring strains greater than those that can be obtained using strain gages. A displacement/strain measurement device that contacts the gage section of the test specimen via a pair of arms, referred to as extensometer, is commonly used. An Instron dynamic strain gage extensometer (2620-601 Series) [81], shown in Fig. 5.6, was employed in this research to measure the axial displacements of the specimens used for the set-up verification tests. The extensometer is a lightweight strain gage that can be used during tensile or compressive test, and low or high cycle fatigue test. It is designed for use with metals, composites, plastics, wood etc. The extensometer has a 12.5 mm gage length with a full scale displacement range of ± 5 mm and a maximum strain of ± 40%. It includes a 12.5 mm extender to give a gage length of 25 mm and a maximum

strain of ± 20%, and a 37.5 mm extender to give a gage length of 50 mm and a maximum strain of ±10%. These extensions enhance test repeatability. The extensometer has a wide frequency response and high accuracy for use in both tension and compression, and can be operated over an ambient temperature range of -80°C to +200°C [81]. The arms usually have sharp edges and are pressed lightly against the specimen, which causes the arms to maintain good contact with the gage section during the test. Generally, the extensometer is clamped to the test specimen gage section with special high-tear strength rubber bands or with tension springs, and it is pulled tight enough to prevent knife edge slippage during specimen testing. As the specimen deforms, the displacement of the arms is recorded and can be related to strain.

To complete a strain measurement using the strain gage or the extensometer, the output signals must be recorded accurately. This can be achieved by using individual strain indicators, strain indicators combined with switch boxes, or data acquisition systems. In this research a data acquisition system, detailed in the following section was used.

5.1.4 Data Acquisition System

Advancements in the productions of analog-to-digital converters and personal computers have led to a wide variety of computer-based data acquisition systems. Data Acquisition systems can be used to automate experiments, obtain experimental data, and monitor and control experimental equipment. The data acquisition system used in this

research consists of a PCI-DAS6402/16 board [82], and a personal computer with data acquisition software.

Analog output signals from the load frame, the signal conditioners, and trigger signals from the digital cameras of the optical strain measurement device are channeled to the data acquisition board. The board acts to digitize the signals for computer analysis and control. It also accepts either 32 differential or 64 single-ended input channels.

The data acquisition software consists of three software packages: Instacal [83], Universal Library [84], and Agilent Vee OneLab [85] that are installed in the data acquisition computer. Instacal [83] is used to simplify the installation, calibration, and testing software as the PC is turned into a measurement system. It furthermore detects new hardware and configures the computer for the board. The Universal Library [84] provides the computer with complete access to the board's function using a range of programming languages.

The programming software used in this research was Agilent Vee OneLab [85]. It is a graphical programming optimized for use with electronic instruments. The Agilent user program, used to control and collect data, is made by placing graphical blocks on a window interface and connecting them together with lines. This serves as a program code for a specific function. The created blocks are then run. The Vee objects can be used for a variety of tasks which include mathematical operations, reading of files, and displaying of microwave spectral. The I/O menu in the program interacts with software and hardware outside the Vee applications. It includes object that communicates accurately with the instruments, files, printers and other processes. The objects in the data menu declare, generate, and access data, while the display menu allows the viewing of the data.

5.2 Test Specimens

The PMMCs used in this research are general purpose Duralcan[‡] materials made of 6061 aluminum alloy reinforced with 10 and 20% by volume alumina (Al_2O_3). The Aluminum Association MMC nomenclature designation for the material is 6061/Al_2O_3/xxp, with xx representing the volume fraction of particles, p. The reinforcing phase for both 10 and 20% volume fraction composite used in this research is a calcined Al_2O_3 powder. The chemical composition of the powder is at least 98.5% Al_2O_3 and the median particle size distribution is 11.0 ± 1.5 μm and 20.8 ± 6.0 μm for the 10 and 20% volume fraction respectively. The powder tends to have a platelike morphology with approximate 3 to 5:1 aspect ratio. The PMMCs used were produced using a wrought process where a molten slurry is poured to an extrusion billet, rolling bloom or rolling ingot. The Duralcan billet was extruded by a company called QED Extrusion Developments located in San Diego, CA, USA. In order to be compatible with the grips on the load frame, both materials were extruded at 350°C to form 1 inch (25.4 mm) solid rods. After extrusion, the rods were heat-treated to T-6 condition (a form of heat treatment of a material that results in maximum tensile and yield strengths with adequate elongation in the material). The chemical compositions of the extruded materials as supplied by [86] are shown in Table 5.1. Micrographs of the rods after extrusion are shown in Fig. 5.7 (a-b). The mechanical properties of the unreinforced alloy, and the reinforced rods are given in Table 5.2. From Table 5.2, it can be observed that the

[‡] DURALCAN, a Division of Alcan Aluminium Ltd., produces and markets the DURALCAN family of PMMCs.

ultimate strength, yield strength, and elastic modulus increase, while the elongation decreases with increasing volume fraction of reinforcing particles.

For the purpose of validating different aspects of the research, four different specimen types were machined. These include: smooth solid specimens (Fig. 5.8), smooth tubular specimens (Fig. 5.9), mild notched specimens (Fig. 5.10), and relatively sharp notched specimens (Fig. 5.11). The dimensions of the smooth specimens were chosen based on the recommended specimen design specifications in ASTM standard E606 [87]. The smooth solid specimens were used for the tensile tests conducted to verify the test set-up, while the smooth tubular specimens were used to verify the suitability of the constitutive models presented in Chapter Three. The mild and relatively sharp notched specimens were used to assess the notch root elastic-plastic strain-stress estimation methods presented in Chapter Four.

5.3 Experimental Tests

In order to provide experimental validation to the theoretical developments outlined in Chapters Three and Four, several tests were performed that can be categorized into four groups:

a) Tests to provide confidence in the testing equipment for use on PMMCs.

b) Tests to assess experimentally the PMMCs constitutive models developed and presented in Chapter Three.

c) Test to obtain the elastic stress concentration factors for the notch geometries shown in Figs. 5.10 and 5.11.

d) Tests to assess the proposed notch root elastic-plastic strain-stress estimation methods, presented in Chapter Four.

5.3.1 Set-Up Verification Tests

Two verifications tests were performed in this research. The first test was employed to gain confidence in the results obtained using the Aramis, and the second test was performed to test the reliability of the testing equipment.

Although the developers of the Aramis have documented [70] the validation of their equipment, confidence in the results obtained using the device was obtained by comparing them with those obtained using other measuring devices such as strain gages and the extensometer. To achieve this, tensile tests were conducted on the smooth solid specimens (10 and 20% volume fractions of reinforcement). The strains were measured using three independent devices (Aramis©, strain gages, and extensometer) in the elastic range for the 10% volume fraction, and two independent devices (Aramis©, and strain gage) in the plastic range for both volume fractions. The extensometer was not used in the plastic range in order to avoid damaging the device. Note that the 20% volume fraction specimen test was conducted twice. The first test, which induced a small plastic deformation on the specimen, produced unreliable results, due to the data acquisition problem encountered during the test.

Figure 5.12 illustrates the setting of the devices on the test specimens; a random pattern was put on one end, a strain gage rosette was fixed on the other end, and an extensometer was clamped on the specimen. For each test, the strain gage signals were

amplified using the signal conditioners. Analog output signals from the load frame, the signal conditioners, and the extensometer were then channeled to the data acquisition board. Fig. 5.13 is the data acquisition system graphical program used to acquire the data.

In order to test the reliability of the testing equipment, three identical tests were performed on the 20% mild notched specimens. These specimens were subjected to a box-shaped load path (Fig. 5.14) using the load frame, and notch root strains were measured during the tests using the Aramis©. The box path was chosen since this 90° out-of-phase loading tests the limits of the ability of load frame to abruptly change from tension to torsion and furthermore, it is a critical verification test of any analytical models that addresses non-proportional cyclic loading.

5.3.2 Constitutive Models Validation Tests

To assess the capability of the two PMMCs constitutive models (described in Chapter Three) to predict the elastic-plastic constitutive behavior of PMMCs, several experimental tests were conducted on the hollow specimens shown in Fig. 5.9. It should be noted that for the verifications of any constitutive model, tubular specimens are normally used because they are more suitable for use for torsional and combined tensile-torsional tests than the corresponding smooth solid specimens. That is, the relationship between the applied torque, T, and the shear stress, τ, can easily be made for tubular specimens in both the elastic and the plastic regions than can be for solid specimens. For a round solid specimen subjected to a torsional load T that is large enough to induce

plasticity in the specimen, the shear stress, τ, within the elastic core, is linear, and therefore, can be obtained from,

$$\tau = \frac{16T}{\pi d^3}, \tag{5.1}$$

where d is the specimen diameter. However, the shear stress distribution at the outer region, that experiences the highest shear stress, is nonlinear. Consequently, the shear stress distribution in the outer region cannot be obtained from the applied torsional load using Eq. (5.1). It can only be obtained by using an approximate method. On the other hand, in the case of a smooth tubular specimen subjected to a torsional load, a uniform shear stress and strain distribution is often assumed across the wall thickness for a sufficiently thin wall. Using the thin-wall assumption, the shear stress distribution in a tubular specimen has been obtained in [2] and [88] as:

$$\tau = \frac{T}{2\pi r_m^2 t}, \tag{5.2}$$

where r_m and t are the mean radius and wall thickness respectively. Equation (5.2) is applicable both to elastic and elastic-plastic material behavior in the outer region. The shear stress obtained in Eq. (5.2) is normally considered to correspond to the strain at the mid-surface of the smooth tubular specimen. Consequently, the smaller the wall thickness of the specimen, the higher the accuracy of the results obtained.

For the constitutive model verifications, if the smooth tubular specimen is subjected to an axial load P, the stress distribution is uniform. It can be obtained from,

$$\sigma = \frac{4P}{\pi\left(d_o - d_i\right)^2}, \tag{5.3}$$

where σ is the is uniform axial stress, and d_o and d_i (shown in Fig. 5.9) are the outer and inner diameters of the tubular specimen in the gage section respectively. It should be noted that Eq. (5.3) applies to both elastic and elastic-plastic material behavior.

Four different load paths shown in Fig. 5.15 to Fig. 5.17 were used. The load paths include: a proportional load path (Fig. 5.15), two variable amplitude non-proportional load paths (Figs. 5.17 a-b) and one non-zero mean stress load path (Fig. 5.17). Similar shaped load paths have been used by several researchers ([2], [6], [34], [89]) to verify the constitutive models developed for metals. In these tests, the strains were measured using the Aramis© in the gage section.

5.3.3 Elastic Stress Concentration factors Determination Tests

To obtain the stress concentration factors of the mild and relatively sharp notched specimen, two tensile tests, and two torsional tests were conducted with the loads applied in the elastic range. The applied loads were sufficient to produce the elastic deformations in the specimens. In these tests, the strains at the notch roots of the specimens were measured using the Aramis©. Knowing the applied loads, and the notch root strains, the stress concentration factors in the various directions were obtained as outline below.

Following the notation in Figs. 5.10, and 5.11, for the tensile tests, when the load (P) is applied to the specimen in the elastic range in the axial (2) direction, it results in

elastic notch root axial, σ_{22}, and hoop, σ_{33}, stresses. The elastic axial (K_{t22}) and hoop (K_{t33}) stress concentration factors can be found using:

$$K_{t22} = \frac{\sigma_{22}}{\sigma_{n.s}}, \tag{5.4}$$

and,

$$K_{t33} = \frac{\sigma_{33}}{\sigma_{n.s}}. \tag{5.5}$$

In Eqs. (5.4) and (5.5), $\sigma_{n.s}$ is the net sectional nominal axial stress obtained by using:

$$\sigma_{n.s} = \frac{4P}{\pi d^2}, \tag{5.6}$$

where d is the net section diameter, shown in Fig. 5.10, and 5.11. The local stresses, σ_{22} and σ_{33} are obtained using the material constitutive model and the strain results from the Aramis© for a particular load (P) applied to the specimen.

If a torsional load (T) is applied to the end of the specimen in the elastic range, it results in elastic notch root shear stress, σ_{23}. The shear stress concentration factor can be determined from:

$$K_{t23} = \frac{\sigma_{23}}{\tau_{n.s}}, \tag{5.7}$$

where $\tau_{n.s}$ is the net sectional nominal torsional stress that can be obtained from Eq. (5.1) , with $\tau = \tau_{n.s}$, and d, being the net section diameter, and σ_{23} obtained from the material constitutive model and strain results from the Aramis© at the torque (T).

5. 3.4 Notch-Root Parameters Validation Tests

The primary objective of the experimental tests was to demonstrate the validity of the proposed models to predict the notch root strains and behavior of the material for a variety of load paths. The mild and the relatively sharp notched specimens were tested using a variety of load-controlled tests conducted on the tension-torsion load frame, and the strains were measured using the Aramis©. Prior to each tests, a random speckle pattern was applied to each specimen as shown in Fig. 5.18. The specimens were subjected to both monotonic and cyclic (proportional and non-proportional, constant and variable amplitude) load paths applied in load control on the load frame. For the cyclic load paths, cycles were applied until stabilized material behavior was observed. All load paths were chosen to induce notch root plasticity. Some of the load paths tested in this research, summarized in Table 5.3, are discussed briefly below.

5.3.4.1 Non-Proportional Monotonic Loading

The mild notch specimens (one each for 10 and 20% volume fractions of

reinforcement) were subjected to torsional and combined torsional and tensile loads applied in a non-proportional manner as shown in Fig. 5.19.

5.3.4.2 Proportional Cyclic Loading

One axial-torsional in-phase load path was tested for each volume fraction and notched specimen geometry. The in-phase load path is shown in Fig. 5.15.

5.3.4.3 Non- Proportional Cyclic Loading

Non-proportionally applied external loads are usually found to be more damaging than in-phase (proportional) loads with identical von-Mises effective stress amplitudes. A variety of non-proportional load paths, described below, were tested in this research.

a) Constant Amplitude Non-Proportional Loading:

The constant amplitude load paths tested were divided into two categories and are divided into i) and ii) below:

i) Balanced loading with equal frequencies: A balanced load path is a load path with a zero mean stress. For balanced loading tests, three load paths of different shapes, but with constant amplitudes and equal frequencies of the axial and torsional nominal loads were tested for the mild notched specimens. These load paths tested for the mild notched specimens included the box-shaped load path (Fig. 5.14), the rhombic-shaped load path (Fig. 5.20 a), and the star-shaped load path (Fig. 5.20 b). Relatively sharp notched specimens

made of both volume fractions of reinforcement were subjected to one box-shaped load path.

ii) Balanced loading with unequal frequency: Non-proportional loading due to unequal frequencies of applied load is a common load path in machine components [59]. Three balanced load paths, of different shapes, with unequal frequencies were tested for each volume fraction of reinforcement of the mild notched specimens. The selected load paths are shown in Figs. 5.21 (a-c). In the first and the second load paths (Figs. 5.21a-b), three cycles of the torsional load were applied in the same time period for one cycle of the tensile load. In the third load path (Fig. 5.21c), five cycles of the torsional load were applied in the same time period for one cycle of the tensile loads. In all the load paths, the load levels corresponded to the most severe box-shaped load paths.

b) Unbalanced Loading/Non-Zero Mean Stress

An unbalanced loading is a load path with a non-zero mean stress. A particularly difficult problem for non-proportional deformation modeling is multiaxial ratcheting. Cycling about a non-zero mean load induces ratcheting (i.e. increasing strains with constant amplitude nominal load paths). In order to discuss the ratcheting behavior of the material at the notch root under non-proportional multiaxial loads, the notched specimens were tested using two different load paths for each volume fraction of reinforcement. The load paths used are shown in Figs 5.22 (a-b).

For the elliptical load paths (Fig. 5.22a), the loading case kept a symmetric axial stress cycling with a constant equivalent normal stress amplitude. The shear stress

cyclic history was given a mean stress with constant amplitude. For the linear load path (Fig. 5.22b), the torsional load was monotonic with a constant equivalent shear stress. The axial load was cyclic with constant amplitude and a zero mean stress.

c) Variable Amplitude Loading

Extension of the experimentally verified domain of the models to the more-complex case of variable amplitude non-proportional loading was also investigated. Non-proportional variable amplitude loading type is the most general loading. Multiaxial deformation at the notch root was investigated by employing the non-symmetric load paths shown in Fig. 5.23 (a-b).

5.4 Summary of Chapter Five

This chapter described all the facilities used in the experimental program developed and implemented in this research. Several load paths were considered. The results obtained using the experimental program presented in this chapter, and the numerical results obtained using the models presented in Chapters Three and Four, are presented and compared in Chapter Six.

Table 5.1: Chemical Compositions of 6061 Alloy (Source: [86])

Si	Fe	Cu	Mn	Mg	Cr	Zn	Ti	Other Elements	Al
0.40-0.80	0.70 Max	0.15-0.40	0.15 Max	0.80-1.20	0.04-0.35	0.25 Max	0.15 Max	0.15 0.05 Max	Remaining

Table 5.2 Tensile Properties of Extruded Rods
(Typical and Minimum Values* (Source: [86])

Material	Ultimate Strength (MPa)	Yield Strength (MPa)	Elastic Modulus (GPa)	Elongation (%)
6061-T6	310 (262)	276 (241)	69	20
6061/Al_2O_3/10p	352 (324)	296 (262)	81	10
6061/Al_2O_3/20p	372 (345)	352 (317)	97	4

*Minimum values represent 99 % confidence interval.

Table 5.3: Summary of Notched Specimens Load Paths

Load Type	Number of mild notch Specimens (V_f = 10%)	Number of mild notch specimens (V_f = 20%)	Number of relatively sharp notch specimens (V_f = 10%)	Number of relatively sharp notch specimen (V_f = 20%)
Monotonic Loading	1	1	-	-
Repeatability tests		3	-	-
Proportional Loading	1	1	1	1
Balanced Non-Proportional Loading (equal frequency)	3	3	1	1
Balanced Non-Proportional Loading (Unequal frequency)	3	3	-	-
Non-zero mean stress	-	-	2	2
Variable amplitude Loading	-	-	1	1

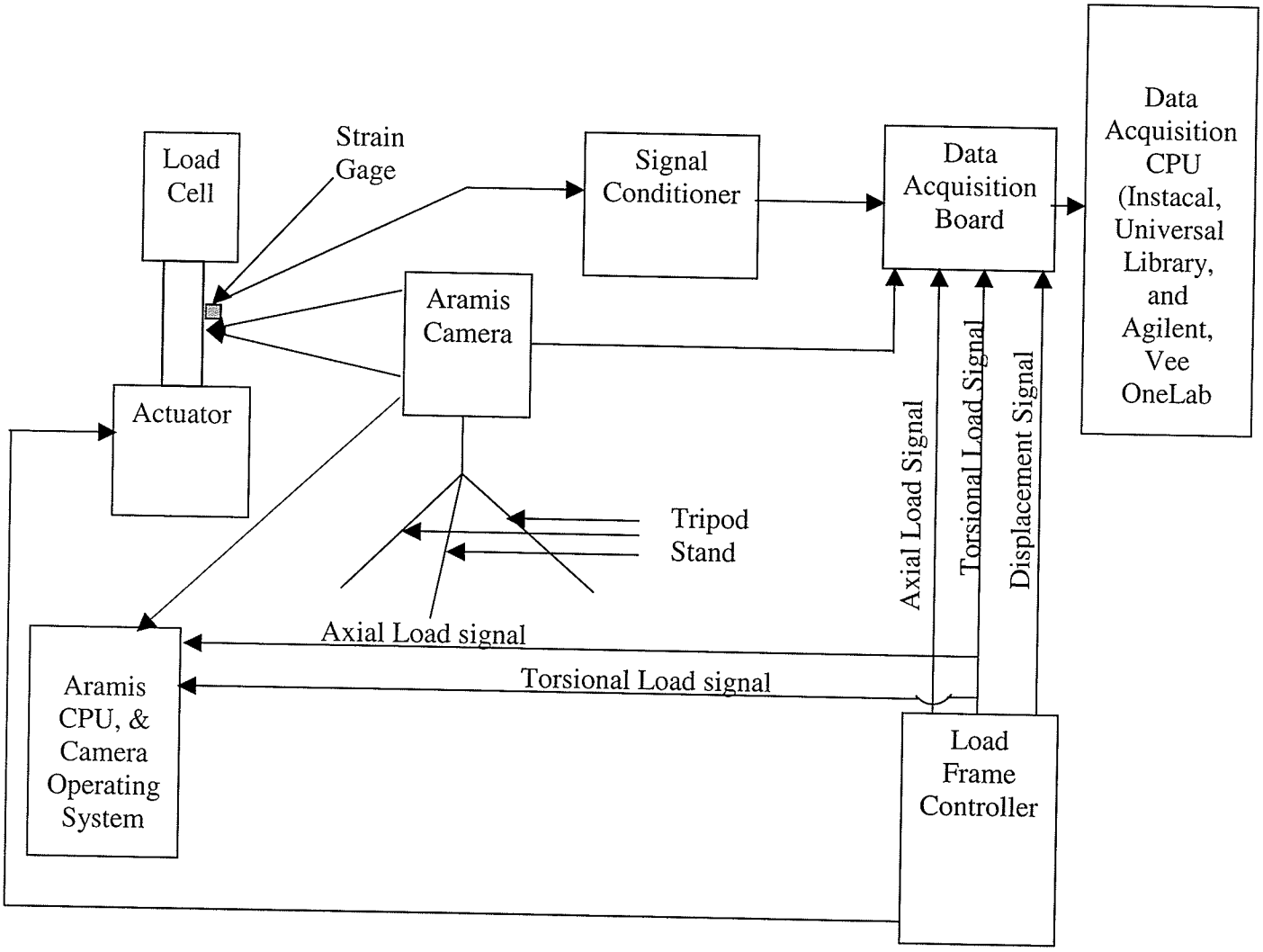

Figure 5.1: Experimental Set Up

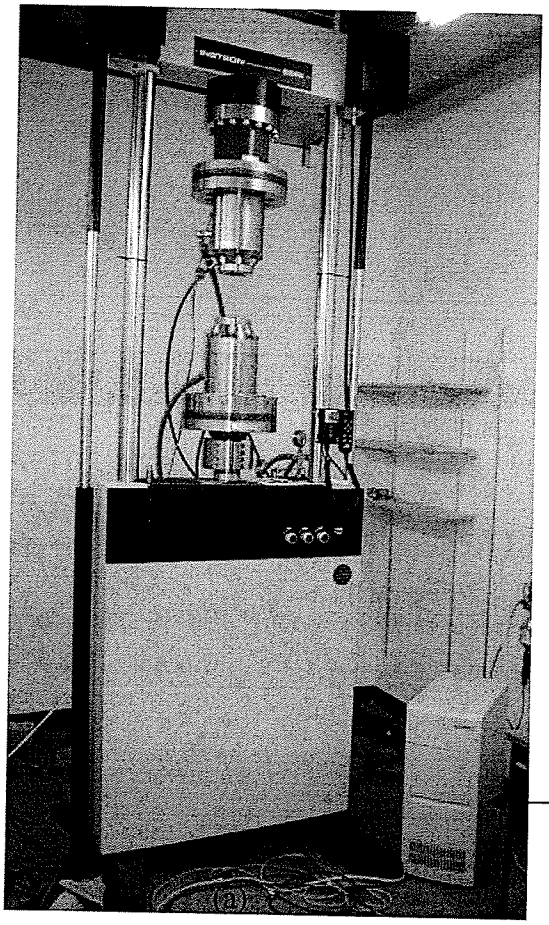

(a)

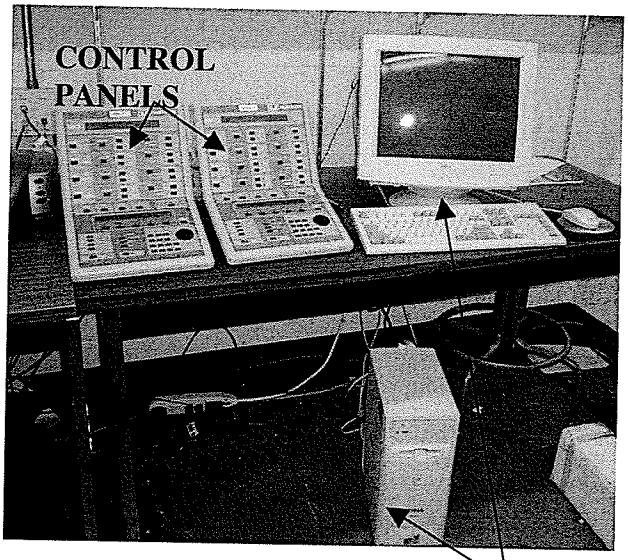

Figure 5.2: Servohydraulic System (a) Load Frame and Controller (b) Hardware and Software Interfaces

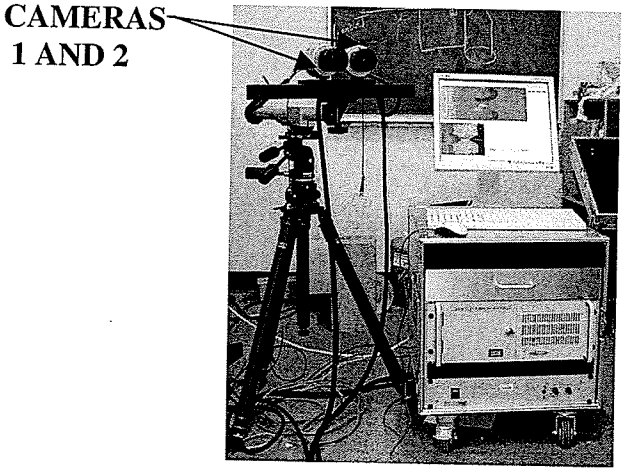

Figure 5.3: Optical Measuring System

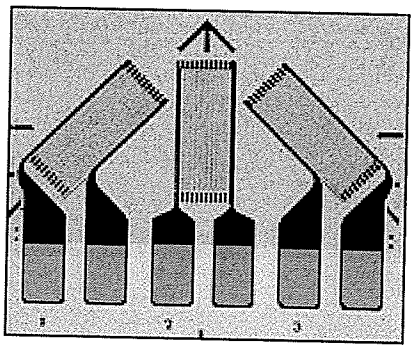

Figure 5.4: A Three-Element Rosettes Strain Gage

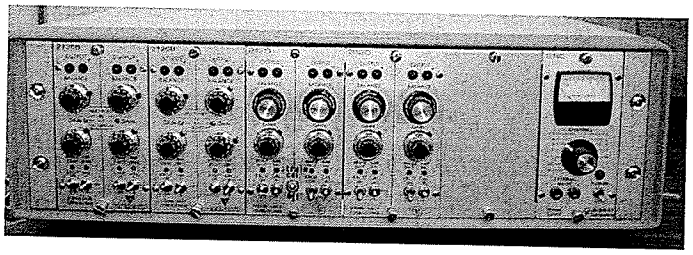

(a)

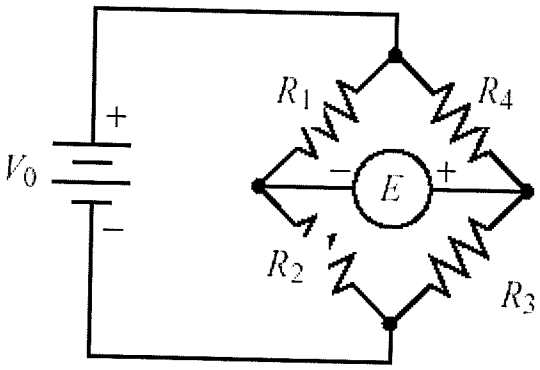

(b)

Figure 5.5: Signal Conditioners and Circuit (a) 2100 System Signal Conditioner/Amplifier (b) Wheatstone Bridge Circuit

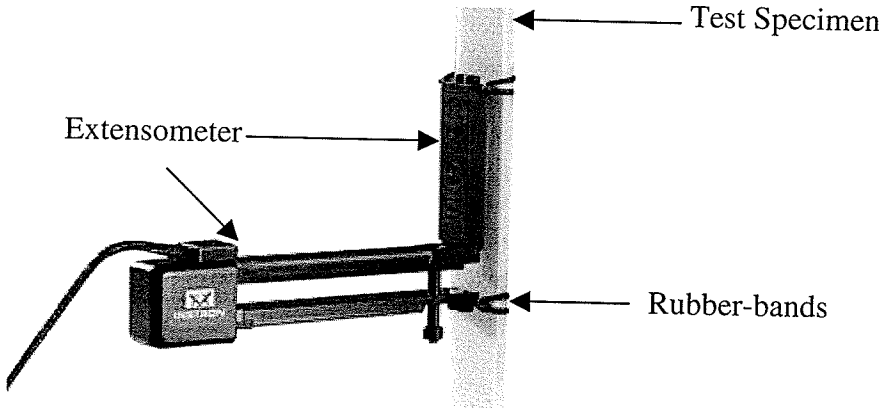

Figure 5.6: 2620 Series Instron Dynamic Extensometer

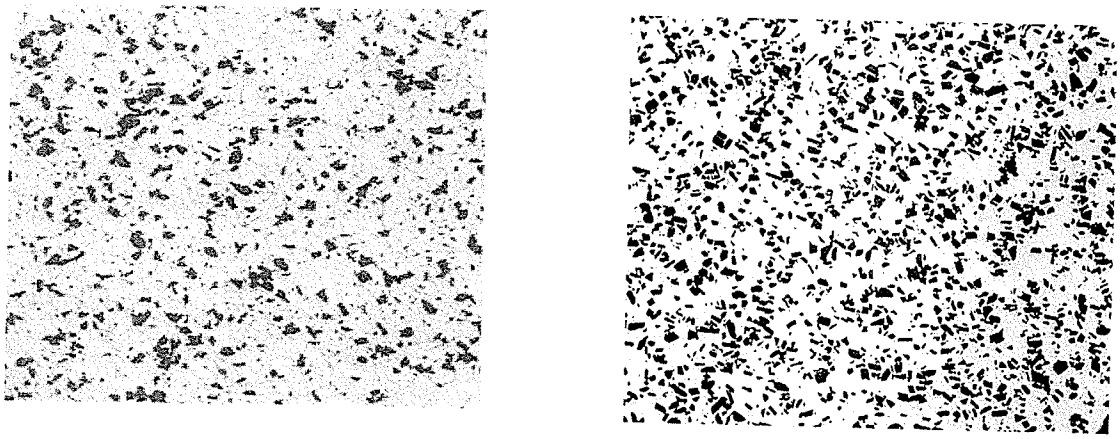

(a) (b)

Figure 5.7: 6061/Al_2O_3/xx-T6 PMMCs Monographs (a) 10 % Al_2O_3 200X (b) 20 %Al_2O_3, 100X

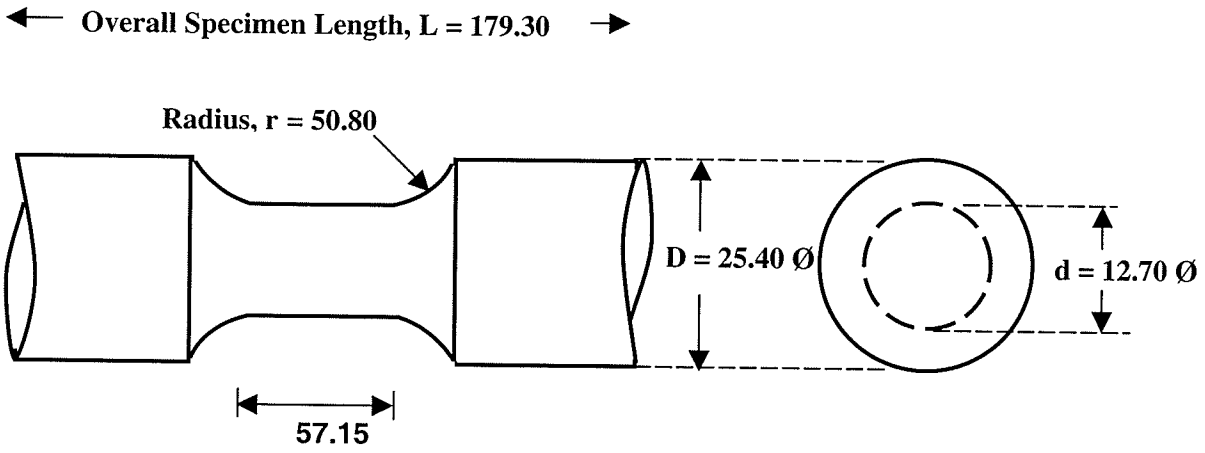

Figure 5.8: Geometry of the Smooth Solid Specimen (All dimensions in mm)

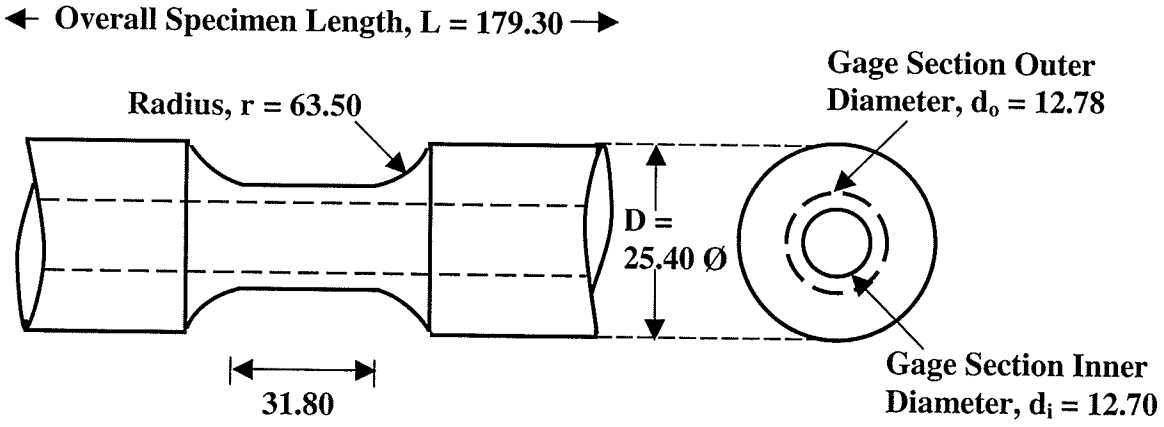

Figure 5.9: Geometry of the Smooth Tubular Specimen (All dimensions in mm)

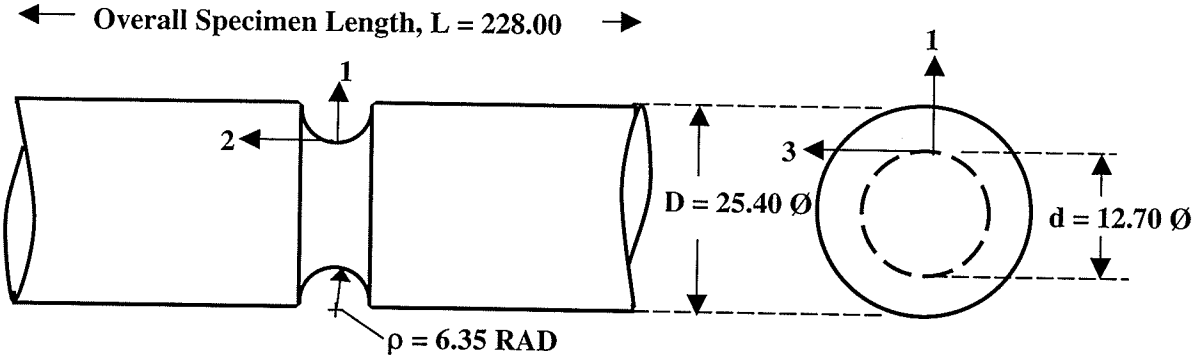

Figure 5.10: Geometry of the Mild Notched Specimen (All dimensions in mm)

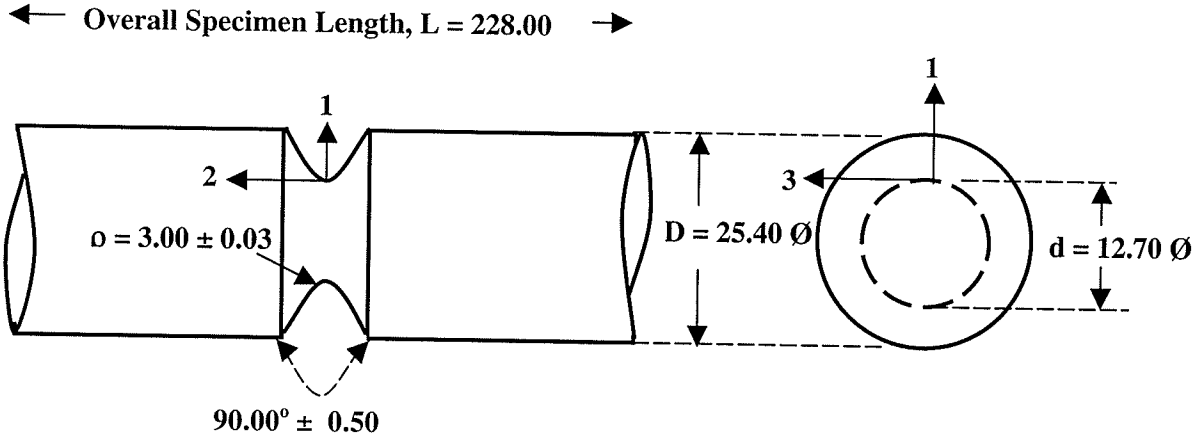

Figure 5.11: Geometry of the Relatively Sharp Notched Specimen (All dimensions in mm)

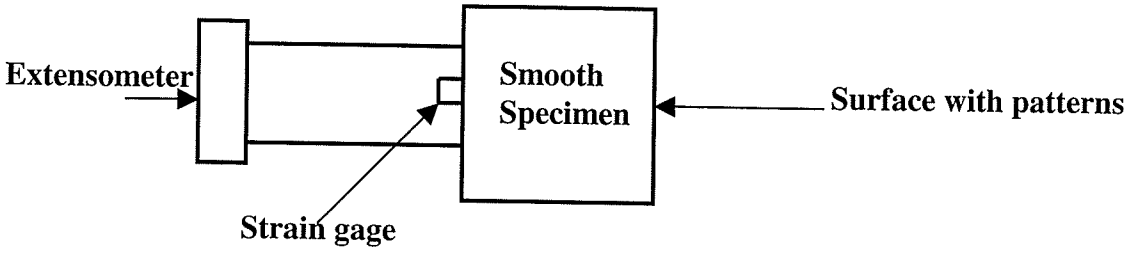

Figure 5.12: Strain Measurements using Three Independent Measuring Devices

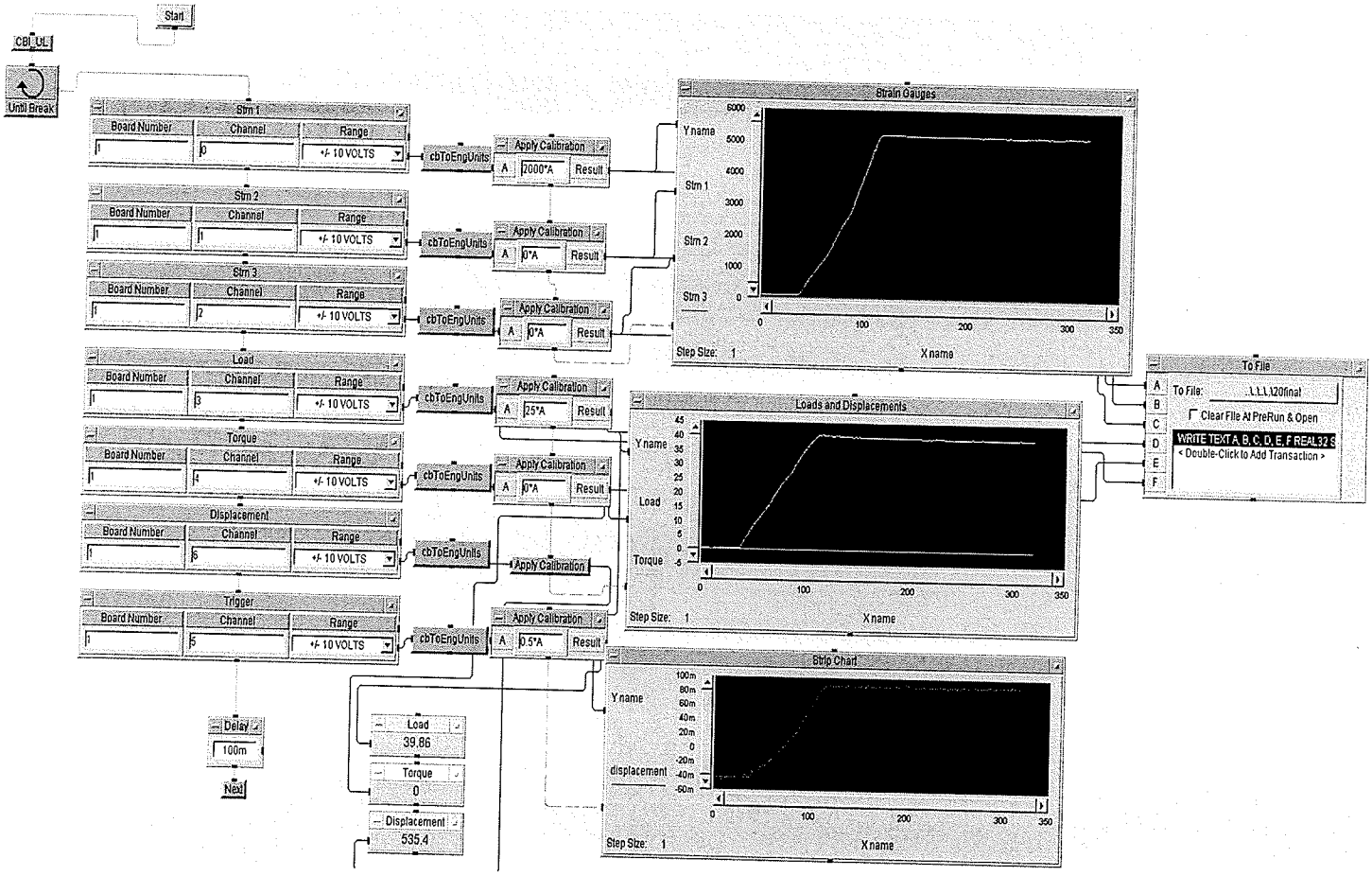

Figure 5.13: Data Acquisition Graphical Programming Flow Chart.

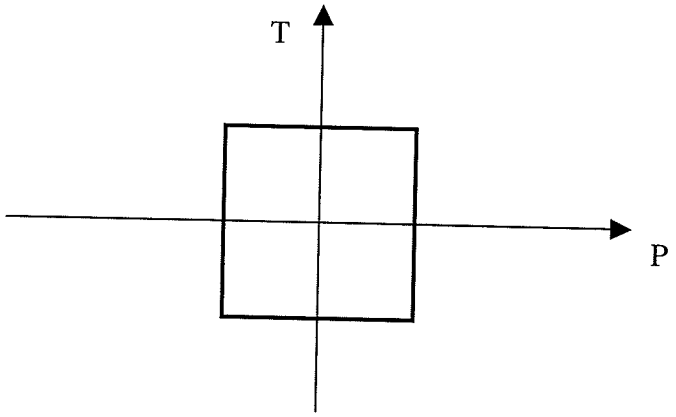

Figure 5.14: Box-Shaped Cyclic Non-Proportional Load Path

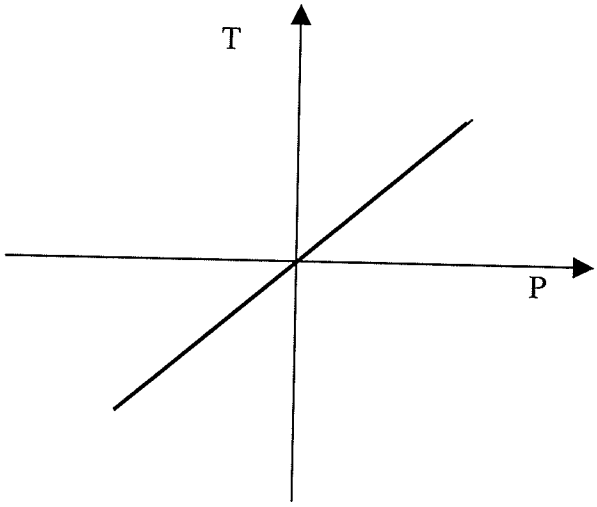

Figure 5.15: Cyclic Proportional Tension-Torsion Load Path

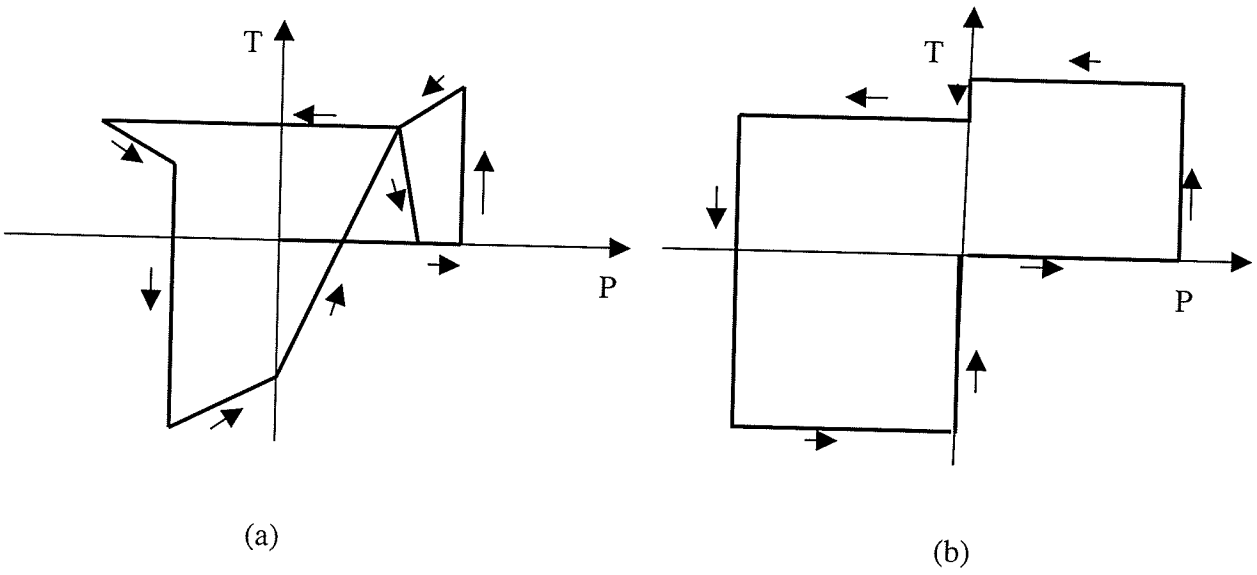

Figure 5.16: Variable Amplitude Non-Proportional Loading (a) Path 1 (b) Path 2

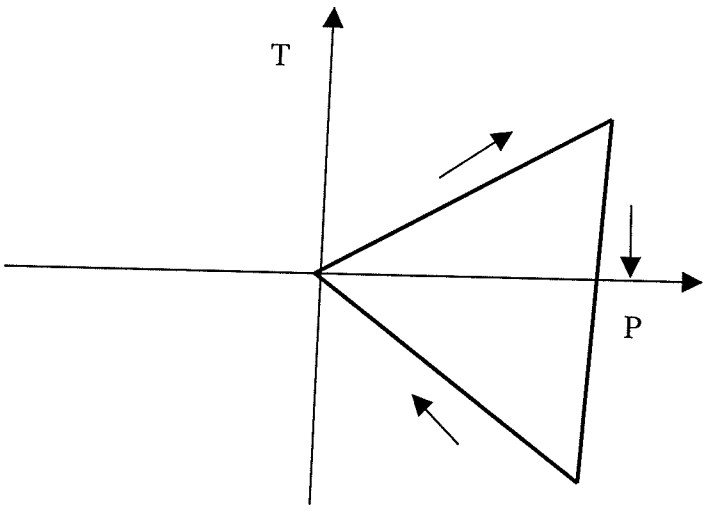

Figure 5.17: Triangular-Shaped Non-Zero Mean Stress Load Path

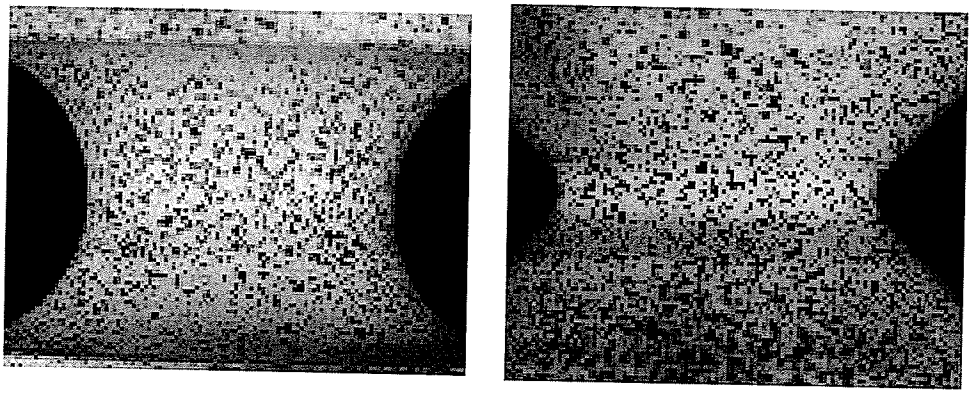

(a) (b)

Figure 5.18: Notched Specimen with Random Patterns (a) Mild Notch (b) Relatively Sharp Notch

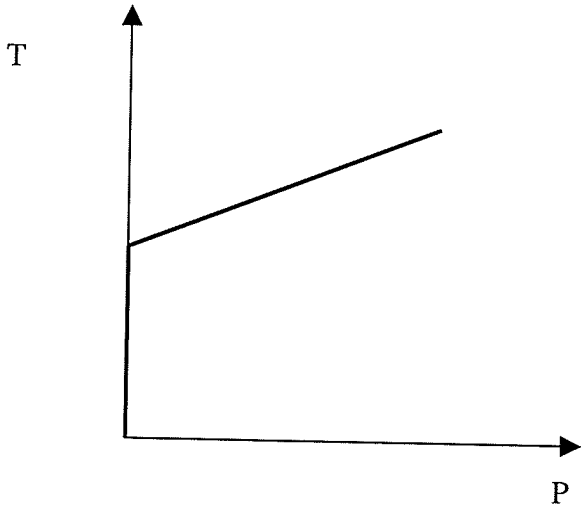

Figure 5.19: Monotonic Torsion-Combined Tension-Torsion Load Path

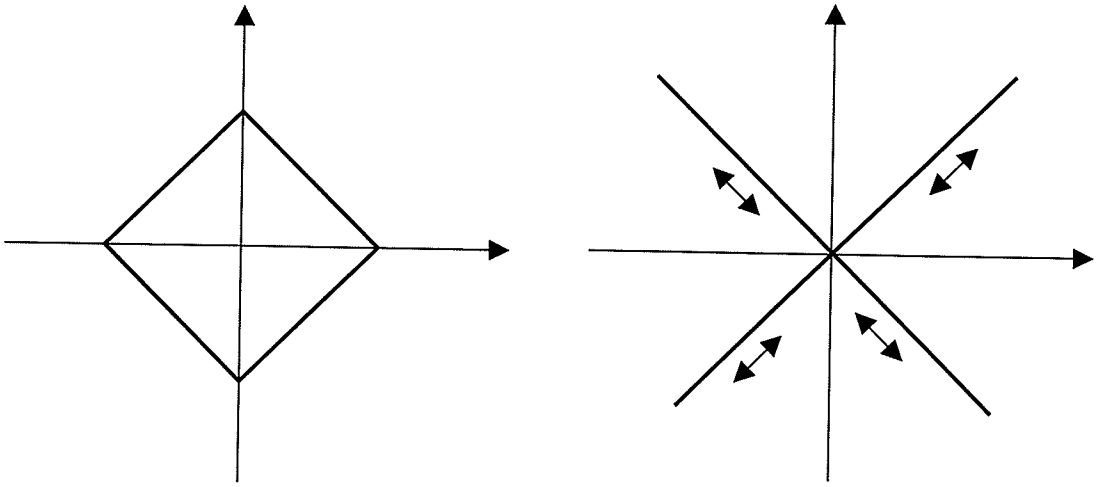

(a) (b)

Figure 5.20: Balanced Loading with Equal Frequencies in Torsion and Tension
(a) Rhombic-Shaped Load Path (b) Star-Shaped Load Path

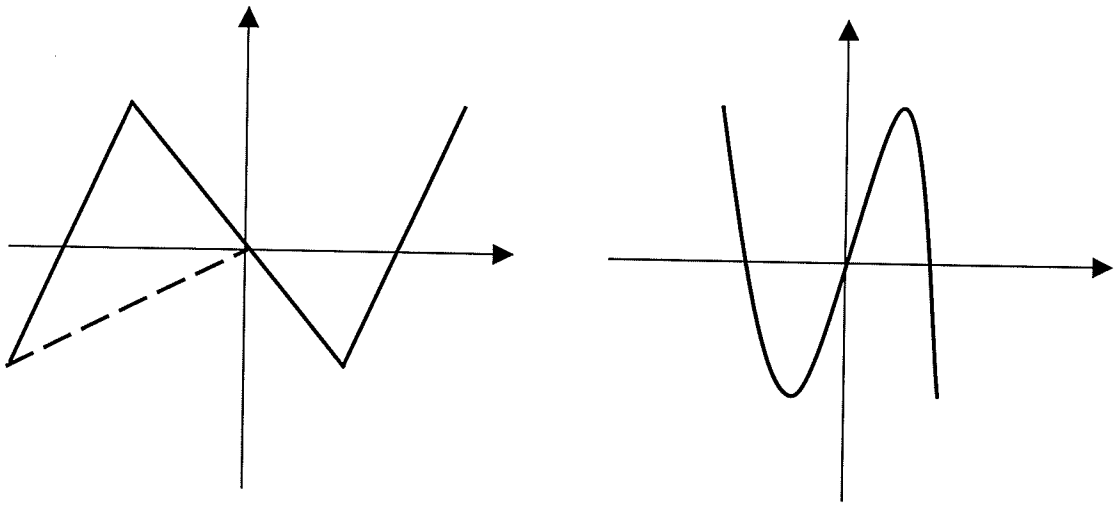

(a) (b)

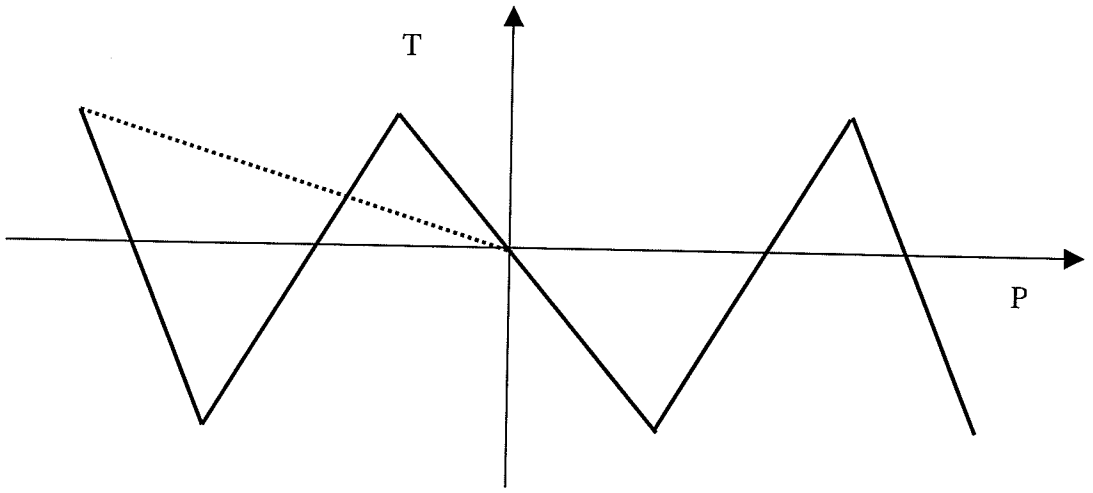

(c)

Figure 5.21: Balanced Load Paths with Unequal Frequencies (a) Tension-Torsion Ratio of 1:3 (b) Tension-Torsion ratio of 1:3 (Sine Wave) (e) Tension-Torsion ratio of 1:5

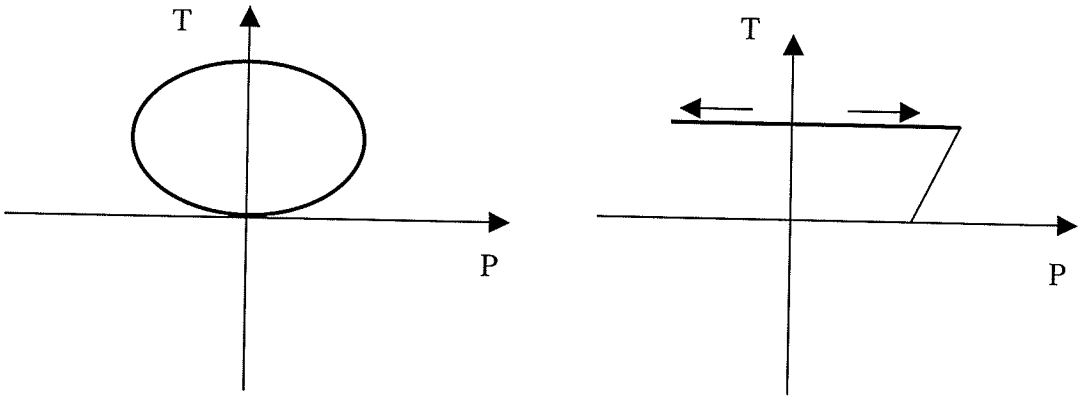

(a) (b)

Figure 5.22: Non-Zero Mean stress Load Path (a) Elliptical-Shaped Load Path (b) Linear-Shaped Load Path

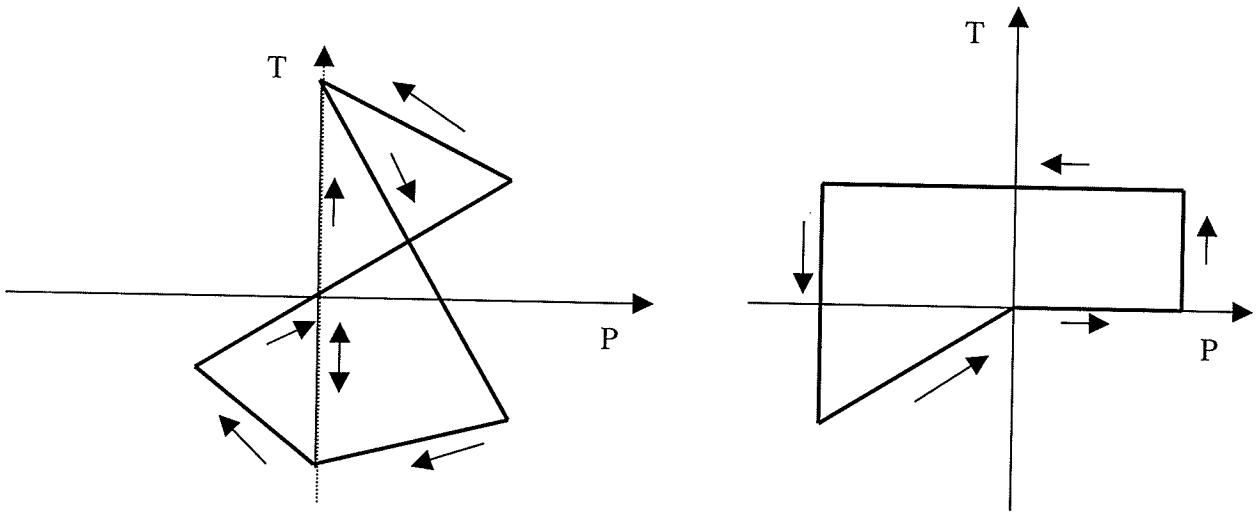

(a) (b)

Figure 5.23: Variable Amplitudes Non-Proportional Loading (a) Path 1 (b) Path 2

CHAPTER SIX: COMPARISON OF ANALYTICALAND EXPERIMENTAL RESULTS

In this chapter, the analytical results obtained using the models presented in Chapters Three and Four are compared to the experimental results of the tests described in Chapter Five. Specifically, Section 6.1 presents an assessment of the testing equipment described in Chapter Five for use in evaluating the developed models. Section 6.2 contains the experimental evaluation of the PMMCs constitutive models described in Chapter Three. The results obtained for the stress concentration factors are presented in Section 6.3. Finally, in Section 6.4, the results of the models developed in Chapter Four for notch root elastic-plastic strain and stress analysis are compared with experimental results.

6.1 Results of the Experimental Set-Up Verification Tests

As stated in Chapter Five, confidence in the results obtained using the Aramis was verified in this research by comparing them with those obtained using strain gages and extensometer. The results obtained from conducting the tensile tests described in Section 5.3.1 are shown in Figs. 6.1 and 6.2. From the figures, it can be observed that the results obtained using the various measuring devices are very close to each other both in the elastic and plastic regions; indicating that the Aramis can measure the strains in a smooth PMMC specimen with the same degree of confidence as the strain gaging technique.

The results obtained for the box-shaped load paths (Fig. 5.14) used for reliability tests described in Chapter Five are shown in Fig. 6.3. From the figure, it can be observed that the three applied load paths compared well with the ideal load path. This result indicates an expected consistency in the applied loads with the exception of very few points that are close to the corners where there are very minimal deviations due to abrupt change in loading direction. This observation is not unexpected because the sharp corners of the load path were not always obtained in the experiment. This has also been noted in [59]. Generally, the nominal load paths were loop tuned and well controlled to obtain good signal inputs. The corresponding plots of the shear strains, ε_{23}, versus axial strains, ε_{22}, for the three identical test specimens subjected to the same loads are shown in Fig. 6.4. The strain results are very close and almost indistinguishable except at the points that are close to the corners where there are sudden directional changes as noted earlier. The figure shows a very good reproducibility of the experimental results.

To illustrate the ability of 3D image correlation photogrametry used to measure the notch-root strains, a section line was drawn through the notch area (Fig. 6.5a) and the surface strain distribution along the line were recorded as the load increased (Fig. 6.5b). As expected, the maximum strain occurred at the notch root.

6.2 Constitutive Models Results and Discussions

In this section, the two elastic-plastic PMMCs constitutive models, developed in Chapter Three, are evaluated to determine their suitability to model the behavior of PMMCs, and their suitability for use in the notch analysis models. The MATLAB

program for each model, both described in Chapter Three, was initially run to evaluate their abilities to predict the uniaxial stress-strain curves of the PMMCs for different volume fractions for stress-controlled loading conditions. Both programs calculate the elastic-plastic composite strain histories using the known stress histories and the matrix and reinforcement material properties (Table 5.2) as inputs. The Mróz-based PMMCs constitutive model uses the yield stresses and hardening moduli of the matrix yield surfaces, while the endochronic theory-based PMMCs constitutive model uses the materials constants in Eq. (3.53) as additional inputs. Specifically, the tangent moduli and the yield stresses of the Mróz surfaces were obtained by descritizing the 6061-T6 aluminum alloy uniaxial stress-strain curve in [2] as shown in Fig. 6.6. The hardening moduli were subsequently obtained using Eq. (3.32). It should be mentioned that the program was run for different combinations of yield surfaces (maximum of 10) and load increments until optimal and convergent results were obtained. The values of the material constants associated with the endochronic theory-based PMMCs constitutive model for the matrix material 6061-T6 alloy are shown in Table 6.1. In Fig. 6.7, the stress-plastic strain curves obtained using one, two, and three terms in Eq. (3.53) are presented and compared with the experimental result for the 6061-T6 aluminum alloy in [2]. As can be observed in the figure, three terms in the series expansion in Eq. (3.53) were found to accurately model the stabilized stress-plastic strain response of the matrix cyclic stress-strain curve in [2]. The variation of the Dirichlet function (Eq. 3.53) with respect to the intrinsic time is also shown in Fig. 6.8. It is important to state that the method, described in Chapter Three, used to extract the material constants, is an approximate method like

other methods that have been previously used by other researchers in [32], [34], [73]. There is yet no unique method for determining the constants.

Figures 6.9 and 6.10 show the predicted response of the PMMCs under axial monotonic loading conditions for the Mróz-based PMMCs constitutive and the endochronic theory-based PMMCs constitutive models respectively for four different volume fractions of reinforcement. Figures 6.11 and 6.12 show the responses for the Mróz–based PMMCs constitutive and the endochronic theory-based PMMCs constitutive models respectively under monotonic torsional loading. As can be seen from the figures, both models predict a uniform increase in stiffness and strength of the composite system with increasing volume fractions of reinforcement. In addition, by comparing Figs. 6.9 and 6.10, the Mróz-based PMMCs constitutive model predicts a stiffer response of the composite constitutive behavior when compared to the endochronic theory-based PMMCs constitutive model for a particular volume fraction. The difference seems to be less significant at very low plastic strain and particle volume fraction but increases with increasing plastic deformation and volume fraction. A similar response is found for monotonic torsional loading in Figs. 6.11 and 6.12.

Figures 6.13 and 6.14 show respectively the composite axial and torsional stress-strain responses predicted by the models and the experimental results obtained from [2] when the tubular specimen was subjected to monotonic axial (P) and torsional (T) loads. Equations (5.3) and (5.2) were used here and in all constitutive relation evaluation tests to obtain the experimental axial and torsional stresses respectively from the applied loads. As can be seen from the figures, the elastic results obtained are similar to the experimental results, thus, the mean field theory works very well in describing the elastic

constitutive behavior of PMMCs. At higher load levels, small differences are observed between the models predictions and the experimental results with the endochronic theory-based PMMCs constitutive model underestimating, while the Mróz-based PMMCs constitutive model overestimating the elastic-plastic response of the composite system.

The results for the two constitutive models are also compared to the experimental results obtained from the tests conducted on the tubular specimens (Fig. 5.9) using the tension-torsion load paths in Fig. 5.15 to Fig. 5.17. Figure 6.15 to Fig. 6.18 show the experimental and the models results obtained. It should be mentioned that although the models calculate all of the components of the stress and strain tensors, for the purpose of comparison to the experimentally determined strains, only the major strains are compared.

Figure 6.15 shows the predicted and experimental results for cyclically stable combined axial/torsional proportional loading (Fig. 5.15) of the tubular specimens. The results of this proportional loading path show the ability of both models to predict the elastic-plastic hysterisis loops associated with cyclic loading. Most of the characteristics exhibited by the experimental results are reflected quite well by both models. However, the major disagreement that can be classified as quantitative is the difference in strain levels prescribed at high plastic strains. The results indicate the Mróz-based PMMCs constitutive model slightly over-predicts, while the endochronic theory-based PMMCs constitutive model slightly under-predicts the experimental shear strains. The small difference between the predicted and experimental results for the endochronic theory-based PMMCs constitutive model may be due to the approximate method used to obtain the material constants in Eq. (3.53). For the Mróz-based PMMCs constitutive model, the

number of surfaces used in the multi-surface model could have influenced the results. The number of surfaces used may have a significant effect on the direction of translation of the yield surfaces, and thus, affect the predicted results.

Figures 6.16 and 6.17 show the strain response of the tubular specimens predicted by the experimental and proposed models to the variable amplitude loading paths shown in Figs. 5.16a-b. Both models predict very similar strain responses for the loading paths and also give reasonable qualitative estimations of the measured strains. However, both models sometimes over-predict and at other times under-predict the measured strains. Generally, the endochronic theory-based PMMCs constitutive model predictions are closer to the experimental results than the Mróz-based PMMCs constitutive model predictions, particularly for the measured peaks and valleys that are essential for fatigue life prediction.

Figures 6.18a-c show the experimental and predicted strain response of the tubular specimen to the triangular shaped load path shown in Fig. 5.17. For this load path, due to a data acquisition problem encountered during the test, only the results of the first three cycles were plotted. The strain responses were plotted on different plots with identical scales in order not to obscure their overall features. The figures clearly indicate that the endochronic theory-based PMMCs constitutive model more closely predicts the shape of the elastic-plastic material strain responses than the Mróz-based PMMCs constitutive model under the loading path in Fig. 5.17. The Mróz-based PMMCs constitutive model does not describe well the characteristics of the experimentally observed material behavior for this loading condition. The Mróz-based PMMCs constitutive model's inability to correlate well with the experimental results may be due

to the influence of the number of surfaces on the direction of translation of the backstress tensors of the yield surfaces. In addition, the number of load increments used may affect the predicted results. Theoretically, the Mróz-based PMMCs constitutive model can be used with large increments, however, as with other cyclic plasticity models, care must be taken in the specification of the input load increments. It was noted during the implementation that smaller divisions yielded more stable strain responses.

For both models, the results obtained could also have been influenced by the direction of the applied loads. In Figs. 5.16 (a-b) and Fig. 5.17, the directions of the applied loads are indicated by the arrows. As could be observed from the results obtained (i.e. Fig. 6.16 to Fig. 6.18), changing the directions significantly shifts the position of the predicted strain responses. This is in agreement with the path dependence nature of any cyclic plasticity used with non-proportional loading conditions. However, only preliminary comments could be made regarding the effects of load paths on the predicted response. That is, more testing is required particularly to make definitive conclusions.

In most of the load paths considered, both models produce a reasonable qualitative and quantitative response of the composite behavior. This research has been able to demonstrate that both models can satisfactorily model the constitutive behavior of PMMCs. The Mróz-based PMMCs constitutive model requires a large number of surfaces, large amount of computer storage and a clearly defined yield point to give good results, while in the endochronic theory-based PMMCs constitutive model, determining the material constants necessary for its implementation is a very difficult task. The Mróz-based PMMCs constitutive model seems to be mathematically more complex and its computer implementation is much time consuming than the endochronic theory-based

PMMCs constitutive model. Although determining the material constants of the endochronic theory-based PMMCs constitutive model is not a simple task, the results obtained in this research show that the model should be used in spite of this difficulty. In general, the endochronic theory-based PMMCs constitutive model predictions are closer to the experimental results than the Mróz-based PMMCs constitutive model predictions, particularly so for the measured peaks and valleys that are essential for fatigue life prediction. Thus, the endochronic theory-based PMMCs constitutive was incorporated in this research with the approximate relations to predict the notch root elastic-plastic behavior.

6.3 Results of Elastic Stress concentration Factors Tests

The results of the experimental tests conducted to determine the stress concentration factors, K_t, written with respect to the coordinate system shown in Figs. 5.10 and 5.11 are presented in Tables 6.2 and 6.3 respectively. These tests are detailed in Section 5.3.3. The stress concentration factors for a homogeneous notched specimen with notch root geometry similar to the ones shown in Fig. 5.10 (i.e. the same r/d and d/D ratios) have been obtained using FEA in [59], as shown in Table 6.2. For the sharp notched geometry, K_{t33} and K_{t22} are not available in [90] as indicated in Table 6.3. It should be noted that the hoop stress induced due to the notch root constraint was less than the nominal net section axial stress and as such the stress concentration factor in the hoop direction, K_{t33}, was found to be less than unity.

6.4 Comparisons of Proposed Models and Experimental Results

The validity of analytical model presented in Chapter Four is evaluated by comparing the notch root strain histories obtained using the models with experimental results for the load paths described in Section 5.3.4 and shown in Figs. 5.14 and 5.15, and Fig. 5.19 to Fig. 5.23. The results of the experiments and models predictions are presented as plots of notch root elastic-plastic axial strain, ε_{22} against shear strain, ε_{23}, for all load paths tested. It should be mentioned that although the models calculate the full elastic-plastic stress and strain histories, for the purpose of comparison to the experimental results, only the major strains are presented. The following subsections describe these results. In all the figures, experimental results are indicated by the dashed-dotted lines, while the simplified model results are indicated by the continuous colored lines.

6.4.1 Monotonic Non-Proportional Loading

Figures 6.19 (a-b) show the experimental and numerical results for a mild notch subjected to a non-proportional monotonic torsion, combined tension-torsion load path shown in Fig. 5.19. The results from this non-proportional monotonic load path (Fig. 6.19a-b) show that the results are the same in the elastic range, and diverge at the onset of yielding, with the PMMCs ESED method slightly under-predicting, while the approximate PMMCs Neuber method slightly over-predicting the elastic-plastic notch root strains for both PMMC volume fractions tested. However, the differences in results

predicted by the models are very small. The difference may be due to the inability of the incremental mean field theory to incorporate the point-to-point deformation field in the ductile matrix and reinforcing particles. In additional the approximate values of the material constants used in the endochronic constitutive models and the approximate nature of the simplified method could also have influenced the results obtained.

It should also be mentioned that the analytical methodologies predict the notch root strains in the specimens with both volume fractions of reinforcements. In this load path (as in all the subsequent load paths tested in this research) a relatively higher load level was applied to the 20% volume fraction specimen than the 10% volume fraction specimen. However, as shown in Figs. 6.19 (a-b) (and also in all subsequent results for all the load paths tested) for both models, the 10% volume fraction results are higher than the 20% volume fraction results, in spite of the relatively higher load level applied to the 20% volume fraction specimen. This clearly shows that the models respect the heterogeneous nature of the material. The difference in the strain results for the 10 and 20% volume fractions may be attributed to the effects of volume fractions on the matrix plastic strains. In the assessment of the constitutive models, the results obtained show that the PMMC materials becomes stiffer with increasing volume fraction of reinforcement, thus, leading to diminishing plastic strains. This heterogeneous nature of the material has been incorporated into the models by accounting for the interactions in the stress fields between the particles in the incremental mean field theory used, and also by incorporating the localized deformation of both the matrix and the reinforcing particles into the proposed simplified models developed. This is an important finding since the models use only the material properties of the constituents separately.

6.4.2 Cyclic Proportional Loading

Figures 6.20 and 6.21 show for the mild and relatively sharp notched specimens respectively, the experimental and predicted notch root results for the proportional biaxial cyclic loading history shown in Fig. 5.15. In general, for both notch geometries, the analytical model predicts the general trend in and all the characteristic phenomena occurring of the experimental test results. An initially elastic region is observed at the onset of loading or unloading, followed by region of elastic-plastic deformation. This confirms that the non-linear elastic-plastic behavior can be predicted from a linear elastic analysis. The results of the proportional loading path clearly show the models ability to predict the elastic-plastic hysteresis loops associated with cyclic loading for both volume fractions of reinforcement and notch geometries. In both the mild and the relatively sharp notched specimens, the PMMCs ESED underestimates, while PMMCs Neuber overestimates the notch root shear strains. For the mild notched specimen, as the nominally applied loads increase, small differences are observed in the estimated and the measured strains. For the relatively sharp notched specimens, though there are differences in both the predicted and measured axial and shear strains, the differences are more noticeable in the shear strain results than the axial strain results. This may be due to the high constraints to the material plastic flow associated with the relatively sharp notched geometry.

6.4.3 Constant Amplitude Non-Proportional Loading

The results of experimental strain measurements and the results of the simplified models for the non-proportional constant amplitude loading paths shown in Fig. 5.14 and Fig. 5.20 are presented in Fig. 6.22 to Fig. 6.26. Figures 6.22 and 6.23 show the results obtained for the mild and relatively sharp notched specimens subjected to non-proportional constant amplitude box-shaped load path shown in Fig. 5.14. For both notch geometries, the simplified models predict the general trends observed in the experimental results. The models predicted regions of elastic unloading at each corner of the loading path, followed by regions of elastic-plastic behavior to the next corner. The results of the box path indicate that the methodologies are capable of predicting the elastic-plastic notch root strains for this 90° out-of-phase loading sequence. Although the results for both volume fractions of reinforcement indicate that the analytical methodologies sometimes over-predict, and at other points under-predict the notch root elastic-plastic strains, the differences are small in all cases for the mild notches. For the relatively sharp notch, noticeable differences are observed between the experimental and predicted results particularly for the axial strains with the PMMCs Neuber over-predicting the notch root axial strains for this load path. As in the cyclic proportional load, this difference may be due to the high constraints to the material plastic flow associated with sharp notch geometry. However, since the difference between the measured and the predicted strains for this load path is higher in comparison to the differences observed between the measured and predicted results for other load paths (e.g. proportional cyclic load path, and variable amplitude load paths) tested with relatively sharp notched specimens, the

obvious difference in the results for this load path may be due to the large strain gradients at the notch root of the relatively sharp notch coupled with the high degree of non-proportionality associated with the box-shaped load path.

Figure 6.24 show the results obtained for a mild notch under the rhombic-shaped load path shown in Fig. 5.20a. As in the box-shaped load path, the predicted results displayed the general trends observed in the experimental results. The results of both volume fractions also indicated that the models some times over-predict and at some other times under-predict the experimental results. However, these differences are very small. The difference between the measured and experimental results may be more pronounced with increasing equivalent net section ratio, since, at this stage, the assumptions of localized plasticity, on which the approximate models are based, may be violated.

Figures 6.25 (a-c) and 6.26 (a-c) show the experimental and predicted results for the X-shape loading path (Fig. 5.20 b). The results were plotted on different plots for the purpose of clarity. In the X-path, the segments are linear between zero and maximum. The cyclic load was applied in a counter-clockwise direction. The results presented were for the mild notch. The models results were very similar in shape to the experimental results. Excellent results were obtained for the axial strains in both models.

Figure 6.27 to Fig. 6.32 show the experimental and predicted strain responses for mild notched specimens subjected to various non-proportional loading paths with unequal frequencies shown in Figs. 5.21 (a-c). For each loading path, several cycles of the measured and calculated strain responses are plotted. The strains are plotted on different plots with identical scale in order to prevent lack of distinction in the overall features of

the results. For all the loading paths used, the calculated strains agree well qualitatively with the strains for the stabilized paths. In terms of the numerical values, the predicted results agree very well with the experimental results for the PMMCs ESED for all the loading cases considered. However, while the PMMCs Neuber shear strain predictions also agree very well with the experimental results, it tends to over-estimate the axial strains particularly for the 1:5 ratio of the applied torsional to axial loads shown in Fig. 6.32.

6.4.4 Unbalanced Loading

Figure 6.33 to Fig. 6.36 show the results for the relatively sharp notched specimen with a mean torsional cyclic and symmetric cyclic load path shown in Figs. 5.22 (a-b). The results were shown only for the first ten cycles for both volume fractions. The numerical and the experimental results are plotted on different plots with the same scales for clarity. Both the experimental and the numerical results show that the material shows an accumulation of the shear strain during plastic deformation. In the experimental results, there is an increase in the plastic strain in the first few cycles. However, the shear strains tend to a limiting value after some few cycles, indicating stress relaxation. This leads to a decreasing rate of strain accumulation. The numerical results indicate that both models predict a reasonable qualitative description of the experimental results. Additionally, both models give reasonable quantitative predictions of the axial strains for both volume fractions. However, a small and nearly limiting rate of shear strains accumulation is predicted for the cycles. It is important to state that limiting values of

strains are attainable for higher number of cycles since the inputs to the simplified models are increments of total and strain energy densities. As the number of cycles increase, the stress will relax and thus resulting in a decrease rate of strain accumulation.

6.4.5 Variable Amplitude Non-Proportional Loading

The experimental and simplified models results for relatively sharp notched specimens under the variable amplitude loading paths shown in Figs 5.23 (a-b) are presented in Figs. 6.37 and 6.38. From the figures, it can be observed that the simplified models predictions agree very well both qualitatively and quantitatively with the experimental results. Although the results for both volume fractions of reinforcement indicate that the simplified models sometimes over-predicts, and at other points under-predicts the notch root elastic-plastic strains, the differences are small in all cases. These differences may be due to the inability of the incremental mean field theory to incorporate the point-to-point stress and strain fields in the composite and its constituents. The differences between the experimental and the predicted results could also have been due to the approximate values of the material constants used in the endochronic theory-based model. However, the results obtained are very reasonable, considering the complexity of the load paths considered.

Table 6.1: Dirichlet Constants

C_1 (MPa)	C_2 (MPa)	C_3 (MPa)	α_1	α_2	α_3
7841132	218948	17115	60172	2097	347

Table 6.2 Stress Concentration Factors for the Mild Notched Specimens, shown in Fig. 5.10)

	FEA†	Experimental	% Difference
K_{t22}	1.41	1.43	1.42
K_{t23}	1.15	1.14	0.86
K_{t33}	0.30	0.30	0.00

† (Source: [59])

Table 6.3 Stress Concentration Factors for the Relatively Sharp Notched Specimens, shown in Fig. 5.11)

	Peterson‡	Experimental	% Difference
K_{t22}	NA	2.24	-
K_{t23}	1.74	1.72	1.15
K_{t33}	NA	0.81	-

‡ (Source: [90]), NA = Non Available

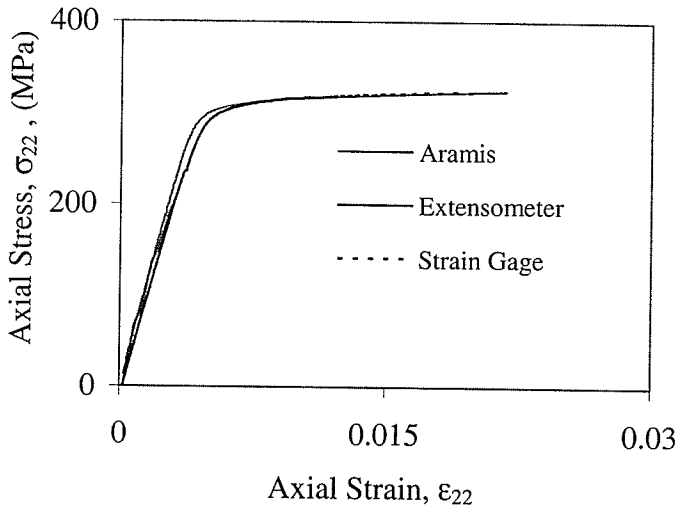

Figure 6.1: Strain-Stress Curve for 10% Volume Fractions of Composite Using Various Measuring Devices

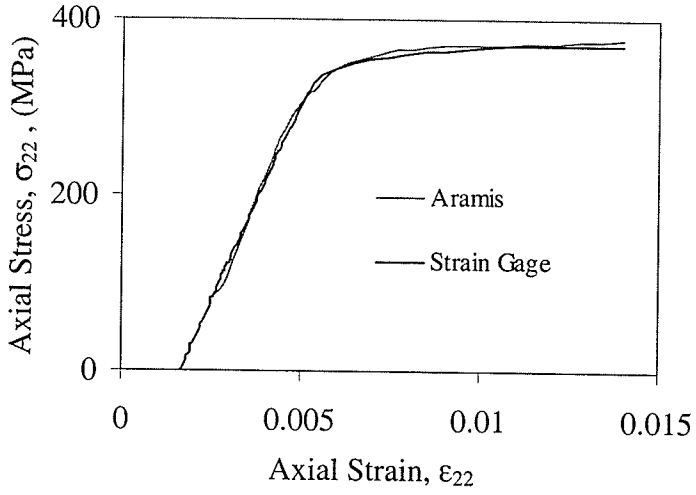

Figure 6.2: Strain-Stress Curve for 20% Volume Fractions of Composite Using Various Measuring Devices

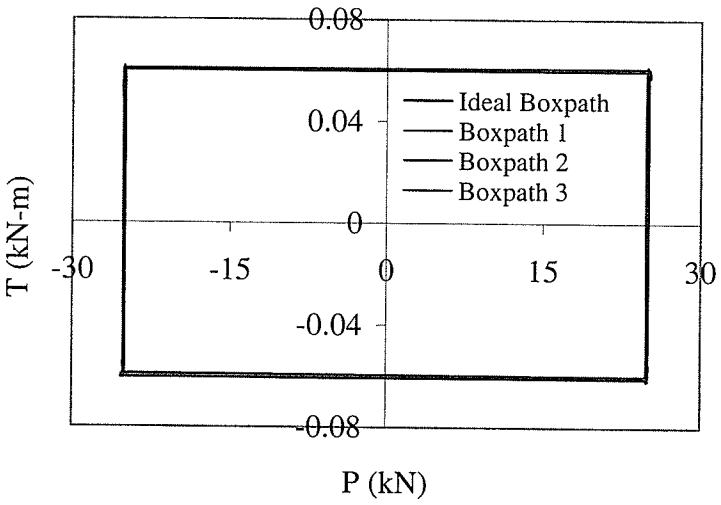

Figure 6.3: Experimental and Ideal Load Paths

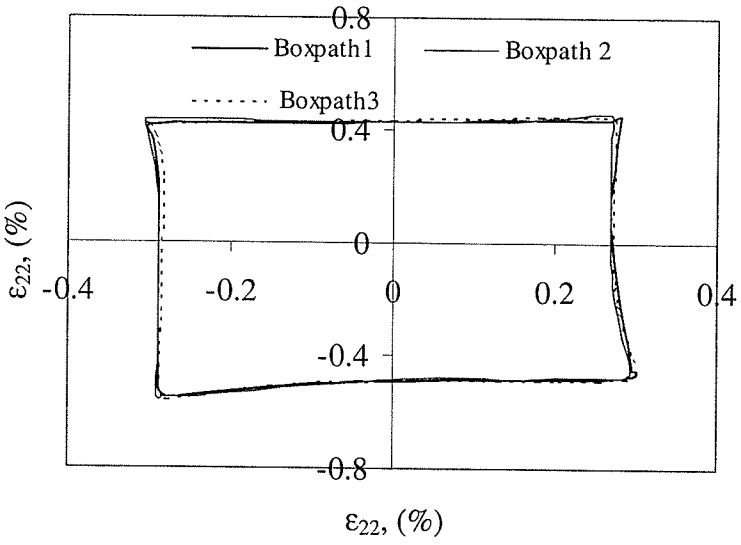

Figure 6.4: Axial vs. Shear Strains for Three Box-Shaped Load Paths (Experimental Results)

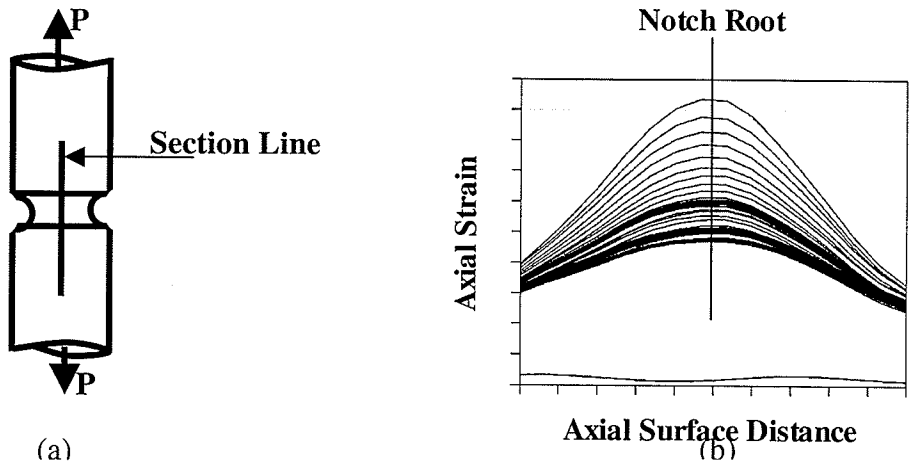

Figure 6.5: Typical Axial Strain Results in the Notch Root Area. (a) Section-Line Across the Notch Area (b) Axial Strain Distribution along the Section Line for Increasing Load

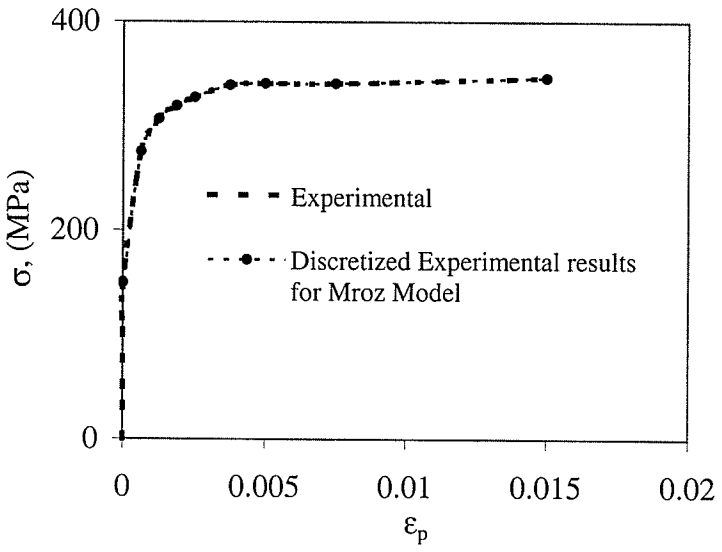

Figure 6. 6: Descretization of 6061-Alloy Uniaxial Stress-Plastic Strain Curve in [2]

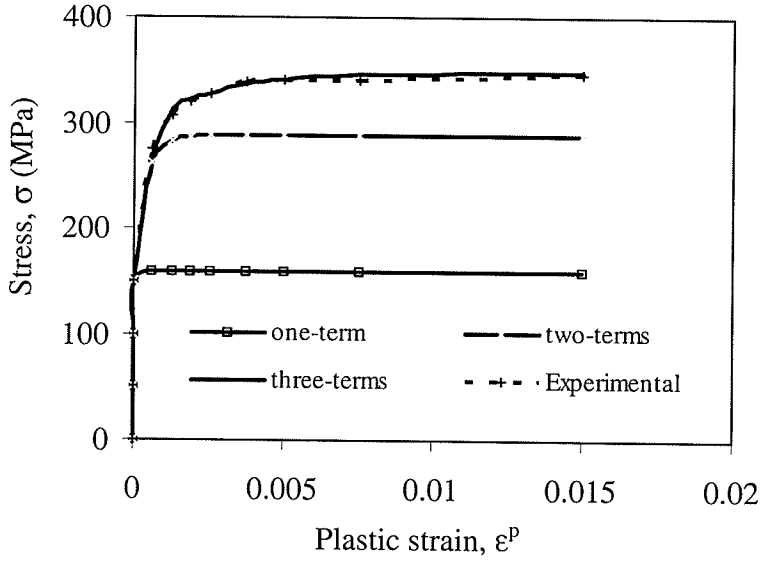

Figure 6.7: Uniaxial Stress Strain Curves Produced by Combining Different Number of Terms of the Dirichlet Series

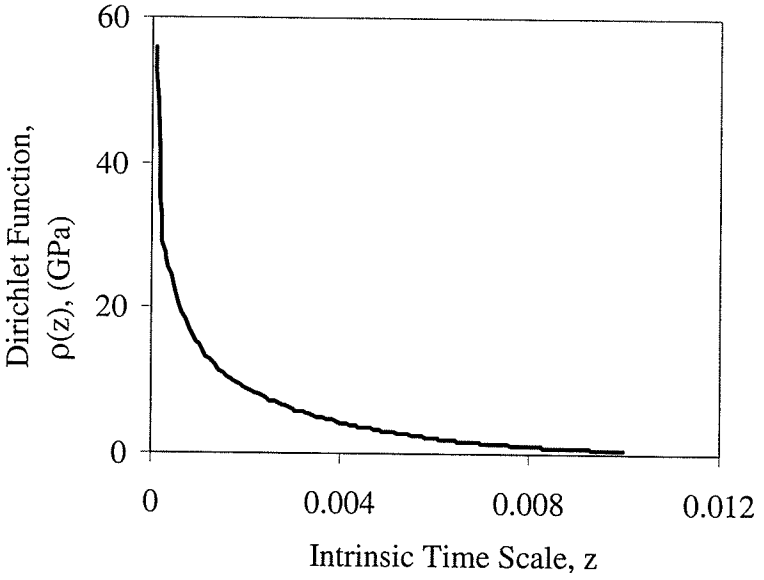

Figure 6.8: Variation of the Kernel Function with Intrinsic Time

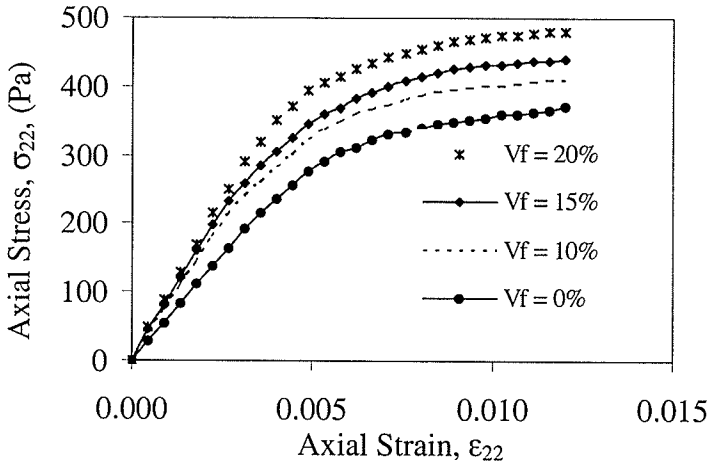

Figure 6.9: Axial Stress-Strain Curves for Various Volume Fractions of Reinforcement (Mróz-Based PMMCs Constitutive Model)

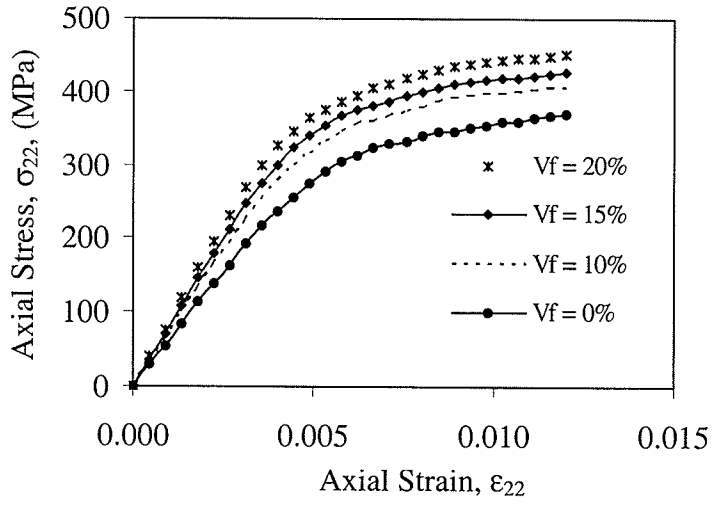

Figure 6.10: Axial Stress-Strain Curves for Various Volume Fractions of Reinforcement (Endochronic Theory-Based PMMCs Constitutive Model)

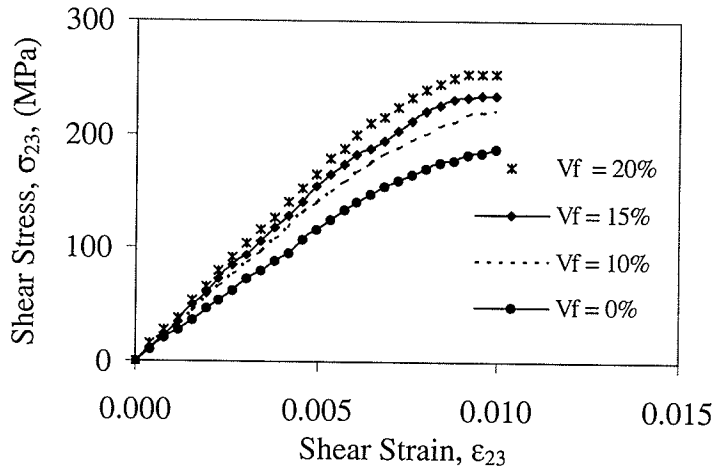

Figure 6.11: Shear Stress-Strain Curves for Various Volume Fractions of Reinforcement (Mróz-Based PMMCs Constitutive Model)

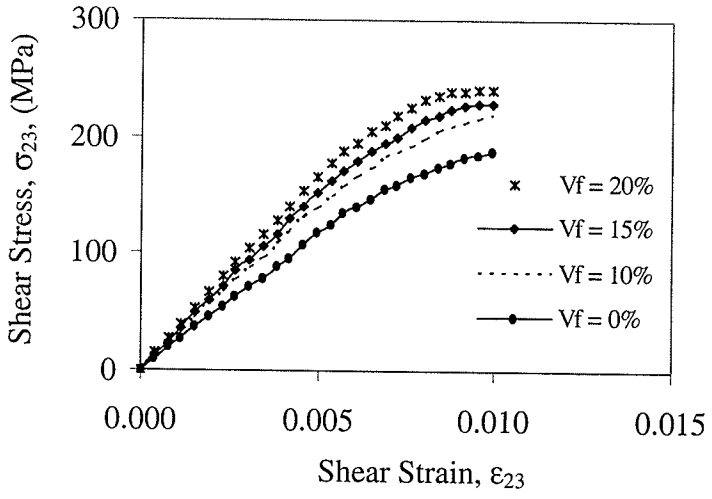

Figure 6.12: Shear Stress-Strain Curves for Various Volume Fractions of Reinforcement (Endochronic Theory-Based Constitutive Model)

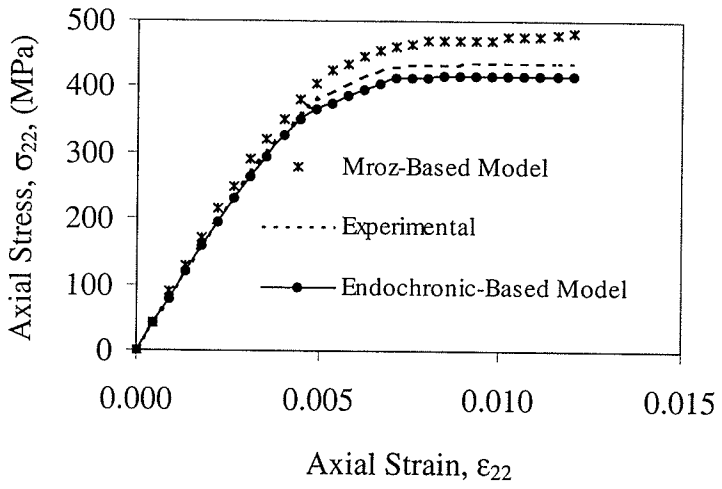

Figure 6.13: Experimental and Simulated Axial Stress Vs. Axial Strain

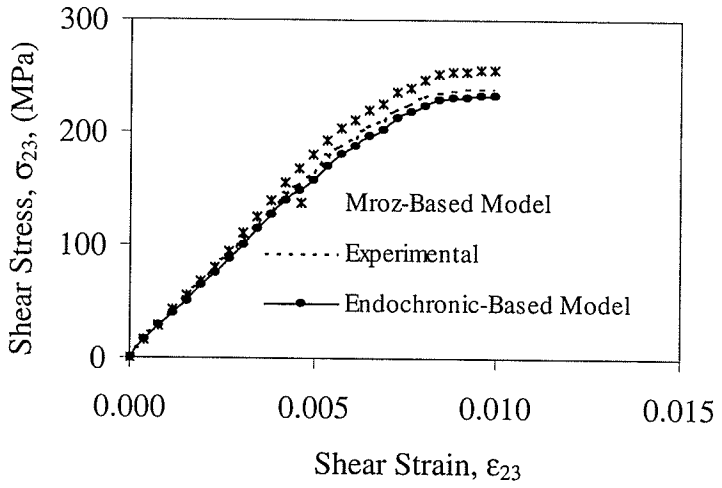

Figure 6.14: Experimental and Simulated Shear Stress Vs. Shear Strain

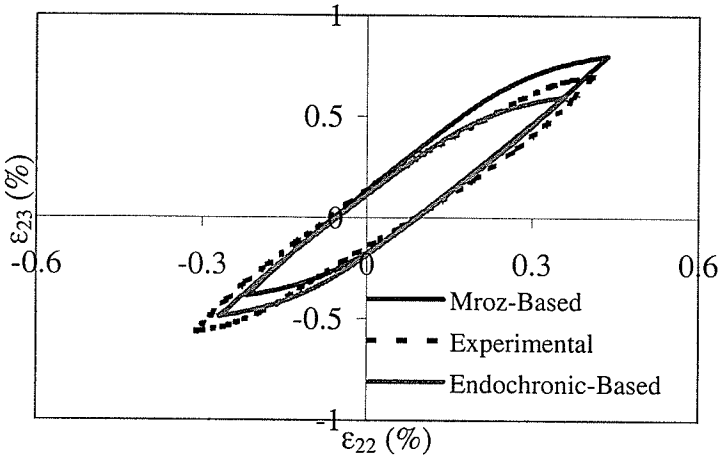

Figure 6.15: Experimental and Simulated Shear Strains Vs. Axial Strains for Hollow Tube Specimen under Proportional Cyclic Load (10% Volume Fraction)

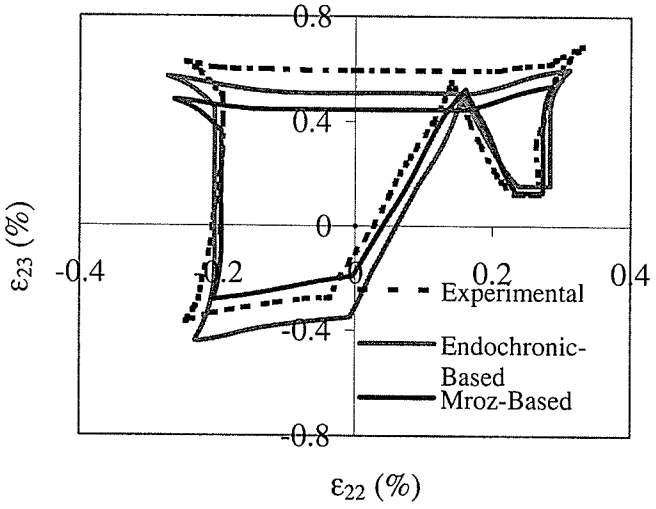

Figure 6.16: Experimental and Simulated Shear Strains Vs. Axial Strains for Hollow Tube Specimen under a variable Amplitude Load Path (Fig. 5.16 (a), 10% Volume Fraction)

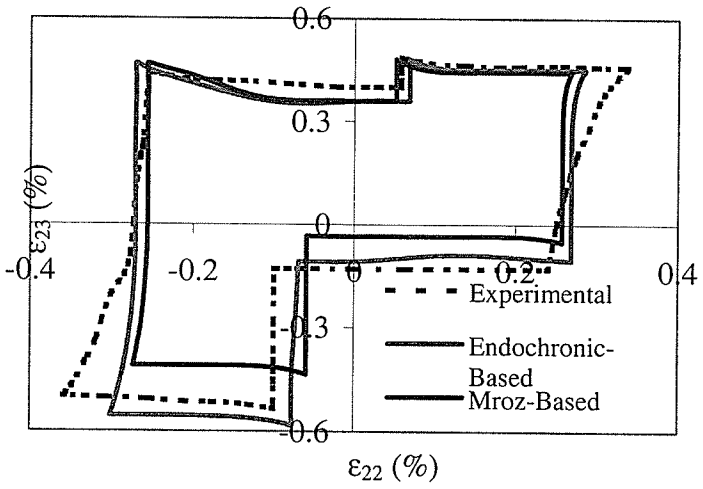

Figure 6.17: Experimental and Simulated Shear Strains Vs. Axial Strains for Hollow Tube Specimen under a variable Amplitude Load Path (Fig. 5.16 (b), 20% Volume Fraction)

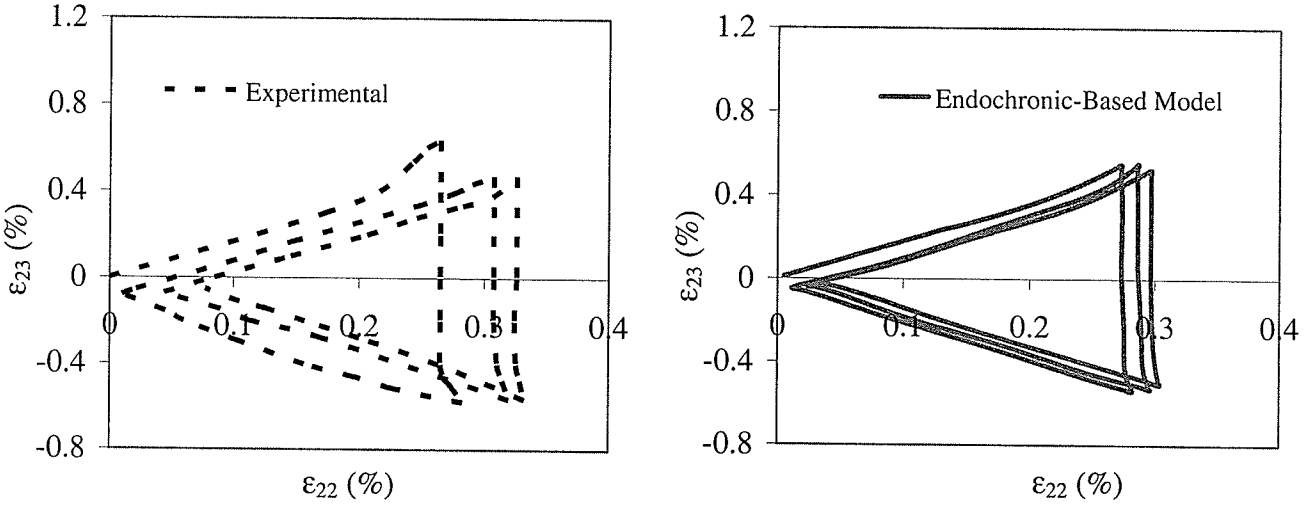

(a) (b)

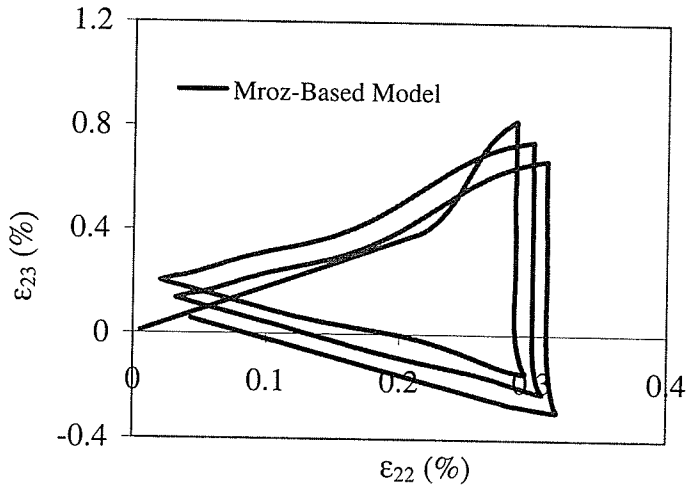

(c)

Figure 6.18: Experimental and Simulated Shear Strains Vs. Axial Strains for Hollow Tube Specimen under a Mean Stress Triangular Load Path (Fig. 5.17, 10% Volume Fraction)

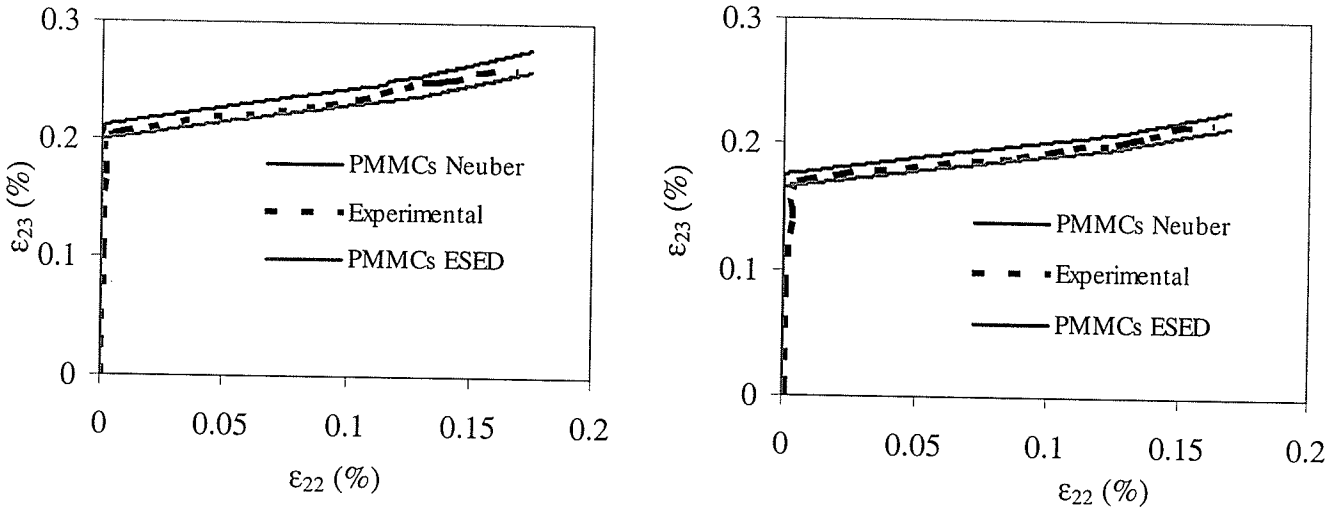

(a) (b)

Figure 6.19: Notch Root Shear Strains Vs. Axial Strains for Torsion, Combined Tension-Torsion Load Path in Fig. 5.19 (a) 10% Volume Fraction (b) 20% Volume Fraction

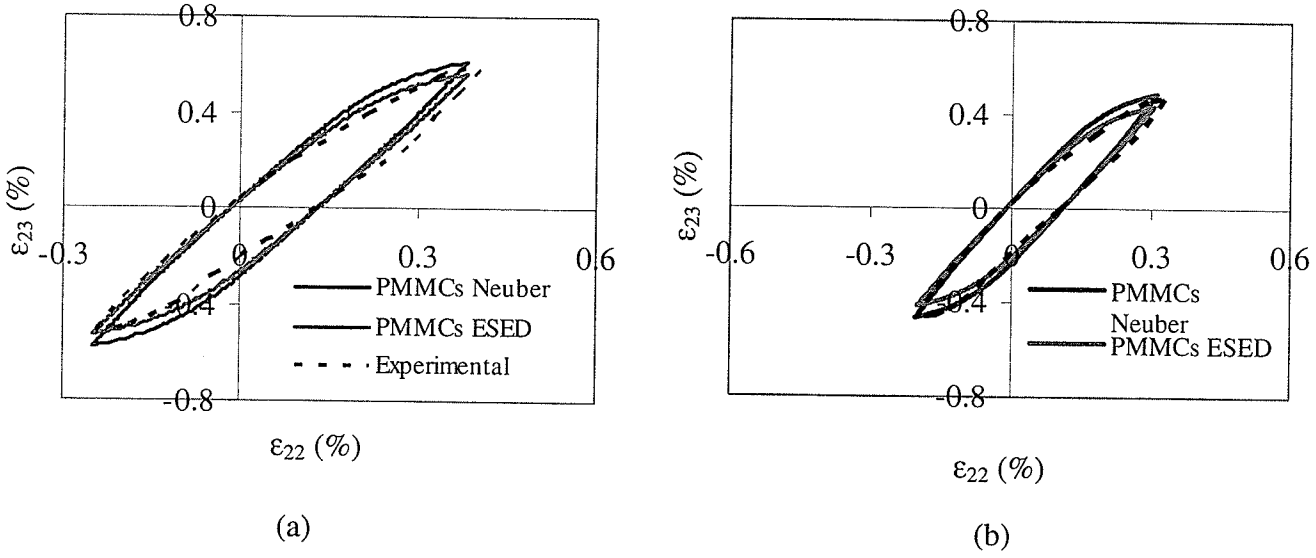

Figure 6.20: Notch Root Shear Strains Vs Axial Strains for Proportional Cyclic Load Path in Fig. 5.15 for Mild Notch (a) 10% Volume Fraction (b) 20% Volume Fraction

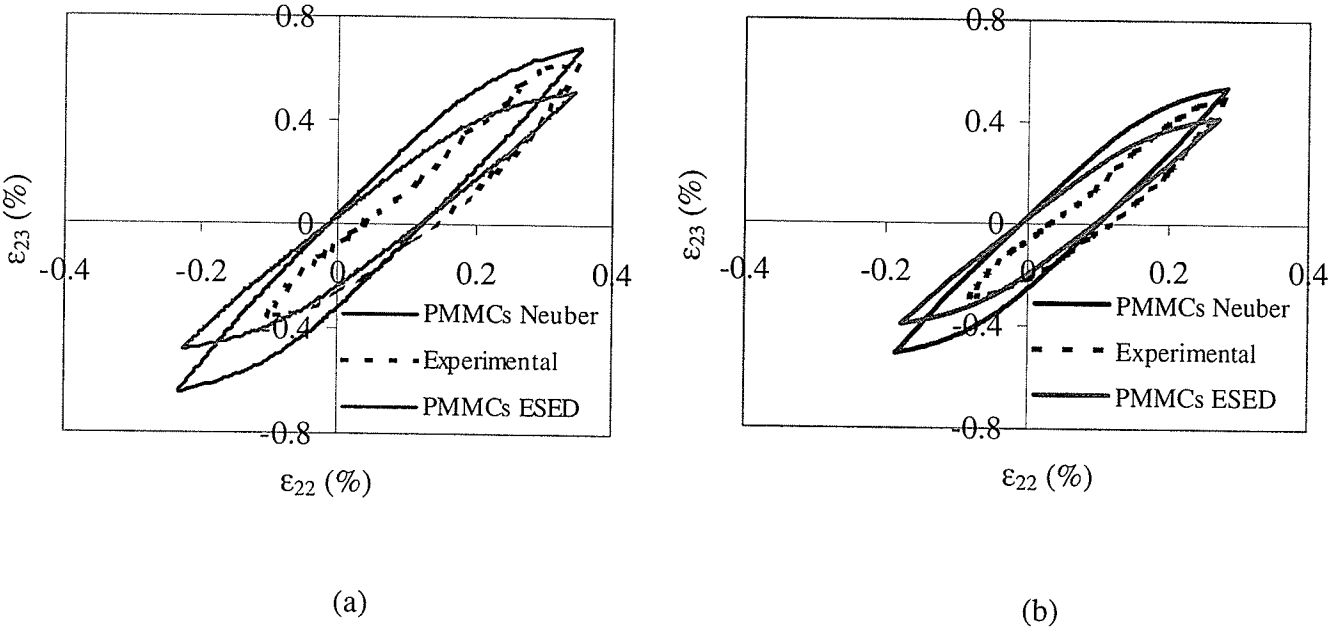

Figure 6.21: Notch Root Shear Strains Vs. Axial Strains for Proportional Cyclic Load Path in Fig. 5.15 for Relatively Sharp Notch (a) 10% Volume Fraction (b) 20% Volume Fraction

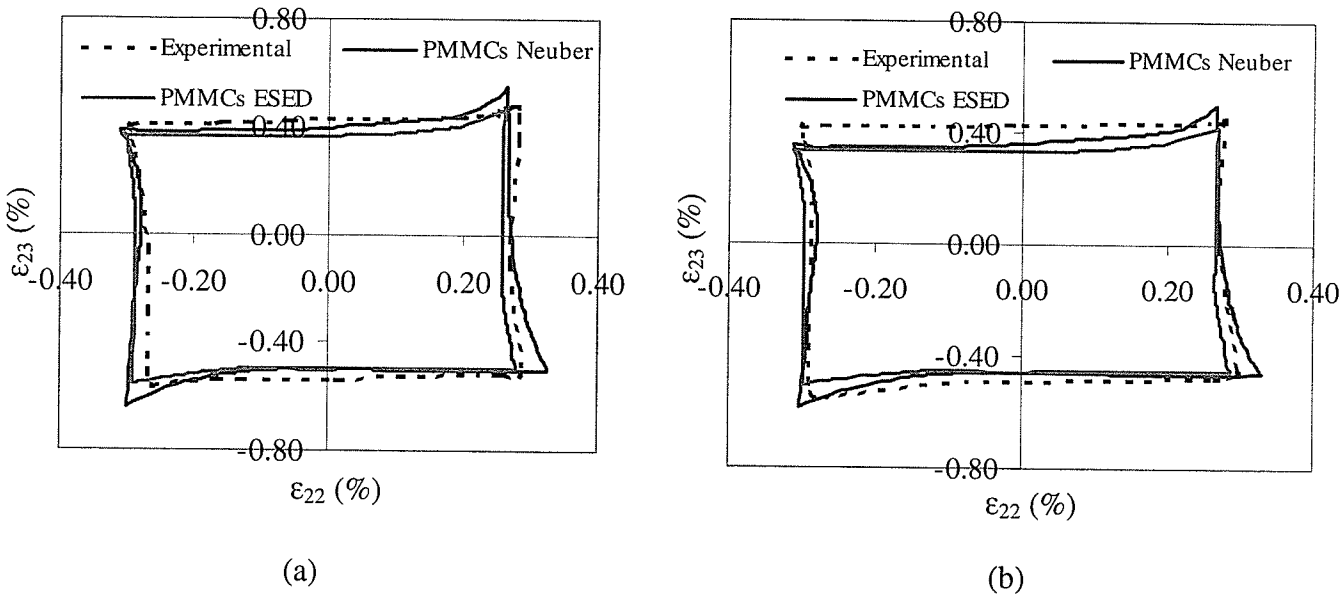

Figure 6.22: Notch Root Shear Strains Vs. Axial Strains for Box-Shape Loading Path Path in Fig. 5.14 for Mild Notch (a) 10% Volume Fraction (b) 20% Volume Fraction

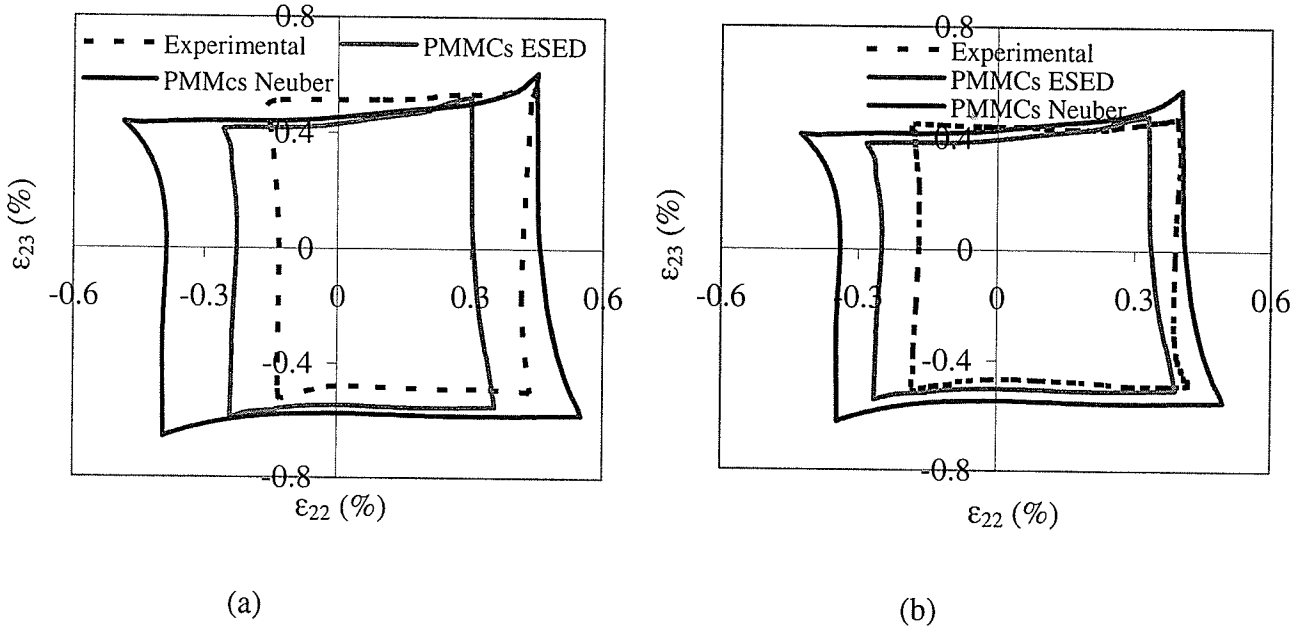

Figure 6.23: Notch Root Shear Strains Vs. Axial Strains for Box-Shaped Load Path in Fig. 5.20a for Sharp Notch (a) 10% Volume Fraction Relatively Sharp Notch (b) 20% Volume Fraction

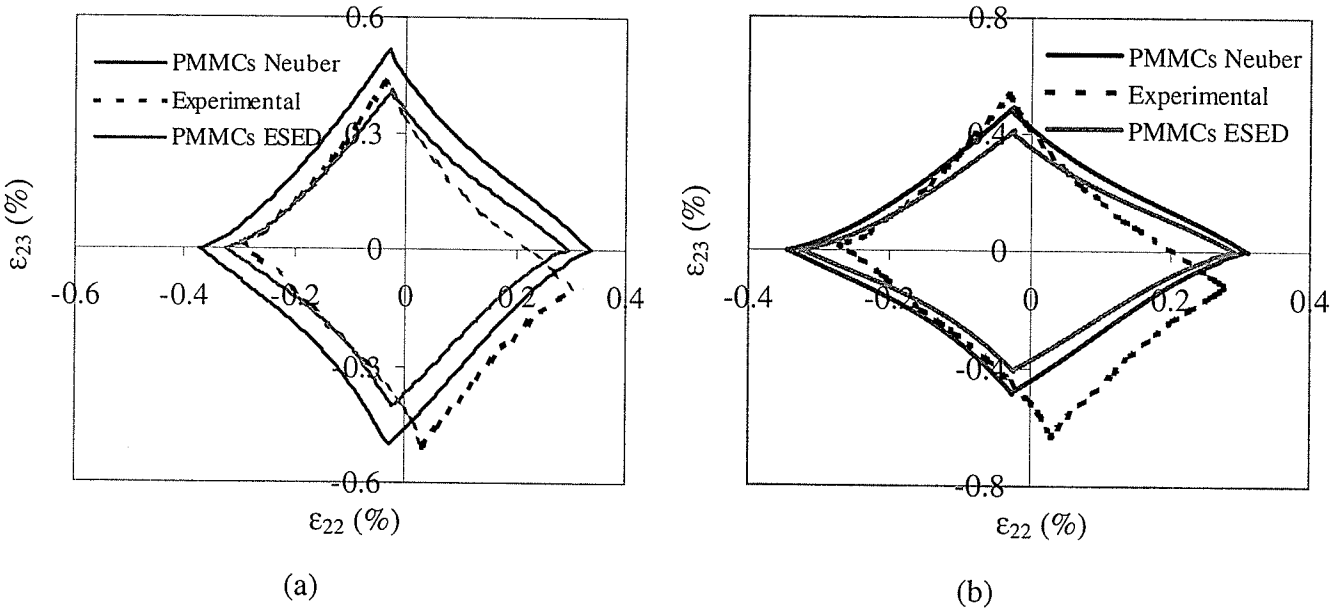

Figure 6.24: Notch Root Shear Strains Vs. Axial Strains for Rhombic-Shape Load Path in Fig. 5.20a for Mild Notch (a) 10% Volume Fraction (b) 20% Volume Fraction

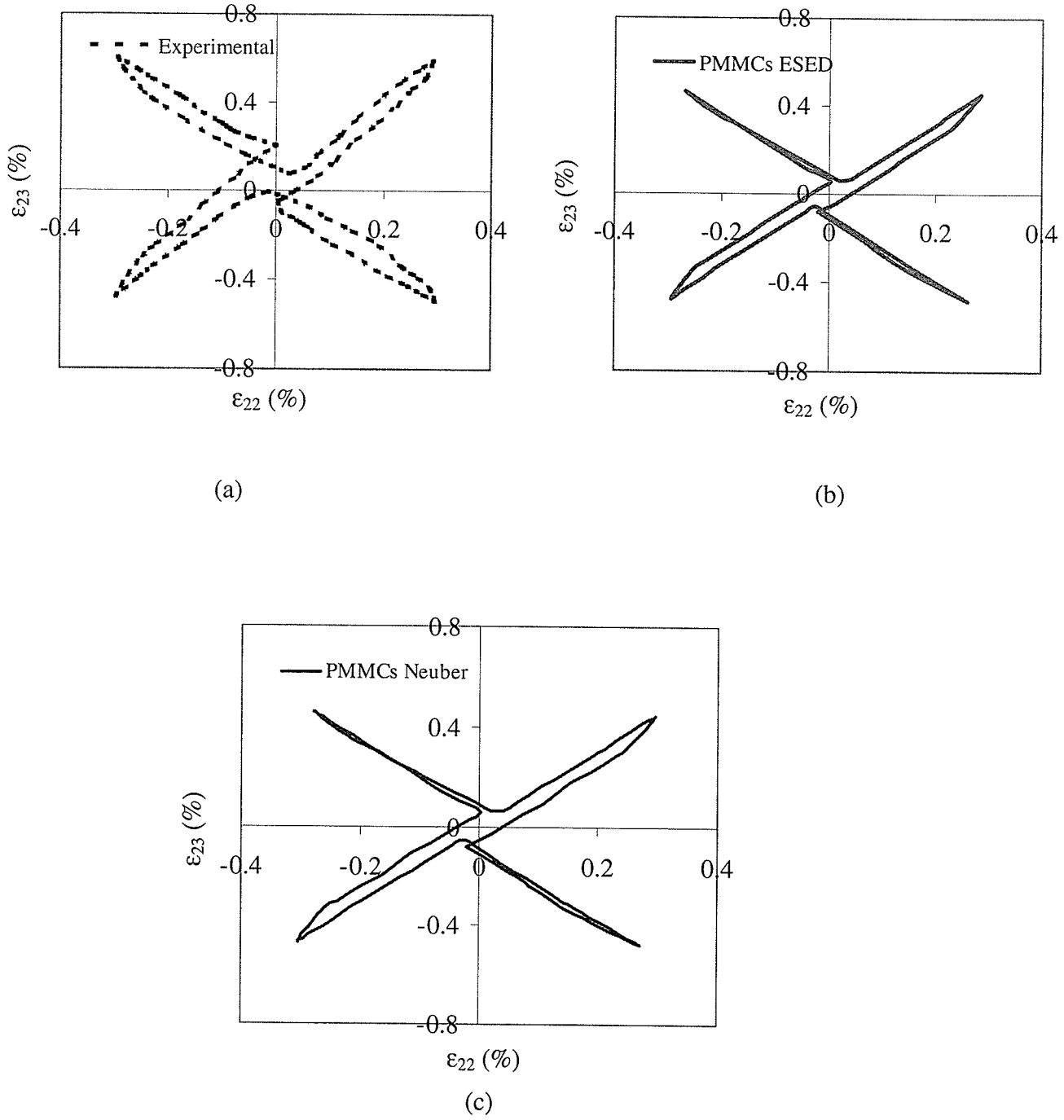

Figure 6.25: Notch Root Shear Strains Vs. Axial Strains for X-Shape Loading Path in Fig. 5.20b for Mild Notch, 10% Volume Fraction (a) Experimental (b) PMMCs ESED (c) PMMCs Neuber

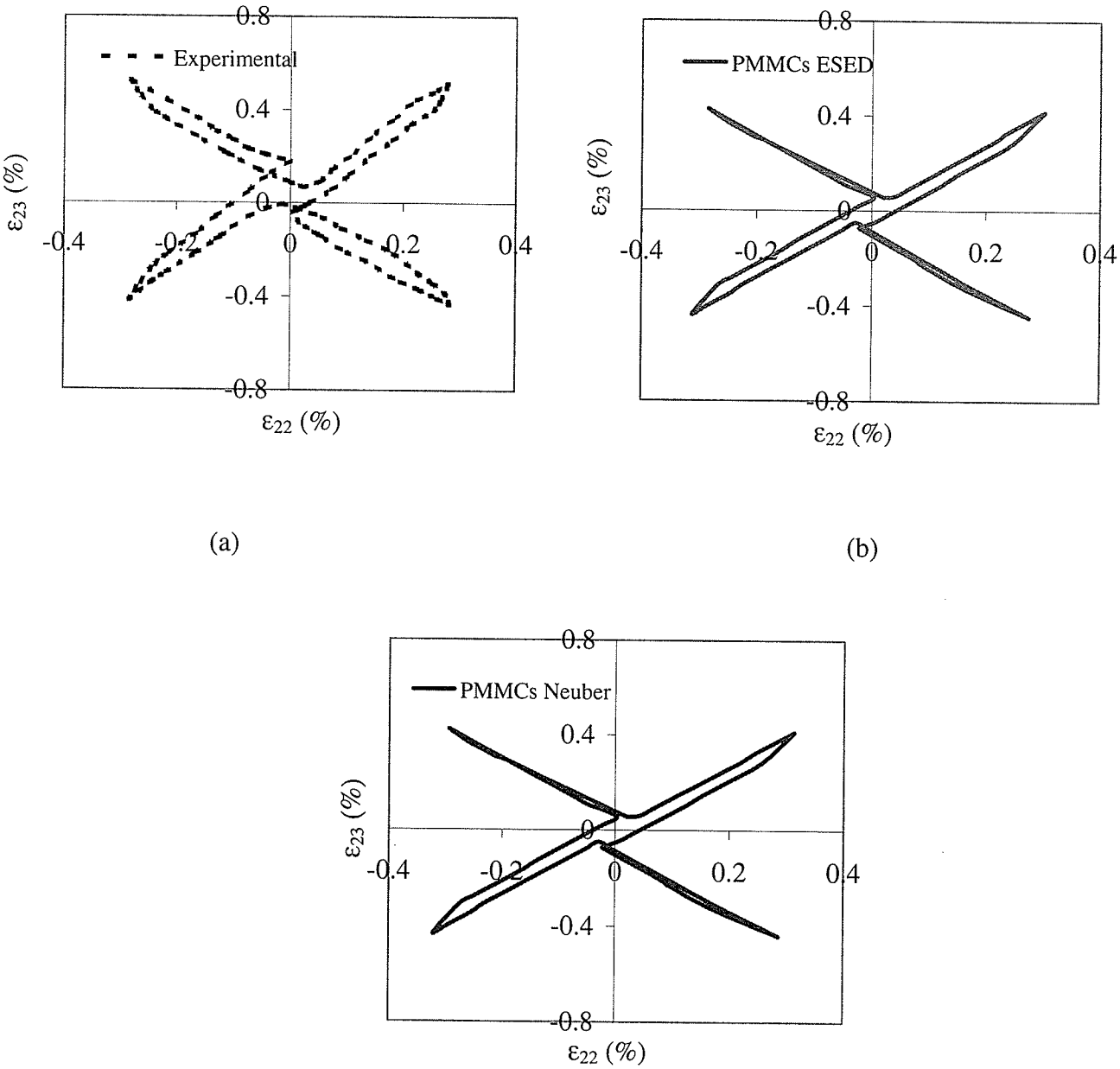

Figure 6.26: Notch Root Shear Strains Vs. Axial Strains for X-Shape Load Path in Fig. 5.20b for Mild Notch, 20% Volume Fraction (a) Experimental (b) PMMCs ESED (c) PMMCs Neuber

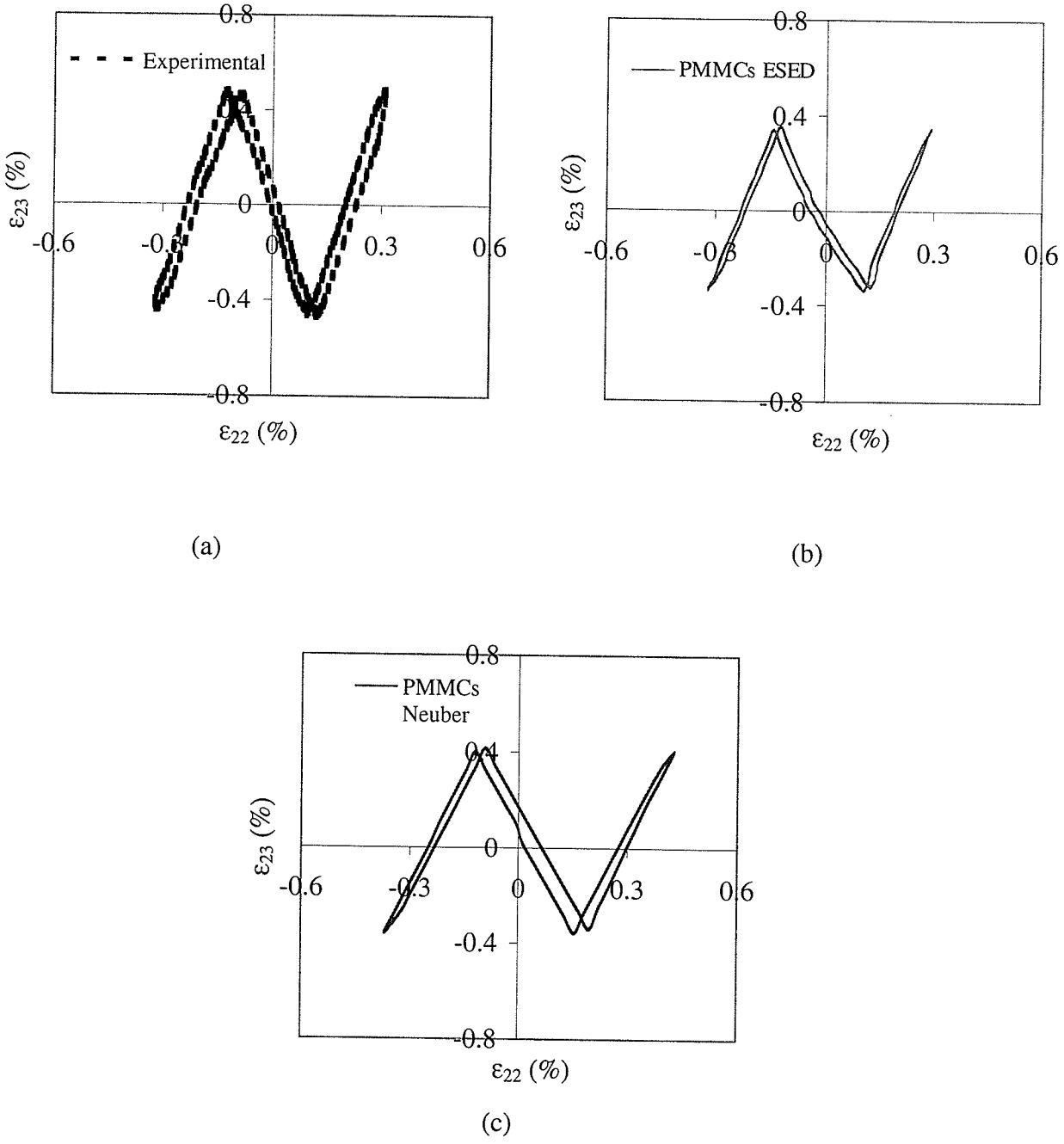

Figure 6.27: Notch Root Shear Strains Vs. Axial Strains for Tension-Torsion Frequency Ratio 1:3 Load Path in Fig. 5.21a for Mild Notch, 10% Volume Fraction (a) Experimental (b) PMMCs ESED (c) PMMCs Neuber

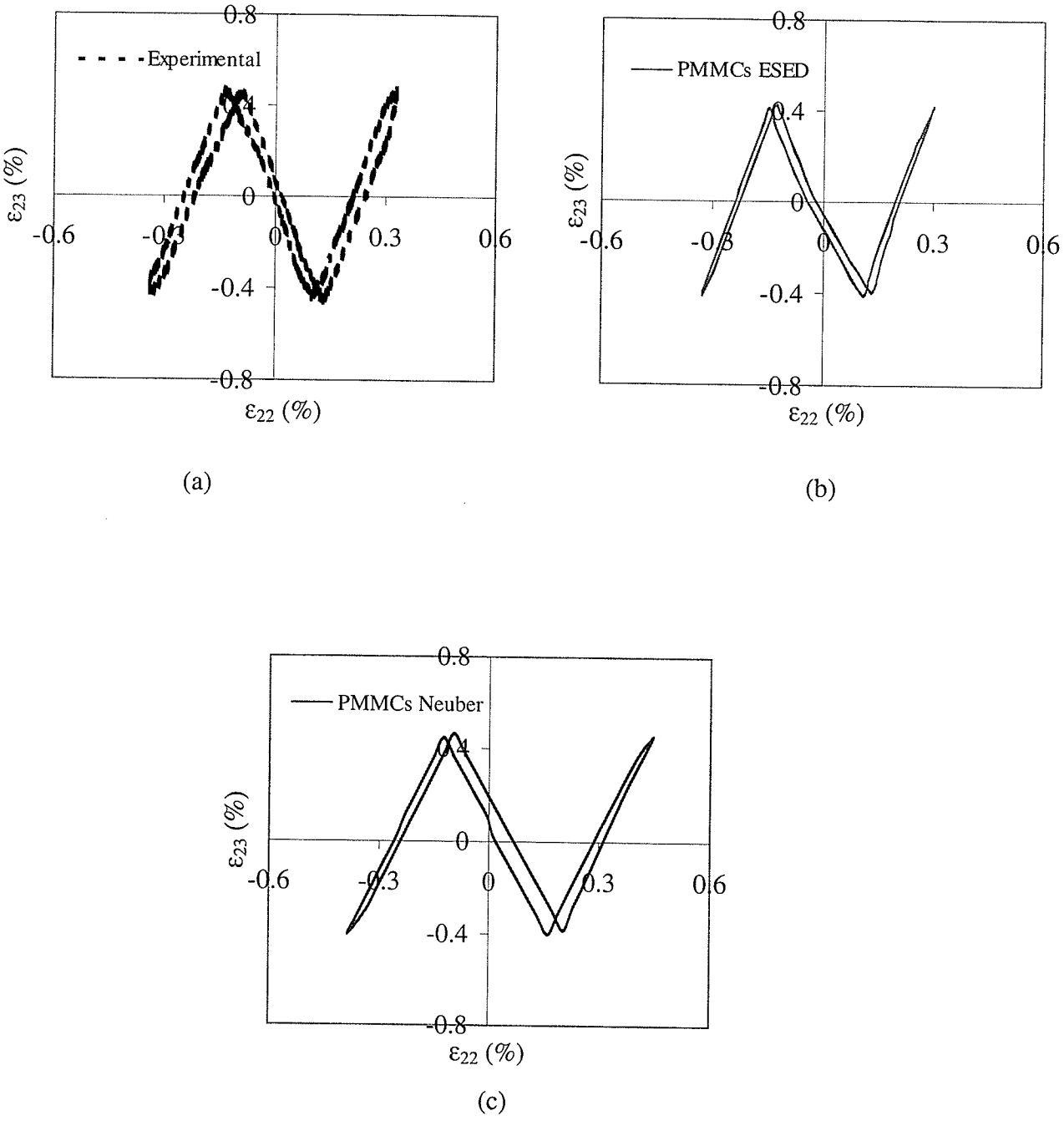

Figure 6.28: Notch Root Shear Strains Vs. Axial Strains for Tension-Torsion Frequency Ratio 1:3 Load Path in Fig. 5.21a for Mild Notch, 20% Volume Fraction (a) Experimental (b) PMMCs ESED (c) PMMCs Neuber

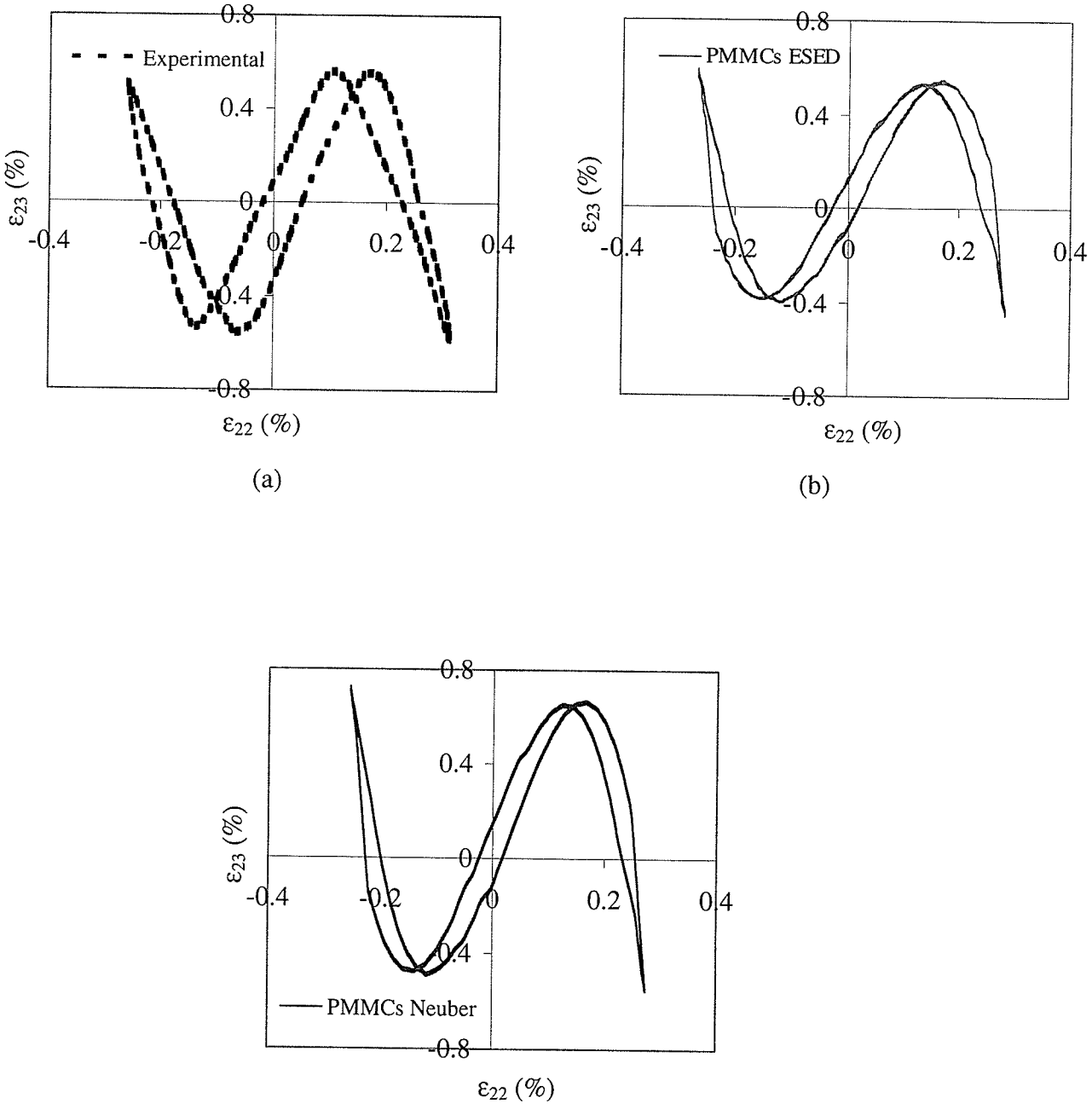

Figure 6.29: Notch Root Shear Strains Vs. Axial Strains for Tension-Torsion Frequency Ratio 1:3 Load Path (Sine Wave), in Fig. 5.21b for Mild Notch 10% Volume Fraction (a) Experimental (b) PMMCs ESED (c) PMMCs Neuber

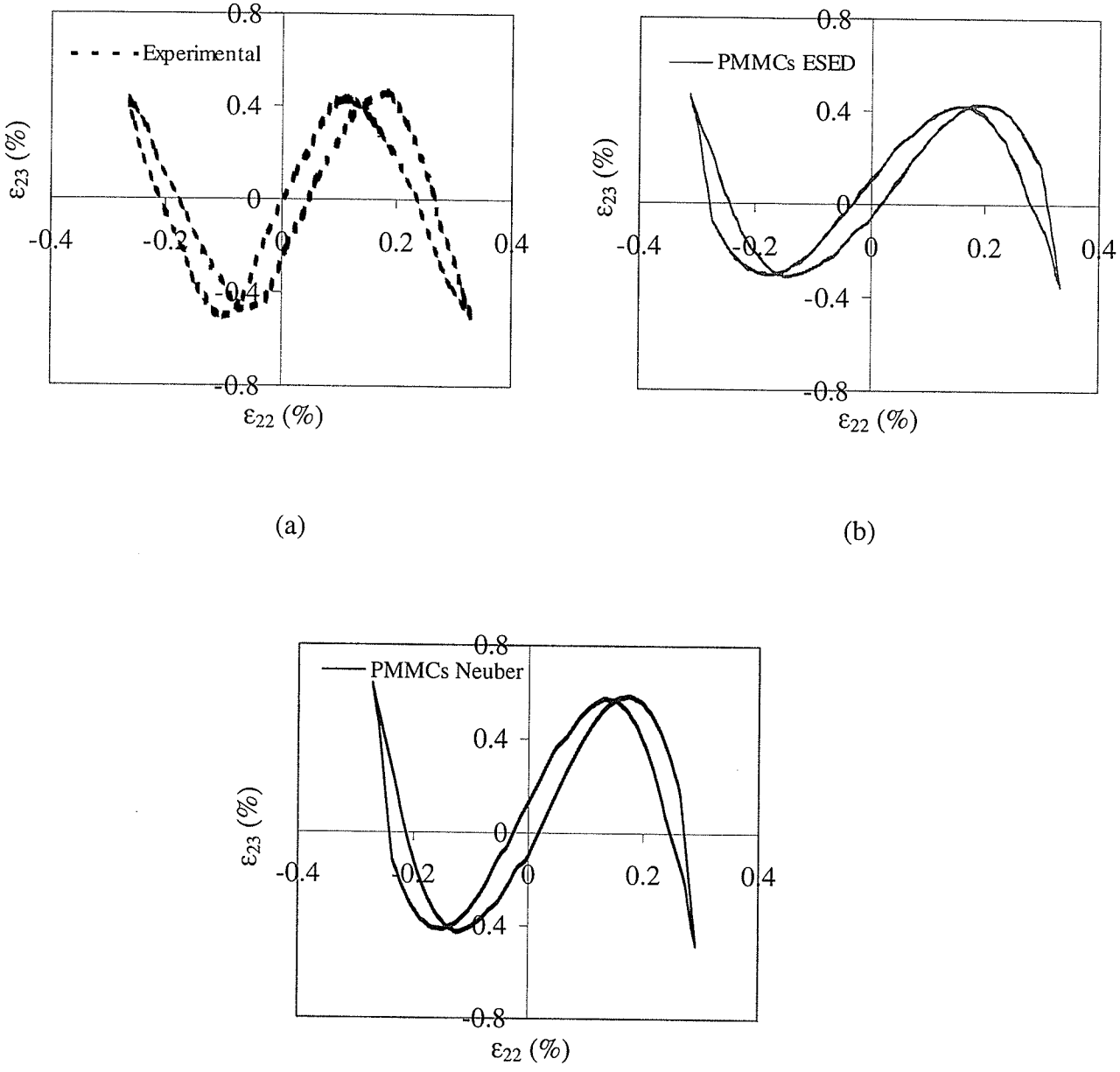

Figure 6.30: Notch Root Shear Strains Vs. Axial Strains for Tension-Torsion Frequency Ratio 1:3 Load Path (Sine Wave) in Fig. 5.21b for Mild Notch, 20% Volume Fraction (a) Experimental (b) PMMCs ESED (c) PMMCs Neuber

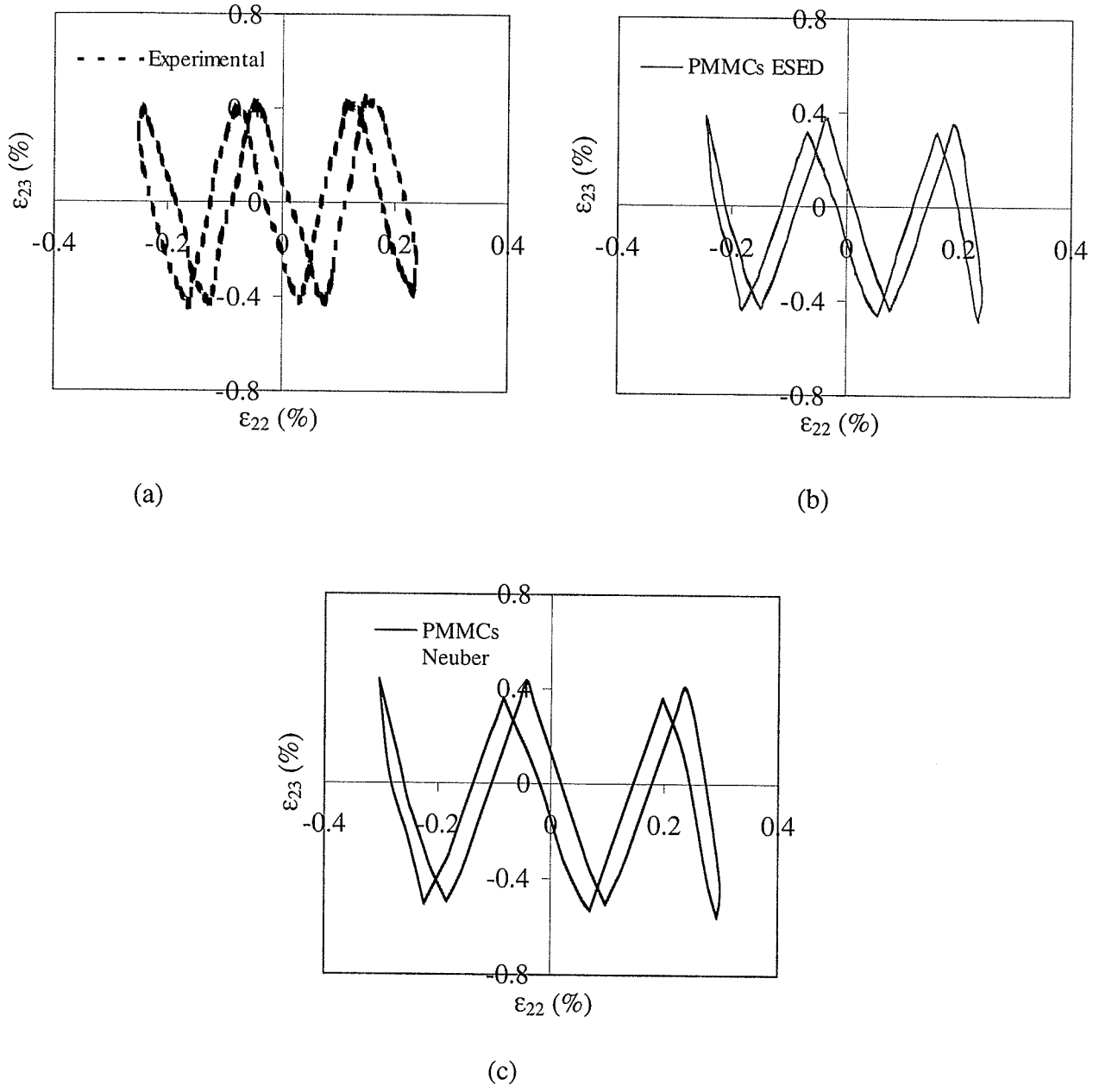

Figure 6.31: Notch Root Shear Strains Vs. Axial Strains for Tension-Torsion Frequency Ratio 1:5 Load Path (Sine Wave) in In Fig. 5.21c for Mild Notch, 10% Volume Fraction (a) Experimental (b) PMMCs ESED (c) PMMCs Neuber

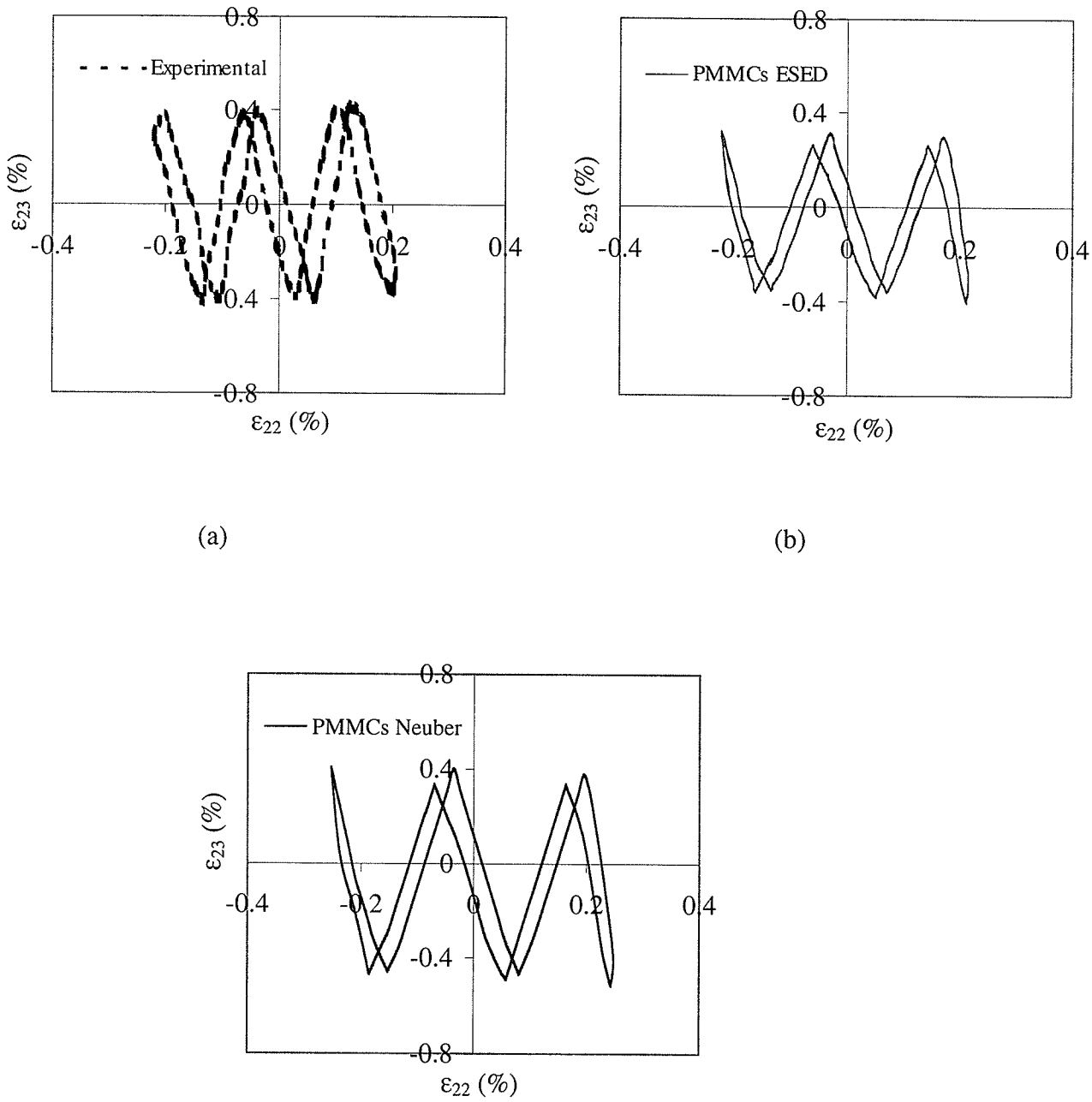

Figure 6.32: Notch Root Shear Strains Vs. Axial Strains for Tension-Torsion Frequency Ratio 1:5 Load Path (Sine Wave) in Fig. 5.21c for Mild Notch, 20% Volume Fraction (a) Experimental (b) PMMCs ESED (c) PMMCs Neuber

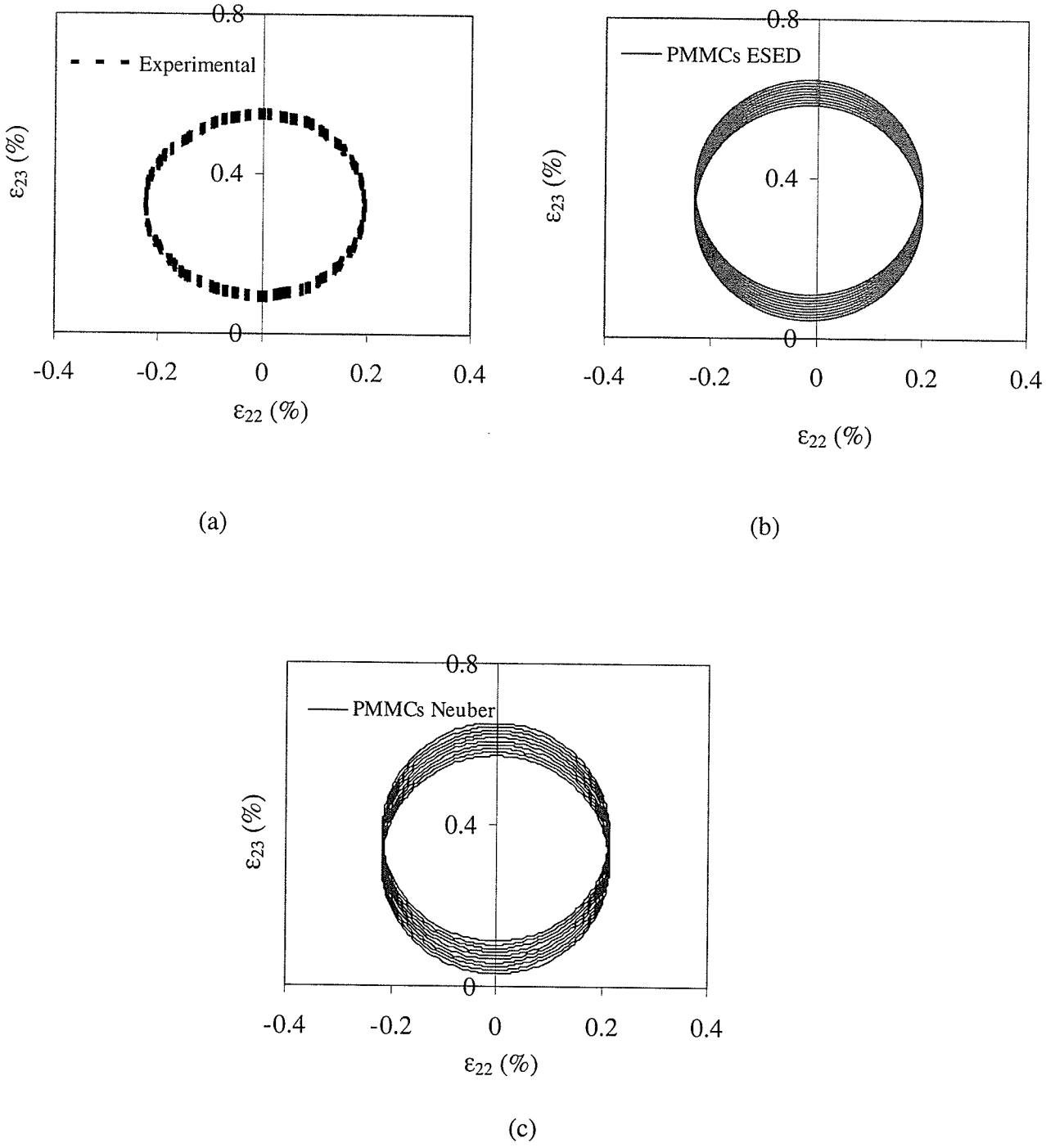

Figure 6.33: Notch Root Shear Strains Vs. Axial Strains for Elliptical-Shape Tension-Torsion Load Path with Non-Zero Mean Stress in Fig. 5.22a for Relatively Sharp Notch, 10% Volume Fraction (a) Experimental (b) PMMCs ESED (c) PMMCs Neuber

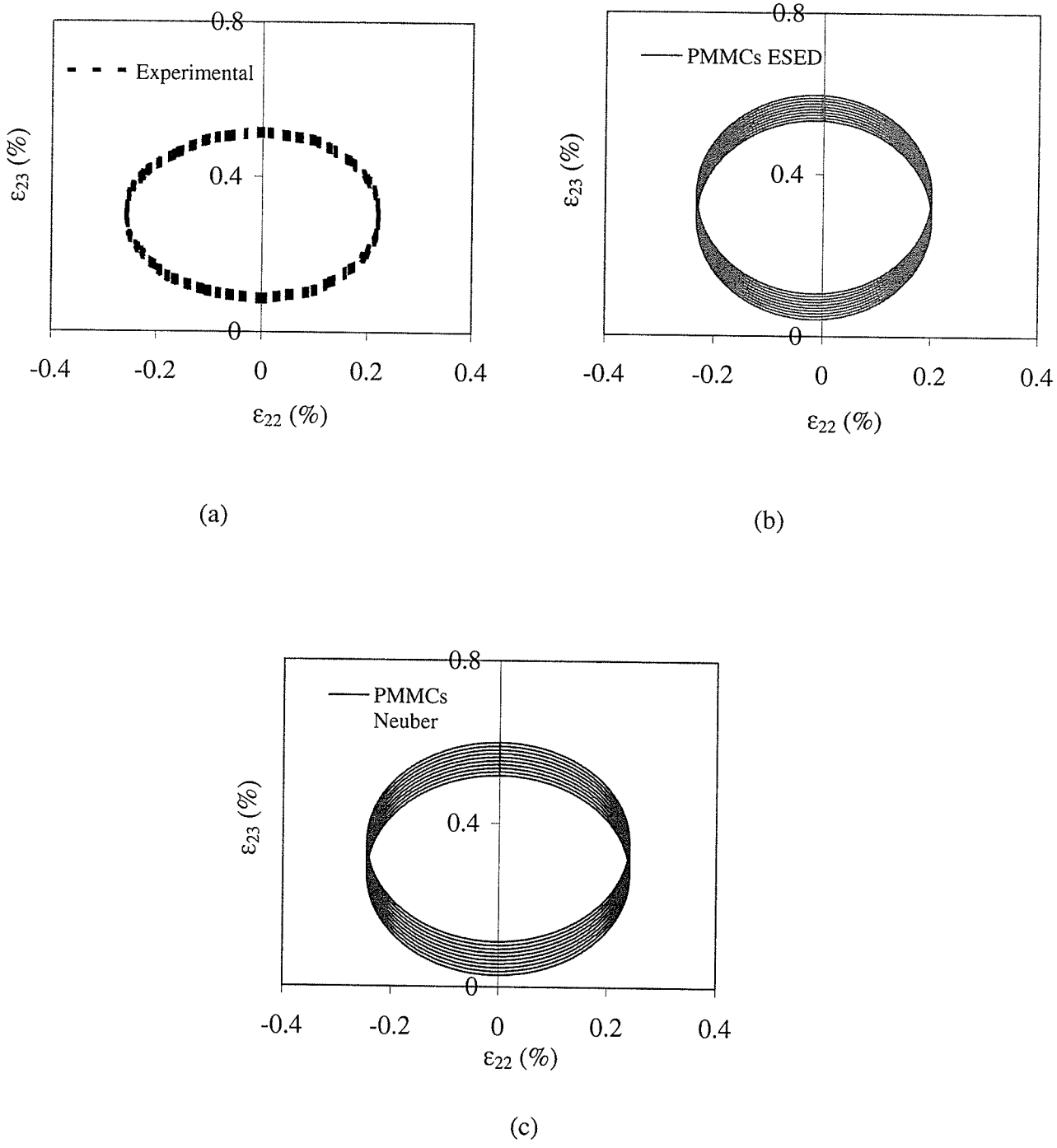

Figure 6.34: Notch Root Shear Strains Vs. Axial Strains for Tension-Torsion Load Path with Non-Zero Mean Stress (Sine Wave) in Fig. 5.22a for Relatively Sharp Notch, 20% Volume Fraction (a) Experimental (b) PMMCs ESED (c) PMMCs Neuber

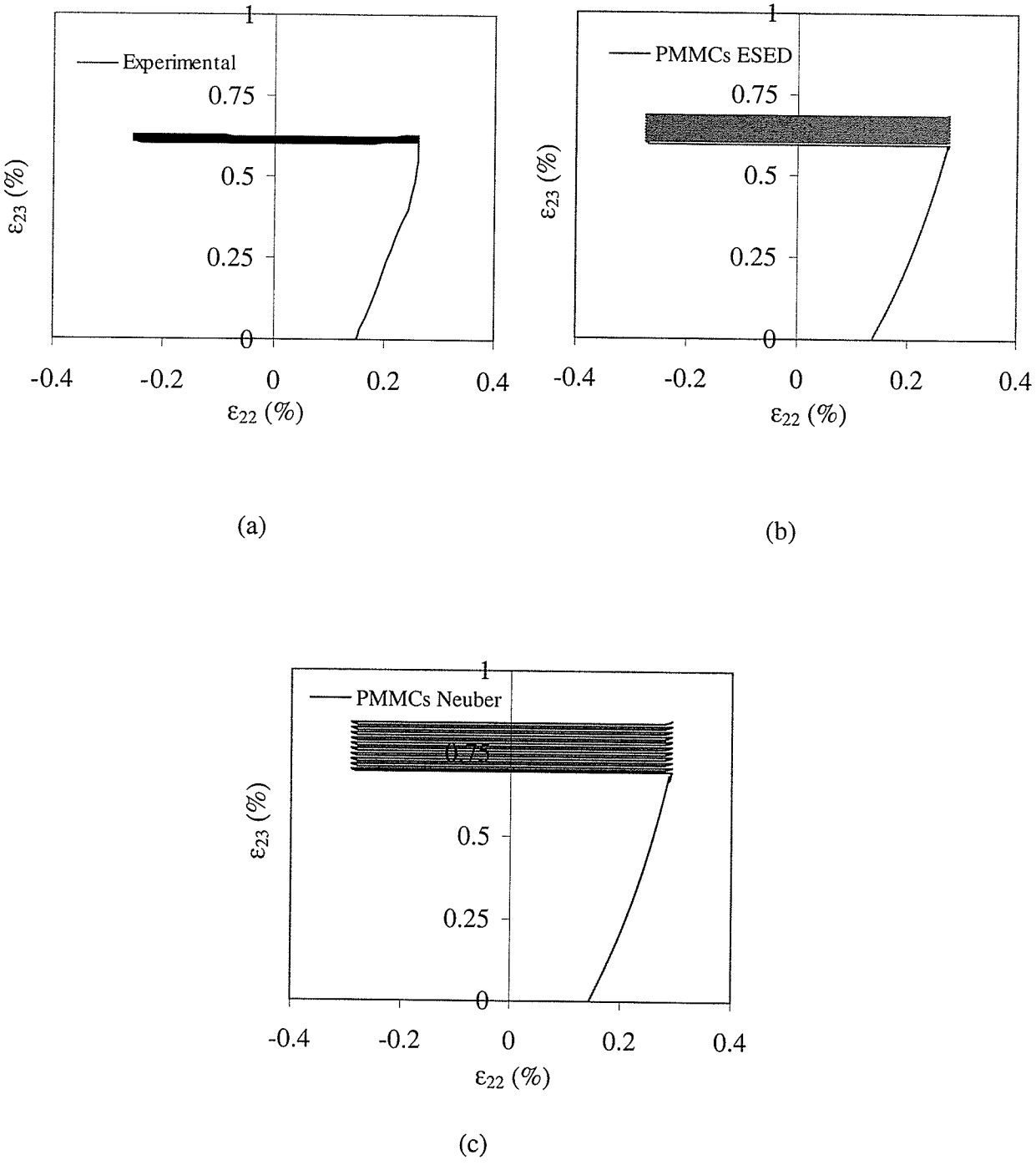

Figure 6.35: Notch Root Shear Strains Vs. Axial Strains for Linear-Shape Tension-Torsion Load Path with Non-Zero Mean Stress in Fig. 5.22b for Relatively Sharp Notch, 10% Volume Fraction (a) Experimental (b) PMMCs ESED (c) PMMCs Neuber

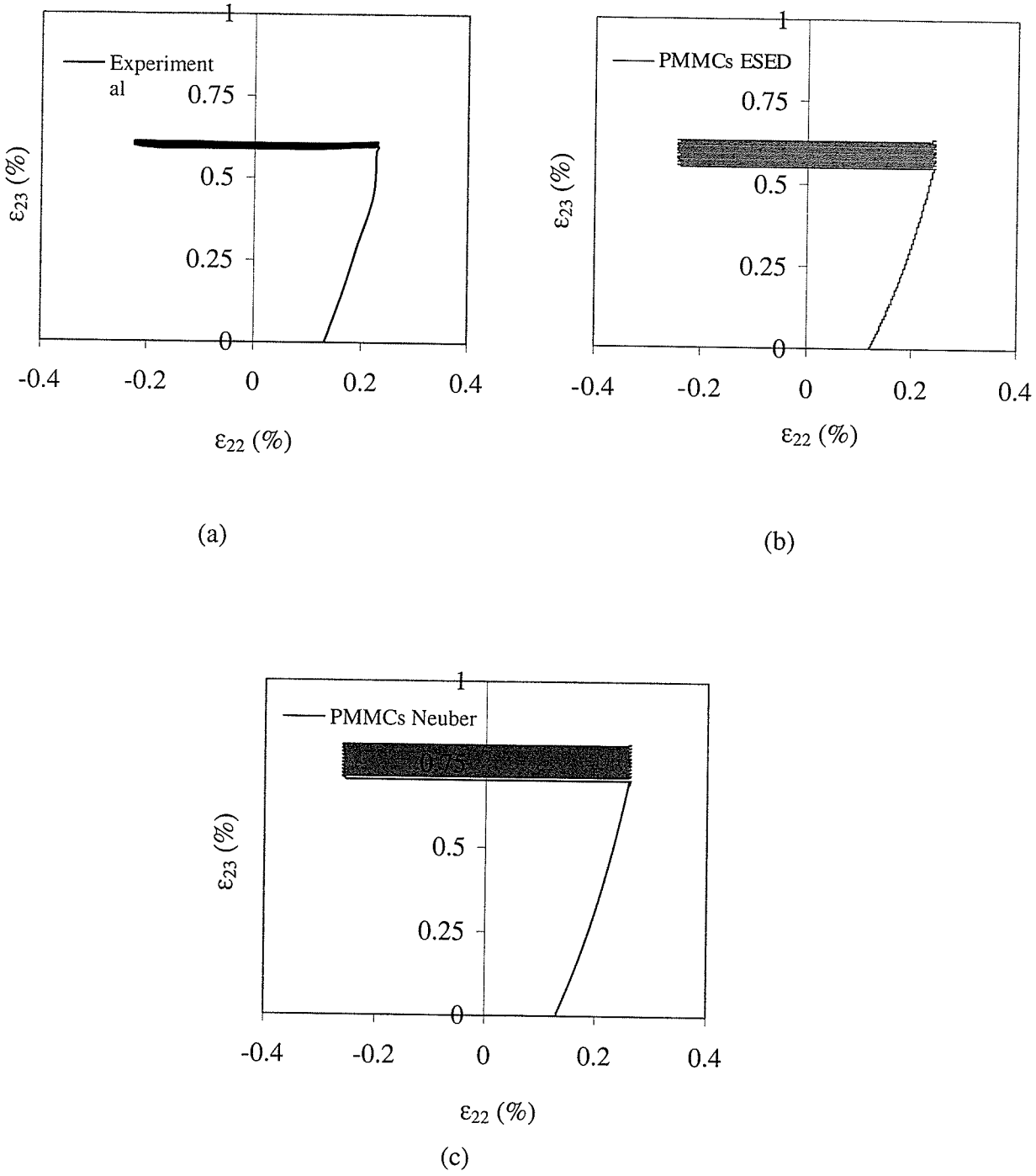

Figure 6.36: Notch Root Shear Strains Vs. Axial Strains for Linear-Shape Tension-Torsion Load Path with Non-Zero Mean Stress in Fig. 5.22b for Relatively Sharp Notch, 20% Volume Fraction (a) Experimental (b) PMMCs ESED (c) PMMCs Neuber

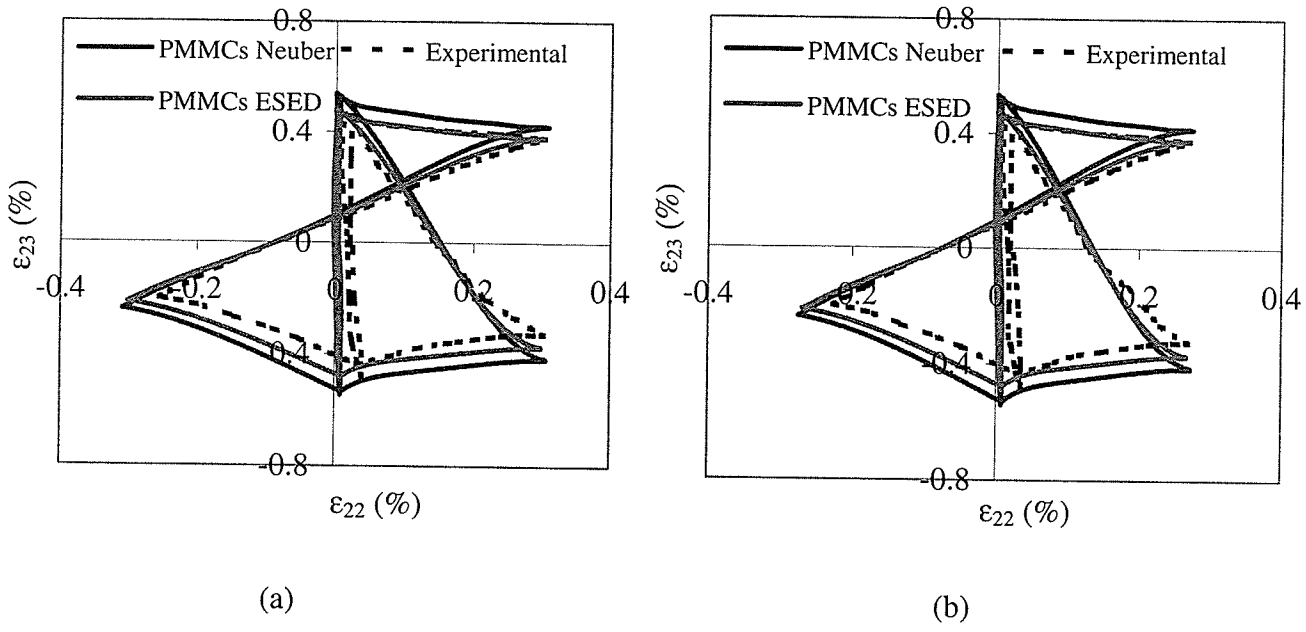

Figure 6.37: Notch Root Shear Strains Vs. Axial Strains for Variable Amplitude Load Path in Fig. 5.23a for Relatively Sharp Notch (a) 10% Volume Fraction (b) 20% Volume Fraction

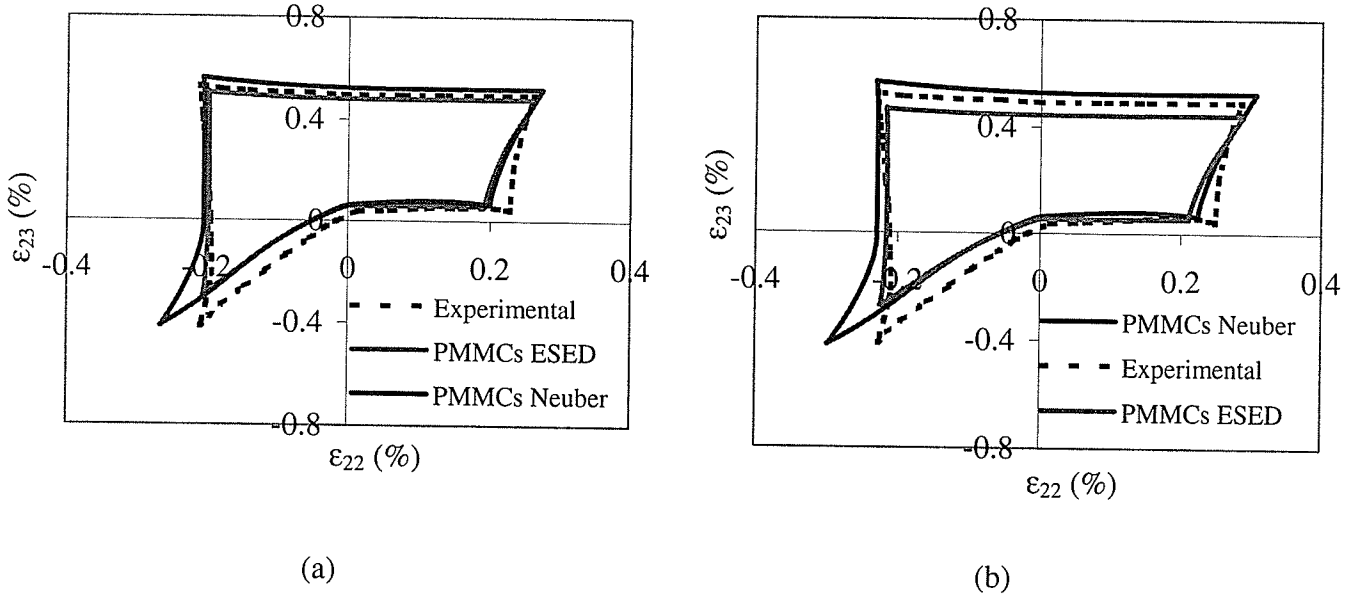

Figure 6.38: Notch Root Shear Strains Vs. Axial Strains for Variable Amplitude Load Path in Fig. 5.22 b for Relatively Sharp Notch (a) 10% Volume Fraction (b) 20% Volume Fraction

CHAPTER SEVEN: CONCLUSIONS AND RECOMMENDATIONS

7.1 Conclusions

As stated in Chapters One and Two, in order to exploit the beneficial properties of PMMCs, complexities in modeling the mechanical behavior of PMMCs in the presence of external (geometric and loading) and internal (heterogeneous, elastic-plastic nature) non-linearities must be overcome. In this thesis, using the proposed PMMCs Neuber's rule and PMMCs ESED method in conjunction with the developed PMMCs elastic-plastic constitutive relations, two simplified methods have been successfully developed and implemented to estimate the composite elastic-plastic strain and stress histories in PMMC components under general loading conditions. Each model provides a complete nonlinear set of equations capable of independently predicting the elastic-plastic strain and stress histories at the notch root of a PMMC component, from an easily obtainable elastic solution. All relations have been developed to respect the heterogeneous nature of PMMCs.

For a complete formulation of the aforementioned set of equations necessary to define the notch root parameters in PMMCs, the development or use of a suitable cyclic constitutive model is first required. However, only a few cyclic plasticity models applicable to PMMC components subjected to non-proportional loading have recently appeared in the literature. In this thesis, two elastic-plastic constitutive models were developed and evaluated for their suitability to model the constitutive behavior of

PMMCs under cyclic non-proportional loading. Specifically, the Mróz multi-surface model and the endochronic theory of plasticity were used in conjunction with the incremental mean field theory and the work principal to predict the constitutive behavior of PMMCs under multiaxial loading. Detailed descriptions of the formulation and procedures for implementing the constitutive models were presented in this thesis. For the purpose of computer implementation, computer flow charts have been shown for the models.

The results obtained using each constitutive model were compared with experimental results obtained using a 3D image correlation device. Based on the experimental tests conducted in this research, the following conclusions could be drawn on the results of the constitutive models. For the investigated load paths, both models predict satisfactorily the amplitudes of the experimental strains. For the proportional loading case, both models predict the trends observed in the experimental results. However, the Mróz-based PMMCs constitutive model over-predicts, while the endochronic theory-based PMMCs constitutive model under-predicts the shear strains. For variable amplitude loading cases, both models can qualitatively predict reasonably the characteristics features of the experimental results. In general, for the load paths considered in this research, qualitatively the endochronic theory-based PMMCs constitutive model gives a better prediction of the experimental results than the Mróz-based PMMCs constitutive model predictions. Some of the factors that could have affected the Mróz-based PMMCs constitutive model predictions, enumerated in Chapter Six, include the number of loading increments and the number of yield surfaces used in its implementation. For small load levels, the number of loading increments and/or yield

surfaces used may not significantly affect the predicted results. However, for high load levels, the numbers of loading increments and yield surfaces have a profound influence on the predicted results. Since a quantitative relation between the number of surfaces, load increments, and the predicted results is difficult to formulate, efforts were made in this research to use a combination of the number of yield surfaces and load increments that gave optimal and convergent results. This is the first attempt to incorporate two cyclic plasticity routines into the development of elastic-plastic constitutive relations for PMMCs components particularly under multiaxial variable amplitude loading conditions.

Either of the developed elastic-plastic PMMCs constitutive models can be used in conjunction with the proposed simplified methods in order to obtain the complete set of nonlinear equations necessary to define the notch root elastic-plastic strain and stress histories. However, the results obtained in the evaluation of the constitutive models show that the endochronic theory-based PMMCs constitutive model should be used in spite of the difficulty in obtaining its materials constants. Endochronic theory-based PMMCs constitutive model is also very promising and versatile, and easier to implement than the Mróz-based PMMCs constitutive model. Detailed descriptions of the formulation of the PMMCs ESED and PMMCs Neuber simplified methods, the coupling of these with the endochronic theory-based PMMCs constitutive model, implementation procedure of the coupled equations, and including the computer flow charts have been given in the thesis.

The validity of the developed models for notch root elastic-plastic strain-stress analysis was assessed by comparing the results obtained with experimental results. A series of biaxial load-controlled tests were performed on notched 6061/Al2O3/xxp-T6 PMMC specimens with 10 and 20% volume fractions of reinforcement under a variety of

loading conditions. The strain fields were obtained from images of several load steps taken by using a 3D image correlation device. A complete understanding of the results was provided because the device was able to provide strain fields and graphically display the experimental results across the notch. The reproducibility and reasonable behavior of the notch root strains obtained in this research shows that 3D image correlation device is a suitable technique for measuring the elastic-plastic strains with reasonable accuracy.

A comparison of the numerical results with the experimental results indicates that both of the developed models are in good agreement with the experimental results. For monotonic loading, it was found that the difference between the models predictions and the experimental results is very small. The results of the monotonic loading also indicate that the PMMC ESED under-predicts, while the PMMC Neuber over-predicts the notch root strains. For the multiaxial non-proportional loading cases considered. In general, both analytical models predict the general trends in and all the characteristic phenomena occurring of the experimental test results. An initially elastic region is observed at the onset of loading or unloading, followed by region of elastic-plastic deformation. At the onset of elastic loading and unloading, both predicted results are very close to the experimental results as expected. In most cases, as the nominally applied loads increase, differences are observed in the estimated and the measured strains. However, unlike in the monotonic case, both models some times over-predict, and some other times under-predict the experimentally obtained notch root strains. It should also be mentioned that the analytical methodologies predict the notch root strains in the materials with both volume fraction of reinforcement for a variety of non-proportional loading paths considered in this research. This is an important finding since the models use only the

material properties of the constituents separately to predict the elastic-plastic behavior for the notched specimens under a variety of loading conditions.

7.2 Recommendations

A basic preview of the research carried out in this thesis is that the test specimens and load paths represent a degree of complexity similar to many existing practical problems. However, more complex situations exist where the models can also be applicable. Some practical engineering problems can be influenced by harsh environments, initial residual stresses, contact loading, and/or multiple out-of-phase applied loads. More theoretical refinements are suggested for future work to incorporate the effects of these variables. For high temperature applications of the models, rate and temperature dependence should also be incorporated. In this research, it was not clear as to which method, the PMMCs Neuber or the PMMCs ESED, yielded better predictions of the experimental elastic-plastic notch root strains. Thus, a procedure for obtaining an optimum result may be pursued in future research. This approach may give results that are closer to the experimental results than those obtained using the two models independently.

Although considerable experimental tests were conducted in this research, it is important to state that more experimental data may still be used to evaluate current and future analytical formulations. Thus, it is recommended that more complex load paths should be tested in future work. However, the implemented experimental program provides a basis for future applications of the proposed models.

Investigations of the ability of the two developed PMMCs elastic-plastic constitutive models to predict the elastic-plastic behavior of PMMCs under variable amplitude loading is critical in engineering design, since it is the most realistic loading type. The results obtained in this research for models indicate that both models can adequately predict the amplitudes of the experimental results. Thus, the results obtained for both models provide a solid foundation for further and more systematic experimental investigations. However, it is suggested that future work should study the effects of different load paths, load increments (for both models) and the number of yields surfaces (Mróz-based PMMCs constitutive model). Since determining the material constants of the endochronic theory-based PMMCs constitutive model is still a very difficult task, future work should also aimed at finding an optimum approach to obtaining them. If the material constants can be easily obtained, particularly for higher number of terms in Eq. (3.53), it is noteworthy that the endochronic theory-based PMMCs constitutive model may predict accurately and with computational ease, the response of the PMMC materials to a variety of loading conditions, without the knowledge of the yield stress associated with the use of classical theory of plasticity.

Finally, it is important to state that the basic elements of fatigue life prediction method, such as inelastic constitutive models for non-proportional loadings and local strain approximation techniques have been adequately covered in this thesis for PMMCs. Possible application of the results include using the predicted notch root strains to determine the fatigue life of notched components made of PMMCs from nominal loadings.

REFERENCES

1 Agarwal, B.D. and Broutman, L.J. (1990), "Analysis and Performance of Fiber Composites," John Wiley and Sons, New York.

2 Lease K.B. (1994), "Deformation and Fatigue of a Particulate Reinforced Metal Matrix Composite," PhD Thesis, University of Iowa, USA.

3 Aluminum Metal Matrix Composites Technology Roadmap, Prepared by Technologies Research Corporation, A Subsidiary of the National Center for Manufacturing Science, Sponsored by ALMMC Consortium, with the Support of The U.S Department of Energy- Office of Industrial Technologies, May 2002.

4 Mortenson A. and Clyne T.W. "Metal Matrix Composites: Challenges and Opportunities,"http://www.mpg.de/pdf/europeanWhiteBook/wb_materials_210_213.pdf

5 Mortenson A. (1994), "Metal Matrix Composites in Industry: an Overview," Laboratoire de Metallugie Mechanique, Department des Materiaux, Ecole Polytechnique Federale de Lausanne, Ch-1015, Lausanne.

6 Lease K.B., Stephens R.I., Jiang Y., and Kurath P. (1996), "Fatigue of a Particulate Reinforced Aluminum Metal Matrix Composites Subjected to Axial, Torsional, and Combined Axial-Torsional Loading Conditions," Fatigue and Fracture of Engineering Materials and Structures, pp. 1031-1043.

7 Suresh S., Mortensen A., and Needleman A. (1993), "Fundamental of Metal Matrix Composites," Butterworth-Heinemann, Soneham, MA.

8 Stephens R.I, Fatemi A., Stephens R.R., and Fuchs H.O. (2000), "Metal Fatigue in Engineering," John Wiley and Sons Inc.

9 Kol S.K, Oh, S.J., and Ellyin F. (1999), "Low Cycle Fatigue of SiC Particulate-Reinforced Al-Si Cast Alloy Composites with Tensile Mean Strain Effects," International Journal of Fatigue, Vol. 21, pp. 1019-1032.

10 Lease K.B., Wu H.C., and Kurath P. (1995), "Elastic-Plastic Multiphase Constitutive Modeling of a Particulate Reinforced Metal Matrix Composite," American Society of Mechanical Engineers, Applied Mechanics Division, AMD, v 202, Micromechanics and Constitutive Modeling of Composite Materials 1995: pp 153-158.

11 Hashin Z. (1965), "On Elastic Behavior of Fibre-Reinforced Materials of Arbitrary Transverse Phase Geometry," Journal of the Mechanics and Physics of Solids, Vol. 13, pp. 119-134.

12 Mura T. and Chen P.C. (1977), "The elastic Field Outside an Ellipsoidal Inclusion," ASME Journal of Applied Mechanics, Vol. 44, 591-594.

13 Weng G.J. (1984), "Some Elastic Properties of Reinforced Solids with Special Reference to Isotropic Ones Containing Spherical Inclusions," Int. Journal of Engineering Science, Vol. 22, No 7, 845-850.

14 Goodier J.N. (1933), "Concentrations of Stress Around Spherical and Cylindrical Inclusions and Flaws," ASME Journal of Applied Mechanics Vol. 5 pp. 39-44.

15 Sadowsky M.A. and Sterberg E. (1952), "On the Axisymmetric Problem of the Theory of Elasticity for an Infinite Region Containing Two Spherical Cavities," ASME Journal of Applied Mechanics Vol. 19 pp 19-27.

16 Eshelby J.D. (1957), "The Determination of the Elastic Field of an Ellipsoidal Inclusion and Related Problems," Proceedings of the Royal Society of London, Vol. A241 pp. 376-396.

17 Hershey A.V. (1954), "The Plasticity of an Isotropic Aggregate of Anisotropic Face-Centered Cubic Crystals," Journal of Applied Mechanics, Vol. 21, pp. 241-249.

18 Kroner E. (1961), "Zur Plastischen Verforming des Veikristalls," Acta Metallurgica, Vol. 9, pp. 151-161.

19 Mori T. and Tanaka K. (1973), "Average Stress in the Matrix and Average Elastic Energy of Materials with Misfitting Inclusions," Acta Metallurgica, Vol. 21, pp 571-574.

20 Hutchison J.W. (1970), "Elastic-plastic Behavior of Polycrystalline Metals and Composites," Proceedings of the Royal Society of London, Vol., A319, pp 247-272.

21 Mori T. and Wakashima K. (1990), "Successive Iteration Method in the Evaluation of Average Fields in Elastically Inhomogeneous Materials," Micromechanic and Inhogeneity: The Toshio Mura 65th Anniversary Volume; Springler, New York, pp 269-282.

22 Ju J.W. and Chen T.M. (1994), "A Micromechanics and Effective Elastic-Plastic Behaviour of Two Phase Metal Matrix Composites," Journal of Engineering Material and Technology", Vol. 116, 310-318.

23 Tandon G.P., and Weng G.J. (1988), "A theory of Particle Reinforced Plasticity," Journal of Applied Mechanics, Vol. 55, 126-145.

24 Li Y.Y. and Chen Y. (1990), "An Incremental Plastic Analysis of Multiphase Materials," Journal of Applied Mechanics, Vol. 57, 562-568.

25 Chaboche J.L. (1986), "Time Independent Constitutive Theories for Cyclic Plasticity," Int. Journal of Plasticity. Vol. 2 No 2, 149-188.

26 Prager W. (1957), "A New Method of Analyzing Stresses and Strains in Work Hardening Plastic Solids," Journal of Applied Mechanics, Vol. 23, pp. 493-496.

27 Ziegler H. (1959), "A Modification of Prager's Hardening Rule," Quarterly of Applied mathematics, Vol. 17 No 1, 55-65.

28 Mróz Z. (1967), "On the Description of Anisotropic Work Hardening," Journal of the Mechanics and Physics of Solids, Vol. 15, 163-175.

29 Armstrong P.J. and Frederick C.O. (1966), "A Mathematical Representation of the Multiaxial Bauschinger Effect," G.E.G.B Report RD/B/N731.

30 Chaboche J.L., Dang V.K., and Cordier G. (1979), "Modelization of the Strain Memory Effect on the Cyclic Hardening of 316 Stainless Steel," Structural Mechanics in Reactor Technology, Trans. Of the Fifth Int. Conf. on Structural Mechanics in Reactor Technology, Div. L Berlin L11/3.

31 Valanis K.C. (1971), "A Theory of Viscoplasticity without a Yield Surface Part I: General Theory," Archives of Mechanics, Vol. 23, 517-533.

32 Hsu S.Y., Jain S.K., and Griffin, O.J. (Jr) (1991), "Verification of Endochronic Theory for Non-Proportional Loading Paths," Journal of Engineering Mechanics, Vol.117, 110-131.

33 Valanis K.C. (1980), "Fundamental Consequences of a New Intrinsic Time Measure: Plasticity as a Limit of the Endochronic Theory," Archives of Mechanics, Vol. 32 171-191.

34 Jain S.K. (1989), "Introduction to the Theories of Plasticity Part I: Stress-Strain Relation," Engineering Publications, Blacksburg, VA.

35 Hunsaker B., Vaughin D.K., and Stricklin, J.A. (1976), " A Comparison of the Capability of Four Hardening Rules to Predict a Material's Plastic Behavior," Journal of pressure Vessel Technology, Trans. ASME, pp. 66-67

36 Lamba H. and Sidebottom D. (1978), "Cyclic Plasticity for Non-Proportional Paths: Part 1-Cyclic Hardening, Erasure of Memory, and Subsequent Strain Hardening Experiments," Journal of Engineering Materials and Technology, Vol. 100, pp. 96-103.

37 Lamba H. and Sidebottom D. (1978), "Cyclic Plasticity for Non-Proportional Paths: Part 2- Comparison with Prediction of Three Incremental Plasticity Models," Journal of Engineering Materials and Technology, Vol. 100, pp. 104-111.

38 Sotolongo W. (1985), "On the Numerical Implementation of Cyclic Elasto-Plastic Material Models," M.S. Thesis, Georgia Institute of Technology, USA.

39 Dafalias Y. and Popov E. (1975), "A Model of Non-Linear Hardening Materials for Complex Loading," Acta Mechanica, Vol. 23, 173-192.

40 Krieg R.D. (1975), "A Practical Two-Surface Plasticity Theory," ASME Journal of Applied Mechanics, Vol. 47, 641-646.

41 Garud Y. (1981), "A New Approach to the Evaluation of Fatigue Under Multiaxial Loading," Journal of Engineering Materials and Technology, Vol. 103, pp. 118-125.

42 Chu C.C. (1984), "A Three-dimensional Model of Anisotropic Hardening in Metals and its Application to the Analysis of Sheet Metal Forming," Journal fo Mechanics and physics of Solids, Vol. 32, pp. 197-212.

43 Valanis K.C. and Read H. (1982), "New Endochronic Plasticity Model for Soils. Soil Mechanics- Transient and Cyclic Loads," Eds. G.N. Pande and O.C. Zienkiewicz). Willey, New York.

44 Valanis K.C. and Lee C.F. (1983), "Some Recent Developments of the Endochronic Theory with Applications," Nuclear Engineering Design, 69, pp. 327-343.

45 Wu H.C. and Wu H.C. (1983), "On the Improved Theory of Viscoplasticity and its Application to Plastic-Wave Propagation," International Journal of Solid Structures, 19, pp. 587-599.

46 Ogarevic V.V. (1992), "Fatigue Behavior and Life Predictions of Particle Reinforced Metal Matrix Composites at Room and Elevated Temperature," PhD Thesis, University of Iowa. USA.

47 Ellyin F. and Xia Z. (1989), "A Rate Independent Constitutive Model for Transient Non-Proportional Loading," Journal of the Mechanics and Physics of Solids, Vol. 37, pp. 71-91.

48 Zihui X., Ellyin F., and Garret M. (1997), "Mechanical Behavior of Al2O3 Particulate Reinforced 6061 Aluminum Alloy under Uniaxial and Multiaxial Cyclic Loading," Journal of Composites Science and Technology, Vol.57, pp. 237-248.

49 Ellyin F., Chinshen L., and Zihui X. (1998), "Mechanical Behavior of Particle-Reinforced Metal Matrix Composite under Multiaxial Loading," Advances in Industrial Materials: Proceedings of the International Symposium, D.S Wilkinson, W.J Poole, and A. Alpas, Eds. pp. 279-288.

50 Neuber H. (1961), "Theory of Stress Concentration in Shear Strained Prismatic Bodies with Arbitrary Non-Linear Stress Law," Journal of Applied Mechanics, Vol. 28, 544-550.

51 Moski K., and Glinka G. (1981), "A Method of Elastic-Plastic Stress-Strain Calculations at the Notch-Root," Material Science and Engineering, Vol. 50, pp. 93-100.

52 Glinka G. (1985), "Calculation of Inelastic Notch-Tip Strain-Stress Histories under Cyclic Loading," Engineering Fracture Mechanics, 22, pp. 839-854.

53 Glinka G., Ott W., and Nowack H. (1988), "Elastoplastic Plane Strain Analysis of Stresses and Strains at the Notch Root," Journal of Engineering Materials and Technology, Vol. 110, pp. 195-204.

54 Walker E.K. (1977), "Multiaxial Stress-Strain Approximations for Notch Fatigue Behavior," Journal of Testing and Evaluation, 5, pp. 106-113.

55 Dowling N.E., Brose W.R., and Wilson W.K. (1979), "Notch Member Fatigue Life Predictions by Local Strain Approach," Advances in Engineering, Vol. 6, edited by Wetzel R.M, SAE, Warrendals, Pa. Pp. 55-84.

56 Topper T.H., Wetzel R.M., and Morrow J. (1969), "Neuber's Rule Applied to Fatigue of Notched Specimens," Journal of Materials, Vol.4 pp. 200-209.

57 Hoffman M. and Seeger T. (1985), "A Generalization Method for Estimating Multiaxial Elastic-Plastic Notch Stresses and Strains," Part 1 and Part 2, Journal of Engineering Materials and Technology," Vol. 107, pp. 250-260.

58 Moftakhar A., Bucznski A., and Glinka G. (1995), "Calculation of Elastic-Plastic Strains and Stress in Notches under Multiaxial Loading," International Journal of Fracture, Vol. 70, pp. 357-373.

59 Barkey M.E. (1993), "Calculation of Notch Strains Under Multiaxial Nominal Loading," PhD Thesis, University of Illinois at Urbana-Champagne.

60 Barkey M.E., Socie D.F., and Hsai K.J. (1994), "A Yield Surface Approach to the Estimation of Notch Strains for Proportional and Non-Proportional Cyclic Loading," Journal of Engineering Materials and Technology. Vol. 116, pp. 173-179.

61 Lee Y., Chiang Y., and Wong H. (1995), "A Constitutive Model for Estimating Notch Strains," Journal of Engineering Materials and Technology, Vol. 117, pp. 33-40.

62 Gu R.J. and Lee Y. (1997), "A New Method for Estimating Non-Proportional Notch Root Stresses and Strains," Journal of Engineering Materials and Technology, Vol. 119, pp. 40-45.

63 Singh M.N.K. (1998), "Notch Tip Stress-Strain Analysis in Bodies Subjected to Non-Proportional Cyclic Loads," PhD Thesis, University of Waterloo, Ontario, Canada.

64 Griffith G.E. (1948), "Experimental Investigation of the Effects of Plastic Flow in a Tension Panel with a Circular Hole," NACA TN 1705.

65 Papirno R. (1971), "Plastic Stress-Strain History at Notch Roots in Tensile Strips under Monotonic Loading," Experimental Mechanics, Vol. 11, pp. 446-452.

66 Yang L. and Ettemeyer A. (2003), "Strain Measurement by Three-Dimensional Electronic Speckle Pattern interferometry: Potentials, Limitations, and Applications," Optical Engineering, 42 (5), pp. 1257-1266.

67 Guillot M.W. and Sharpe W.N. Jr. (1983), "A Technique for Cyclic–Plastic Notch-Strain Measurement," Experimental Mechanics, Vol. 23, pp. 354-360.

68 Sharpe W.N., Yang C.H., and Tregoning R.L. (1992), "An Evaluation of the Neuber and Glinka Relations for Monotonic Loading," Journal of Applied Mechanics, Vol. 59, pp. 50-56.

69 Aramis Users Manual, Version 5, GOM Measurements, Braunschweig, Germany, 2003.

70 Schmidt T. and Tyson, J. (2003), "Advanced Photogrammetry for Robust Deformation and Strain Measurement," Proceedings of the SEM 2003 Annual Conference, Charlotte North Carolina, NC, June 2-4, 8 pages.

71 Sandler I.S. (1978), "On the Uniqueness and Stability of Endochronic Theory of Material Behavior," Journal of Applied Mechanics, Vol. 45, 263-266.

72 Valanis K.C. (1984), "Continuum Foundations of Endochronic Plasticity," Journal of Engineering Materials and Technology, Vol.106, pp.367-375.

73 Fan J. (1983), "A Comprehensive Numerical Study and Experimental Verification of Endochronic Theory, "PhD Thesis, University of Cincinnati, USA.

74 MATLAB Student Version Release 12, Learning MATLAB, (2001) by the Math Works Inc.

75 Duva J.M. and Hutchinson J.W. (1984), "Constitutive Potentials for Dilutely Voided Nonlinear Materials," Mechanics of Materials, 3, 41-54.

76 Instron 8800 Servohydrualic Testing Systems, Operating Instruction, Instron Corporation, 1992.

77 Instron Fast Tack 8800 Materials Test Control System (FastTack Console Version 5): Operating Manual, Instron Corporation, 2000.

78 Schmidt T. (2003), "Personal Correspondence," Trilion Quality System, West Conshohocken, PA, USA.

79 Strain Gages and Accessories, Vishay Micro-Measurements, Available on: www.vishay.com/brands/measurements_groups/strain_gage/mm.htm.

80 2100 System: Strain Gage Conditioner and Amplifier System, Instruction Manual Vishay, 2003.

81 Operation and Calibration Instructions for Dynamic Strain Gage Extensometers, 2620-600 Series, Manual 1-7-68-3, Instron Limited, Buckinghamshire, England.

82 PCI-DAS6402/16, PCI Bus-Compatible Data Acquisition Board User's Manuel, Measurement Computing, Corporation, 2001.

83 Instacal, Vishay Micro_measurements, Available on: http://www.measurementcomputing.com/cbicatalog/cbiproduct.asp?dept_id=265 &pf_id=1385

84 Universal Library, Data Acquisition and Control Programming Tools, User's Guide, Measurement Computing, 2002, 16 Commerce Boulevard, MA, USA.

85 Vee OneLab, User's Guide, Agilent Technologies Inc., Edition 1, 2000.

86 Bill D. (2003), "Personal Correspondence," QED Extrusion Development Inc. San Diego, CA.

87 Standard E606, Annual Book of ASTM Standards, Vol. 03.01, 1995.

88 Wu H.C., Zhiyou X., and Wang P. (1992),"The Shear Stress-Strain Curve Determination from the Tension Test in the Large Strange Range," Journal of Testing and Evaluation, Vol. 20, 6, 192, pp. 396-402.

89 Bannantine J. A. (1989), "Variable Amplitude Multiaxial Fatigue Life Prediction Method," PhD Thesis, University of Illinois at Urbana-Champaign.

90 Peterson R.E. (1974), "Stress Concentration Factors," John Wiley and Sons, New York.